



THE HONG KONG  
POLYTECHNIC UNIVERSITY

香港理工大學

Pao Yue-kong Library

包玉剛圖書館

---

## Copyright Undertaking

This thesis is protected by copyright, with all rights reserved.

**By reading and using the thesis, the reader understands and agrees to the following terms:**

1. The reader will abide by the rules and legal ordinances governing copyright regarding the use of the thesis.
2. The reader will use the thesis for the purpose of research or private study only and not for distribution or further reproduction or any other purpose.
3. The reader agrees to indemnify and hold the University harmless from and against any loss, damage, cost, liability or expenses arising from copyright infringement or unauthorized usage.

### IMPORTANT

If you have reasons to believe that any materials in this thesis are deemed not suitable to be distributed in this form, or a copyright owner having difficulty with the material being included in our database, please contact [lbsys@polyu.edu.hk](mailto:lbsys@polyu.edu.hk) providing details. The Library will look into your claim and consider taking remedial action upon receipt of the written requests.

**BEHAVIOR OF LARGE-SCALE HYBRID FRP-  
CONCRETE-STEEL DOUBLE-SKIN TUBULAR  
COLUMNS SUBJECTED TO CONCENTRIC AND  
ECCENTRIC COMPRESSION**

**XIE PAN**

**Ph.D**

**The Hong Kong Polytechnic University**

**2018**



**The Hong Kong Polytechnic University**

**Department of Civil and Environmental Engineering**

**BEHAVIOR OF LARGE-SCALE HYBRID FRP-  
CONCRETE-STEEL DOUBLE-SKIN TUBULAR  
COLUMNS SUBJECTED TO CONCENTRIC AND  
ECCENTRIC COMPRESSION**

**XIE PAN**

**A thesis submitted in partial fulfilment of the requirements for the  
degree of Doctor of Philosophy**

**March 2018**



## **CERTIFICATE OF ORIGINALITY**

I hereby declare that this thesis is my own work and that, to the best of my knowledge and belief, it reproduces no material previously published or written, nor material that has been accepted for the award of any other degree or diploma, except where due acknowledgement has been made in the text.

(Signed)

---

XIE Pan

(Name of student)

---

*To My Family*

## **ABSTRACT**

Hybrid FRP-concrete-steel double-skin tubular columns (DSTCs) are a new form of hybrid structural members. A hybrid DSTC consists of an outer FRP tube, an inner steel tube, and a concrete infill between them. Hybrid DSTCs have attracted increasing research attention worldwide since their invention due to the many important advantages they possess over conventional structural members, including their excellent corrosion resistance as well as excellent ductility. However, the existing studies on hybrid DSTCs have generally been limited to small-scale specimens. Besides, the use of self-compacting concrete (SCC) has not been paid sufficient attention despite the fact that SCC is obviously more suitable than normal concrete (NC) as the infill material for the relatively narrow annular space of hybrid DSTCs. Against this background, the present thesis presents an in-depth investigation into the structural behavior of large-scale SCC-filled hybrid DSTCs subjected to concentric and eccentric compression. To this end, several issues related to the use of filament-wound FRP tubes and SCC in concrete-filled FRP tubes (CFFTs) are also examined in this thesis as a prerequisite.

The thesis first proposes a compression test method and a hydraulic pressure test method to characterize the longitudinal and the circumferential properties of filament-wound FRP tubes for confining concrete, respectively. A theoretical model for CFFTs subjected to axial compression is next developed, in which the biaxial stress state and the material nonlinearity of the FRP tube are properly accounted for. In parallel, results of concentric compression tests conducted on 23 CFFTs filled with NC or SCC of four different sizes are presented. The test results reveal that the behavior of SCC-filled FRP tubes is appreciably different from that of NC-filled FRP tubes due to the relatively large shrinkage of SCC, especially under weak confinement.

The experimental program on large-scale hybrid DSTCs comprised concentric compression testing of 11 short hybrid DSTCs and eccentric compression testing of six short and nine slender hybrid DSTCs, under various combinations of test parameters, which include mainly the load eccentricity, column slenderness, thickness of FRP tube and void ratio. The majority of the specimens were filled with SCC. The test results show that large-scale hybrid DSTCs possess excellent ductility under both concentric and eccentric compression although the relatively large shrinkage of SCC may lead to a delayed activation of the confinement action of the FRP tube. To capture the effects of slenderness and eccentricity on the behavior of hybrid DSTCs, a theoretical column model, which traces the lateral deflection of columns using the numerical integration method and incorporates an eccentricity-dependent stress-strain model for concrete in hybrid DSTCs, was formulated. It is shown that the column model is accurate in predicting the axial load capacity of hybrid DSTCs and reasonably accurate in predicting the lateral deflection. Finally, a slenderness limit expression, which differentiates short hybrid DSTCs from the slender ones, is proposed, based on the results of a comprehensive parametric study performed using the theoretical column model, to complete an existing design procedure for short hybrid DSTCs.

## LIST OF PUBLICATIONS

### Conference Papers

**Xie, P.**, Lin G., Teng, J.G. and Yu, T. (2017). “Modelling of Concrete-Filled FRP Tubes Considering Nonlinear Biaxial Tube Behavior”, *APFIS2017 - 6th Asia-Pacific Conference on FRP in Structures*, Singapore, 19-21 July.

**Xie, P.**, Yu, T., Wong, Y.L. and Teng, J.G. (2011). “Compression Behavior of Large-scale Hybrid FRP-Concrete-Steel Double-Skin Tubular Columns”, *CEABM2011 - International Conference on Civil Engineering, Architecture and Building Materials*, Haikou, China, 18-20 June.



## **ACKNOWLEDGEMENTS**

First and most importantly, I would like to express my heartfelt gratitude to my supervisor, Prof. Jin-Guang Teng, for providing me with the opportunity to become his student, and for his generous support and enlightening guidance throughout my PhD study. His meticulous attitude towards academic research has deeply affected me and will benefit my whole career. I also greatly appreciate his kind encouragement during difficult times of my PhD study when I contemplated giving it up.

I would also like to express my sincere appreciation to my co-supervisor, Dr. Tao Yu, for his support and guidance from the very beginning of my PhD study. I also owe a debt of gratitude to Drs. Tao Jiang, Lik Lam and Guan Lin, for their invaluable suggestions and constructive comments that helped me complete my PhD thesis and for spending their precious time to help me with the revision of my PhD thesis.

Some of the tests presented in Chapter 6 were conducted at The Hong Kong Polytechnic University (PolyU) when I worked as a Research Assistant under the supervision of Dr Yue-Long Wong and co-supervision of Prof. Jin-Guang Teng and Dr. Tao Yu. I am most grateful to all of them for starting me on this long research journey and for all their help. I also received generous help from PolyU technicians (Messrs. K.H. Wong, M.C. Ng, Y.H. Yiu, T.T. Wai and C.F. Cheung) which is gratefully acknowledged.

I appreciate the help from Profs. Li-Juan Li, Feng Liu, Yong-Chang Guo and Messrs. Zhen-Xiong Wang and Shun-De Xu when I conducted my experimental work at the Structural Engineering Laboratory of Guangdong University of Technology.

My sincere thanks also go to many former and current members of Prof. Teng's research group for their generous help. Special thanks should go to Drs. Guang-Ming Chen, Jun-Liang Zhao, Wan-Yang Gao, Bing Fu, Jun-Jie Zeng, Li Xing and Ms. Ji-Ji Wang not only for their valuable comments and discussions on my research work, but also for their encouragement during my hard times. My appreciation also goes to Drs.

Shi-Shun Zhang, Qiong-Guan Xiao, Bing Zhang, Yu-Lei Bai, Yi-Nan Yang, Jing-Yun Wu, Zi-Hao Wang, Wei Qiu and Cheng Jiang as well as Messrs. Xiao-Liang Fang, Xue-Fei Nie, Qing-Kai Wang, Jie-Kai Zhou, Pan Zhang, Kai-Cheng Liu and Tao Ding, and Ms. Yue-Xin Zhang, Ms. Yi-wen Zhang for their constructive discussions.

I am very grateful to my colleagues and friends in the College of Water Conservancy and Civil Engineering, South China Agriculture University. Thanks should go to Profs. Pei-Tong Cong, Xiao-Yan Xie, Cun-En Chen and Jiu-Hao Li, and Messrs. Ze-Hua Long, Xiao-Dong Chen and Gui-Long Zhong, as well as many others. Without their help and support, I would not have had a chance to embark on my PhD study.

Last but certainly not least, my deepest thanks would go to my beloved family, to whom this thesis is dedicated. Without their everlasting love and great understanding through all these years, it is inconceivable that I could have persisted in finishing my PhD study. I wish to express my profound gratitude to my parents and my mother-in-law for their help in taking care of my two sons during the course of my PhD study. My special thanks go to my husband, Zi-Ming Lv, for his initiative to take over much of my responsibility towards our family and his encouragement and patience through all these years. I owe my deepest apologies to my sons, Mo-Ya and Mo-Xiu, for missing many important moments of your growing-up. Nevertheless, I hope that the most precious fortune I reaped from my experience of PhD study, persistence and composedness, will take root in your young hearts and guide your future exploration of the world.

# CONTENTS

<b>CERTIFICATE OF ORIGINALITY .....</b>	<b>I</b>
<b>ABSTRACT</b>	<b>III</b>
<b>LIST OF PUBLICATIONS .....</b>	<b>V</b>
<b>ACKNOWLEDGEMENTS.....</b>	<b>VII</b>
<b>CONTENTS</b>	<b>IX</b>
<b>LIST OF FIGURES .....</b>	<b>XVII</b>
<b>LIST OF TABLES.....</b>	<b>XXII</b>
<b>LIST OF ACRONYMS.....</b>	<b>XXIII</b>
<b>NOTATION .....</b>	<b>XXIV</b>
<b>CHAPTER 1 INTRODUCTION.....</b>	<b>1</b>
1.1 BACKGROUND .....	1
1.2 HYBRID FRP-CONCRETE-STEEL DOUBLE-SKIN TUBULAR MEMBERS .....	3
1.3 ISSUES RELATED TO THE USE OF FILAMENT-WOUND FRP TUBES AND SELF-COMPACTING CONCRETE.....	5
1.4 RESEARCH OBJECTIVES .....	8
1.5 LAYOUT OF THE THESIS .....	9
1.6 REFERENCES.....	13
<b>CHAPTER 2 LITERATURE REVIEW.....</b>	<b>25</b>
2.1 INTRODUCTION .....	25

2.2 FILAMENT-WOUND FRP TUBES.....	25
2.2.1 Fabrication Method of Filament-Wound FRP Tubes .....	25
2.2.2 Test methods for FRP composites.....	26
2.3 NONLINEAR BIAXIAL BEHAVIOR OF FILAMENT-WOUND FRP TUBES IN CFFTS .....	28
2.4 FRP-CONFINED SELF-COMPACTING CONCRETE .....	30
2.5 EFFECT OF SIZE ON THE BEHAVIOR OF FRP-CONFINED CONCRETE.....	32
2.6 STRESS-STRAIN MODELS FOR FRP-CONFINED CONCRETE.....	34
2.6.1 General .....	34
2.6.2 Design-oriented stress-strain models .....	36
2.6.3 Analysis-oriented stress-strain models.....	40
2.7 HYBRID FRP-CONCRETE-STEEL DOUBLE-SKIN TUBULAR COLUMNS .....	42
2.7.1 General .....	42
2.7.2 Hybrid DSTCs subjected to concentric compression.....	45
2.7.3 Hybrid DSTCs subjected to eccentric compression.....	49
2.8 REFERENCES.....	51

<b>CHAPTER 3 CHARACTERIZATION OF LONGITUDINAL AND CIRCUMFERENTIAL PROPERTIES OF FILAMENT-WOUND FRP TUBES .....</b>	<b>73</b>
3.1 INTRODUCTION .....	73
3.1.1 Test Methods for Strip Specimens .....	74
3.1.2 Test Methods for Ring Specimens .....	74
3.1.3 Test Methods for Tube Specimens .....	76
3.2 STRIP TESTS FOR LONGITUDINAL TENSILE PROPERTIES OF FILAMENT-WOUND GFRP TUBES.....	78

3.3 STRIP TESTS FOR LONGITUDINAL COMPRESSIVE PROPERTIES OF FILAMENT-WOUND GFRP TUBES.....	79
3.4 SPLIT DISK TESTS FOR HOOP MODULUS OF ELASTICITY OF FILAMENT-WOUND GFRP TUBES.....	80
3.5 TUBE TESTS FOR LONGITUDINAL COMOPRESSIVE PROPERTIES FOR FILAMENT-WOUND GFRP TUBES .....	83
3.6 TESTS FOR HOOP PROPERTIES OF FILAMENT-WOUND GFRP TUBES UNDER INTERNAL HYDRAULIC PRESSURE .....	84
3.7 CONCLUSIONS.....	87
3.8 REFERENCES.....	89

**CHAPTER 4 EFFECT OF SELF-COMPACTING CONCRETE ON THE  
BEHAVIOR OF LARGE-SCALE CONCRETE-FILLED FRP TUBES.. 115**

4.1 INTRODUCTION .....	115
4.2 EXPERIMENTAL PROGRAM.....	117
4.2.1 Specimen Details.....	117
4.2.2 Concrete Mixtures.....	118
4.2.3 Filament-Wound GFRP tubes .....	118
4.2.4 Preparation of Test Specimens .....	119
4.2.5 Test Setup and Instrumentation.....	120
4.3 TEST RESULTS AND DISCUSSIONS .....	121
4.3.1 Failure Mode .....	121
4.3.2 FRP Hoop Rupture Strains.....	122
4.3.3 Load Capacity and Ultimate Axial Strain .....	123
4.3.4 Stress-Strain Responses .....	124
4.3.5 Lateral Strain and Dilation Properties of Confined Concrete .....	125
4.3.6 Effect of SCC on the Behavior of CFFT Specimens .....	127
4.4 CONCLUSIONS.....	128

4.5 REFERENCES.....	129
---------------------	-----

## **CHAPTER 5 MODELING OF CONCRETE-FILLED FRP TUBES**

<b>CONSIDERING NONLINEAR BIAXIAL TUBE BEHAVIOR.....</b>	<b>149</b>
---	------------

5.1 INTRODUCTION .....	149
------------------------	-----

5.2 BIAXIAL BEHAVIOR OF FRP TUBE.....	151
---------------------------------------	-----

5.3 NONLINEAR ANALYSIS OF FRP LAMINAE.....	152
--	-----

5.3.1 Hahn and Tsai's (1973) model .....	152
--	-----

5.3.2 Jones and Nelson's (1975) model .....	154
---	-----

5.4 TEST SPECIMENS .....	155
--------------------------	-----

5.4.1 Concrete-Filled GFRP Tubes .....	155
--	-----

5.4.2 Nonlinear Properties of GFRP tubes.....	156
---	-----

5.4.2.1 Hahn and Tsai's (1973) model .....	156
--	-----

5.4.2.2 Jones and Nelson's (1975) model .....	157
---	-----

5.5 COMPARISON FOR NC-FILLED FRP TUBES BASED ON JIANG AND TENG'S (2007) MODEL.....	159
---	-----

5.5.1 Analysis Procedure.....	159
-------------------------------	-----

5.5.2 Comparison and Discussions .....	161
--	-----

5.6 COMPARISON WITH JIANG AND TENG'S (2007) MODEL FOR NC, SCC AND SCEC-FILLED FRP TUBES .....	164
--	-----

5.7 CONCLUSIONS.....	165
----------------------	-----

5.8 REFERENCES.....	167
---------------------	-----

## **CHAPTER 6 LARGE-SCALE HYBRID DSTCS SUBJECTED TO**

<b>CONCENTRIC COMPRESSION.....</b>	<b>193</b>
------------------------------------	------------

6.1 INTRODUCTION .....	193
------------------------	-----

6.2 EXPERIMENTAL PROGRAM.....	194
-------------------------------	-----

6.2.1 Specimen Details.....	194
-----------------------------	-----

6.2.2 Material Properties .....	196
6.2.2.1 Properties of GFRP tubes.....	196
6.2.2.2 Properties of concrete.....	196
6.2.2.3 Properties of steel tubes .....	196
6.2.3 Specimen Preparation.....	197
6.2.4 Test Setup and Instrumentation .....	198
6.3 TEST RESULTS AND DISCUSSIONS .....	199
6.3.1 Test Observations .....	199
6.3.2 Axial Strain .....	199
6.3.3 Hoop Rupture Strain .....	200
6.3.4 Total Axial Load-Axial Strain Curves.....	201
6.3.5 Key Test Results.....	204
6.3.6 Axial Stress-Axial Strain Behavior of Concrete in Hybrid DSTCs	207
6.3.6.1 Effects of type of concrete and FRP tube.....	207
6.3.6.2 Effect of number of fiber layers .....	208
6.3.6.3 Effect of void ratio .....	208
6.4 COMPARISON WITH A STRESS-STRAIN MODEL.....	209
6.4.1 Yu <i>et al.</i> 's (2010a) Model for Hybrid DSTCs.....	209
6.4.2 Comparison with Yu <i>et al.</i> 's (2010a) model.....	212
6.5 CONCLUSIONS.....	212
6.6 REFERENCES.....	214

<b>CHAPTER 7 LARGE-SCALE SHORT HYBRID DSTCS SUBJECTED TO ECCENTRIC COMPRESSION.....</b>	<b>245</b>
7.1 INTRODUCTION .....	245
7.2 EXPERIMENTAL PROGRAM.....	247
7.2.1 Specimen Details.....	247
7.2.2 Material Properties .....	248

7.2.3 Specimen Preparation.....	248
7.2.4 Test Setup and Instrumentation.....	249
<b>7.3 TEST RESULTS AND DISCUSSIONS .....</b>	<b>251</b>
7.3.1 Test Observations .....	251
7.3.2 Axial Strain Distribution over Mid-height Section .....	251
7.3.3 Column Lateral Deflection.....	252
7.3.4 Axial Load-Axial Strain Response.....	253
7.3.5 Key Test Results.....	255
<b>7.4 THEORETICAL ANALYSIS .....</b>	<b>255</b>
7.4.1 Eccentricity-Dependent (EccD) Stress-Strain Models.....	255
7.4.1.1 Yu et al.'s (2010b) EccD Model.....	256
7.4.1.2 Lin's (2016) EccD Model .....	257
7.4.2 Theoretical Column Model .....	258
7.4.3 Comparison with Test Results.....	262
7.4.4 Axial Load-Bending Moment Interaction Diagrams.....	264
<b>7.5 CONCLUSIONS.....</b>	<b>265</b>
<b>7.6 REFERENCES.....</b>	<b>266</b>

**CHAPTER 8 LARGE-SCALE SLENDER HYBRID DSTCS SUBJECTED TO ECCENTRIC COMPRESSION..... 293**

<b>8.1 INTRODUCTION .....</b>	<b>293</b>
<b>8.2 EXPERIMENTAL PROGRAM.....</b>	<b>295</b>
8.2.1 Specimen Details.....	295
8.2.2 Material Properties.....	296
8.2.3 Specimen Preparation.....	296
8.2.4 Test Setup and Instrumentation.....	297
<b>8.3 TEST RESULTS AND DISCUSSIONS .....</b>	<b>298</b>
8.3.1 Test Observations .....	298

8.3.2 Axial Strain Distribution over Mid-height Section .....	300
8.3.3 Column Lateral Deflection.....	301
8.3.4 Axial Load-Axial Strain and Axial Load-Lateral Deflection Responses .....	301
8.3.4.1 Effect of load eccentricity .....	302
8.3.4.2 Effect of slenderness .....	302
8.3.4.3 Effect of thickness of GFRP tube.....	303
8.3.5 Key Test Results.....	304
8.4 THEORETICAL ANALYSIS .....	305
8.4.1 Comparison with Test Results.....	305
8.4.2 Axial Load-Bending Moment Interaction Diagrams.....	307
8.5 CONCLUSIONS.....	309
8.6 REFERENCES.....	311
<b>CHAPTER 9 SLENDERNESS LIMIT FOR SHORT HYBRID DSTCS.....</b>	<b>347</b>
9.1 INTRODUCTION .....	347
9.2 DEFINITION OF SLENDERNESS LIMIT .....	349
9.2 ANALYTICAL APPROACH .....	349
9.3 PARAMETRIC STUDY .....	350
9.3.1 Parameters Considered.....	350
9.3.2 Results of Parametric Study .....	353
9.4 PROPOSED SLENDERNESS LIMIT EXPRESSION .....	357
9.4.1 Slenderness Limit Expression Proposed by Jiang and Teng (2012b) .....	357
9.5 CONCLUSIONS.....	360
9.6 REFERENCES.....	361
<b>CHAPTER 10 CONCLUSIONS .....</b>	<b>373</b>



## LIST OF FIGURES

<b>Figure 1. 1</b> Corrosion failure of bridge deck slabs, beams and piers .....	24
<b>Figure 1. 2</b> Typical cross section forms of hybrid DSTMs .....	24
<b>Figure 2. 1</b> Filament winding process .....	69
<b>Figure 2. 2</b> Strip specimens .....	69
<b>Figure 2. 3</b> The compression test fixture.....	70
<b>Figure 2. 4</b> Split disk test.....	70
<b>Figure 2. 5</b> Illustration of the assembled compression fixture and specimen ...	71
<b>Figure 2. 6</b> Typical arrangements for pressure testing of pipes [ISO 7509 (2015)]: (a) Testing with end thrust; (b) Testing without end thrust, external seals; and (c) Testing without end thrust, internal seals .....	71
<b>Figure 2. 7</b> Treatments for axial load resisted by FRP tube in a CFFT specimen .....	72
<b>Figure 3. 1</b> Strip specimen for tension test and tension test setup .....	100
<b>Figure 3. 2</b> Tensile stress-strain curves of FRP strip specimens .....	100
<b>Figure 3. 3</b> Failure mode of FRP strip specimens .....	101
<b>Figure 3. 4</b> Strip specimen for compression test and compression test setup .	101
<b>Figure 3. 5</b> Results of compression test on FRP strip specimens.....	102
<b>Figure 3. 6</b> Failure mode of compression test on FRP strip specimens .....	103
<b>Figure 3. 7</b> Development of a ring specimen .....	103
<b>Figure 3. 8</b> Setup of split disk tests .....	103
<b>Figure 3. 9</b> Location of gauge section .....	104
<b>Figure 3. 10</b> Location of failure section .....	104
<b>Figure 3. 11</b> Results of split disk tests (Position-1).....	105
<b>Figure 3. 12</b> Results of split disk tests (Position-2).....	106
<b>Figure 3. 13</b> Relationship between pull force and radial stress.....	106
<b>Figure 3. 14</b> Loading platens with a groove to fit the ends of tube specimen.	107
<b>Figure 3. 15</b> Compression test setup for filament-wound GFRP tubes.....	107

<b>Figure 3. 16</b>	Failure mode of compression tests on bare GFRP tubes .....	107
<b>Figure 3. 17</b>	Results of compression tests on bare GFRP tubes.....	109
<b>Figure 3. 18</b>	Hydraulic pressure test setup .....	110
<b>Figure 3. 19</b>	Failure mode of hydraulic pressure test.....	111
<b>Figure 3. 20</b>	Tension tests of steel screws .....	111
<b>Figure 3. 21</b>	Test results of tension test of steel screws .....	112
<b>Figure 3. 22</b>	Results of hydraulic pressure tests on GFRP tubes .....	113
<b>Figure 4. 1</b>	Slump flow of SCC.....	137
<b>Figure 4. 2</b>	Control cylinder test.....	137
<b>Figure 4. 3</b>	Preparation of filament-wound GFRP tubes.....	137
<b>Figure 4. 4</b>	Strain measurement of specimens filled with SCEC .....	138
<b>Figure 4. 5</b>	Expansive strains of Specimen SE-3-400-II.....	138
<b>Figure 4. 6</b>	Test setup of large-scale specimens .....	138
<b>Figure 4. 7</b>	LVDT and strain gauge layout for 300-mm and 400-mm diameter specimens .....	139
<b>Figure 4. 8</b>	Failure mode of CFFT specimens.....	140
<b>Figure 4. 9</b>	FRP hoop rupture strains .....	140
<b>Figure 4. 10</b>	Load-axial strain curves.....	142
<b>Figure 4. 11</b>	Normalized axial stress-strain curves .....	144
<b>Figure 4. 12</b>	Normalized lateral strain-axial strain curves .....	146
<b>Figure 4. 13</b>	Normalized axial stress-volumetric strain curves.....	148
<b>Figure 5. 1</b>	Principal material axes of a composite lamina .....	171
<b>Figure 5. 2</b>	Compression test of a bare GFRP tube.....	171
<b>Figure 5. 3</b>	Hydraulic test of a bare GFRP tube .....	171
<b>Figure 5. 4</b>	Material property-versus-strain energy density curves.....	172
<b>Figure 5. 5</b>	Comparison of Axial load-strain curves of NC-filled FRP tube specimens.....	175
<b>Figure 5. 6</b>	Flowchart of generation of axial load-strain curves of CFFTs considering nonlinear biaxial tube behavior based on Jones and Nelson's	

(1975) model .....	176
<b>Figure 5. 7</b> Flowchart of generation of axial load-strain curves of CFFTs considering nonlinear biaxial tube behavior based on Hahn and Tsai's (1973) model .....	177
<b>Figure 5. 8</b> Contribution of FRP tube to total axial load .....	180
<b>Figure 5. 9</b> Performance of Jiang and Teng's (2007) model .....	192
<b>Figure 6. 1</b> Cross section of hybrid DSTCs .....	222
<b>Figure 6. 2</b> Test setup and buckling of bare steel tubes under axial compression .....	222
<b>Figure 6. 3</b> Axial load-axial strain curves of bare steel tubes .....	223
<b>Figure 6. 4</b> Layout of strain gauges and LVDTs .....	223
<b>Figure 6. 5</b> Setup for concentric compression tests on DSTCs.....	223
<b>Figure 6. 6</b> Failure mode of hybrid DSTCs under axial compression.....	225
<b>Figure 6. 7</b> Global buckling of the inner steel tube of hybrid DSTCs .....	226
<b>Figure 6. 8</b> Comparison of axial strains obtained by different ways.....	226
<b>Figure 6. 9</b> Distribution of hoop rupture strains.....	226
<b>Figure 6. 10</b> Total axial load-axial strain curves .....	227
<b>Figure 6. 11</b> Development of strains during tests.....	230
<b>Figure 6. 12</b> Contribution of FRP tube, concrete and steel tube to total axial load.....	234
<b>Figure 6. 13</b> Effects of type of concrete and FRP tube .....	235
<b>Figure 6. 14</b> Effect of FRP thickness.....	237
<b>Figure 6. 15</b> Effect of void ratio .....	239
<b>Figure 6. 16</b> Comparison of axial stress-axial strain curves of concrete in hybrid DSTCs.....	243
<b>Figure 7. 1</b> Layout of strain gauges and LVDTs .....	274
<b>Figure 7. 2</b> End loading assembly .....	275
<b>Figure 7. 3</b> Local failure of specimen CE325-10-P4N-100 (damaged) .....	275
<b>Figure 7. 4</b> Steel cap of eccentrically-loaded DSTCs .....	276

<b>Figure 7. 5</b> Setup of eccentric compression tests on DSTCs .....	276
<b>Figure 7. 6</b> Failure mode of eccentrically-loaded DSTCs.....	278
<b>Figure 7. 7</b> Buckling of inner steel tube .....	279
<b>Figure 7. 8</b> Axial strain distributions over the mid-height section .....	281
<b>Figure 7. 9</b> Lateral deflections along column height.....	283
<b>Figure 7. 10</b> Effect of eccentricity on axial load-axial strain response .....	284
<b>Figure 7. 11</b> Effect of thickness of FRP tube on axial load-axial strain response .....	285
<b>Figure 7. 12</b> Diagram of EccD stress-strain model .....	285
<b>Figure 7. 13</b> Axial stress-axial strain curve of the simple model for FRP tubes .....	286
<b>Figure 7. 14</b> Axial load-axial strain at extreme compression fiber curves .....	288
<b>Figure 7. 15</b> Axial load-lateral deflection curves .....	290
<b>Figure 7. 16</b> Axial load-moment interaction diagrams.....	291
<b>Figure 8. 1</b> Schematic diagram of eccentrically-loaded slender DSTCs.....	318
<b>Figure 8. 2</b> Construction of the corbel ends of eccentrically-loaded slender DSTCs.....	319
<b>Figure 8. 3</b> Layout of strain gauges and LVDTs of Specimen C6-11-50 .....	320
<b>Figure 8. 4</b> Test setup of eccentrically-loaded slender DSTCs .....	321
<b>Figure 8. 5</b> General view of all slender hybrid DSTCs after tests .....	322
<b>Figure 8. 6</b> Failure mode of slender eccentrically loaded hybrid DSTCs.....	328
<b>Figure 8. 7</b> General view of steel tubes after test .....	329
<b>Figure 8. 8</b> Close-up view of steel tubes after test .....	329
<b>Figure 8. 9</b> Axial strain distribution over mid-height section .....	332
<b>Figure 8. 10</b> Lateral deflections along column height.....	335
<b>Figure 8. 11</b> Effect of eccentricity .....	336
<b>Figure 8. 12</b> Effect of slenderness .....	337
<b>Figure 8. 13</b> Effect of thickness of GFRP tube .....	338
<b>Figure 8. 14</b> Comparisons between experimental and predicted axial load-axial	

strain at extreme compression fiber curves.....	341
<b>Figure 8. 15</b> Comparisons between experimental and predicted axial load- lateral deflection curves .....	344
<b>Figure 8. 16</b> Experimental axial load-bending moment loading paths and theoretical section interaction diagrams.....	345
<b>Figure 8. 17</b> Interaction diagrams of hybrid DSTCs.....	346
<b>Figure 9. 1</b> Effect of end eccentricity ratio.....	364
<b>Figure 9. 2</b> Effect of normalized eccentricity ratio .....	365
<b>Figure 9. 3</b> Effect of strength enhancement ratio .....	366
<b>Figure 9. 4</b> Effect of strain ratio .....	367
<b>Figure 9. 5</b> Effect of void ratio .....	368
<b>Figure 9. 6</b> Effect of steel tube diameter-to-thickness ratio .....	369
<b>Figure 9. 7</b> Performance of Eq. (9.1) based on 5% axial load reduction criterion .....	370
<b>Figure 9. 8</b> Performance of Eq. (9.3) based on 5% axial load reduction criterion .....	370
<b>Figure 9. 9</b> Performance of Eq. (9.3) based on 10% axial load reduction criterion .....	371

## LIST OF TABLES

<b>Table 3. 1</b> ASTM and ISO standards for FRP composite testing.....	94
<b>Table 3. 2</b> Results of tension tests using the strip method.....	96
<b>Table 3. 3</b> Results of compression tests using the strip method .....	97
<b>Table 3. 4</b> Hoop modulus of elasticity from split disk tests (GPa).....	97
<b>Table 3. 5</b> Longitudinal properties of filament-wound GFRP tube in compression .....	98
<b>Table 3. 6</b> Hoop modulus of elasticity of filament-wound GFRP tubes.....	99
<b>Table 4. 1</b> Geometric and material properties of specimens.....	134
<b>Table 4. 2</b> Proportions of concrete mixtures.....	135
<b>Table 4. 3</b> Expansive strains in FRP tubes for Series SE specimens at final measurement .....	135
<b>Table 4. 4</b> Key test results.....	136
<b>Table 5. 1</b> Constants in Jones and Nelson’s model.....	170
<b>Table 6. 1</b> Geometrical and material properties of DSTC specimens .....	219
<b>Table 6. 2</b> Key test results of concentrically-loaded DSTCs.....	220
<b>Table 7. 1</b> Geometric and material properties of DSTC specimens .....	271
<b>Table 7. 2</b> Key test results of eccentrically-loaded DSTCs .....	272
<b>Table 8. 1</b> Geometric and material properties of DSTC specimens .....	315
<b>Table 8. 2</b> Key test results of eccentrically-loaded slender DSTCs.....	316
<b>Table 9. 1</b> Values of parameters considered in the parametric study.....	363

## LIST OF ACRONYMS

1D	one dimensional
2D	two dimensional
3D	three dimensional
AFRP	aramid fiber-reinforced polymer
CFFTs	concrete-filled FRP tubes
CFRP	carbon fiber-reinforced polymer
DSTBs	FRP-concrete-steel double-skin tubular beams
DSTCs	FRP-concrete-steel double-skin tubular columns
DSTMs	FRP-concrete-steel double-skin tubular members
EC	expansive cement
EccD	eccentricity-dependent
EccI	eccentricity-independent
FE	finite element
FLAC	full lightweight aggregate concrete
FRP	fiber-reinforced polymer
GFRP	glass fiber-reinforced polymer
HSC	high strength concrete
H&T	Hahn and Tsai's (1973) model
J&N	Jones and Nelson's (1975) model
LVDT	linear variable displacement transducer
NC	normal concrete
PET	polyethylene terephthalate
PolyU	The Hong Kong Polytechnic University
RC	reinforced concrete
SCC	self-compacting concrete
SCEC	self-compacting expansive concrete

## NOTATION

$A_c$	cross-section area of concrete
$A_i$	initial value for the $i$ th material property
$A_{in}$	area enclosed by the inner wall of an FRP tube
$A_{frp}$	cross-section area of an FRP tube
$A_g$	gross area of a column section
$A_s$	cross-sectional area of a steel tube
$a, b$	constants in Eqs. (5.10) and (5.11)
$B, C$	constants in Eqs. (5.10) and (5.11)
$B_i, C_i$	constants in Eq. (5.6)
$c$	depth of the compression region
$D$	diameter of a circular column
$D_{in}$	inner diameter of an FRP tube
$D_o$	outer diameter of annular concrete in a hybrid DSTC
$D_o/c$	outer diameter-to-compression depth ratio
$D_{o,s}$	outer diameter of a steel tube
$D_{o,s}/t_s$	diameter-to-thickness ratio of a steel tube
$d$	diameter of a split disk
$e$	eccentricity of axial loading; initial eccentricity of axial loading in Chapters 7 and 8
$e_1, e_2$	eccentricities at two column ends under eccentric loading
$e_1/e_2$	eccentricity ratio
$e_2/D_o$	normalized eccentricity
$e'$	lateral deflection of a column

$e'_u$	lateral deflection of a column at ultimate condition
$e_{sum}$	total eccentricity
$E_2$	slope of the linear second portion of a stress-strain curve
$E_{2,con}$	slope of the second linear portion of a concentric-loading stress-strain curve
$E_{2,ecc}$	slope of the second linear portion of an eccentric-loading stress-strain curve
$E_c$	modulus of elasticity of unconfined concrete
$E_{frp}$	modulus of elasticity of an FRP jacket
$E_s$	modulus of elasticity of a steel tube
$E_{seco}$	secant modulus of unconfined concrete
$E_x$	longitudinal modulus of elasticity of an FRP tube
$E_{x,tan}^*$	tangent modulus of elasticity of an FRP tube in the longitudinal direction at peak load
$E_{x,sec}$	secant modulus of elasticity of an FRP tube in the longitudinal direction
$E_\theta$	hoop modulus of elasticity of an FRP tube
$E_{\theta,sec}$	secant modulus of elasticity of an FRP tube in the hoop direction
$F_f$	friction force
$f'_{co}$	compressive strength of unconfined concrete
$f'_{cu}$	axial stress at ultimate axial strain
$f'_{cc}$	compressive strength of confined concrete
$f'_{cc}/f'_{co}$	strength enhancement ratio
$f'_{cc}^*$	peak axial stress of concrete under a specific constant confining pressure

$f_l$	confining pressure provided by an FRP jacket when it ruptures
$f_u$	tensile strength of a steel tube
$f_y$	yield strength of a steel tube
$I_g$	gross moment of inertia of cross section
$k$	effective length factor of a column
$L$	clear length of a column
$L_{crit}$	maximum physical length of a pinned-end hybrid DSTC
$L_{crit}/D_o$	slenderness limit for a pinned-end hybrid DSTC
$L_{eff}$	effective length of a column
$M$	moment
$M_u$	moment at ultimate condition
$N$	pull force applied by the hydraulic jack in Chapter 3; axial load in Chapters 7 and 8
$N_{peak}$	peak axial load
$N_u$	axial load at ultimate condition
$P$	water pressure
$P_c$	axial load carried by concrete section corresponding to $P_{total}$
$P_{co}$	unconfined concrete strength times area of concrete section
$P_{frp}$	axial load carried by an FRP tube corresponding to $P_{total}$
$P_{total}$	ultimate applied axial load
$P_s$	axial load carried by a steel tube corresponding to $P_{total}$
$P_{sum}$	sum of axial load carried by concrete core and that taken by an FRP tube
$r$	parameter accounting for the brittleness of concrete
$r_g$	gyration radius of the cross section of a column

$R$	radius of confined concrete core
$R_o$	outer radius of annular concrete section
$s$	width of an FRP ring
$S_{11}, S_{22}, S_{66}, S_{12}, S_{1111}, S_{2222}, S_{6666}, S_{1122}, S_{1112}, S_{1222}$	coefficients in Eq. (5.2)
$\overline{S_{11}}, \overline{S_{22}}, \overline{S_{12}}$	coefficients in Eq. (5.5a)
$T$	total axial load carried by steel screws
$t_{frp}$	thickness of an FRP jacket
$t_s$	thickness of a steel tube
$U$	strain energy density
$U^*$	maximum strain energy density
$\overline{W}^*$	complementary energy density
$\alpha$	angle between the reference coordinate system and the principal material coordinate (1-2)
$\gamma_{x\theta}$	in-plane shear strain
$\Delta\sigma_x$	difference in axial stress of an FRP tube in the strain range for modulus calculation
$\Delta\sigma_\theta$	difference in hoop stress of an FRP tube in the strain range for modulus calculation
$\Delta\varepsilon_x$	difference in axial strain of an FRP tube in the strain range for modulus calculation
$\Delta\varepsilon_\theta$	difference in hoop strain of an FRP tube in the strain range for modulus calculation
$\varepsilon_1, \varepsilon_2$	strains in the longitudinal direction and the transverse direction of a composite lamina

$\varepsilon_6$	shear strain of a composite lamina
$\varepsilon_c$	axial strain of confined concrete
$\varepsilon_{cc}^*$	axial strain of concrete corresponding to $f_{cc}^*$
$\varepsilon_{cu}$	ultimate axial strain of confined concrete; axial strain of extreme compression fiber at the mid-height section at ultimate condition in Chapters 7 and 8
$\varepsilon_{cu,con}$	ultimate axial strain of a concentric-loading stress-strain curve
$\varepsilon_{cu,ecc}$	ultimate axial strain of an eccentric-loading stress-strain curve
$\varepsilon_{co}$	axial strain at the compressive strength of unconfined concrete
$\varepsilon_l$	lateral strain of confined concrete
$\varepsilon_h$	hoop strain of an FRP jacket
$\varepsilon_{h,rup}$	hoop rupture strain of an FRP jacket
$\varepsilon'_{h,rup}$	nominal hoop rupture strain of an FRP tube
$\varepsilon_t$	axial strain at a transition point (transition strain)
$\varepsilon_v$	volumetric strains
$\varepsilon_x$	strain of an FRP laminae in $x$ direction which corresponds to the axial direction of an FRP tube
$\varepsilon_y$	strain of an FRP laminae in $y$ direction which corresponds to the hoop direction of an FRP tube
$\varepsilon_\theta$	hoop strain of an FRP tube
$\lambda$	slenderness ratio of a column
$\mu$	friction coefficient
$\nu_{x\theta}$	Poisson's ratio for the strain in the hoop direction of an FRP tube when stressed in the axial direction
$\nu_{x\theta,tan}^*$	tangent Poisson's ratio for the strain in the hoop direction of an FRP

	tube when stressed in the axial direction at peak load
$\nu_{x\theta,sec}$	secant Poisson's ratio for the strain in the hoop direction of an FRP tube when stressed in the axial direction
$\nu_{\theta x}$	Poisson's ratio for the strain in the axial direction of an FRP tube when stressed in the hoop direction
$\rho_k$	FRP confinement stiffness ratio
$\rho_\varepsilon$	FRP rupture strain ratio
$\sigma_1, \sigma_2$	stresses in the longitudinal direction and the transverse direction of a composite lamina
$\sigma_6$	shear stress of a composite lamina
$\sigma_c$	axial stress of confined concrete
$\sigma_l$	confining pressure provided by a FPR jacket
$\sigma_r$	radial stress
$\sigma_x$	stress of an FRP laminae in $x$ direction which corresponds to the longitudinal direction of an FRP tube
$\sigma_y$	stress of an FRP laminae in $y$ direction which corresponds to the circumferential direction of an FRP tube
$\sigma_\theta$	hoop stress of an FRP tube
$\sigma_{\theta u}$	hoop stress of an FRP tube corresponding to $\varepsilon_{h,rup}$
$\phi$	void ratio of a hybrid DSTC



# CHAPTER 1

## INTRODUCTION

### 1.1 BACKGROUND

It is well known that the corrosion of steel reinforcement in conventional reinforced concrete (RC) structures causes huge economic losses and has become a global challenge. For example, according to a report released by American Federal Highway Administration (FHWA) in 2012 (Lee 2012), during the decade before the report was published, the annual direct cost expended to mitigate the corrosion of highway bridges is approximately US\$ 8.3 billion, and the average indirect cost was up to more than 10 times the direct cost. Typical corrosion failures of bridge deck slabs, beams and piers are exemplified in Figure 1.1. In China, due to the rapid economic growth and the continuously increasing transportation demand, numerous bridges have been or are being constructed along or near the coastal line. The completion of several world-class sea-crossing bridges, such as the Hangzhou Bay Bridge (36 km long and opened in 2008) and the Hong Kong-Zhuhai-Macau Bridge (roughly 50 km long and will be opened in 2018), is testimony to the massive scale of bridge construction. The issue of corrosion is aggravated in these bridges as many of them are exposed to the harsh marine environment (e.g. chloride attacks and frequent wet-dry cycles). To address this issue, fiber-reinforced polymer (FRP) composites have attracted intensive research attention due to their excellent corrosion resistance and other accompanied advantages such as their high strength-to-weight ratio and designability. Various composite structural forms combining the advantages of FRP and traditional construction materials (e.g. concrete and steel) have been proposed and extensive studies have been conducted to explore the possibility of realizing corrosion-resistant structures with the

incorporation of FRP.

Among the many possible forms of structural members involving the use of FRP composites, one attractive form is concrete-filled FRP tubes (CFFTs). A CFFT consists of an FRP tube filled with plain or steel-reinforced concrete. When a CFFT is loaded under axial compression, the lateral expansion of concrete is confined by the FRP tube, and as a result, the compressive strength and the ductility of the concrete are significantly enhanced (Teng and Lam. 2002), leading to high load bearing capacity and excellent ductility of CFFTs. In addition, CFFTs are lightweight and possess excellent corrosion resistance. They are thus particularly attractive for use in aggressive environment (e.g., marine environment). Extensive research has been carried out to explore the behavior of CFFTs under various loading conditions (e.g., Mirmiran and Shahawy 1997; Fam and Rizkalla 2001a, b; Xiao 2004; Burgueño and Bhide 2006; Zhu *et al.* 2006; Ahmad *et al.* 2008; Ji *et al.* 2008; Ozbakkaloglu and Oehlers 2008; Yu and Teng 2011; Zhohrevand and Mirmiran 2013; Zhang *et al.* 2015a; Teng *et al.* 2016).

In a CFFT, the FRP tube is commonly prefabricated via filament winding (filament-wound FRP tubes). Filament winding is an automated method for the manufacture of tubular composite components by winding fiber filaments under tension over a rotating mandrel in the desired angle. In a CFFT, the outer filament-wound FRP tube not only provides external confinement to the concrete core (referred to as FRP-confined concrete) but also serves as stay-in-place formwork and protects the inner steel reinforcement and concrete from environmental attacks.

## **1.2 HYBRID FRP-CONCRETE-STEEL DOUBLE-SKIN TUBULAR MEMBERS**

Considering the limited contribution of the concrete core in a CFFT when flexure is dominant, hybrid columns with a hollow section is preferred to reduce self-weight. Hybrid FRP-concrete-steel double-skin tubular members (hybrid DSTMs) are a successful example of such type of structural members, recently developed at the Hong Kong Polytechnic University (PolyU) (Teng *et al.* 2004; Teng *et al.* 2007) and originally intended for use as bridge piers and bridge girders. A DSTM consists of an outer FRP tube and an inner steel tube, with the space between filled with concrete (Figure 1.2). The two tubes may be concentrically placed to produce a section form more suitable for columns [DSTCs, see Figure 1.2(a)], or eccentrically placed to produce a section form more suitable for beams [DSTBs, see Figure 1.2(b)]. The sections of the two tubes may be both circular, rectangular, or in another shape; they may also have shapes different from each other.

This new form of hybrid members represents an innovation which combines the advantages of all three constituent materials and delivers excellent structural and durability performance (Teng *et al.* 2004; Teng *et al.* 2007). In hybrid DSTMs, the steel tube is surrounded by both the concrete core and the FRP tube, the outward buckling (elephant foot buckling) of the steel tube can be avoided or postponed due to the confinement. Both the outer surface and inner surface of the steel tube are isolated from the outer environment and thus there is no need for protective paint. The concrete core is confined by the FRP tube and the steel tube, so its strength and ductility can be greatly enhanced. The concrete is also well protected from outer environment by the FRP tube and its long-term performance is enhanced as a result. The FRP tube offers

mechanical resistance primarily in the hoop direction to confine the concrete and to enhance the shear resistance of the member. The mechanical properties of the FRP tube can be tailored to fulfil various design need. Its long-term performance can be further improved by the use of additives (e.g. UV stabilizers, flame spread inhibitors) during manufacture. In summary, the advantages of the three constituent materials in hybrid DSTMs are combined while their weaknesses are avoided. The most important advantages of hybrid DSTMs include: (1) improved strength and ductility due to confinement; and (2) supreme corrosion-resistance offered by FRP tube. It also possesses other advantages such as ease in construction, little need for maintenance, among others.

A large number of investigations have been carried out on the behavior of DSTMs. Investigations on DSTMs as flexural members (DSTBs) revealed that DSTBs provide a very ductile response under flexural loads, and DSTBs with an eccentric steel tube could significantly improve the flexural stiffness, ultimate load and cracking (Yu *et al.* 2006; Zhao *et al.* 2016). In comparison with research on DSTBs, research on DSTCs started earlier and has been more intensive. At PolyU, a great deal of research has been conducted on hybrid DSTCs to study not only their static behavior, including compressive (Wong *et al.* 2008; Xie *et al.* 2011; Yu and Teng 2013; Zhang *et al.* 2017) and beam-column behavior (Yu *et al.* 2010b), but also their behavior under cyclic loading (e.g., cyclic axial compression, combined axial compression and cyclic lateral loading) (Yu *et al.* 2012; Zhang *et al.* 2015b). A stress-strain model for the confined concrete in hybrid DSTCs has also been developed (Yu *et al.* 2010a) based on the available experimental observations and numerical results from a finite element model developed at PolyU (Yu *et al.* 2010c, d). Based on these studies, a design approach for hybrid DSTCs has been proposed in the Chinese Technical Code for Infrastructure

Application of FRP Composites (GB50608 2010). Besides research carried out at PolyU, work has also been undertaken by a large volume of researchers (e.g., Xu and Tao 2005; Yu 2006; Liu 2007; Wang and Tao 2009; Hollaway 2010; Han *et al.* 2010; Wang *et al.* 2012; Ozbakkaloglu and Fanggi 2014, 2015). These studies have further confirmed the good performance of hybrid DSTCs subjected to different loading conditions.

The existing studies on hybrid DSTCs undertaken at PolyU and elsewhere have been generally limited to small-scale specimens. Besides, the use of self-compacting concrete (SCC) has not been paid sufficient attention despite the fact that SCC is obviously more suitable than normal concrete (NC) as the infill material for the relatively narrow annular space of hybrid DSTCs. Against this background, this present thesis presents an in-depth investigation into the structural behavior of large-scale SCC-filled hybrid DSTCs, short or slender, subjected to concentric and eccentric compression. To this end, several issues related to the use of filament-wound FRP tubes and SCC in concrete-filled FRP tubes (CFFTs) are also examined in this thesis as a prerequisite, as briefly introduced in the subsequent sub-section.

### **1.3 ISSUES RELATED TO THE USE OF FILAMENT-WOUND FRP TUBES AND SELF-COMPACTING CONCRETE**

Due to automation in manufacture and good quality control of the filament winding technique, filament-wound FRP tubes are the idealized choice for use in hybrid DSTCs as well as in CFFTs. In the existing research on CFFTs (e.g., Mirmiran and Shahawy 1997; Park *et al.* 2011; Ozbakkaloglu and Oehlers 2008; Teng *et al.* 2016) and hybrid DSTCs (e.g., Qian and Liu 2006, 2008) subjected to axial compression, the filament-wound FRP tubes have commonly been assumed to be under a uniaxial stress state

(hoop tension). However, the fibers in filament-wound FRP tubes are always oriented at less than  $90^\circ$  with respect to the longitudinal axis (e.g.,  $\pm 80^\circ$ ). This means that filament-wound FRP tubes also possess a significant axial stiffness. Thus, in a CFFT or a hybrid DSTC under axial compression, the filament-wound FRP tube is subjected to a biaxial stress state (i.e., axial compression combined with hoop tension induced by the lateral expansion of the inner concrete), which will compromise the confinement effectiveness of the FRP tube and should be taken into account in the analysis of CFFTs (Fam and Rizkalla 2001a, 2003) and hybrid DSTCs under axial compression. In addition, filament-wound FRP tubes also exhibit a certain degree of nonlinear behavior, mainly stemming from the nonlinear matrix material, especially in the direction perpendicular to the orientation of the fibers (Jones and Morgon 1977). The nonlinear behavior of the FRP tube has a certain effect on the structural response of CFFTs and hybrid DSTCs, which should be taken into account in the theoretical analysis but has not been paid enough attention.

In order to obtain an exact understanding of the effects of biaxial stress state and material nonlinearity on the behavior of the filament-wound FRP tubes, their mechanical properties in the longitudinal direction and the circumferential direction must be accurately identified. The present test methods for characterizing the properties of composite materials generally fall into the following three categories in terms of specimen forms: (1) test methods based on strip specimens (e.g., ASTM D638-14 2014; ASTM D3039/D3039M-14 2014; ASTM D3410/D3410M-16 2016; ASTM D6641/D6641-16e1 2016; ASTM D7565/D7565 M-10 2017); (2) test methods based on ring specimens (e.g., ASTM D2290-16 2016; ISO8521 2009; Kaynak *et al.* 2005; Yoon *et al.* 1997; Jones *et al.* 1996; Wang *et al.* 2002; Arsene and Bai 1996, 1998; Cohen *et al.* 1995; Cohen 1997); and (3) test methods based on tube specimens

(e.g., Hull *et al.* 1978; Soden *et al.* 1978; Rosenow 1984; Soden *et al.* 1993; ISO 7509 2015; Al-Khalil *et al.* 1996; Ellyin and Wolodko 1977; ISO 8521 2009; Card 1965; Lee *et al.* 1989). Among all the above test methods, burst tests (i.e., tube tests) are especially recommended because the achieved loading condition is the most similar to that of the FRP tube in confinement applications. However, the adaptability of the burst tests is very limited owing to the rigid requirements on the variations in the dimension of tube specimens as a result of the need of sealing test fixtures. Therefore, new reliable test methods which are not only able to accommodate relatively large variations in the dimension of FRP tubes but also easy to operate are desired.

On the other hand, self-compacting concrete (SCC) is attractive for use in CFFTs and hybrid DSTCs due to its high flowability. Compared with normal concrete (NC), however, SCC is featured with relatively larger shrinkage. This feature may lead to the formation of an initial gap between the FRP tube and the concrete core, which will compromise the confining effect of the FRP tube. Indeed, it has been reported that the structural performance of FRP-confined SCC is different from that of FRP-confined NC under the same confinement condition based on test results of small-scale specimens with about 150 mm in diameter (e.g. El Chabib *et al.* 2005, Yu *et al.* 2014). It should be noted that the detrimental effect of shrinkage of SCC may be amplified in large-scale CFFTs and hybrid DSTCs, but this important issue has not been investigated so far.

Against this background, the first few chapters of this thesis are concerned with a number of issues related to the use of filament-wound FRP tubes and SCC. The characterization of the mechanical properties of filament-wound FRP tubes, including their modulus of elasticity in the longitudinal and circumferential direction and the

Poisson's ratio, is first dealt with. With the mechanical properties determined, a theoretical model for CFFTs subjected to axial compression is next developed, in which the biaxial stress state and the material nonlinearity of the FRP tubes are properly accounted for. In parallel, axial compression tests on CFFTs are carried out in which the specimens were filled with three different types of concrete and scaled in four different sizes, with the aim to understand the effect of shrinkage of SCC on the stress-strain behavior of the confined concrete core especially in large-scale CFFTs. A clear understanding of the stress-strain behavior of the confined concrete forms the basis to understand and model the compressive behavior of hybrid DSTCs.

## **1.4 RESEARCH OBJECTIVES**

In summary, this thesis deals with the following five aspects sequentially: (1) the material properties of filament-wound FRP tubes in their axial and hoop direction; (2) the effect of shrinkage of SCC on the stress-strain behavior of the confined concrete in large-scale CFFTs; (3) the nonlinear biaxial behavior of filament-wound FRP tubes; (4) behavior and modelling of short and slender large-scale hybrid DSTCs subjected to concentric compression and eccentric compression; and (5) development of a slenderness limit expression that differentiates the short hybrid DSTCs from the slender ones.

The main objectives of the research program presented in this thesis are:

- (1) To develop economic and efficient test methods to characterize the mechanical properties of filament-wound GFRP tubes (chapter 3);
- (2) To clarify the effect of shrinkage of SCC on the compressive behavior of large-scale CFFTs (chapter 4);
- (3) To investigate the nonlinear biaxial behavior of filament-wound GFRP tubes in

- confinement applications (chapter 5);
- (4) To investigate the behavior of large-scale hybrid DSTCs subjected to concentric compression (chapter 6);
  - (5) To investigate the behavior of large-scale short hybrid DSTCs subjected to eccentric compression (chapter 7);
  - (6) To investigate the behavior of large-scale slender hybrid DSTCs subjected to eccentric compression (chapter 8);
  - (7) To develop a slenderness limit expression to differentiate short hybrid DSTCs from the slender ones for design use (chapter 9).

## **1.5 LAYOUT OF THE THESIS**

The thesis totally consists of 10 chapters and the content of each chapter is summarized as follows.

Chapter 2 presents a review of existing knowledge of or related to hybrid DSTCs, including prevailing test methods for determining the mechanical properties of composite materials, relevant studies on the compressive behavior of FRP-confined SCC and a comprehensive review of existing experimental and theoretical studies on hybrid DSTCs.

To obtain accurate mechanical properties of the filament-wound GFRP tubes for use in subsequent analysis of the behavior of CFFTs and hybrid DSTCs, chapter 3 explores novel test techniques for determining the longitudinal and circumferential properties of filament-wound FRP tubes. According to the specimen forms including strip, ring and tube specimens, existing test standards and methods for FRP composites are classified and reviewed, and their limitations are discussed. Furthermore, various types

of tests including strip tension and compression tests, split disk tests, compression tests on FRP tubes and hydraulic pressure tests on filament-wound GFRP tubes were conducted. The test results indicate that the compression tests on FRP tubes and the hydraulic pressure tests can more accurately characterize the mechanical properties of the filament-wound GFRP tubes than the other test methods. These two methods are also advantageous over the others because of their simple operation and strong adaptability.

Chapter 4 presents an experimental program which investigated the effect of SCC on the behavior of large-scale CFFTs. A total of 23 CFFT specimens respectively filled with NC, SCC and SCEC of four different sizes of diameter ranging from 150 mm to 400 mm, were tested under axial compression. The test results reveal that, due to the relatively large shrinkage, SCC-filled FRP tubes exhibit significantly different behavior compared with NC specimens, especially under a weak confinement level. The detrimental effect of SCC can be mitigated by using moderate shrinkage-reducing admixture or enhancing the confinement level provided by the FRP tube.

Chapter 5 is concerned with the modelling of CFFTs considering the nonlinear biaxial behavior of the FRP tube, making use of the material properties of filament-wound GFRP tubes obtained in Chapter 3 and the test results of the concentrically-loaded CFFTs filled with NC presented in Chapter 4. The test results are compared with Jiang and Teng's (2007) analysis-oriented stress-strain model, which was developed based on a test database limited to concrete confined with FRP wraps. In the analytical approach, two different models, namely Hahn and Tsai's (1973) model and Jones and Nelson's (1975) model, are respectively incorporated into Jiang and Teng's (2007) model to take into account the nonlinear behavior as well as the biaxial stress state of

the FRP tube. The comparisons show that Jiang and Teng's (2007) model incorporating Jones and Nelson's (1975) model provides accurate predictions for the test results, especially for small-scale specimens. Furthermore, the proposed analytical approach is used to clarify the behavior of the CFFTs filled with SCC and SCEC. It is shown that Jiang and Teng's (2007) model is applicable to SCEC in CFFTs, but is not sufficiently accurate for SCC in CFFTs.

Chapter 6 presents an experimental study on large-scale hybrid DSTCs subjected to concentric compression. The experimental program was carefully designed to take into account the following important effects that had previously been paid little attention, including the effect of shrinkage of SCC and the effect of nonlinear biaxial behavior of filament-wound FRP tubes, on the axial compressive behavior of hybrid DSTCs. In addition, the predictions of Yu *et al.*'s (2010a) design-oriented stress-strain model which was developed based on the test results of small-scale hybrid DSTCs made with NC and confined with FRP wraps are compared with the test results. It is shown that Yu *et al.*'s (2010a) model provides reasonably accurate predictions for large-scale hybrid DSTCs with the ascending type stress-strain curves, but fails to predict the axial stress drops due to the large shrinkage of SCC.

Chapter 7 presents an experimental study on large-scale short hybrid DSTCs under eccentric compression with the eccentricity and the thickness of filament-wound GFRP tube being the major test variables. The results of tests, including two series of eccentrically-loaded columns which were respectively filled with NC and SCC, are firstly presented. Then a theoretical column model which can capture the slenderness effect was formulated to compare with the test results. The use of a column model instead of simple section analysis for short hybrid DSTCs is intended to achieve higher

accuracy of analysis since a certain slenderness effect existed in the tested columns despite their short length. In the column model, the following three stress-strain models are respectively incorporated to describe the stress-strain relationship of the confined concrete in hybrid DSTCs under eccentric compression: (1) Yu *et al.*'s (2010a) model originally developed for confined concrete in concentrically-loaded hybrid DSTCs (eccentricity-independent, EccI); (2) Yu *et al.*'s (2010b) model and (3) Lin's (2016) model both of which are eccentricity-dependent (EccD) stress-strain models for FRP-confined concrete. Compared with the other two models, Lin's (2016) EccD model provides more accurate predictions for the ultimate axial strain of the confined concrete and the lateral deflection of the specimens due to a proper account of the axial strain enhancement phenomenon caused by eccentric compression.

Further to the tests on short hybrid DSTCs presented in Chapter 7, Chapter 8 presents a series of tests on large-scale slender hybrid DSTCs subjected to eccentric compression. The effects of confinement stiffness, load eccentricity and slenderness ratio, are carefully investigated. The column model presented in Chapter 7 is employed to analyze the behavior of slender hybrid DSTCs with separate incorporation of the three stress-strain models used in Chapter 7 [i.e., Yu *et al.*'s (2010a) EccI model, Yu *et al.*'s (2010b) EccD model and Lin's (2016) EccD model]. The comparisons show that the column model is more accurate with the incorporation of Lin's (2016) stress-strain model than the other two stress-strain models for the same reason explained in the preceding paragraph.

Chapter 9 proposes a slenderness limit expression for short hybrid DSTCs below which the slenderness effect is negligible. To this end, a comprehensive parametric study is performed using the theoretical column model presented in Chapter 7 to clarify

the effects of a variety of parameters on the slenderness limit for short hybrid DSTCs. The examined parameters include the end eccentricity ratio, the normalized eccentricity ratio, the strength enhancement ratio, the strain ratio, the void ratio and the diameter-to-thickness ratio of steel tube. Parameters of a major, moderate or minor effect on the slenderness limit are identified based on the results of the parametric study, laying a solid theoretical foundation for developing the slenderness limit expression.

The thesis ends in Chapter 10, in which the main conclusions drawn from the previous chapters are summarized. Finally, the issues worthy of further investigation are highlighted.

## **1.6 REFERENCES**

- Ahmad, I., Zhu, Z.Y., Mirmiran, A. and Fam, A.Z. (2008). "Shear Strength Prediction of Deep CFFT Beams", *ACI Special Publication. SP-230-61* (CD-ROM), pp.1085-1102.
- Al-Khalil, M.F.S., Soden, P.D., Kitching, R. and Hinton, M.J. (1996). "The Effects of Radial Stresses on the Strength of Thin-walled Filament Wound GRP Composite Pressure Cylinders", *International Journal of Mechanical Sciences*. Vol. 38(1), pp.97-120.
- Arsene, S. and Bai, J. (1996). "A New Approach to Measuring Transverse Properties of Structural Tubing by a Ring Test", *Journal of Testing and Evaluation*. Vol. 24(6), pp.386-391.
- Arsene, S. and Bai, J. (1998). "A New Approach to Measuring Transverse Properties of Structural Tubing by a Ring Test-Experimental Investigation", *Journal of Testing and Evaluation*. Vol. 26(1), pp.26-30.

- ASTM D638-14 (2014). “Standard Test Method for Tensile Properties of Plastic”, American Society for Testing and Materials (ASTM), Philadelphia, USA.
- ASTM D2290-16 (2016). “Standard Test Method for Apparent Hoop Tensile Strength of Plastic or Reinforced Plastic Pipe”, American Society for Testing and Materials (ASTM), Philadelphia, USA.
- ASTM D3039/D3039M-14 (2014). “Standard Test Method for Tensile Properties of Polymer Matrix Composite Materials”, American Society for Testing and Materials (ASTM), Philadelphia, USA.
- ASTM D3410/D3410M-16 (2016). “Standard Test Method for Compressive Properties of Polymer Matrix Composite Materials with Unsupported Gage Section by Shear Loading”, American Society for Testing and Materials (ASTM), Philadelphia, USA.
- ASTM D6641/D6641-16e1 (2016). “Standard Test Method for Compressive Properties of Polymer Matrix Composite Materials Using a Combined Loading Compression (CLC) Test Fixture”, American Society for Testing and Materials (ASTM), Philadelphia, USA.
- ASTM D7565/D7565 M-10 (2017). “Standard Test Method for Determining Tensile Properties of Fiber Reinforced Polymer Matrix Composites Used for Strengthening of Civil Structures”, American Society for Testing and Materials (ASTM), Philadelphia, USA.
- Burgueño, R. and Bhide. K. (2006). “Shear Response of Concrete-Filled FRP Composite Cylindrical Shells”, *Journal of Structural Engineering*, ASCE. Vol.132(6), pp.949-960.
- Card, M.F. (1965). “Experiments to Determine Elastic Moduli for Filament-Wound Cylinders”, Nasa Technical Note, NASA TN D-3110. Langley Research Center, Langley Station, Hampton, Va.

- Cohen, D., Toombes, Y.T., Johnson, A.K. and Hansen, M.F. (1995). "Pressurized Ring Test for Composite Pressure Vessel Hoop Strength and Stiffness Evaluation", *Journal of Composite Technology & Research, JCTRER*. Vol. 17(4), pp.331-340.
- Cohen, D. (1997). "Influence of Filament Winding Parameters on Composite Vessel Quality and Strength", *Composites Part A*. Vol. 28A, pp.1035-1047.
- El Chabib, H., Nehdi, M. and El Naggar, M.H. (2005). "Behavior of SCC Confined in Short GFRP Tubes", *Cement & Concrete Composites*. Vol. 27(1), pp.55-64.
- Ellyin, F. and Wolodko, J.D. (1977). "Testing Facilities for Multiaxial Loading of Tubular Specimens", *Multiaxial Fatigue and Deformation Testing Techniques*, ASTM STP 1280, S. Kalluri and P.J. Bonacuse, Eds., American Society for Testing and Materials, pp.7-24.
- Fam, A.Z. and Rizkalla, S.H. (2001a). "Confinement Model for Axially Loaded Concrete Confined by Circular Fiber-Reinforced Polymer Tubes", *ACI Structural Journal*. Vol. 98(4), pp.451-461.
- Fam, A.Z. and Rizkalla, S.H. (2001b). "Behavior of Axially Loaded Concrete-Filled Circular Fiber-Reinforced Polymer Tubes", *ACI Structural Journal*. Vol. 98(3), pp.280-289.
- Fam, A., Flisak, B. and Rizkalla, S. (2003). "Experimental and Analytical Modeling of Concrete-Filled Fiber-Reinforced Polymer Tubes Subjected to Combined Bending and Axial Loads", *ACI Structural Journal*. Vol. 100(4), pp.499-509.
- GB-50608. (2010). "Technical Code for Infrastructure Application of FRP Composites", GB-50608, China Planning Press, Beijing, China.
- Hahn, H.T. and Tsai, S.W. (1973). "Nonlinear Elastic Behavior of Unidirectional Composite Laminae", *Journal of Composite Materials*. Vol.7, pp.102-118.
- Han, L.H., Tao, Z., Liao, F.Y. and Xu, Y. (2010). "Tests on Cyclic Performance of FRP-Concrete-Steel Double-Skin Tubular Columns", *Thin-Walled Structures*. Vol.

- 48(6), pp.430-439. Hahn, H.T. (1973). "Nonlinear Behavior of Laminated Composites", *Journal of Composite Materials*. Vol.7, pp.257-271.
- Hollaway, L.C. (2010). "A Review of the Present and Future Utilization of FRP Composites in the Civil Infrastructure with Reference to their Important in-Service Properties", *Construction and Building Materials*. Vol. 24(12), pp. 2419-2445.
- Hull, D. Legg, M.J. and Spencer, B. (1978). "Failure of Glass/ Polyester Filament Wound Pipe", *Composites*. Vol.1, pp.17-24.
- ISO 7509 (2015). "Plastics Piping Systems - Glass-Reinforced Thermosetting Plastics (GRP) Pipes - Determination of Time to Failure under Sustained Internal Pressure", the International Organization for Standardization (ISO).
- ISO8521 (2009). "Plastics Piping Systems — Glass-Reinforced Thermosetting Plastics (GRP) Pipes -Test Methods for The Determination of The Apparent Initial Circumferential Tensile Strength", the International Organization for Standardization (ISO).
- Ji, G., Li, G., Li, X., Pang, S. and Jones, R. (2008). "Experimental Study of FRP Tube Encased Concrete Cylinders Exposed to Fire", *Composite Structures*. Vol. 85(2), pp.149-154.
- Jiang, T. and Teng, J.G. (2007). "Analysis-Oriented Stress-Strain Models for FRP-Confined Concrete", *Engineering Structures*. Vol. 29(11), pp.2968-2986.
- Jones, I.A., Middleton, V. and Owen, M.J. (1996). "Roller-Assisted Variant of the Split Disc Test for Filament-Wound Composites", *Composites: Part A*. Vol. 27, pp.287-294.
- Jones, R.M. and Nelson JR, D.A.N. (1975). "A New Material Model for The Nonlinear Biaxial Behavior of ATJ-S Graphite", *Journal of Composite Materials*. Vol.9, pp.10-27.

- Jones, R.M. and Morgon, H.S. (1977). "Analysis of Nonlinear Stress-Strain Behavior of Fiber-Reinforced Composite Material", *AIAA Journal*. Vol. 15(12), pp.1669-1676.
- Kaynak, C., Erdiller, E.S., Parnas, L. and Senel, F. (2005). "Use of Split-Disk Tests for the Process Parameters of Filament Wound Epoxy Composite Tubes", *Polymer Testing*. Vol.24, pp.648-655.
- Lee, J., Soden, P.D., Kitching, R. and Tse, P.C. (1989). "Strength of Filament Wound GRP Tube with Axisymmetric Steps", *Composites*. Vol. 20(3), pp.234-243.
- Lee, S.K. (2012). "Current State of Bridge Deterioration in the U.S. - Part 1", *Materials Performance*. Vol. 51(1), pp.62-67.
- Lin, G. (2016). "Seismic Performance of FRP-Confined RC Columns:Stress-Strain Models and Numerical Simulation", Ph.D. thesis, The Hong Kong Polytechnic University, Hong Kong, China.
- Liu, M.X. (2007) "Studies on Key Behavior of FRP-Concrete-Steel Double Skin Tubular Columns", Ph. D. Thesis, Tsinghua University. (in Chinese)
- Mirmiran, A. and Shahawy, R. (1997). "Behavior of Concrete Columns Confined by Fiber Composites", *Journal of Structural Engineering*. Vol. 5(583), pp.583-590.
- Ozbakkaloglu, T. and Oehlers. D. (2008). "Concrete-Filled Square and Rectangular FRP Tubes under Axial Compression", *Journal of Composites for Construction*, ASCE. Vol. 12(4), pp.469-477.
- Ozbakkaloglu, T. and Fanggi, B.A.L. (2014). "Axial Compressive Behavior of FRP-Concrete- Steel Double-Skin Tubular Columns Made of Normal- and High-Strength Concrete", *Journal of Composites for Construction*. Vol. 18(1), 04013027.
- Ozbakkaloglu, T. and Fanggi, B.A.L. (2015). "FRP-HSC-Steel Composite Columns: Behavior under Monotonic and Cyclic Axial Compression", *Material and*

- Structures*. Vol. 48(4), pp.1075-1093.
- Park, J.H., Jo, B.W, Yoon, S.J. and Park, S.K. (2011). “Experimental Investigation on the Structural Behavior of Concrete Filled FRP Tubes wth/without Steel Re-Bar”, *KSCE Journal of Civil Engineering*. Vol. 15(2), pp.337-345.
- Qian, J.R. and Liu, M.X. (2006). “Experiment of FRP-Concrete-Steel Double-Skin Tubular Long Columns under Axial Compressive Load”, *Journal of Concrete (Theoretical Research)*. Vol. 203, pp.31-34. (in Chinese).
- Qian, J.R. and Liu, M.X. (2008). “Experimental Investigation of FRP-Concrete-Steel Double-Skin Tubular Stubs under Axial Compressive Loading”, *Journal of Building Structures*. Vol. 29(2), pp.104-113. (in Chinese).
- Rosenow, M.W.K. (1984). “Winding Angle Effects in Glass Fiber-Reinforced Polyester Filament Wound Pipes”, *Composites*. Vol. 10, pp.247-250.
- Soden, P.D., Leadbetter, D., Griggs, P.R. and Eckold, G.C. (1978). “The Strength of a Filament Wound Composite under Biaxial Loading”, *Composites*. Vol.10, pp.247-250.
- Soden, P.D., Kitching, R., Tse, P.C. and Tsavalas, Y. (1993). “Influence of Winding Angle on the Strength and Deformation of Filament-Wound Composite Tubes Subjected to Uniaxial and Biaxial Loads”, *Composites Science and Technology*. Vol. 46(4), pp.363-378.
- Teng, J.G. and Lam, L. (2002). “Compressive Behavior of Carbon Fiber Reinforced Polymer Confined Concrete in Elliptical Columns”, *Journal of Structural Engineering*, ASCE. Vol. 128(12), pp.1535-1543.
- Teng, J.G., Yu, T. and Wong, Y.L. (2004). “Behaviour of Hybrid FRP-Concrete-Steel Double-Skin Tubular Columns”, *Proceedings, 2<sup>nd</sup> International Conference on FRP Composites in Civil Engineering*. Adelaide, Australia, 2004, pp. 811-818.
- Teng, J.G., Yu, T., Wong, Y.L. and Dong, S.L. (2007). “Hybrid FRP-Concrete-Steel

- Tubular Columns: Concept and Behavior”, *Construction and Building Materials*. Vol. 21(4), pp. 846-854.
- Teng, J.G., Zhao, J.L., Yu, T., Li, L.J. and Guo, Y.C. (2016). “Behavior of FRP-Confined Compound Concrete Containing Recycled Concrete Lumps”, *Journal of Composites for Construction*. Vol. 20(1), 04015038.
- Wang, H., Bouchard, R., Eagleson, R., Martin, P. and Tyson, W.R. (2002). “Ring Hoop Tension Test (RHTT): a Test for Transverse Tensile Properties of Tubular Materials”, *Journal of Testing and Evaluation*, JTEVA. Vol. 30(5), pp.382-391.
- Wang, Z.B. and Tao, Z. (2009). “Experimental Behavior of FRP-Concrete-Steel Double-Skin Tubular Beams”, *Industrial Construction*. Vol. 39(4), pp.5-8. (in Chinese)
- Wang, J., Liu, W.Q., Fang, H. and Zhu, L. (2012). “Experiment and Capacity Calculation Theory Research of Hybrid GFRP-Concrete-Steel Double Skin Tubular Columns under Axial Compression”, *Building structure*. Vol. 42(2), pp.133-138. (in Chinese).
- Wong, Y.L., Yu, T., Teng, J.G. and Dong, S.L. (2008). “Behavior of FRP-Confined Concrete in Annular Section Columns”, *Composites Part B-Engineering*. Vol. 39(3), pp. 451-466.
- Xiao, Y. (2004). “Applications of FRP Composites in Concrete Column”, *Advances in Structural Engineering*. Vol. 7(4), pp.335-343.
- Xie, P., Yu, T., Wong, Y.L. and Teng J.G. (2011). “Compression Behavior of Large-Scale Hybrid FRP-Concrete-Steel Double-Skin Tubular Columns”, *International Conference on Civil Engineering, Architecture and Building Materials, CEABM2011*, 18-20 June, Haikou, China.
- Xu, Y. and Tao, Z. (2005). “Key Issues of Dynamic Behavior of Hybrid FRP-Concrete-Steel Double Skin Tubular Columns”, *Journal of Fuzhou University*

(*Natural Science*). Vol. 33, pp.309-315. (in Chinese).

- Yoon, S.H., Kim, C.G. and Cho, W.M. (1997). “Measurement of Tensile Properties Using Filament Wound Ring Specimens”, *Journal of Reinforced Plastics and Composites*. Vol. 16(9), pp.810-824.
- Yu, T., Wong, Y.L., Teng, J.G. and Dong, S.L. (2006). “Flexural Behavior of Hybrid FRP-Concrete-Steel Double-Skin Tubular Members”, *Journal of Composites for Construction*. Vol. 10(5), pp. 443-452.
- Yu, T., Teng, J.G. and Wong, Y.L. (2010a). “Stress-Strain Behavior of Concrete in Hybrid Double-Skin Tubular Columns”, *Journal of Structural Engineering*, ASCE. Vol. 136(4), pp.379-389.
- Yu, T., Wong, Y.L. and Teng, J.G. (2010b). “Behavior of Hybrid FRP-Concrete-Steel Double-Skin Tubular Columns Subjected to Eccentric Compression”, *Advances in Structural Engineering*. Vol. 13(5), pp.961-974.
- Yu, T., Teng, J.G., Wong, Y.L. and Dong, S.L. (2010c). “Finite Element Modeling of Confined Concrete-I: Drucker-Prager Type Plasticity Model”, *Engineering Structures*. Vol. 32 (2010), pp. 665-679.
- Yu, T., Teng, J.G., Wong, Y.L. and Dong, S.L. (2010d). “Finite Element Modeling of Confined Concrete-II: Plastic-Damage Model”, *Engineering Structures*. Vol. 32, pp. 680-691.
- Yu, T. and Teng, J.G. (2011). “Design of Concrete-Filled FRP Tubular Columns: Provisions in the Chinese Technical Code For Infrastructure Application of FRP Composites”, *Journal of Composites for Construction*, ASCE. Vol. 15(3), pp.451-461.
- Yu, T., Zhang, B., Cao, Y.B. and Teng, J.G. (2012). “Behavior of Hybrid FRP-Concrete-Steel Double-Skin Tubular Columns Subjected to Cyclic Axial Compression”, *Thin-Walled Structures*. Vol. 61, pp. 196-203.

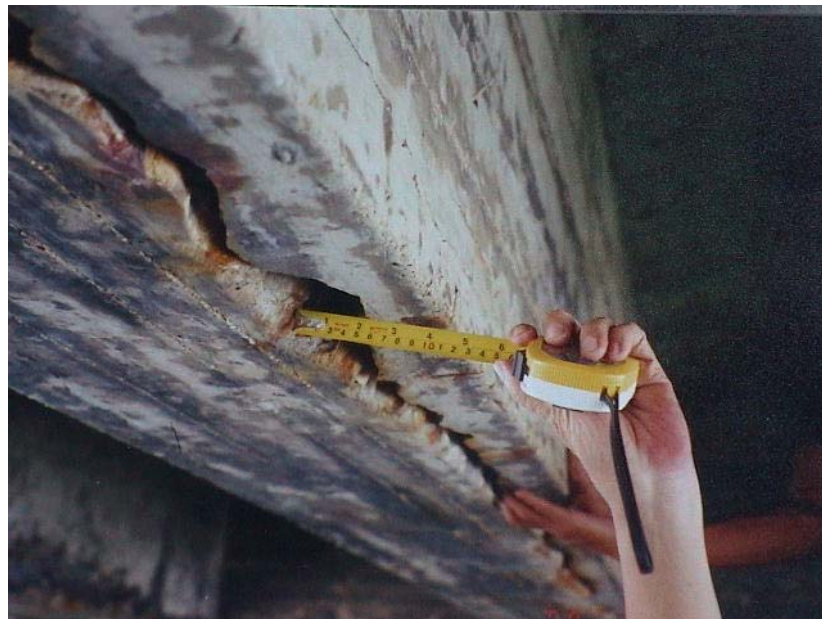
- Yu, T. and Teng, J.G. (2013). "Behavior of Hybrid FRP-Concrete-Steel Double-Skin Tubular Columns with a Square Outer Tube and a Circular Inner Tube Subjected to Axial Compression", *Journal of Composites for Construction*. Vol. 17, pp.271-279.
- Yu, T., Fang, X.L. and Teng, J.G. (2014). "FRP-Confined Self-Compacting Concrete under Axial Compression", *Journal of Materials in Civil Engineering*. Vol. 26(11), 04014082.
- Yu, X.W. (2006) "Behavior of Hybrid CFRP-Concrete-Steel Double-Skin Tubular Columns under Axial Compression", M.Sc. Thesis, Harbin Institute of Technology. (in Chinese)
- Zhang, B., Yu, T., J. G. Teng, J.G. (2015a). "Behavior of Concrete-Filled FRP Tubes under Cyclic Axial Compression", *Journal of Composites for Construction*, ASCE. Vol. 19(3), 04014060.
- Zhang, B., Teng, J.G. and Yu, T. (2015b). "Experimental Behaviour of Hybrid FRP-Concrete-Steel Double-Skin Tubular Columns under Combined Axial Compression and Cyclic Lateral Loading", *Engineering Structures*. Vol. 99(15), pp.214-231.
- Zhang, B., Teng, J.G. and Yu, T. (2017). "Compressive Behavior of Double-Skin Tubular Columns with High-Strength Concrete and a Filament-Wound FRP Tube", *Journal of Composites for Construction*, ASCE. Vol. 21(5), 04017029.
- Zhao, J.L., Teng, J.G., Yu, T. and Li, L.J. (2016). "Behavior of Large-Scale Hybrid FRP-Concrete-Steel Double-Skin Tubular Beams with Shear Connectors", *Journal of Composites for Construction*, ASCE. 04016015.
- Zhu, Z., Ahmad, I. and Mirmiran, A. (2006). "Seismic Performance of Concrete-Filled FRP Tube Columns for Bridge Substructure", *Journal of Bridge Engineering*, ASCE. Vol. 11(3), pp.359-370.

Zohrevand, P. and Mirmiran. A. (2013). “Seismic Response of Ultra-High Performance Concrete-Filled FRP Tube Columns”, *Journal of Earthquake Engineering*. Vol. 17(1), pp.155-170.



(a) Corrosion of reinforcement in a bridge deck slab

(<http://www.twce.org.tw/modules/freecontent/include.php?fname=twce/paper/736/3-1.htm>)



(b) Corrosion of reinforcement in a bridge beam

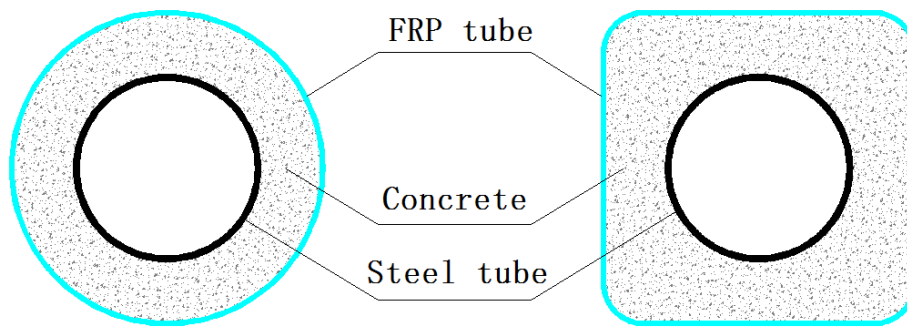
(<http://classroom.dufe.edu.cn/spsk/c494/jzcl1/4/4.5b.htm>)



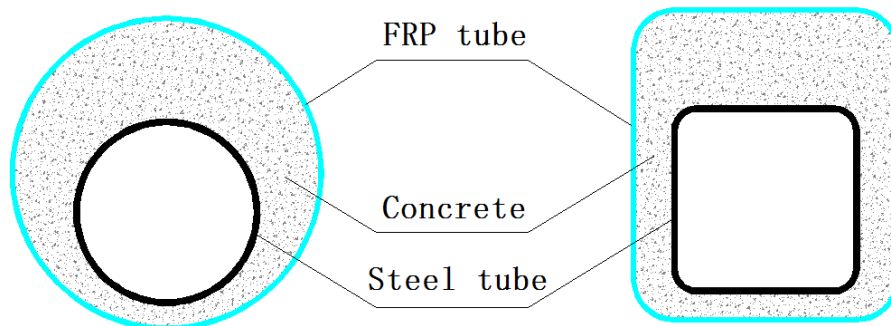
(c) Corrosion of reinforcement in a bridge pier

([http://blog.sina.com.cn/s/blog\\_5d418b210100ay4m.html](http://blog.sina.com.cn/s/blog_5d418b210100ay4m.html))

**Figure 1. 1** Corrosion failure of bridge deck slabs, beams and piers



(a) Cross section forms suitable for columns



(b) Cross section forms suitable for beams

**Figure 1. 2** Typical cross section forms of hybrid DSTMs

## **CHAPTER 2**

### **LITERATURE REVIEW**

#### **2.1 INTRODUCTION**

This chapter presents a review of existing knowledge of or related to hybrid DSTCs in accordance with the objectives of the present research program specified in Chapter 1. The existing knowledge about the test methods of composite materials is firstly summarized, followed by a review of the nonlinear biaxial behavior of filament-wound FRP tubes in confinement applications. The behavior of FRP-confined SCC and the effect of size on the behavior of FRP-confined concrete are next reviewed. Then, stress-strain models for FRP-confined concrete are reviewed with one design-oriented stress-strain model and one analysis-oriented stress-strain model that lay the foundation for the theoretical work of this thesis being reviewed in detail. Finally, previous experimental and theoretical studies on hybrid DSTCs subjected to various loading conditions are discussed in which the attention is focused on hybrid DSTCs subjected to concentric and eccentric compression.

#### **2.2 FILAMENT-WOUND FRP TUBES**

##### **2.2.1 Fabrication Method of Filament-Wound FRP Tubes**

The filament winding technique is very suitable for the manufacture of the FRP tubes in CFFTs and hybrid DSTCs because it is well suited to automation and thus offers good quality control. The manufacture process involves winding resin-impregnated fiber filaments under tension over a rotating mandrel in the desired angle (Figure 2.1). The filaments are delivered from a carriage that traverses horizontally in parallel with the axis of the mandrel while the mandrel rotates (Figure 2.1) so the fibers are always

oriented at an angle less than  $90^\circ$  with respect to the axis of the tube. This means that filament-wound FRP tubes also possess a significant axial stiffness in addition to the hoop stiffness. When used in CFFTs and hybrid DSTCs, the filament-wound FRP tubes not only provide lateral confinement to the concrete but also serve as the stay-in-place formwork.

### **2.2.2 Test methods for FRP composites**

The characterization of the mechanical properties of filament-wound FRP tubes is a prerequisite for the subsequent modelling and analysis of CFFTs and hybrid DSTCs. In this regard, many test methods and test standards have been developed for determining the tensile and compressive properties of FRP composites. These test methods fall into three main categories according to the specimen form, including strip specimen tests for obtaining the in-plane tensile and compressive properties of FRP composites given by ASTM D3039/D 3039M-14 (2014) and ASTM D3410/D3410M-16 (2016) respectively, ring specimen tests by ASTM D2290-16 (2016), and tube specimen tests by ASTM D5449/D5449M-16 (2016) and ISO 7509 (2015).

In ASTM D3039/D3039M-14 (2014) and ASTM D3410/D3410M-16 (2016), a flat strip of material having a constant rectangular cross section is loaded in tension or compression to acquire the corresponding ultimate strength and the stress-strain response of the material. A schematic illustration of such specimens is displayed in Figure 2.2. In the tension tests, the composite material forms are limited to continuous or discontinuous fiber-reinforced composites in which the laminate is balanced and symmetric with respect to the test direction. In the compression tests, the compression is applied by a shear force via grips in a specially-designed fixture (Figure 2.3).

As described in ASTM D2290-16 (2016), for reinforced thermosetting resin tubes regardless of the fabrication method, the apparent hoop tensile strength and the modulus of elasticity can be determined utilizing the split disk method as shown in Figure 2.4. It is worth noting that an apparent tensile strength rather than the true tensile strength is obtained in this test because of the existence of bending within the gauge length due to the split between the two split disks during testing.

ASTM D5449/D5449M-16 (2016) specifies a standard for determining the transverse compressive properties of hoop wound (90°) tubes under axial compression. As shown in Figure 2.5, the compression fixture consists of an outer steel shell and an insert where the latter is fastened inside the hollow of the former to form the concentric cavity, and the specimen ends are firmly inserted into the bottom of the fixture's groove with potting material. So the axial compression can be applied to the test specimen through the steel platens.

ISO 7509 (2015) describes the testing of the time-to-failure of glass-reinforced thermosetting plastic tubes subjected to an internal hydrostatic pressure which creates a state of lateral stress in the wall of pipes, referred to as “burst tests”. The key of the test method is that the end sealing of the system should be capable of keeping the pressure within the specified limits, which imposes strict requirements to the precision of the specimen geometry. For example, the diameter, and wall thickness should be with an accuracy of within  $\pm 1.0\%$ . Figure 2.6 shows the end sealing concept. Furthermore, assuming the end sealing device is free to slide or not, a uniaxial or biaxial stress state is induced accordingly in the tube specimen, according to which the burst tests can be categorized into “open-ended burst tests” or “closed-ended burst tests” (Hull *et al.* 1978; Rosenow 1984; Soden *et al.* 1993; Al-Khalil *et al.* 1996).

## **2.3 NONLINEAR BIAXIAL BEHAVIOR OF FILAMENT-WOUND FRP TUBES IN CFFTS**

In most existing studies on FRP-confined concrete (e.g., Toutanji 1999; Lam and Teng 2003; Jiang and Teng 2007), the FRP jacket for confining concrete is formed by wrapping resin-impregnated fiber sheets around hardened concrete specimens. Such-formed FRP jackets only have very limited axial stiffness and can thus be considered to be under a uniaxial stress state (hoop tension due to lateral expansion of concrete) when the confined concrete column is axially loaded. For CFFTs, however, the FRP tubes are commonly prefabricated by filament winding. Filament-wound FRP tubes are featured with a fiber winding angle less than  $90^\circ$  with respect to the longitudinal axis of the tube and large matrix content, dictating that they also possess a significant axial stiffness in addition to the hoop stiffness. Therefore, when a CFFT is loaded under axial compression, the outer filament-wound FRP tube is under a biaxial stress state of axial compression combined with hoop tension. To the best knowledge of the author, among the existing theoretical studies on CFFTs under axial compression, only Fam and Rizkalla (2001a, 2003) took the biaxial behavior of FRP tubes into account in their analysis of the behavior of CFFTs. The rest of the studies generally treated the axial load contribution of filament-wound FRP tubes in one of the three following ways.

The first way is ignoring the axial load contribution of filament-wound FRP tubes. Teng *et al.* (2016) conducted a series of axial compression tests on filament-wound GFRP tubes filled with compound concrete. The direct contribution of the FRP tube to the axial load resistance was ignored because the axial stiffness of the FRP tubes was considered small due to the small cross-sectional area of the tubes. In Park *et al.*'s

(2011) tests, the axial load was only imposed on the concrete core through a specially-designed loading plate, thus the filament-wound GFRP tube was considered not to take any axial load. Similarly, Mirmiran and Shahawy (1997) cut a groove on the FRP tube at each tube end to avoid direct axial loading on the FRP tube. In fact, however, the axial load was transmitted from the concrete to the FRP tube through friction force.

The second way is considering the axial stiffness of the filament-wound FRP tubes without considering the Poisson's effect (e.g., Saafi *et al.* 1999; Mohamed and Masmoudi 2010; Li *et al.* 2010, 2011). This means that the axial stress and the hoop stress of the FRP tube were taken to be solely dependent on its axial strain and hoop strain; the interaction between the two directions due to the Poisson's effect was not accounted for.

The third way is extrapolating the axial load resisted by the filament-wound FRP tubes from the axial load-axial strain curves obtained from uniaxial compression tests on bare FRP tubes, as illustrated in Figure 2.7. Because the ultimate axial strain of the filament-wound FRP tube in a CFFT is significantly larger than that of the same bare tube in the uniaxial stress state, the axial load carried by the FRP tube after the axial strain of the CFFT exceeds the failure strain of the corresponding bare tube has to be treated. Fam and Rizkalla (2001b) [Figure 2.7(a)] assumed that the axial load-axial strain curve of the FRP tube kept increasing with the initial modulus of elasticity, El Chabib *et al.* (2005) [Figure 2.7(b)] presumed that the curve stopped at the ultimate axial strain of the bare tube while Zhang *et al.* (2015a) [Figure 2.7(c)] assumed that the curve kept a horizontal line thereafter.

On the other hand, filament-wound FRP tubes also exhibit a certain degree of nonlinear

behavior, mainly stemming from the nonlinear matrix material, especially in the direction perpendicular to the orientation of the fibers (Jones and Morgon 1977). For example, in Zhang *et al.*'s (2015a) tests mentioned above, an obvious nonlinear response of the bare filament-wound GFRP tubes under uniaxial compression was observed; the increasing rate of the axial stress with respect to the axial strain evidently decreased in the later stages of loading. To meet the requirements of engineering applications, many numerical models and finite element techniques have been proposed to describe the off-axis tensile and compressive nonlinear response of FRP composites (e.g., Hahn and Tsai 1973; Jones and Nelson 1975; Haj-Ali and Kilic 2002; Abu-Farsakh and Almasri 2011). To the best knowledge of the author, however, the effect of nonlinearity of FRP tubes on the compressive behavior of CFFTs has not been investigated yet. Therefore, a reliable model that can accurately describe the nonlinear behavior of composite laminae is desired in the modeling of CFFTs under axial compression. Many models of this type have been proposed (e.g., Hahn 1973; Hahn and Tsai 1973; Jones and Nelson 1975; Jones and Morgon 1977; Jones 1980; Haj-Ali and Kilic 2002; Zindel and Bakis 2011). Among these models, Hahn and Tsai's (1973) model and Jones and Nelson's (1975) model possess both simplicity and accuracy and have been widely adopted by other researchers (e.g., Ishikawa and Chou 1983; Xia *et al.* 1986; Xiao *et al.* 2009). These two models will be reviewed in detail in Chapter 5.

## **2.4 FRP-CONFINED SELF-COMPACTING CONCRETE**

Self-compacting concrete (SCC) is featured by its excellent flowability without the need of vibration, making it especially suitable for use in relatively narrow space (e.g., the annular space between the outer FRP tube and the inner steel tube in a hybrid DSTC). Due to the omission of vibration, the efficiency of concrete casting can be largely enhanced and the work environment can be improved by eliminating the noise

associated with vibration. Since SCC was first invented in 1986 (Su *et al.* 2001), based on a large volume of research and practice, many specifications and guidelines for SCC have been developed (e.g., EFNARC 2002; TR-6-03 2003; EPG 2005; CECS 203 2006).

Yu *et al.* (2014) conducted axial compression tests on 24 SCC cylinders confined with either carbon FRP (CFRP) or glass FRP (GFRP) FRP wraps. The specimens were 152.5mm in diameter and 305mm in height. The compressive strength of the unconfined concrete was 29.6, 47.0 or 105 MPa. It was reported that the responses of FRP-confined SCC were reasonably well predicted by Jiang and Teng's (2007) analysis-oriented stress-strain model originally developed for FRP-confined NC (this model will be reviewed in detail in a later section in this Chapter). However, according to the results of Yu *et al.*'s (2014) tests, the lateral confining pressure was larger for SCC than for NC with the same amount of FRP at the same axial strain of concrete due to the relatively larger lateral deformation of SCC.

El Chabib *et al.* (2005) conducted axial compression tests on 12 short CFFTs with a diameter of 150 mm and a height of 300 mm and a filament-wound GFRP tube with the fibers oriented at  $\pm 55^\circ$  with respect to the longitudinal axis of the tube. Six of the GFRP tubes were filled with NC and the others were filled with SCC. Pure Portland cement was used in the concrete for half of the specimens with NC or SCC, while expansive cement (EC) was added in the concrete for the rest to control the shrinkage and enhance the interfacial contact between the concrete and the confining FRP tube. In the case that EC was not used in the concrete, the axial stress-axial strain curves of confined concrete in the SCC specimens demonstrated a sudden transition from the initial ascending branch to the linear second branch, while this transition was

progressive for the NC specimens. The difference between the specimens with NC and SCC was not observed when EC was added into the concrete.

Khairallah (2013) conducted axial compression tests on 20 reinforced circular concrete specimens (150 mm in diameter and 600 mm in height) where half of the specimens were prepared with NC and the others were prepared with SCC. The specimens were confined with CFRP wraps, GFRP wraps, FRP tubes (the type of FRP was not mentioned) or steel spirals. The test results showed that the enhancements in strength and ductility were slightly higher for specimens prepared with SCC than for those prepared with NC.

The findings of the above three studies indicate that there exist some differences between the behavior of FRP-confined SCC and FRP-confined NC. The detrimental effect of large shrinkage of SCC may be amplified in CFFTs or hybrid DSTCs where confinement is provided by prefabricated FRP tubes instead of FRP wraps. However, little research has been carried out on this important issue, thus a careful investigation into the behavior of SCC-filled FRP tubes is necessary.

## **2.5 EFFECT OF SIZE ON THE BEHAVIOR OF FRP-CONFINED CONCRETE**

Most existing studies on FRP-confined concrete were conducted on small-scale cylinders with a diameter around 150 mm or smaller. The possible effect of size needs to be clarified before the conclusions drawn from these small-scale tests can be applied to the design of large-scale columns.

Thériault *et al.* (2004) investigated the effect of specimen size on the compressive

behavior of FRP-confined concrete columns, based on their own tests in which the columns were 51mm, 152mm and 304mm in diameter and tests by other researchers (Harmon and Slattery 1992; Kestner *et al.* 1997; Kono *et al.* 1998; Mirmiran *et al.* 1998; Demers and Neale 1999; Toutanji 1999). All specimens were confined with FRP wraps. It was concluded that the effect of specimen size was not significant on the compressive strength of FRP-confined concrete, except for the 51 mm-diameter cylinders in which an appreciable size effect was observed.

Carey and Harries (2005) presented a review of the test database collected by Carey (2003), which included 251 test results of axially-loaded circular concrete columns confined with FRP wraps, covering specimen sizes from small ( $< 102$  mm diameter), medium (102 to 305 mm diameter) to large ( $\leq 508$  mm diameter). Based on the test results, Carey *et al.* (2005) suggested that increasing specimen size had very minor effect on the compressive strength, but slightly reduced the strain capacity of FRP-confined concrete. They also presented the results of their own tests on circular CFRP-confined concrete columns 152 mm, 254 mm and 610 mm in diameter. The results of their own tests also supported the conclusion that the column size had insignificant influence on the behavior of FRP-confined concrete.

Wang and Wu (2011) tested a series of concrete columns (70 mm, 105 mm and 194 mm in diameter) confined with aramid FRP (AFRP) wraps. The test results indicated that the effect of specimen size was insignificant on the failure modes and stress-strain curves, but was significant on the strength of the confined concrete. They proposed a size-dependent strength model for AFRP-confined concrete based on Bazant's size-effect law (1984) with certain modifications.

Zhou *et al.* (2016) studied the compressive behavior of concrete cylinders of different sizes (70 mm, 100 mm, 150 mm, 190 mm and 310 mm in diameter) confined with CFRP wraps and modified Lam and Teng's (2003) stress-strain model for FRP-confined concrete (this model will be reviewed in detail in a later section in this Chapter) to account for the size effect based on their test results.

Ozbakkaloglu (2013) conducted axial compression tests on seven circular CFFTs with CFRP or AFRP tubes prefabricated via a wet-layup process. In their tests, the concrete strength varied from 36.3 MPa to 110.1 MPa and the specimens had a diameter of 74 mm, 100 mm, 152 mm or 300 mm. Their test results showed that the small-scale specimens exhibited slightly better performance in terms of compressive strength and ultimate axial strain than their large-scale counterparts.

In summary, the above studies seem to indicate that a consensus has not been reached on whether the column size has a significant effect on the compressive behavior of FRP-confined concrete. It should also be noted that the studies reviewed above are all concerned with concrete confined with FRP wraps rather than an FRP tube except the study of Ozbakkaloglu (2013). The possible segregation of concrete from the FRP tube due to concrete shrinkage (especially when SCC is used) and lack of bonding between the two might further complicate the issue of size effect.

## **2.6 STRESS-STRAIN MODELS FOR FRP-CONFINED CONCRETE**

### **2.6.1 General**

The behavior of FRP-confined concrete is distinctly different from that of steel-

confined concrete because the two types of confinement are different in nature. The FRP confinement is passive in nature (i.e., passive confinement) because the confining pressure is dependent on the lateral dilation of concrete; it continuously increases with the concrete dilation as the applied axial load increases. In contrast, the steel confinement can be regarded as active in nature (i.e., active confinement) as the confining steel soon enters the yielding stage due to the small yielding strain of steel, after which the confining pressure remains almost constant (little depends on the lateral dilation of concrete). As a result, existing stress-strain models for steel-confined concrete are not directly applicable to FRP-confined concrete.

Since 1981 (Fardis and Khalili 1981), extensive studies have been conducted on the behavior of FRP-confined concrete and have shown that the strength and ductility of concrete can be greatly enhanced by FRP confinement (e.g., Mirmiran and Shahawy 1996, 1997; Saafi *et al.* 1999; Toutanji 1999; Xiao and Wu 2000, 2003; Teng and Lam 2002; Lam and Teng 2002, 2003, 2004, 2006, 2009; Fam and Rizkalla 2001a; Binici 2005; Teng *et al.* 2007a, 2009; Jiang and Teng 2007; Wei and Wu 2012). Based on the test results obtained from the numerous experimental studies, many stress-strain models for FRP-confined concrete have been proposed, which can be classified into two main categories: design-oriented models (e.g., Karbhari and Gao 1997; Saafi *et al.* 1999; Toutanji 1999; Xiao and Wu 2000, 2003; Lam and Teng 2003; Teng *et al.* 2009) and analysis-oriented models (e.g., Mirmiran and Shahawy 1996; Spoelstra and Monti 1999; Fam and Rizkalla 2001a; Chun and Park 2002; Harries and Kharel 2002; Marques *et al.* 2004; Binici 2005; Teng *et al.* 2007a; Jiang and Teng 2007). The design-oriented models treat FRP-confined concrete as a single material (i.e., the interaction between the FRP jacket and the concrete core is not accounted for) and express the stress-strain curve of FRP-confined concrete using closed-form equations directly

derived from the interpretation and regression of test results. Their simplicity makes them suitable for design use. In contrast, the analysis-oriented models predict the stress-strain curve of FRP-confined concrete using an incremental numerical procedure with an explicit account of the interaction between the FRP jacket and the concrete core via radial displacement compatibility and equilibrium conditions. Therefore, they are more versatile than design-oriented models as they are easily extendible to concrete confined with materials other than FRP. Analysis-oriented models are more suitable for incorporation in more sophisticated analysis than are required in design (e.g., nonlinear finite element analysis of concrete structures with FRP confinement).

### **2.6.2 Design-oriented stress-strain models**

Among the existing design-oriented stress-strain models for FRP-confined concrete, Lam and Teng's (2003) model has gained wide acceptance (e.g., Rocca *et al.* 2009; Mohamed and Masmoudi 2010; Fahmy and Wu 2010; Zohrevand and Mirmiran 2011; Karimi *et al.* 2011; Elsanadedy *et al.* 2012; Biskinis and Fardis 2013; Carrazedo *et al.* 2013; Ozbakkaloglu *et al.* 2013; Liu *et al.* 2013; Casas and Chambi 2014; Pham *et al.* 2015; Faustino and Chastre 2015; Guler and Ashour 2016; Al-Nimry and Jawarneh 2017) due to its simplicity and accuracy. In particular, Lam and Teng's (2003) model and its refined version (Teng *et al.* 2009) have been adopted by a number of prevailing design codes/guidelines for or related to FRP-strengthened RC structures [e.g., GB50608 (2010), ACI 440.2R-08 (2008) and TR 55 (2012)].

Lam and Teng's (2003) design-oriented model was developed based on a large database of axial compression tests on FRP-confined circular concrete columns. This model naturally reduces to a stress-strain model for unconfined concrete in many

existing design codes/guidelines when no FRP confinement is provided. The model adopts a parabolic first portion plus a linear second portion meeting at a transition strain  $\varepsilon_t$  to describe the stress-strain curve of FRP-confined concrete, as can be expressed by

$$\sigma_c = \begin{cases} E_c \varepsilon_c - \frac{(E_c - E_2)^2}{4f'_{co}} \varepsilon_c^2 & \text{for } 0 \leq \varepsilon_c \leq \varepsilon_t \\ f'_{co} + E_2 \varepsilon_c & \text{for } \varepsilon_t \leq \varepsilon_c \leq \varepsilon_{cu} \end{cases} \quad (2.1)$$

where  $\sigma_c$  and  $\varepsilon_c$  are respectively the axial stress and the axial strain of the confined concrete;  $f'_{co}$  and  $E_c$  are respectively the cylinder compressive strength and the modulus of elasticity of unconfined concrete in which  $E_c = 4730\sqrt{f'_{co}}$  (in MPa) (ACI-318 2005).

The transition strain  $\varepsilon_t$  between the parabolic first portion and the linear second portion is given by

$$\varepsilon_t = \frac{2f'_{co}}{E_c - E_2} \quad (2.2)$$

The slope of the linear second portion is given by

$$E_2 = \frac{f'_{cc} - f'_{co}}{\varepsilon_{cu}} \quad (2.3)$$

where  $f'_{cc}$  and  $\varepsilon_{cu}$  are respectively the compressive strength and the ultimate axial strain of the confined concrete and are given by

$$\frac{f'_{cc}}{f'_{co}} = \begin{cases} 1 + 3.3 \frac{f_l}{f'_{co}} & \text{if } \frac{f_l}{f'_{co}} \geq 0.07 \\ 1 & \text{if } \frac{f_l}{f'_{co}} < 0.07 \end{cases} \quad (2.4)$$

$$\frac{\varepsilon_{cu}}{\varepsilon_{co}} = 1.75 + 12 \frac{f_l}{f'_{co}} \left( \frac{\varepsilon_{h,rupt}}{\varepsilon_{co}} \right)^{0.45} \quad (2.5)$$

where  $\varepsilon_{co}$  is the axial strain at the compressive strength of unconfined concrete and was taken to be 0.002 for calculating the ultimate axial strain of confined concrete in Eq. (2.5);  $\varepsilon_{h,rupt}$  is the FRP hoop rupture strain;  $f_l$  is the confining pressure provided by the FRP jacket when it ruptures and is related to  $\varepsilon_{h,rupt}$  by the following equation

$$f_l = \frac{E_{frp} t_{frp} \varepsilon_{h,rupt}}{R} \quad (2.6)$$

where  $E_{frp}$  and  $t_{frp}$  are respectively the modulus of elasticity and the thickness of the FRP jacket and  $R$  is the radius of the confined concrete core. Eq. (2.6) means that in Lam and Teng's (2003) model, a horizontal line is predicted for the second portion of the stress-strain curve to represent the descending branch observed in tests when the confinement is insufficient to lead to an enhancement in the compressive strength of the concrete core.

On the basis of Lam and Teng's (2003) model and an additional test database, Teng *et al.* (2009) proposed more accurate equations for the ultimate condition of FRP-confined concrete to replace Eqs. (2.4) and (2.5) in Lam and Teng's (2003) model by taking into account the effects of the confinement stiffness and the strain capacity of FRP jacket. The new ultimate condition equations are given by Eqs. (2.7) and (2.8)

$$\frac{f'_{cc}}{f'_{co}} = \begin{cases} 1 + 3.5(\rho_K - 0.01)\rho_\varepsilon & \text{if } \rho_K \geq 0.01 \\ 1 & \text{if } \rho_K < 0.01 \end{cases} \quad (2.7)$$

$$\frac{\varepsilon_{cu}}{\varepsilon_{co}} = 1.75 + 6.5\rho_K^{0.8}\rho_\varepsilon^{1.45} \quad (2.8)$$

where  $\rho_k$  and  $\rho_\varepsilon$  are respectively the confinement stiffness ratio and the strain ratio and are defined as

$$\rho_K = \frac{E_{frp}t_{frp}}{(f'_{co}/\varepsilon_{co})R} \quad (2.9)$$

$$\rho_\varepsilon = \frac{\varepsilon_{h,rup}}{\varepsilon_{co}} \quad (2.10)$$

According to the definition of the confinement stiffness ratio  $\rho_K$  and the strain ratio  $\rho_\varepsilon$ , the confinement ratio  $f_l/f'_{co}$  can be expressed as the product of the above two ratios as follows

$$\frac{f_l}{f'_{co}} = \frac{E_{frp}t_{frp}\varepsilon_{h,rup}}{f'_{co}R} = \rho_K\rho_\varepsilon \quad (2.11)$$

In addition, a second version of the model was also proposed in Teng *et al.* (2009) which predicts a descending second portion rather than a horizontal one when the confinement is insufficient, to better simulate the behavior of the confined concrete in such a case. This version of the model can be expressed as

$$\sigma_c = \begin{cases} E_c\varepsilon_c - \frac{(E_c - E_2)^2}{4f'_{co}}\varepsilon_c^2 & \text{for } 0 \leq \varepsilon_c \leq \varepsilon_t \\ \left\{ \begin{array}{ll} f'_{co} + E_2\varepsilon_c & \text{if } \rho_K \geq 0.01 \\ f'_{co} - \frac{f'_{co} - f'_{cu}}{\varepsilon_{cu} - \varepsilon_{co}}(\varepsilon_c - \varepsilon_{co}) & \text{if } \rho_K < 0.01 \end{array} \right. & \text{for } \varepsilon_t \leq \varepsilon_c \leq \varepsilon_{cu} \end{cases} \quad (2.12)$$

where  $f'_{cu}$  is the axial stress at the ultimate axial strain and is given by

$$\frac{f'_{cu}}{f'_{co}} = 1 + 3.5(\rho_K - 0.01)\rho_\varepsilon \quad (2.13)$$

It is obvious that the axial stress at the ultimate axial strain ( $f'_{cu}$ ) and the compressive strength of confined concrete ( $f'_{cc}$ ) given in Eq. (2.7) are the same when the stress-strain curve features an ascending second portion under sufficient confinement.

### 2.6.3 Analysis-oriented stress-strain models

Ozbakkaloglu *et al.* (2013) reviewed 88 existing stress-strain models for FRP-confined concrete and assessed 68 of them, including both design-oriented and analysis-oriented stress-strain models. It was concluded from the assessment that the analysis-oriented model proposed by Jiang and Teng (2007) is one of the best-performance stress-strain models especially in the prediction of the ultimate axial strain. Similar conclusions were also drawn by Al Abadi *et al.* (2016) and Zhou *et al.* (2016) based on their own assessments. In addition, the accuracy of Jiang and Teng's (2007) model has also been verified by many other researchers (e.g., Lee and Hegemier 2009; Lim and Ozbakkaloglu 2014; Kwan *et al.* 2015).

Jiang and Teng's (2007) model was refined from an earlier version developed by the same research group (Teng *et al.* 2007a). It comprises an active-confinement model as the base model and an explicit axial-to-lateral strain equation to describe the dilation behavior of the confined concrete. It is built on the assumption that the axial stress and the axial strain of concrete confined with an FRP jacket at a given hoop strain are the same as those of the same concrete confined with a constant confining pressure which is equal to that supplied by the FRP jacket.

The active-confinement model adopted by Jiang and Teng's (2007) model can be described by the following equations

$$\frac{\sigma_c}{f_{cc}^{t*}} = \frac{(\varepsilon_c/\varepsilon_{cc}^*)^r}{r-1+(\varepsilon_c/\varepsilon_{cc}^*)^r} \quad (2-14)$$

$$r = \frac{E_c}{E_c - f_{cc}^{t*}/\varepsilon_{cc}^*} \quad (2-15)$$

$$\frac{f_{cc}^{t*}}{f_{co}^t} = 1 + 3.5 \frac{\sigma_l}{f_{co}^t} \quad (2-16)$$

$$\frac{\varepsilon_{cc}^*}{\varepsilon_{co}} = 1 + 17.5 \frac{\sigma_l}{f_{co}^t} \quad (2-17)$$

where  $f_{cc}^{t*}$  and  $\varepsilon_{cc}^*$  are respectively the peak axial stress and the corresponding axial strain of concrete under a specific constant confining pressure;  $r$  is a parameter accounting for the brittleness of the concrete;  $\sigma_l$  is the confining pressure provided by the FRP jacket and is equal to

$$\sigma_l = \frac{\sigma_{\theta} t_{frp}}{R} \quad (2-18)$$

where  $\sigma_{\theta}$  is the hoop stress of the FRP jacket. In Jiang and Teng's (2007) model, the FRP jacket in the hoop direction is assumed to be linear elastic, so the hoop stress can be calculated by

$$\sigma_{\theta} = E_{frp} \varepsilon_h \quad (2-19)$$

where  $\varepsilon_h$  is the hoop strain of the FRP jacket. According to the sign convention in Jiang and Teng's (2007) model, the hoop strain  $\varepsilon_h$  has the same magnitude as but the opposite sign to the lateral strain of the confined concrete  $\varepsilon_l$  ( $\varepsilon_h = -\varepsilon_l$ ).

The relationship between the axial strain and the lateral strain of the confined concrete is expressed by the following equation

$$\frac{\varepsilon_c}{\varepsilon_{co}} = 0.85 \left( 1 + 8 \frac{\sigma_l}{f'_{co}} \right) \times \left\{ \left[ 1 + 0.75 \left( \frac{-\varepsilon_l}{\varepsilon_{co}} \right) \right]^{0.7} - \exp \left[ -7 \left( \frac{-\varepsilon_l}{\varepsilon_{co}} \right) \right] \right\} \quad (2.20)$$

## **2.7 HYBRID FRP-CONCRETE-STEEL DOUBLE-SKIN TUBULAR COLUMNS**

### **2.7.1 General**

In a hybrid DSTC, the advantages of the three constituent materials (i.e., FRP, concrete and steel) are combined and their weaknesses are avoided. The most significant advantages of hybrid DSTCs include: (1) improved strength and ductility due to confinement; (2) excellent corrosion resistance offered by the FRP tube. These advantages make hybrid DSTCs highly potential for use as bridge piers as they can meet both the requirements of seismic resistance and corrosion resistance. It is anticipated that hybrid DSTCs can serve as bridge piers especially in seismic zones and harsh environment to reduce maintenance work, extend bridge life and to bring economic benefits. Due to their excellent performance, hybrid DSTCs have attracted extensive research attention from many parts of the world (e.g., Hollaway 2010; Qian and Liu 2006, 2008a, b, c; Ozbakkaloglu and Fanggi 2014, 2015).

Besides the systematic studies conducted by Teng's group at the Hong Kong Polytechnic University, a large amount of follow-up research on the behavior of hybrid DSTCs has been conducted, both experimentally and theoretically, since their

invention.

The experimental studies on hybrid DSTCs have covered various loading conditions, including: hybrid DSTCs under concentric compression (Qian and Liu 2006, 2008a; Teng *et al.* 2007b; Wong *et al.* 2008; Xie *et al.* 2011; Wang *et al.* 2012; Yu and Teng 2013; Wang *et al.* 2013; Fanggi and Ozbakkaloglu 2013, 2015a, b; Ozbakkaloglu and Fanggi 2014, 2015; Ozbakkaloglu 2015; Hu and Yao 2016; Zhang 2017; Zhou *et al.* 2017; Yu *et al.* 2017; Cao *et al.* 2017) and eccentric compression loading (Yu *et al.* 2010b; Xu *et al.* 2014; Ma 2013; Yao *et al.* 2015), flexural loading (Teng *et al.* 2004; Yu *et al.* 2006; Liu and Qian 2007; Wang and Tao 2009; Idis and Ozbakkaloglu 2014, 2015; Zhao *et al.* 2016), cyclic axial compressive loading (Yu *et al.* 2012; Ozbakkaloglu and Fanggi 2015; Albitar *et al.* 2015; Abdelkarim and ElGawady 2016a) and combined axial and lateral cyclic loading (Qian and Liu 2008b; Han *et al.* 2010; Ozakkaloglu and Idris 2014; Zhang *et al.* 2015b; Idris and Ozakkaloglu 2016; Abdelkarim *et al.* 2017), as well as vehicle collision loading (Abdelkarim and ElGawady 2016b). The above systematic experimental research over the past decade has proved the supreme performance of hybrid DSTCs, such as enhanced strength and ductility and excellent seismic resistance.

In parallel with the above experimental studies, the theoretical studies on hybrid DSTCs have also acquired considerable achievements. A sophisticated 3D finite element (FE) model for DSTCs was proposed by Yu *et al.* (2010c, d). Based on the numerical results of the FE model and the test results, a design-oriented stress-strain model for concrete in hybrid DSTCs was also developed (Yu *et al.* 2010a). Furthermore, based on the analytical results of hybrid DSCTs under concentric compression loading (Wong *et al.* 2008) and the section analysis results of hybrid

DSTCs under flexural and eccentric compression loading (Yu *et al.* 2006, 2010b), Teng and Yu (2010) proposed a design method for the ultimate bearing capacity of eccentrically-loaded hybrid DSTCs with a circular section. This method has been adopted by “Chinese Technical Code for Infrastructure Application of FRP Composites” (GB 50608 2010). More recently, considering the failure mode of the inner steel tube, a new ultimate condition model for circular and square hybrid DSTCs was presented by Ozbakkaloglu *et al.* (2016) based on available test results in the open literature.

On the other hand, Liu and Qian (2007, 2008) not only deduced a simplified expression for the flexural strength and a tri-linear moment-curvature model expressed as a function of the section bending stiffness for hybrid DSTMs (FRP-concrete-steel double-skin tubular members), but also identified the bearing capacity of eccentrically-loaded hybrid DSTCs and their axial force-moment interaction relationship. Qian and Liu (2008c) adopted Clough’s bilinear hysteretic model to establish a hysteretic model of moment-rotation relationship for plastic hinge zone of hybrid DSTCs. Based on the results of a comprehensive FE analysis, Abdelkarim *et al.* (2017) proposed an equation for the development length of the inner steel tube in hybrid DSTCs and developed a preliminary design procedure for hybrid DSTCs under seismic loading.

In the remainder of this section, only existing studies on hybrid DSTCs subjected to concentric compression and eccentric compression are reviewed in detail as hybrid DSTCs subjected to these two loading conditions form the focus of the present research program.

### **2.7.2 Hybrid DSTCs subjected to concentric compression**

In practice, filament-wound FRP tubes are the ideal choice for use in hybrid DSTCs. But in laboratory tests, especially small-scale tests, the FRP tube in a hybrid DSTC specimen is often prefabricated via a wet-layup process with the fibers oriented along the hoop direction (wet-layup FRP tubes). In some other tests, the inner steel tube and the surrounding annular concrete are first made and FRP wraps are then applied along the hoop direction also via a wet-layup process to serve as the outer tube (post-applied FRP wraps). In the remainder of this section, the specific form of the FRP tubes (i.e., filament-wound tubes, wet-layup tubes or post-applied wraps) used in the experimental studies reviewed will be clearly stated if this information is available in the original source. It should be noted that when post-applied wraps are used, the formation of an initial gap between the concrete and the FRP wraps due to shrinkage of concrete is much less likely because the wraps are applied after the hardening of concrete and interfacial adhesive bonding exists between the concrete and the FRP wraps.

Wong *et al.* (2008) presents the results of a series of axial compression tests on short hybrid DSTCs. FRP-confined concrete columns with or without a void were also tested for comparison. The specimens had an outer diameter of 152.5 mm and a height of 305 mm with a concrete cylinder strength ranging from 36.7 MPa to 46.7 MPa. In their tests, post-applied FRP wraps were used. The investigated parameters included the void ratio, the diameter-to-thickness ratio of the steel tube and the thickness of the FRP tube. Qian and Liu (2008a) tested ten concentrically-loaded short hybrid DSTCs in which filament-wound FRP tubes were used. The outer diameter (excluding the thickness of the FRP tube) and the height of the specimens were respectively 190 mm

and 500 mm. The results of both test series indicate that hybrid DSTCs feature excellent load capacity and ductility because the annular concrete between the outer FRP tube and the inner steel tube is effectively confined and the local buckling of the inner steel tube is delayed by the surrounding concrete.

On the basis of an FE model (Yu *et al.* 2010 c, d) which was validated by experimental results of hybrid DSTCs under axial compression (Wong *et al.* 2008), Yu *et al.* (2010a) conducted a parametric study on parameters including the stiffness of the FRP tube, the stiffness of the steel tube and the size of the inner void, and developed a design-oriented stress-strain model for concrete in hybrid DSTCs. The proposed stress-strain model takes a similar form as Teng *et al.*'s (2009) design-oriented model for FRP-confined concrete but has a different equation for the ultimate axial strain to reflect the effect of the void ratio of hybrid DSTCs,  $\phi$ . The new ultimate axial strain equation was modified from Eq. (2.8) of Teng *et al.*'s (2009) model and is given by

$$\frac{\varepsilon_{cu}}{\varepsilon_{co}} = 1.75 + 6.5\rho_K^{0.8}\rho_\varepsilon^{1.45}(1 - \phi)^{-0.22} \quad (2.21)$$

Besides the above tests on circular hybrid DSTCs, Yu and Teng (2013) conducted the first axial compression tests on eight square hybrid DSTCs with post-applied GFRP wraps. The specimens had an outer side length of 150 mm and a concrete cylinder compressive strength of 37.5 MPa to investigate the effects of the void ratio and the thickness of the FRP tube. Square FRP-confined solid and hollow columns with the same scale were also tested for comparison. It was concluded from the test results that the square hybrid DSTCs also exhibit good ductility as the circular ones and the behavior of the confined concrete in the square hybrid DSTCs is very similar to that

of the square FRP-confined solid columns.

In the recent years, research on hybrid DSTCs has also been extended to the use of high performance materials, such as high strength concrete (HSC) and large rupture strain FRP materials.

Zhang *et al.* (2011) conducted the first study on hybrid DSTCs with HSC and post-applied FRP wraps under axial compression. In their tests, six specimens 204 mm in diameter and 400 mm in height were tested and the filled concrete had a compressive strength of 83.5 MPa. The research group led by Ozbakkaloglu (Fanggi and Ozbakkaloglu 2013, 2015a, b; Ozbakkaloglu and Fanggi 2014, 2015; Ozbakkaloglu 2015) in University of Adelaide conducted four series of tests on the axially-loaded hybrid DSTCs with the unconfined concrete strength ranging from 36.7 MPa to 113.8MPa. The specimens were 150 mm in diameter and 300 mm in height and were confined with wet-layup FRP tubes. Besides the strength of concrete and the regular parameters (i.e., the void ratio and the thickness of FRP tube), the FRP type (Aramid FRP tubes were used), the presence or absence of concrete filled in the steel tube and the cross-sectional shape of FRP tube and steel tube (i.e., circular and square) were also considered as the key parameters in the experimental studies of the University of Adelaide. In Zhang *et al.*'s (2017) study, nine 200 mm or 300mm diameter hybrid DSTCs with HSC and a filament-wound GFRP tube were tested under axial compression. These studies have further confirmed the excellent ductility of hybrid DSTCs in spite of the use of HSC.

More recently, Zhou *et al.* (2017) reported the first series of axial compression tests on hybrid DSTCs filled with full lightweight aggregate concrete (FLAC). All specimens

had a diameter of 153 mm and a height of 300 mm. The test results show that the strength and the ductility of FLAC filled in hybrid DSTCs are significantly enhanced.

Cao *et al.* (2017) tested 20 circular hybrid DSTCs under axial compression in which all specimens were confined with wet-layup CFRP tubes and had a dimension of 150 mm in diameter by 300 mm in height. Ten specimens were filled with SCC and the others were filled with SCEC. The test results show that the use of an expansive agent does not appear to have a significant effect on the behavior of the tested specimens.

Yu *et al.* (2017) conducted the first ever axial compression tests on hybrid DSTCs with post-applied polyethylene terephthalate (PET, one type of FRP composites with a large rupture strain) wraps. Their results show that the use of PET enables the specimens to have an outstanding deformability (the ultimate axial strain of the specimen reached up to about 0.17), which has not been achieved before when the confining tube is made of CFRP or GFRP.

The studies reviewed above have been limited to small-scale hybrid DSTCs with a diameter less than 200 mm; the only exception is Zhang *et al.*'s (2017) tests in which the specimens had a diameter of 300 mm. For the confident use of hybrid DSTCs in practice, axial compression tests on large-scale hybrid DSTCs must be conducted to verify the conclusions drawn from these small-scale tests. On the other hand, SCC is suitable for use as the infill in the relatively thin concrete layer of hybrid DSTCs due to its segregation resistance and excellent flowability, while filament-wound FRP tubes not only providing hoop confinement for concrete but also acting as the stay-in-place formwork are an ideal choice for hybrid DSTCs (Zhang *et al.* 2017). So the present research program will be focused on the compressive behavior of large-scale hybrid

DSTCs with SCC and a filament-wound GFRP tube.

### 2.7.3 Hybrid DSTCs subjected to eccentric compression

Yu *et al.* (2010b) conducted the first series of eccentric compression tests on six short hybrid DSTCs 155 mm in outer diameter and 465 mm in height. The specimens were confined with post-applied FRP wraps. The load eccentricity was the only studied parameter. Considering the reduced effectiveness of FRP confinement on concrete as a result of the existence of the strain gradient under eccentric compression, a so-called “variable confinement model” for the concrete in the eccentrically-loaded hybrid DSTCs was proposed and was shown to provide reasonable predictions of the test results. The model was modified from the stress-strain model for concrete in hybrid DSTCs subjected to concentric compression developed by the same research group (Wong *et al.* 2008; Yu *et al.* 2010a, c, d). To account for the effect of the load eccentricity, the slope of the second linear portion of the stress-strain curve of the confined concrete was defined to be dependent on the load eccentricity, using the expression proposed by Fam *et al.* (2003)

$$E_{2,ecc} = E_{2,con} \frac{D_o}{D_o + e} \quad (2.22)$$

where  $E_{2,con}$  and  $E_{2,ecc}$  are respectively the slope of the second linear portion under concentric and eccentric compression cases in which the former can be calculated using Eq. (2.3);  $D_o$  is the outer diameter of annular concrete in hybrid DSTCs;  $e$  is the eccentricity of axial loading. Eq. (2.22) means that the ultimate axial strain of the confined concrete was considered not to be affected by the load eccentricity while the compressive strength of the confined concrete in hybrid DSTCs was considered to

decrease with the load eccentricity.

Compared with conventional circular DSTCs, Ma (2013) conducted eccentric compression tests on nine square hybrid DSTCs. The square specimens all had a side length of 150 mm and a height of 500 mm, and were confined with 2-ply post-applied GFRP wraps. The major variables were the eccentricity and the number of GFRP layers oriented along the longitudinal direction of columns. Based on the test results, an expression for the axial load capacity of square DSTCs under eccentric compression was proposed.

The research group led by Yao in Zhejiang University conducted the first series of eccentric compression tests on slender hybrid DSTCs (Xu *et al.* 2014; Yao *et al.* 2015). All specimens had a diameter of 300 mm and a height of 1800 mm and were confined with a filament-wound GFRP tube. The effects of various parameters, including the void ratio, the thickness of FRP tube and the eccentricity, were investigated. The thickness of FRP tube was either 3 mm, 6 mm or 10 mm, which is far larger than the desirable thickness for practical applications (2 mm to 4 mm). The maximum eccentricity was only 90 mm which was not large enough to represent real cases where flexure is dominant. Another deficiency of their studies is that the column slenderness was fixed, leaving the effect of column slenderness not well interpreted.

To address the limitations of the research reviewed above, the present research program will conduct an experimental study on the behavior of large-scale slender hybrid DSTCs subjected to eccentric compression where SCC and filament-wound GFRP tubes will be adopted. The column specimens will have a more reasonable FRP tube thickness of 2 mm, 3 mm and 4 mm, a wider range of the load eccentricities of

50 mm, 100 mm and 150 mm and various values of slenderness. In addition, a slenderness limit expression which is intended to differentiate short hybrid DSTCs from slender ones will be developed based on a comprehensive parametric study performed using a column model modified from Jiang and Teng's (2012) column model to capture the slenderness effect.

## 2.8 REFERENCES

- Abdelkarim, O.I. and ElGawady, M.A. (2016a). "Behavior of Hollow FRP-Concrete-Steel Columns under Static Cyclic Axial Compressive Loading", *Engineering Structures*. Vol. 123, pp.77-88.
- Abdelkarim, O.I. and ElGawady, M.A. (2016b). "Performance of Hollow-Core FRP-Concrete-Steel Bridge Columns Subjected to Vehicle Collision", *Engineering Structures*. Vol. 123, pp.517-531.
- Abdelkarim, O.I., ElGawady, M.A., Gheni, A., Anumolu, S. and Abdulazeez, M. (2017). "Seismic Performance of Innovative Hollow-Core FRP-Concrete-Steel Bridge Columns", *Journal of Bridge Engineering*. Vol. 22(2): 0416120.
- Abu-Farsakh, G.A. and Almasri, A.H. (2011). "A Composite Finite Element to Predict Failure Progress in Composite Laminates Accounting for Nonlinear Material Properties", *Structural Control and Health Monitoring*. Vol. 18, pp. 752-768.
- ACI 440.2R-08 (2008). "Guide for the Design and Construction of Externally Bonded FRP Systems for Strengthening Concrete Structures", American Concrete Institute (ACI), Farmington Hills, MI.
- Al-Khalil, M.F.S., Soden, P.D., Kitching, R. and Hinton, M.J. (1996). "The Effects of Radial Stresses on the Strength of Thin-walled Filament Wound GRP Composite Pressure Cylinders", *International Journal of Mechanical Sciences*. Vol. 38(1), pp.97-120.

- Al Abadi, H., El-Naga, H.A., Shaia, H. and Paton-Cole, Vidal. (2016). “Refined Approach for Modelling Strength Enhancement of FRP-Confined Concrete”, *Construction and Building Materials*. Vol. 119, pp.152-174.
- Albitar, M., Ozbakkaloglu, T. and Fanggi, B.A.L. (2015). “Behavior of FRP-HSC-Steel Double-Skin Tubular Columns under Cyclic Axial Compression”, *Journal of Composites for Construction*, ASCE. Vol. 19(2): 04014041.
- Al-Nimry, H. and Jawarneh, M. (2017). “Effects of Increased Slenderness in Short Heat-Damaged RC Columns Confined with FRP Composites”, *Materials and Structures*. Vol. 50(1), pp.95-105.
- ASTM D2290-16 (2016). “Standard Test Method for Apparent Hoop Tensile Strength of Plastic or Reinforced Plastic Pipe”, American Society for Testing and Materials (ASTM), Philadelphia, USA.
- ASTM D3039/D3039M-14 (2014). “Standard Test Method for Tensile Properties of Polymer Matrix Composite Materials”, American Society for Testing and Materials (ASTM), Philadelphia, USA.
- ASTM D3410/D3410M-16 (2016). “Standard Test Method for Compressive Properties of Polymer Matrix Composite Materials with Unsupported Gage Section by Shear Loading”, American Society for Testing and Materials (ASTM), Philadelphia, USA.
- ASTM D5449/D5449M-16 (2016). “Standard Test Method for Transverse Compressive Properties of Hoop Wound Polymer Matrix Composite Cylinders”, American Society for Testing and Materials (ASTM), Philadelphia, USA.
- Bazant, Z. P. (1984). “Size Effect in Blunt Fracture: Concrete, Rock, Metal”, *Journal of Engineering Mechanics*, ASCE. Vol. 110(4), pp.518-535.
- Binici, B. (2005). “An Analytical Model for Stress-Strain Behavior of Confined Concrete”, *Journal of Structural Engineering*, ASCE. Vol. 27(7), pp.1040-1051.

- Biskinis, D. and Fardis, M.N. (2013). "Models for FRP-Wrapped Rectangular RC Columns with Continuous or Lap-Spliced Bars under Cyclic Lateral Loading", *Engineering Structures*. Vol. 57, pp.199-212.
- Cao, Q., Tao, J.J., Wu, Z.M. and Ma, Z.G.J. (2017). "Behavior of FRP-Steel Confined Concrete Tubular Columns Made of Expansive Self-Consolidating Concrete under Axial Compression", *Journal of Composites for Construction*. Vol. 21(5): 04017037.
- Carey, S. A. (2003). "Effects of Shape, 'Gap,' and Scale on the Behavior and Modeling of Variably Confined Concrete," M.Sc. thesis, University of South Carolina, Columbia, S.C.
- Carey, S.A. and Harries, K.A. (2005). "Axial Behavior and Modeling of Confined Small-, Medium-, and Large-Scale Circular Sections with Carbon Fiber-Reinforced Polymer Jackets". *ACI Structural Journal*. Vol. 103(4), pp.596-604.
- Carrazedo, R., Mirmiran, A. and de Hanai, J.B. (2013). "Plasticity Based Stress-Strain Model for Concrete Confinement", *Engineering Structures*. Vol., 48, pp.645-657.
- Casas, J.R. and Chambi, J.L. (2014). "Partial Safety Factors for CFRP-Wrapped Bridge Piers: Model Assessment and Calibration", *Composite Structures*. Vol. 118(1), pp.267-283.
- CECS 203 (2006). "Technical Specifications for Self-Compacting Concrete Application", China Planning Press, Beijing, China. (in Chinese)
- Chabib, H.E., Nehdi, M. and Naggar, M.H.E. (2005). "Behavior of SCC Confined in Short GFRP Tubes", *Cement & Concrete Composites*. Vol. 27, pp.55-64.
- Chun, S.S. and Park, H.C. (2002). "Load Carrying Capacity and Ductility of RC Columns Confined by Carbon Fiber Reinforced Polymer", *Proceedings, 3rd International Conference on Composites in Infrastructure (CD-Rom)*.
- Demers, M. and Neale, K.W. (1999). "Confinement of Reinforced Concrete Columns

- with Fiber Reinforced Composite Sheets-An Experimental Study”, *Canadian Journal of Civil Engineering*. Vol.26, pp.226-241.
- EFNARC (2002). “Specification and Guidelines for Self-Compacting Concrete”, EFNARC, Surry, UK.
- El Chabib, H., Nehdi, M. and El Naggar, M.H. (2005). “Behavior of SCC Confined in Short GFRP Tubes”, *Cement & Concrete Composites*. Vol. 27(1), pp.55-64.
- Elsanadedy, H.M., Al-Salloum, Y.A., Alsayed, S.H. and Iqbal, R.A. (2012). “Experimental and Numerical Investigation of Size Effects in FRP-Wrapped Concrete Columns”, *Construction and Building Materials*. Vol. 29, pp.56-72.
- EPG (2005). “The European Guidelines for Self-Compacting Concrete: Specification, Production and Use”, the Self-Compacting Concrete European Project Group (EPG).
- Fahmy, M.F.M. and Wu, Z.S. (2010). “Evaluating and Proposing Models of Circular Concrete Columns Confined with Different FRP Composites”, *Composites Part B: Engineering*. Vol. 41(3), pp.199-213.
- Fam, A.Z. and Rizkalla, S.H. (2001a). “Confinement Model for Axially Loaded Concrete Confined by Circular Fiber-Reinforced Polymer Tubes”, *ACI Structural Journal*. Vol. 98(4), pp.451-461.
- Fam, A. Z., and Rizkalla, S.H. (2001b). “Behavior of Axially Loaded Concrete-Filled Circular Fiber-Reinforced Polymer Tubes”, *ACI Structural Journal*. Vol. 98(3), pp.280-289.
- Fam, A., Flisak, B. and Rizkalla, S. (2003). “Experimental and Analytical Modeling of Concrete-Filled Fiber-Reinforced Polymer Tubes Subjected to Combined Bending and Axial Loads”, *ACI Structural Journal*. Vol. 100(4), pp.499-509.
- Fanggi, B.A.L. and Ozbakkaloglu, T. (2013). “Compressive Behavior of Aramid FRP-HSC-Steel Double-Skin Tubular Columns”, *Construction and Building Materials*.

Vol. 48, pp.554-565.

- Fanggi, B.A.L. and Ozbakkaloglu, T. (2015a). "Behavior of Hollow and Concrete-Filled FRP-HSC and FRP-HSC-Steel Composite Columns Subjected to Concentric Compression", *Advances in Structural Engineering*. Vol. 18(5), pp. 715-738.
- Fanggi, B.A.L. and Ozbakkaloglu, T. (2015b). "Square FRP-HSC-Steel Composite Columns Behavior under Axial Compression", *Engineering Structure*. Vol.92, pp.156-171.
- Fardis, M.N. and Khalili, H. (1981). "Concrete Encased in Fibre Glass-Reinforced Plastic", *ACI Journal*. Vol. 78, pp.440-445.
- Faustino, P. and Chastre, C. (2015). "Analysis of Load-Strain Models for RC Square Columns Confined with CFRP", *Composites Part B: Engineering*. Vol. 74, pp.23-41.
- GB50608 (2010). "Technical Code for Infrastructure Application of FRP Composites", China Planning Press, Beijing, China. (in Chinese)
- Guler, S. and Ashour, A. (2016). "Review of Current Design Guidelines for Circular FRP-Wrapped Plain Concrete Cylinders", *Journal of Composites for Construction*, ASCE. Vol. 20(2): 04015057.
- Hahn, H.T. (1973). "Nonlinear Behavior of Laminated Composites", *Journal of Composite Materials*. Vol.7, pp.257-271.
- Hahn, H.T. and Tsai, S.W. (1973). "Nonlinear Elastic Behavior of Unidirectional Composite Laminae", *Journal of Composite Materials*. Vol.7, pp.102-118.
- Haj-Ali, R. and Kilic, H. (2002). "Nonlinear Behavior of Pultruded FRP Composite", *Composite Part B*. Vol. 33(3), pp.173-191.
- Han, L.H., Tao, Z., Liao, F.Y. and Xu, Y. (2010). "Tests on Cyclic Performance of FRP-Concrete-Steel Double-Skin Tubular Columns", *Thin-Walled Structures*. Vol.

48(6), pp.430-439.

Harmon, T. G. and Slattery, K.T. (1992). "Advanced Composite Confinement of Concrete", *Advanced composite materials in bridges and structures*. K. W. Neale and P. Labossie`re, eds., Canadian Society for Civil Engineering, Montre´al, pp.299-306.

Harries K.A. and Kharel, G. (2002). "Behavior and Modeling of Concrete Subject to Variable Confining Pressure", *ACI Materials Journal*. Vol. 99(2), pp.180-189.

Hollaway, L.C. (2010). "A Review of the Present and Future Utilization of FRP Composites in the Civil Infrastructure with Reference to their Important in-Service Properties", *Construction and Building Materials*. Vol. 24(12), pp.2419-2445.

Hu, F. and Yao, J. (2016). "Experimental Study of FRP-Concrete-Steel Double-Skin Tubular Long Columns Subjected to Axial Compression", *Industrial Construction*. Vol. 46(9), pp.130-139. (in Chinese)

Hull, D. Legg, M.J. and Spencer, B. (1978). "Failure of Glass/ Polyester Filament Wound Pipe", *Composites*. Vol.1, pp.17-24.

Idris, Y. and Ozbakkaloglu, T. (2014). "Flexural Behavior of FRP-HSC-Steel Composite Beams", *Thin-Walled Structures*. Vol. 80, pp.207-216.

Idris, Y. and Ozbakkaloglu, T. (2015). "Flexural Behavior of FRP-HSC-Steel Double Skin Tubular Beams under Reversed-Cyclic Loading", *Thin-Walled Structures*. Vol.87, pp.89-101.

Idris, Y. and Ozbakkaloglu, T. (2016). "Behavior of Square Fiber Reinforced Polymer-High-Strength Concrete-Steel Double-Skin Tubular Columns under Combined Axial Compression and Reversed-Cyclic Lateral Loading", *Engineering Structures*. Vol. 118, pp.307-319.

Ishikawa, T. and Chou, T.W. (1983). "Nonlinear Behavior of Woven Fabric

- Composites”, *Journal of Composite Materials*. Vol. 17, pp.399-413.
- ISO 7509 (2015). “Plastics Piping Systems - Glass-Reinforced Thermosetting Plastics (GRP) Pipes-Determination of Time to Failure under Sustained Internal Pressure”, the International Organization for Standardization (ISO).
- Jiang, T. and Teng, J.G. (2007). “Analysis-Oriented Stress-Strain Models for FRP-Confined Concrete”, *Engineering Structures*. Vol. 29(11), pp.2968-2986.
- Jiang, T. and Teng, J.G. (2012). “Theoretical Model for Slender FRP-Confined Circular RC Columns”, *Construction and Building Materials*. Vol. 32(4), pp.66-76.
- Jones, R.M. and Nelson JR, D.A.N. (1975). “A New Material Model for the Nonlinear Biaxial Behavior of ATJ-S Graphite”, *Journal of Composite Materials*. Vol.9, pp.10-27.
- Jones, R.M. and Morgon, H.S. (1977). “Analysis of Nonlinear Stress-Strain Behavior of Fiber-Reinforced Composite Material”, *AIAA Journal*. Vol. 15(12), pp.1669-1676.
- Jones, R.M. (1980). “Modeling Nonlinear Deformation of Carbon-Carbon Composite Materials”, *Journal of Composite Materials*. Vol. 18(8), pp.995-1001.
- Karbhari, V.M. and Gao, Y. (1997). “Composite Jacketed Concrete under Uniaxial Compression-Verification of Simple Design Equations”, *Journal of Materials in Civil Engineering*, ASCE. Vol. 9(4), pp.185-193.
- Karimi K., Tait M.J. and El-Dakhakhni, W.W. (2011). “Testing and Modeling of a Novel FRP-Encased Steel-Concrete Composite Column”, *Composite Structures*. Vol. 93(5), pp.1463-1473.
- Kestner, J.T., Harries, K.A., Pessiki, S.P., Sausee, R. and Ricles, J.M. (1997). “Rehabilitation of Reinforced Concrete Columns Using Fiber Reinforced Polymer Composite Jackets”, ATLSS Rep. No. 97-07, Lehigh Univ., Bethlehem,

Pa.

- Khairallah, F. (2013). "Mechanical Behavior of Confined Self-Compacting Reinforced Concrete Circular Columns under Concentric Axial Loading", *Ain Sham Engineering Journal*. Vol. 4(4), pp.641-649.
- Kono, S., Inazumi, M., and Kaku, T. (1998). "Evaluation of Confining Effects of CFRP Sheets on Reinforced Concrete Members", *Fiber composites in infrastructure*, ICCI '98, H. Saadatmanesh and R. Eshani, eds., Univ. of Arizona, Tucson, Ariz., pp.343-355.
- Kwan, A. K. H., Dong, C. X. and Ho, J. C. M. (2015). "Axial and Lateral Stress-Strain Model for FRP Confined Concrete", *Engineering Structures*. Vol. 99, pp.285-295.
- Lam, L. and Teng, J.G. (2002). "Strength Models for Fiber-Reinforced Plastic-Confined Concrete", *Journal of Structural Engineering*, ASCE. Vol. 128(5), pp.612-623.
- Lam, L. and Teng, J.G. (2003). "Design-Oriented Stress-Strain Model for FRP-Confined Concrete", *Construction and Building Materials*. Vol. 17(6), pp.471-489.
- Lam, L. and Teng, J.G. (2004). "Ultimate Condition of Fiber Reinforced Polymer-Confined Concrete", *Journal of Composites for Construction*, ASCE. Vol. 8, pp.539-548.
- Lam, L. and Teng, J.G. (2006). "FRP-Confined Concrete under Axial Cyclic Compression", *Cement and Concrete Composites*. Vol. 28(10), pp.949-958.
- Lam, L. and Teng, J.G. (2009). "Stress-Strain Model for FRP-Confined Concrete under Cyclic Axial Compression", *Engineering Structures*. Vol. 31(2), pp.308-321.
- Lee, C.S. and Hegemier, G.A. (2009). "Model of FRP-Confined Concrete Cylinders

- in Axial Compression”, *Journal of Composites for Construction*. Vol. 13(5), pp.442-454.
- Li, G.Q., Torres,S., Alaywan, W. and Abadie, C. (2010). “Experimental Study of FRP Tube-Encased Concrete Columns”, *Journal of Composites Materials*. Vol. 39(13), pp.1131-1145.
- Li, G.Q., Pang, S.S., Ibekwe, S.I. (2011). “FRP Tube Encased Rubberized Concrete Cylinders”, *Materials and Structures*. Vol. 44, pp.233-243.
- Lim, J.C. and Ozbakkaloglu, T. (2014). “Confinement Model for FRP-Confined High-Strength Concrete”, *Journal of Composites for Construction*. Vol. 18(4): 04013058.
- Liu, H., He, M.H., Luan, Y.Q., Guo, J. and Liu, L.L. (2013). “A Modified Constitutive Model for FRP Confined Concrete in Circular Sections and its Implementation with Opensees Programming”, *Journal of Zhejiang University: Science A*. Vol. 14(12), pp.856-866.
- Liu, M.X. and Qian, J.R. (2007). “Moment-Curvature Relationships of FRP-Concrete-Steel Double-Skin Tubular Members”, *Journal of Tsinghua University (Sci&Tech)*. Vol. 47(12), pp. 2105-2110. (in Chinese)
- Liu, M.X. and Qian, J.R. (2008). “Study on Axial Force-Moment Interaction Relationship of FRP-Concrete-Steel Double-Skin Tubes”, *Building Structures*, Vol. 38(8), pp. 83-86. (in Chinese)
- Ma, Z.Q. (2013). “Performance Investigation of FRP-Concrete-Steel Double-Skin Square Columns under Eccentric Compressive Loading”, M.Sc. thesis, Zhengzhou University, China. (in Chinese)
- Marques, S.P.C., Marques D.C.D.S.C., Lins, da. Silva. J. and Cavalcante, M.A.A. (2004). “Model For Analysis of Short Columns of Concrete Confined by Fiber-Reinforced Polymer”, *Journal of Composites for Construction, ASCE*. Vol. 8(4),

pp.332-340.

- Mirmiran, A. and Shahawy, M. (1996). "A New Concrete-Filled Hollow FRP Composite Column", *Composites Part B: Engineering*. Vol. 27B(3), pp.263-268.
- Mirmiran, A. and Shahawy, M. (1997). "Behavior of Concrete Columns Confined by Fiber Composites", *Journal of Structural Engineering*, ASCE. Vol. 123(5), pp.583-590.
- Mirmiran, A., Shahawy, M., Samaan, M., El Echary, H., Mastrapa, J.C. and Pico, O. (1998). "Effect of Column Parameters on FRP-Confined Concrete." *Journal of Composite for Construction*. Vol. 2(4), pp.175-185.
- Mohamed, H.M. and Masmoudi, R. (2010). "Axial Load Capacity of Concrete-Filled FRP Tube Columns: Experimental Versus Theoretical Predictions", *Journal of Composites for Construction*, ASCE. Vol. 14(2), pp.231-243.
- Ozbakkaloglu, T. (2013). "Compression Behavior of Concrete-Filled FRP Tube Columns: Assessment of Critical Column Parameters", *Engineering Structures*. Vol. 51, pp.188-199.
- Ozbakkaloglu, T., Lim, J. C. and Vincent, T. (2013). "FRP-Confined Concrete in Circular Sections: Review and Assessment of Stress-Strain Models", *Engineering Structures*. Vol. 49, pp.1068-1088.
- Ozbakkaloglu, T. and Idris, Y. (2014). "Seismic Behavior of FRP-High-Strength Concrete-Steel Double-Skin Tubular Columns", *Journal of Structural Engineering*, ASCE. Vol. 140(6): 04014019.
- Ozbakkaloglu, T. and Fanggi, B.A.L. (2014). "Axial Compressive Behavior of FRP-Concrete-Steel Double-Skin Tubular Columns Made of Normal- and High-Strength Concrete", *Journal of Composites for Construction*, ASCE. Vol. 18(1): 04013027.
- Ozbakkaloglu, T. (2015). "A Novel FRP-Dual-Grade Concrete-Steel Composite

- Column System”, *Thin-Walled Structures*. Vol. 96, pp.295-306.
- Ozbakkaloglu, T. and Fanggi, B.A.L. (2015). “FRP-HSC-Steel Composite Columns Behavior under Monotonic and Cyclic Axial Compression”, *Material and Structures*. Vol. 48, pp.1075-1093.
- Ozbakkaloglu, T. and Fanggi, B.A.L and Zheng, J. (2016). “Confinement Model for Concrete in Circular and Square FRP-Concrete-Steel Double-Skin Composite Columns”, *Materials and Design*. Vol. 96, pp.458-469.
- Park, J.H., Jo, B.W, Yoon, S.J. and Park, S.K. (2011). “Experimental Investigation on the Structural Behavior of Concrete Filled FRP Tubes with/without Steel Re-Bar”, *KSCE Journal of Civil Engineering*. Vol. 15(2), pp.337-345.
- Pham, T.M., Hadi, M.N.S. and Youssef, J. (2015). “Optimized FRP Wrapping Schemes for Circular Concrete Columns under Axial Compression”, *Journal of Composites for Construction*, ASCE. Vol. 19(6): 04015015.
- Qian, J.R. and Liu, M.X. (2006). “Experiment of FRP-Concrete-Steel Double-Skin Long Columns under Axial Compressive Load”, *Concrete*. Vol. 203(9), pp.31-34. (in Chinese)
- Qian, J.R. and Liu, M.X. (2008a). “Experimental Investigation of FRP-Concrete-Steel Double Skin Tubular Stubs under Axial Compressive Loading”, *Journal of Building Structures*. Vol. 29(2), pp.104-113. (in Chinese)
- Qian, J.R. and Liu, M.X. (2008b). “Test of Seismic Behavior of FRP-Concrete-Steel Double-Skin Tubular Columns”, *China Civil Engineering Journal*. Vol. 41(3), pp. 29-36. (in Chinese)
- Qian, J.R. and Liu, M.X. (2008c). “A Hysteretic Model of Moment-Rotation Relationship for Plastic Hinge Zone of FRP-Concrete-Steel Double Skin Tubular Columns”, *Engineering Mechanics*. Vol. 25(11), pp.48-52. (in Chinese)
- Rocca, S., Galati, N. and Nanni, A. (2009). “Interaction Diagram Methodology for

- Design of FRP-Confined Reinforced Concrete Column”, *Construction and Building Materials*. Vol. 23, pp.1508-1520.
- Rosenow, M.W.K. (1984). “Winding Angle Effects in Glass Fiber-Reinforced Polyester Filament Wound Pipes”, *Composites*. Vol. 10, pp.247-250.
- Saafi, M., Toutanji, H.A. and Li, Z. (1999). “Behavior of Concrete Columns Confined with Fiber Reinforced Polymer Tubes”, *ACI Materials Journal*. Vol. 96(4), pp.500-509.
- Spoelstra, M.R. and Monti, G. (1999). “FRP-Confined Concrete Model”, *Journal of Composites for Construction*, ASCE. Vol. 15, pp.143-150.
- Soden, P.D., Kitching, R., Tse, P.C. and tsavalas, Y. (1993). “Influence of Winding Angle on the Strength and Deformation of Filament-Wound Composite Tubes Subjected to Uniaxial and Biaxial Loads”, *Composites Science and Technology*. Vol. 46(4), pp.363-378.
- Su, N., Hsu, K.C. and Chai, H.W. (2001). “A Simple Mix Design Method for Self-compacting Concrete”, *Cement and Concrete Research*. Vol. 31(12), pp.1799-1807.
- Teng, J.G. and Lam, L. (2002). “Compressive Behavior of Carbon Fiber Reinforced Polymer Confined Concrete in Elliptical Columns”, *Journal of Structural Engineering*, ASCE. Vol. 128(12), pp.1535-1543.
- Teng, J.G., Yu, T. and Wong, Y.L. (2004). “Behaviour of Hybrid FRP-Concrete-Steel Double-Skin Tubular Columns”, *Proceedings, Second International Conference on FRP Composites in Civil Engineering*, 8-10 December, Adelaide, Australia, pp.811-818.
- Teng, J. G., Huang, Y. L., Lam, L. and Ye, L. P. (2007a). “Theoretical Model for Fiber Reinforced Polymer-Confined Concrete”, *Journal of Composites for Construction*, ASCE. Vol. 11(2), pp.201-210.

- Teng, J.G., Yu, T. Wong, Y.L. and Dong, S.L. (2007b). “Hybrid FRP-Concrete-Steel Tubular Columns: Concept and Behavior”, *Construction and Building Material*. Vol. 21(4), pp.846-854.
- Teng, J.G., Jiang, T., Lam, L. and Luo, Y.Z. (2009). “Refinement of a Design-Oriented Stress-Strain Model for FRP-Confined Concrete”, *Journal of Composites for Construction*, ASCE. Vol. 13(4), pp.269-278.
- Teng, J.G. and Yu, T. (2010). “Hybrid FRP-Concrete Tubular Columns: Design Provisions in the Draft Chinese Code”, *Proceedings International Symposium on Life-Cycle Performance of Bridges and Structures*. 27-29 June, 2010, Changsha, China, pp. 387-394.
- Teng, J.G., Zhao, J.L., Yu, T., Li, L.J. and Guo, Y.C. (2016). “Behavior of FRP-Confined Compound Concrete Containing Recycled Concrete Lumps”, *Journal of Composites for Construction*. Vol. 20(1), 04015038.
- Thériault, M, Neale, K.W. and Claude, S. (2004). “Fiber-Reinforced Polymer-Confined Circular Concrete Columns: Investigation of Size and Slenderness Effects”, *Journal of Composites for Construction*. Vol. 8(4), pp.323-331.
- Toutanji, H.A. (1999). “Stress-Strain Characteristics of Concrete Columns Externally Confined with Advanced Fiber Composite Sheets”, *ACI Materials Journal*. Vol. 96(3), pp.397-404.
- TR-6-03 (2003). “Interim Guidelines for the Use of Self-Consolidating Concrete in Precast/Prestressed Concrete”, Institute Member Plants, Precast/Prestressed Concrete Institute, Chicago, Illinois, USA.
- TR 55 (2012). “Design Guidance for Strengthening Concrete Structures Using Fibre Composite Materials”, Concrete Society Technical Report 55. The Concrete Society, Crowthorne, UK.
- Wang, Y.F. and Wu, H.L. (2011). “Size Effect of Concrete Short Columns Confined

- with Aramid FRP Jackets”, *Journal of Composites for Construction*. Vol. 15(4), pp.535-544.
- Wang, Z.B. and Tao, Z. (2009). “Experimental Behavior of FRP-Concrete-Steel Double-Skin Tubular Beams”, *Industrial Construction*. Vol. 39(4), pp.5-8. (in Chinese)
- Wang, J., Liu, W.Q., Fang, H. and Zhu, L. (2012). “Experiment and Capacity Calculation Theory Research of Hybrid GFRP-Concrete-Steel Double Skin Tubular Columns under Axial Compression”, *Building Structure*. Vol. 42(2), pp.133-138. (in Chinese)
- Wang, D., Duan, X.P. and Wang, Y.Z. (2013). “The Experimental Study on the Square FRP-Concrete-Steel Double-Skin Tubular Columns under Axial Concentric Compression”, *China Concrete and Cement Products*. Vol. 10, pp.39-42. (in Chinese)
- Wong, Y.L., Yu, T., Teng, J.G. and Dong, S.L. (2008). “Behavior of FRP-Confined Concrete in Annular Section Columns”, *Composites Part B: Engineering*. Vol. 39(3), pp.451-466.
- Wei, Y.Y. and Wu, Y.F. (2012). “Unified Stress-Strain Model of Concrete for FRP-Confined Columns”, *Construction and Building Materials*. Vol. 26(1), pp.381-392.
- Xia, Y.M., Yang, B.C. and Xu, Z. (1986). “Nonlinear Constitutive Relation of Unidirectional Composite Laminae”, *Acta Materiae Compositae Sinica*. Vol. 3(4), pp.44-50. (in Chinese)
- Xiao, Q., Jiang, S. and Růžička, M. (2009). “Experimental Verification and Theory Analysis of Nonlinear Behavior of Filament Wound Composite Products”, *Proceedings of the 3rd ICMEM, International Conference on Mechanical Engineering and Mechanics*, 21-23 Oct, 2009, Beijing, China.

- Xiao, Y. and Wu, H. (2000). “Compressive Behavior of Concrete Confined by Carbon Fiber Composite Jackets”, *Journal of Materials in Civil Engineering*, ASCE. Vol. 12(2), pp.139-146.
- Xiao, Y. and Wu, H. (2003). “Compressive Behavior of Concrete Confined by Various Types of FRP Composites Jackets”, *Journal of Reinforced Plastics and Composites*. Vol. 22(13), pp.1187-1202.
- Xie, P., Yu, T., Wong, Y.L and Teng, J.G. (2011). “Compression Behavior of Large-scale Hybrid FRP-Concrete-Steel Double-Skin Tubular Columns”, *International Conference on Civil Engineering, Architecture and Building Materials*. CEABM2011, Haikou, China, pp.1138-1144.
- Xu, P., Yao, J. and Lu, Z.G. (2014). “Experimental Study of FRP-Concrete-Steel Double-Skin Tubular Long Columns Subjected to Eccentric Compression”, *Industrial Construction*. Vol. 44(1), pp.134-137. (in Chinese)
- Yao, J., Jiang, T., Xu, P. and Lu, Z.G. (2015). “Experimental Investigation on Large-Scale Slender FRP-Concrete-Steel Double-Skin Tubular Columns Subjected to Eccentric Compression”, *Advanced in Structural Engineering*. Vol. 18(10), pp.1737-1746.
- Yu, T., Wong, Y.L., Teng, J.G., Dong, S.L. and Lam, E.S.S. (2006). “Flexural Behavior of Hybrid FRP-Concrete-Steel Double-Skin Tubular Members”, *Journal of Composites for Construction*, ASCE, Vol. 10(5), pp.443-452.
- Yu, T., Teng, J.G. and Wong, Y.L. (2010a). “Stress-Strain Behavior of Concrete in Hybrid FRP-Concrete-Steel Double Skin Tubular Columns”, *Journal of Structural Engineering*, ASCE. Vol. 136(4), pp.379-389.
- Yu, T., Wong, Y.L. and Teng, J.G. (2010b). “Behaviour of Hybrid FRP-Concrete-Steel Double-Skin Tubular Columns Subjected to Eccentric Compression”, *Advances in Structural Engineering*. Vol. 13(5), pp.961-974.

- Yu, T., Teng, J.G., Wong, Y.L. and Dong, S.L. (2010c). "Finite Element Modeling of Confined Concrete-I: Drucker-Prager Type Plasticity Model", *Engineering Structures*. Vol. 32(3), pp.665-679.
- Yu, T., Teng, J.G., Wong, Y.L. and Dong, S.L. (2010d). "Finite Element Modeling of Confined Concrete-II: Plastic Damage Model", *Engineering Structures*. Vol. 32(3), pp.680-691.
- Yu, T., Zhang, B. Cao, Y.B. and Teng, J.G. (2012). "Behavior of Hybrid FRP-Concrete-Steel Double-Skin Tubular Columns Subjected to Cyclic Axial Compression", *Thin-Walled Structures*. Vol. 61, pp.96-203.
- Yu, T. and Teng, J.G. (2013). "Behavior of Hybrid FRP-Concrete-Steel Double-Skin Tubular Columns with a Square Outer Tube and a Circular Inner Tube Subjected to Axial Compression", *Journal of Composites for Construction*. Vol. 17, pp.271-279.
- Yu, T., Fang, X.L. and Teng, J.G. (2014). "FRP-Confined Self-compacting Concrete under Axial Compression", *Journal of Materials in Civil Engineering*. Vol. 26(11): 04014082.
- Yu, T., Zhang, S.S., Huang, L. and Chan, C. (2017). "Compressive Behavior of Hybrid Double-Skin Tubular Columns with A Large Rupture Strain FRP Tube", *Composite Structures*. Vol. 171, pp.10-18.
- Zhang, B., Yu, T. and Teng, J.G. (2011). "Axial Compression Tests on Hybrid Double-Skin Tubular Columns Filled with High Strength Concrete", *Proceedings, Third International Postgraduate Conference on Infrastructure and Environment*, 11-12 July, Hong Kong, China, pp.171-176.
- Zhang, B., Yu, T., J. G. Teng, J.G. (2015a). "Behavior of Concrete-Filled FRP Tubes under Cyclic Axial Compression", *Journal of Composites for Construction*, ASCE. Vol. 19(3), 04014060.

- Zhang, B., Teng, J.G. and Yu, T. (2015b). “Experimental Behaviour of Hybrid FRP-Concrete-Steel Double-Skin Tubular Columns under Combined Axial Compression and Cyclic Lateral Loading”, *Engineering Structures*. Vol. 99, pp. 214-231.
- Zhang, B., Teng, J.G. and Yu, T. (2017). “Compressive Behavior of Double-Skin Tubular Columns with High-Strength Concrete and a Filament-Wound FRP Tube”, *Journal of Composites for Construction*, ASCE. Vol. 21(5): 04017029.
- Zhao, J.L., Teng, J.G., ASCE, M., Yu, T. and Li, L.J. (2016). “Behavior of Large-Scale Hybrid FRP-Concrete-Steel Double-Skin Tubular Beams with Shear Connectors”, *Journal of Composites for Construction*, ASCE. Vol. 20(5): 04016015.
- Zhou, J.K, Bi, F.T., Wang, Z.Q. and Zhang, J. (2016). “Experimental Investigation of Size Effect on Mechanical Properties of Carbon Fiber Reinforced Polymer (CFRP) Confined Concrete Circular Specimens”, *Construction and Building Materials*. Vol. 127, pp. 643-652.
- Zhou, Y.W., Hu, J.J., Li, M.L., Sui, L.L. and Xing, F. (2016). “FRP-Confined Recycled Coarse Aggregate Concrete: Experimental Investigation and Model Comparison”, *Polymers*. Vol. 8(375): 8100375.
- Zhou, Y.W., Liu, X.M., Xing, F., Li, D.W., Wang, Y.C. and Sui, L.L. (2017). “Behavior and Modeling of FRP-Concrete-Steel Double-Skin Tubular Columns Made of Full Lightweight Aggregate Concrete”, *Constructions and Building Materials*. Vol.139, pp.52-63.
- Zindel, D. and Bakis, Ch.E. (2011). “Nonlinear Micromechanical Model of Filament-Wound Composite Considering Fiber Undulation”, *Mechanics of Composite Materials*. Vol. 47(1): pp.73-94.
- Zohrevand, P. and Mirmiran, A. (2011). “Behavior of Ultrahigh-Performance Concrete Confined by Fiber-Reinforced Polymers”, *Journal of Materials in Civil*

*Engineering*, ASCE. Vol. 23(12), pp.1727-1734.

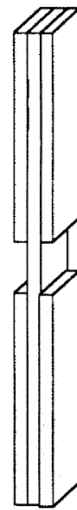


**Figure 2. 1** Filament winding process



(a) Coupon for tension test

[ASTM D3039/D 3039M-14 (2014)]



(b) Coupon for compression test

[ASTM D 3410/ D 3410M-16 (2016)]

**Figure 2. 2** Strip specimens

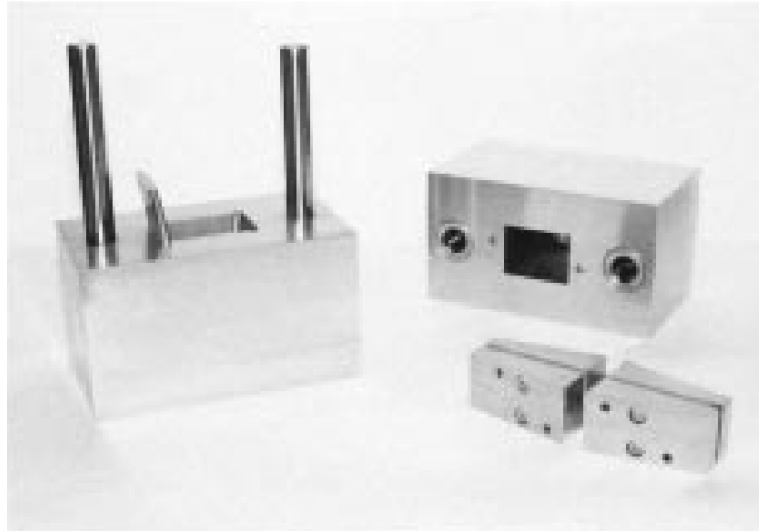
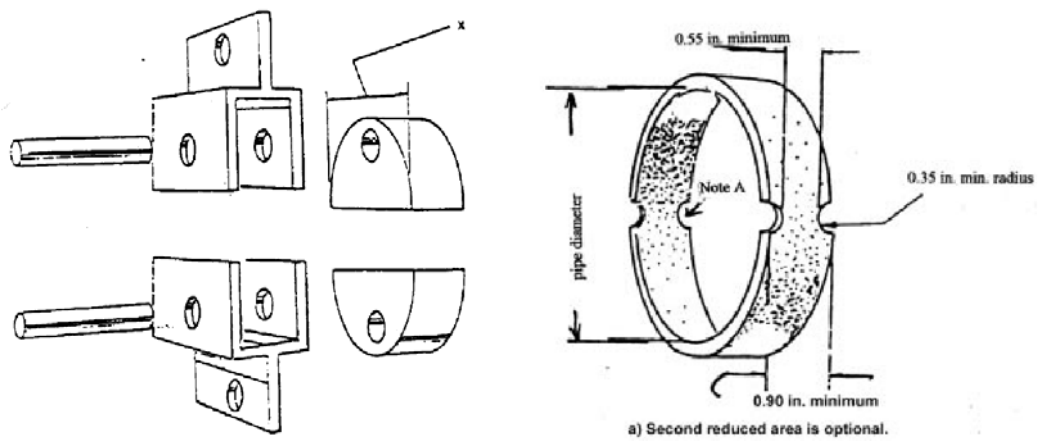


**Figure 2. 3** The compression test fixture

[ASTM D 3410/ D 3410M-16 (2016)]



(a) Fixture of split disk test

(b) Reduced-section ring specimen

**Figure 2. 4** Split disk test

[ASTM D2290-16(2016)]

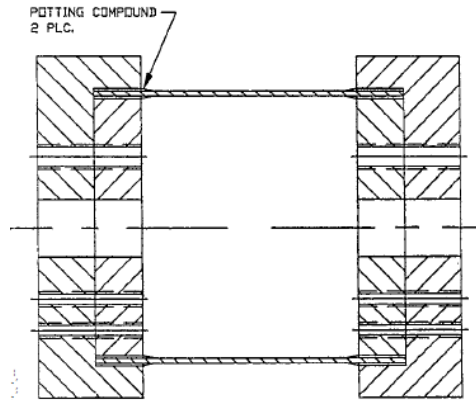


**Figure 2. 5** Illustration of the assembled compression fixture and specimen

[ASTM D5449/D5449M-16 (2016)]

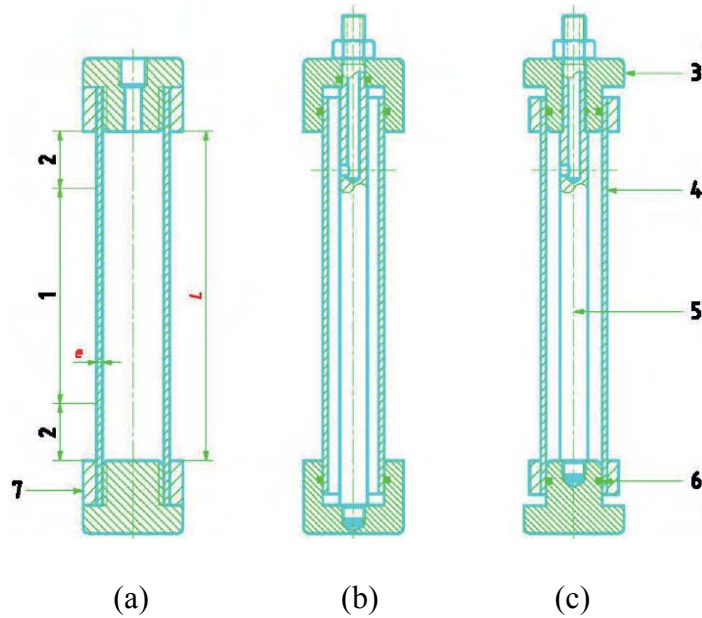
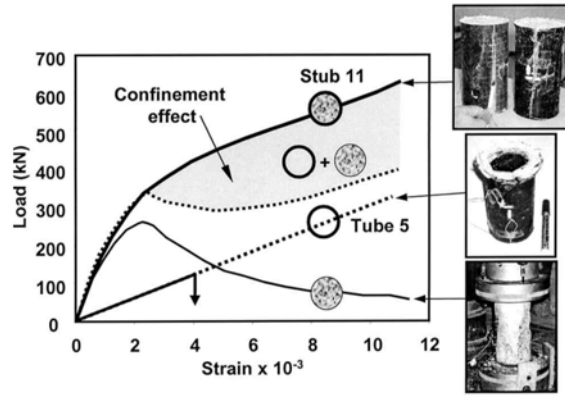


**Figure 2. 6** Typical arrangements for pressure testing of pipes [ISO 7509 (2015)]: (a) Testing with end thrust; (b) Testing without end thrust, external seals; and (c) Testing without end thrust, internal seals

Key: 1-valid failure zone; 2-end fixture influence zone; 3-end cap; 4-test specimen; 5-tie rod to carry end thrust; 6-elastomeric seal; 7-end seal device; L-free length between end fixtures.



(a) Tests by Fam *et al.* (2001b)

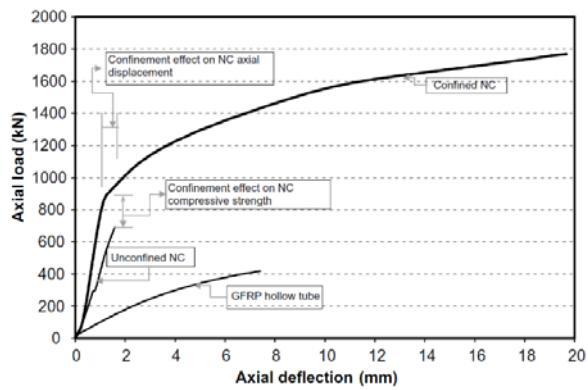
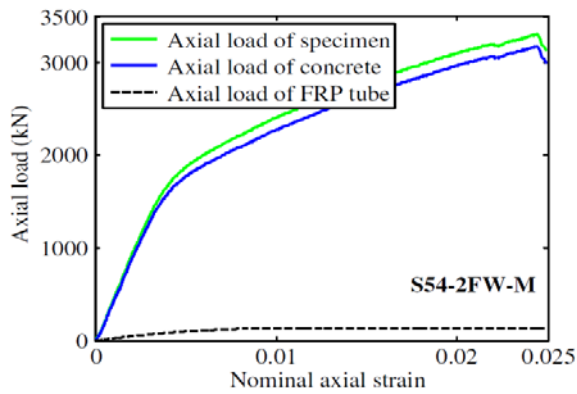


Fig. 3. Axial load–deformation response of NC cylinders and GFRP tube.

(b) Tests by El Chabib *et al.* (2005)



(c) Tests by Zhang *et al.* (2015a)

**Figure 2. 7** Treatments for axial load resisted by FRP tube in a CFFT specimen

# CHAPTER 3

## CHARACTERIZATION OF LONGITUDINAL AND CIRCUMFERENTIAL PROPERTIES OF FILAMENT-WOUND FRP TUBES

### 3.1 INTRODUCTION

As reviewed in Chapter 2, CFFTs and hybrid DSTCs have shown promise as compressive members particularly for situations where corrosion and seismic resistance abilities are of primary concern. In CFFTs and hybrid DSTCs, the FRP tube is typically manufactured via a filament winding process (i.e., filament-wound FRP tube). When a CFFT/hybrid DSTC is under uniaxial compression, lateral dilation of concrete occurs and induces tension in the FRP tube in the circumferential direction, which in turn provides lateral confining pressure to the concrete core. So the mechanical properties of the FRP tube in the circumferential direction should be determined as a prerequisite for the subsequent structural analysis.

On the other hand, as the fibers in a filament-wound FRP tube are always oriented at an angle smaller than  $90^\circ$  with respect to the longitudinal axis of the tube, the FRP tube also has a significant stiffness in the axial direction. When both the concrete and the FRP tube in a CFFT/hybrid DSTC are loaded simultaneously in axial compression, the FRP tube is subjected to a biaxial stress state. For this reason, the axial stiffness and the Poisson's effect of filament-wound FRP tubes should be exactly identified. In this section, a variety of test methods for characterizing the mechanical properties of filament-wound FRP tubes are reviewed, according to the forms of specimens (i.e., strip, ring and tube specimens). A summary of standard test methods in ASTM and ISO is provided in Table 3.1.

### **3.1.1 Test Methods for Strip Specimens**

Existing standard test methods are based mainly on strip specimens cut from materials in the forms of sheets, plates and slabs. While many standard methods are available for determining the tensile properties of plastics or polymer matrix composite materials based on strip specimens (e.g., ASTM D638 2014; ASTM D3039 2014; ASTM D7565 2017; ISO 8521 2009; ISO 8513 2016), the method described in ASTM D3039 has more frequently been used in studies on FRP for civil engineering applications (e.g., Lam and Teng 2004). However, these methods are not directly applicable to filament-wound FRP tubes. For example, if a strip specimen is cut from a filament-wound FRP tube in the longitudinal direction following the method of ISO 8513 (2016), the fibers are free to move and lose straightness due to lack of anchorage, preventing the accurate determination of FRP tensile properties. On the other hand, if a strip specimen is cut circumferentially from the tube following the method of ISO 8521 (2009), which is used to determine conformity to a minimum strength requirement, the bending-tension coupling of the strip in the tension test would not be negligible. It should be mentioned that although ASTM D638-14 (2014) is recommended by ASTM 2996-15 (2015) for filament-wound “fiberglass” (glass fiber-reinforced thermosetting-resin) tubes, the errors induced by the lack of enough anchorage of the cut fibers in the determination of FRP tube tensile properties should not be neglected.

### **3.1.2 Test Methods for Ring Specimens**

In some standard test methods, full cross-section segments of a specified length cut from plastic or FRP tubes are used as test specimens for the determination of longitudinal and circumferential properties of the tubes. One of the methods is the ring-

splitting test (ASTM D2290-16 2016; ISO8521 2009) where an external force is applied to the two self-aligning test fixtures consisting of two half-circle disks installed inside the ring-shaped specimen. The split of the half disks results in the tensioning of the ring specimen until rupture. This test has been used in studies on concrete confinement with externally wrapped FRP (e.g., Lam and Teng 2004; Kaynak *et al.* 2005) to compare with the results of strip tests. The main shortage of the method is the difficulty in obtaining the exact tensile strains within a gauge length as a result of bending in addition to tensioning of the ring specimen induced by the split of the half disks and the non-uniform distribution of stresses and strains due to the friction between the ring specimen and the half disks.

In order to eliminate the effect of friction on the measurement of hoop modulus, Yoon *et al.* (1997) averaged the readings of eight hoop strain gauges uniformly distributing around the perimeter of the ring specimen when the specimen experienced a complete process of loading and unloading. Jones *et al.* (1996) modified the established split disk method by introducing needle rollers between the disk and the ring specimen for reducing the friction to a low value.

In order to minimize the effect of bending, Wang *et al.* (2002) suggested using notched ring specimens and locating the notches at an angle away from the gap between the split disks. Arsene and Bai (1996, 1998) proposed a new experimental technique to determinate the circumferential properties of structural tubes (e.g., steel tubes) based on the ring-split disk test method. The two half disks are replaced by a steel assembly consisting of three parts, a bone-shaped steel part with two curved ends having the same curvature as the inner surface of the ring specimen and two symmetrical self-aligning steel blocks installed on both sides of the bone-shaped part to receive the split

force. The bone-shaped part is fixed into the central position of the ring specimen to block the radial displacement of the ring specimen during testing. In such way, the effect of bending can be much reduced and a more uniform stress distribution can be achieved. On the other hand, a pressurized ring test using an internal rubber bladder to load the specimen was used by Cohen *et al.* (1995) and Cohen (1997) with the objective of achieving a uniform stress distribution.

### **3.1.3 Test Methods for Tube Specimens**

Another type of methods of testing with a full cross-section specimen is the “burst test” of tubes (Hull *et al.* 1978; Rosenow 1984; Soden *et al.* 1993; ISO 7509 2015). In such a test, internal pressure is applied in the manner of either open-ended burst or close-ended burst to provide a uniaxial or biaxial state of stresses. In open-ended burst tests, the uniform internal pressure is applied to the tube specimen, assuming that the ends of the specimen are free to slide and thus the axial stress is zero, although in fact a small shortening of tube may occur and the frictional constraints at seals will lead to axial stresses (Al-Khalil *et al.* 1996). For the close-ended burst tests, various combinations of internal pressure and axial loading (provided by the dynamic rod seals) have been used (Ellyin and Wolodko 1977; Soden *et al.* 1978). Ellyin *et al.* (1977) designed a hydraulic tensile machine which was able to apply axial load, differential pressure and torsion to a tubular specimen simultaneously. In close-ended burst tests, axial stresses are not zero because both ends of the tube are sealed and clamped to end platens (ISO 8521 2009; Card 1965; Lee *et al.* 1989).

Basalo (2011) developed a novel test method to measure the ultimate hoop strain in FRP circular jackets using the expansion property of water when it is changed in state

from liquid to solid.

On the other hand, in standard methods for tube tests as listed in Table 3.1, tube segments with a specified length are used to determine the longitudinal compressive and tensile properties. In methods described in ASTM D5449/D5449M-16 (2016) and ASTM D5450/D5450M-16 (2016), the specimens are firmly secured between the end fixtures by using a potting material. Zhang *et al.* (2009) modified the above standard methods by bonding each end of the GFRP tube with an inner steel cap and an outer strengthening steel ring for the determination of compressive and tensile properties. In ASTM D2105-01 (2014) and ISO 8513 (2016) the test specimen is fixed using a tapered mandrel with end grips for the application of load to determine the longitudinal tensile properties of tubes. In ASTM D695-15 (2015), uniaxial compressive loads are directly applied to a cylinder or prism specimen, which imposes strict requirements to the precision of the specimen geometry.

Among different testing techniques reviewed above in this section, the burst tests offer the closest estimate of the circumferential mechanical properties of filament-wound GFRP tubes, because the loading condition of the tube specimens under uniform internal pressure in the tube tests is very similar to that of the FRP tubes in concrete confinement applications. To achieve an accurate determination of the GFRP tube properties using the burst tests, the dimensions of the tubes must be strictly controlled to tighten connections between the specimen and the test fixtures. Nevertheless, variations of wall thickness and inner diameter are inevitable during the fabrication process of filament-wound FRP tubes due to the variations of the resin content and the draft angle of mandrel. The hydraulic tensile machine designed by Ellyin *et al.* (1977) is very attractive due to its ease of use and stability in performance, but its high cost

becomes the obstacle in the way of its application.

In this chapter, an experimental investigation into the mechanical properties of the filament-wound GFRP tubes used in the present study will be presented. The longitudinal and circumferential properties of the GFRP tubes will be determined using three test methods, namely, strip tests, ring tests and tube tests. The results from different tests will be compared and the results of axial compression tests and hydraulic tests of FRP tubes will be recommended. The following sign convention is adopted in the present chapter: tensile stresses and strains are positive, while compressive stresses and strains are negative.

All the GFRP tubes were manufactured with fibers oriented at  $\pm 80^\circ$  with respect to the longitudinal axis of the tube with a nominal fiber volume fraction of 55% and supplied by Guangdong Sunny FRP Co. Ltd.

### **3.2 STRIP TESTS FOR LONGITUDINAL TENSILE PROPERTIES OF FILAMENT-WOUND GFRP TUBES**

The filament-wound GFRP tubes tested in this section had an inner diameter of 400 mm and a thickness of 5 mm or 7 mm (including the thickness of tube inner lining), corresponding to 4 or 6 layers of helically wound fibers at a winding angle of  $\pm 80^\circ$  relative to the tube axis. For each type of GFRP tubes, five rectangular strips, cut from the GFRP tube along the longitudinal direction, were tested in accordance with ASTM D3039/D 3039M-14 (2014). Each end of the specimen was bonded with two pieces of aluminum sheet to prevent gripping damage. The test length of specimens was 150mm (excluding the length of tab) and the width was 25mm as shown in Figure 3.1. For each strip specimen, two strain gauges with a gauge length of 20 mm were installed,

each at the middle of either face, to measure the longitudinal strains.

Figure 3.2 (a) and (b) illustrate the axial stress-axial strain curves of FRP strip specimens with a thickness of 5mm and 7mm, respectively. Figure 3.3 shows the failure mode of the specimens. The key test results, including the longitudinal tensile strength and the longitudinal modulus of elasticity, are provided in Table 3.2.

For all of the 5-mm thick specimens and two of the 7-mm thick specimens (Specimen F1 and F6), the stress-strain curves experienced a sudden drop followed by a gradual rise in stress as shown in Figure 3.2 as a result of the fact that the fibers of the specimen relocated under tension force and then were re-grappled by the resin matrix. Figure 3.3 (c) displays the failure mode of all specimens under uniaxial tension in which the resin fractures and the fibers are completely pulled out from the resin. In addition, it can be seen from Table 3.2 that a significant scatter exists in the obtained values of longitudinal tensile strength and modulus of elasticity.

### **3.3 STRIP TESTS FOR LONGITUDINAL COMPRESSIVE PROPERTIES OF FILAMENT-WOUND GFRP TUBES**

For each type of GFRP tubes (5 mm or 7 mm wall thickness), five rectangular strip specimens of 25 mm in width and 20 mm in effective length were tested to determine the compressive properties following the method described in ASTM D 3410/D 3410M-16 (2016). Figure 3.4 shows the setup of the compression test in which the compressive load was applied to the specimen via the tapered wedge grips. The compressive stress-axial strain curves are shown in Figure 3.5 and the test results are presented in Table 3.3, where values of the compressive strength are not available for Specimens B1 and A1 suffering from early damages and there is no available test data

for specimen B5. Failure of the strip specimens under uniaxial compression was by shear along the thickness direction of specimens as shown in Figure 3.6.

It can be seen from Tables 3.2 and 3.3 that the difference between the longitudinal modulus of elasticity of the GFRP tubes obtained respectively from standard tension and compression tests using strip specimens is significant due to the unavoidable defect of strip specimens as a result of the lack of enough anchorage of the cut fiber. This contradicts the expectation that a typical composite lamina has the similar compressive and tensile elastic properties. Using these test results to represent the compressive and tensile properties of GFRP tube in the longitudinal direction may lead to grossly erroneous results.

### **3.4 SPLIT DISK TESTS FOR HOOP MODULUS OF ELASTICITY OF FILAMENT-WOUND GFRP TUBES**

A total of 24 ring specimens with full cross-section were cut respectively from two types of filament-wound GFRP tubes with a wall thickness of 2 mm or 3 mm, corresponding to 4 or 6 layers of fibers. Note that this batch of tubes did not have a lining layer. The split disk tests were conducted following the method described in ASTM D2290-16 (2016). The GFRP tubes also had a fiber winding angle of  $\pm 80^\circ$  and an inner diameter of 400 mm. As shown in Figure 3.7, the ring specimens were 30 mm in width in the 200-mm long gauge sections and were 50 mm in width elsewhere. Strain gauges were installed at the gauge sections to measure axial and hoop strains.

The test setup is shown in Figure 3.8. As the 400 mm diameter and 60 mm thick steel-made split disks were too heavy to handle, the tests were carried out using a self-aligning test fixture set horizontally on a frictionless work table. Loads were applied

using a hydraulic jack to the split disks which caused tensioning of the FRP ring. Grease was applied to minimize the friction between the split disks and the inner surface of the ring specimen.

To investigate the influence of friction, the gauge sections of ring specimens were placed at two different positions with respect to the gap of split disks as shown in Figure 3.9: (1) gauge sections were centered at 50 mm from the gap (referred to as “Position-1”); and (2) gauge sections were centered at  $\pm 90^\circ$  from the gap (referred to as “Position-2”), where the maximum friction force was expected. As shown in Figure 3.10, the failure section was respectively located nearby the center and at the edge of gauge section for the former and latter schemes (i.e., “Position-1” and “Position-2”). This was due to the fact that the closer is the section to the gap, the greater is the pull stress of the section because of the existence of friction. The hoop stress-hoop strain curves of GFRP tubes obtained at gauge sections centered at Position-1 and Position-2 are shown in Figures 3.11 and 3.12, respectively.

Table 3.4 lists the hoop modulus of elasticity of the GFRP tubes obtained from the ring tensile tests, which will be later compared with that obtained from the hydraulic pressure tests of the same batch of tubes. Each type of filament-wound GFRP tubes was given a name starting with a letter “T” for “tube”, followed by a number “400” to represent the diameter of the GFRP tube in millimeter and then a number (4 or 6) to indicate the number of fiber layers, and ending at a number to define the batch of the GFRP tube. It can be seen from Table 3.4 that the hoop modulus of elasticity obtained from “Position-2” is significantly larger than that obtained from “Position-1”. This is attributed to the omission of the friction force in the calculation of “Position-2”. The analysis of the friction force is given below.

The relationship between the pull force applied by the hydraulic jack ( $N$ ) and the radial stress ( $\sigma_r$ ) (see Figure 3.13) may be described by the following equation

$$\sigma_r = \frac{N}{sd} \quad (3.1)$$

where  $s$  is the width of the FRP ring and  $d$  is the diameter of the split disk. The total friction force can then be given by

$$F_f = \sigma_r \cdot \frac{\pi d}{4} \cdot s \cdot \mu = \frac{N}{sd} \cdot \frac{\pi d}{4} \cdot s \cdot \mu = N \cdot \frac{\pi}{4} \cdot \mu \quad (3.2)$$

where  $F_f$  is the total friction force and  $\mu$  is the friction coefficient.

Based on the results of split disk tension tests and hydraulic pressure tests presented in the following section, the friction coefficient between FRP and steel could be worked out;  $\mu = 0.261$  and  $0.257$  for tubes T400-4-2 and T400-6-2, respectively. These values are close to the empirical value of friction coefficient between steel and polyethylene, one kind of polymer, 0.2.

On the other hand, although the values of hoop modulus of elasticity obtained from “Position-1” were much less affected by the friction, they suffered from the existence of bending in the gauge section of the ring specimen. The hoop strain induced by bending at the outer surface of the ring specimen was expected to counteract that induced by tensioning of the ring specimen, so the values of the hoop modulus of

elasticity obtained from “Position-1” was expected to be greater than the actual values. In summary, the split disk test is unable to accurately identify the hoop modulus of elasticity of filament-wound FRP tubes.

### **3.5 TUBE TESTS FOR LONGITUDINAL COMPRESSION PROPERTIES FOR FILAMENT-WOUND GFRP TUBES**

In order to determine the longitudinal compressive modulus, axial compression tests on filament-wound GFRP tubes were carried out on the basis of the method described in ASTM D5449/D5449M-16 (2016) with a modification as detailed below. The loading platens with a groove along the edge were used to insert the end of tube specimens, as shown in Figure 3.14. It can be seen that the groove is formed by a cylinder and two pieces of curved strips on the loading platens. The width of the groove can be adjusted to some extent by the relocation of the curved strips according to the diameter and thickness of tube specimens while it is fixed in ASTM D5449/D5449M-16 (2016). So the designed fixture can be used for the filament-wound FRP tubes fabricated in industrial production line which always have relatively large variation in the geometry. Because of the large diameter-to-thickness ratio, it was difficult to grind the end sections of the tube specimens to be completely flat and perpendicular to the longitudinal axis. So, prior to testing, the tube specimen was carefully installed between the platens. A high-strength gypsum potting material was filled into the spaces between the ends of the specimen and the grooves so that the ends of the specimen were firmly secured in the grooves and the top and the bottom compression platens remained parallel during testing.

The tube specimens had an effective length of 100 mm excluding the inserted parts in the grooves of load platens, which was shown to be long enough to eliminate the end

effect by an FE analysis. Strain gauges with a gauge length of 20 mm were installed to measure the axial and the hoop strains, which were uniformly distributed at the mid-height of the tube, as shown in Figure 3.15. The compression tests were carried out at a constant strain rate of 0.0125/min.

The specimens were loaded to failure which was accompanied by local buckling or splitting of the tube wall (Figure 3.16). The longitudinal compressive properties including the modulus of elasticity  $E_x$  and the Poisson's ratio  $\nu_{x\theta}$  are given in Table 3.5, where the specimens were named in the same manner as those in the split disk tests. The tubes tested covered four different sizes (i.e., nominally 150 mm, 200 mm, 300 mm and 400 mm in inner diameter). The 150-mm and 200-mm diameter tubes had six layers of fibers, the 300-mm diameter tubes had four, six or eight layers of fibers and the 400-mm diameter tubes had four or six layers of fibers. Because the number of available GFRP tubes for material property tests were limited after CFFT and hybrid DSTC specimens were fabricated for testing in later chapters, the number of tests was less than five for some types of tubes. The actual inner diameters and wall thicknesses of the specimens are provided in Table 3.5, showing variations of the tube dimensions from the nominal values, which were accommodated by the proper design of the grooves in the loading platens. The axial stress-axial strain curves and the hoop strain-axial strain curves of Specimens T400-4-2 and T400-6-2 are shown in Figure 3.17.

### **3.6 TESTS FOR HOOP PROPERTIES OF FILAMENT-WOUND GFRP TUBES UNDER INTERNAL HYDRAULIC PRESSURE**

Hydraulic pressure tests were carried out on filament-wound GFRP tubes using a specifically designed test fixture shown in Figure 3.18. Each of the tube specimens was machined so that the ends were smooth and parallel to each other as far as possible.

The neoprene gaskets, which have remarkable elasticity and can tolerate a small variation of thickness and diameter of the tested tubes, were inserted between the platens and the ends of the tubes. The two steel platens were settled and the seal load was applied by several steel screws. The internal pressure was applied using a manual pressure machine with a pressure capacity of 56 MPa at a loading rate of 0.4MPa/min. The height of the tube specimen was the same as its inner diameter, also determined based on the results of an FE analysis to eliminate the end effect. The strain gauge layout was the same as that employed in the compression tests on bare GFRP tubes. The overall shortening of steel screws was also recorded with use of strain gauges attached at the mid-height of steel screws to monitor the change of axial stress of steel screws during loading. The hydraulic pressure test fixture designed and employed in the present tests owns two important merits compared with the normal burst tests, including: (1) being easy to operate; and (2) being able to accommodate relatively large tolerance for the precision of the tube geometry.

Two types of tubes, either strengthened with an additional 30 mm-wide CFRP strip at the top and the bottom ends or not, were tested. The failure modes of the two types of tubes were different and are shown in Figure 3.19. For tubes without end strengthening, premature end failure occurred. For tubes with end strengthening, the end failure mode was suppressed and the desired failure mode of FRP rupture at the mid-height region of the tube, similar to the failure mode of the tube in CFFTs/hybrid DSTCs under axial compression as a result of hoop tension, was successfully achieved.

After completion of the pressurization tests, the steel screws were tested under tension following BS 18 (1987) as shown in Figure 3.20. The typical tension load-axial strain curves are displayed in Figure 3.21. These curves were utilized in the calculation of

the axial load carried by the FRP tube by subtracting the axial load carried by the steel screws from the total axial load applied using Eq. 3.3.

The water pressure-strain curves and the water pressure-stress curves are displayed in Figure 3.22 for Specimens T400-4-2 and T400-6-2 in which the strains were averaged from the readings of the corresponding strain gauges. The stresses in the FRP tube were computed by the following two equations

$$\sigma_x = \frac{P \cdot A_{in} - T \cdot 1000}{A_{frp}} \quad (3.3)$$

$$\sigma_\theta = \frac{P \cdot D_{in}}{2t_{frp}} \quad (3.4)$$

where  $\sigma_x$  is the axial stress of FRP tube (MPa);  $\sigma_\theta$  is the hoop stress of FRP tube (MPa);  $P$  is the water pressure (MPa);  $A_{in}$  is the area enclosed by the inner wall of FRP tube (mm<sup>2</sup>);  $T$  is the total axial load carried by steel screws (kN), which is obtained using tension load-axial strain curves of steel screws shown in Figure 3.21;  $A_{frp}$  is the cross-section area of FRP tube (mm<sup>2</sup>);  $t_{frp}$  and  $D_{in}$  are the thickness and inner diameter of FRP tube (mm), respectively.

Though the hydraulic tests were intended to produce a uniaxial stress state (hoop tension only) in the tested tube, it can be seen from Figure 3.22 that the test procedure still induced small, nearly constant axial compressive or tensile stresses in the wall of FRP tube due to the sealing load. So the calculation of hoop modulus of elasticity was based on the tubes in a biaxial stress state using the following equations:

$$\begin{bmatrix} \Delta\sigma_x \\ \Delta\sigma_\theta \end{bmatrix} = \begin{bmatrix} \frac{E_x}{1-\nu_{x\theta}\nu_{\theta x}} & \frac{\nu_{\theta x}E_x}{1-\nu_{x\theta}\nu_{\theta x}} \\ \frac{\nu_{\theta x}E_x}{1-\nu_{x\theta}\nu_{\theta x}} & \frac{E_\theta}{1-\nu_{x\theta}\nu_{\theta x}} \end{bmatrix} \begin{bmatrix} \Delta\varepsilon_x \\ \Delta\varepsilon_\theta \end{bmatrix} \quad (3.5)$$

$$\frac{\nu_{x\theta}}{E_x} = \frac{\nu_{\theta x}}{E_\theta} \quad (3.6)$$

where  $\Delta\sigma_x$  and  $\Delta\sigma_\theta$  are differences in axial and hoop stress of FRP tube respectively in the strain range for modulus calculation (MPa);  $\Delta\varepsilon_x$  and  $\Delta\varepsilon_\theta$  are differences in axial and hoop strain of FRP tube respectively in the axial strain range (0.001~0.003) for modulus calculation ( $\varepsilon$ );  $E_x$  and  $\nu_{x\theta}$  are longitudinal modulus of elasticity and Poisson's ratio of FRP tube respectively, which are determined by compression tests on bare FRP tubes;  $E_\theta$  and  $\nu_{\theta x}$  are hoop modulus of elasticity and Poisson's ratio of FRP tube respectively.

The hoop moduli of elasticity of the tested GFRP tubes are specified in Table 3.6. As expected, the values are significantly smaller than those obtained from the split disk tests, even for those obtained from the gauge section being centered near the gap of the two half disks.

### 3.7 CONCLUSIONS

The purpose of this chapter is to explore suitable test techniques for characterizing the properties of filament-wound FRP tubes. Several test methods to determine the longitudinal and circumferential properties of filament-wound GFRP tubes, including strip tension tests, strip compression tests, split disk tests, compression tests on bare FRP tubes and hydraulic pressure tests, are presented. The first three types of tests were conducted under the guidance of ASTM D3039/D 3039M-14 (2014), ASTM

D3410/D3410M-16 (2016) and ASTM D2290-16 (2016) respectively. For the last two types of tests, since ASTM D5449/D5449M-16 (2016) and conventional burst test methods are not directly applicable to tube specimens with a relatively large dimensional variation, a compression test method on bare FRP tubes and a hydraulic pressure test method, both involving the use of specifically designed test fixtures, were proposed. The proposed test methods were shown to provide more accurate characterization of mechanical properties of filament-wound FRP tubes than strip tests and split disk tests. The test results and discussions presented in this chapter allow the following conclusions to be drawn:

- (1) Strip tension and compression tests in which the strips were cut along the longitudinal direction of the tube cannot supply accurate measure of properties of filament-wound FRP tubes with a large fiber winding angle due to the lack of enough anchorage of the cut fibers. So specimens with full cross-section should be used to measure the mechanical properties of filament-wound FRP tubes.
- (2) For split disk tests, the gauge sections of ring specimens were respectively centered at near the gap of the two half disks and the top of arc of the disks. The hoop moduli of elasticity obtained via both schemes are not accurate enough. The former scheme suffers from the existence of bending in the gauge section while the latter scheme suffers from the existence of friction between the disks and the ring specimen. The hoop modulus of elasticity obtained via the former scheme is closer to that obtained from the proposed hydraulic pressure test method.
- (3) The proposed compression test method for bare FRP tubes and the proposed hydraulic pressure test method are recommended for the characterization of

mechanical properties of filament-wound GFRP tube in the longitudinal direction and the circumferential direction, respectively. The proposed methods are more accurate than conventional test methods based on strip specimens and ring specimens. Meanwhile, they are easier to operate and allow for a relatively large dimensional variation in the tube specimens, compared with existing test methods of the same type.

- (4) The computation of the hoop modulus of elasticity of filament-wound GFRP tubes using hydraulic pressure test results should be based on the tubes in a biaxial stress state instead of a uniaxial stress state.

### **3.8 REFERENCES**

- Al-Khalil, M.F.S., Soden, P.D., Kitching, R. and Hinton, M.J. (1996). “The Effects of Radial Stresses on the Strength of Thin-walled Filament Wound GRP Composite Pressure Cylinders”, *International Journal of Mechanical Sciences*. Vol. 38(1), pp.97-120.
- Arsene, S. and Bai, J. (1996). “A New Approach to Measuring Transverse Properties of Structural Tubing by a Ring Test”, *Journal of Testing and Evaluation*. Vol. 24(6), pp.386-391.
- Arsene, S. and Bai, J. (1998). “A New Approach to Measuring Transverse Properties of Structural Tubing by a Ring Test-Experimental Investigation”, *Journal of Testing and Evaluation*. Vol. 26(1), pp.26-30.
- ASTM D638-14 (2014). “Standard Test Method for Tensile Properties of Plastic”, American Society for Testing and Materials (ASTM), Philadelphia, USA.
- ASTM D695-15 (2015). “Standard Test Method for Compressive Properties of Rigid Plastics”, American Society for Testing and Materials (ASTM), Philadelphia,

USA.

ASTM D2105-01 (2014). “Standard Test Method for Longitudinal Tensile Properties of “Fiberglass” (Glass-Fiber- Reinforced Thermosetting-Resin) Pipe and Tube”, American Society for Testing and Materials (ASTM), Philadelphia, USA.

ASTM D2290-16 (2016). “Standard Test Method for Apparent Hoop Tensile Strength of Plastic or Reinforced Plastic Pipe”, American Society for Testing and Materials (ASTM), Philadelphia, USA.

ASTM 2996-15 (2015). “Standard Specification for Filament-Wound “Fiberglass” (Glass-Fiber-Reinforced Thermosetting-Resin) Pipe”, American Society for Testing and Materials (ASTM), Philadelphia, USA.

ASTM D3039/D3039M-14 (2014). “Standard Test Method for Tensile Properties of Polymer Matrix Composite Materials”, American Society for Testing and Materials (ASTM), Philadelphia, USA.

ASTM D3410/D3410M-16 (2016). “Standard Test Method for Compressive Properties of Polymer Matrix Composite Materials with Unsupported Gage Section by Shear Loading”, American Society for Testing and Materials (ASTM), Philadelphia, USA.

ASTM D5449/D5449M-16 (2016). “Standard Test Method for Transverse Compressive Properties of Hoop Wound Polymer Matrix Composite Cylinders”, American Society for Testing and Materials (ASTM), Philadelphia, USA.

ASTM D5450/D5450M-16 (2016). “Standard Test Method for Transverse Tensile Properties of Hoop Wound Polymer Matrix Composite Cylinders”, American Society for Testing and Materials (ASTM), Philadelphia, USA.

ASTM D6641/D6641-16e1 (2016). “Standard Test Method for Compressive Properties of Polymer Matrix Composite Materials Using a Combined Loading Compression (CLC) Test Fixture”, American Society for Testing and Materials

(ASTM), Philadelphia, USA.

ASTM D7565/D7565 M-10 (2017). “Standard Test Method for Determining Tensile Properties of Fiber Reinforced Polymer Matrix Composites Used for Strengthening of Civil Structures”, American Society for Testing and Materials (ASTM), Philadelphia, USA.

Basalo, F.J.D.Y., Matta, F. and Nanni, A. (2011). “Novel Test Method for Ultimate Hoop-Strain Characterization in FRP Jackets”, *Journal of Material in Civil Engineering*, Vol. 23, pp.1633-1641.

BS 18. (1987). “Tensile Testing of Metals (Including Aerospace Materials)”, British Standards Institution, UK.

Card, M.F. (1965). “Experiments to Determine Elastic Moduli for Filament-Wound Cylinders”, Nasa Technical Note, NASA TN D-3110. Langley Research Center, Langley Station, Hampton, Va.

Cohen, D., Toombes, Y.T., Johnson, A.K. and Hansen, M.F. (1995). “Pressurized Ring Test for Composite Pressure Vessel Hoop Strength and Stiffness Evaluation”, *Journal of Composite Technology & Research*, JCTRER. Vol. 17(4), pp.331-340.

Cohen, D. (1997). “Influence of Filament Winding Parameters on Composite Vessel Quality and Strength”, *Composites Part A*. Vol. 28A, pp.1035-1047.

Ellyin, F. and Wolodko, J.D. (1977). “Testing Facilities for Multiaxial Loading of Tubular Specimens”, *Multiaxial Fatigue and Deformation Testing Techniques*, ASTM STP 1280, S. Kalluri and P.J. Bonacuse, Eds., American Society for Testing and Materials, pp.7-24.

Hull, D. Legg, M.J. and Spencer, B. (1978). “Failure of Glass/ Polyester Filament Wound Pipe”, *Composites*. Vol.1, pp.17-24.

ISO 7509 (2015). “Plastics Piping Systems - Glass-Reinforced Thermosetting Plastics (GRP) Pipes-Determination of Time to Failure under Sustained Internal Pressure”,

- the International Organization for Standardization (ISO).
- ISO 8513 (2016). “Plastics Piping Systems-Glass-Reinforced Thermosetting Plastics (GRP) Pipes-Test Methods for the Determination of the Initial Longitudinal Tensile Strength”, the International Organization for Standardization (ISO).
- ISO8521 (2009). “Plastics Piping Systems-Glass-Reinforced Thermosetting Plastics (GRP) Pipes-Test Methods for the Determination of the Apparent Initial Circumferential Tensile Strength”, the International Organization for Standardization (ISO).
- Jones, I.A., Middleton, V. and Owen, M.J. (1996). “Roller-Assisted Variant of the Split Disc Test for Filament-Wound Composites”, *Composites: Part A*. Vol. 27, pp.287-294.
- Kaynak, C., Erdiller, E.S., Parnas, L. and Senel, F. (2005). “Use of Split-Disk Tests for the Process Parameters of Filament Wound Epoxy Composite Tubes”, *Polymer Testing*. Vol.24, pp.648-655.
- Lam, L. and Teng, J.G. (2004). “Ultimate Condition of Fiber Reinforced Polymer-Confined Concrete”, *Journal of Composites for Construction*, ASCE. Vol. 8, pp.539-548.
- Lee, J., Soden, P.D., Kitching, R. and Tse, P.C. (1989). “Strength of Filament Wound GRP Tube with Axisymmetric Steps”, *Composites*. Vol. 20(3), pp.234-243.
- Rosenow, M.W.K. (1984). “Winding Angle Effects in Glass Fiber-Reinforced Polyester Filament Wound Pipes”, *Composites*. Vol. 10, pp.247-250.
- Soden, P.D., Leadbetter, D., Griggs, P.R. and Eckold, G.C. (1978). “The Strength of a Filament Wound Composite under Biaxial Loading”, *Composites*. Vol.10, pp.247-250.
- Soden, P.D., Kitching, R., Tse, P.C. and Tsavalas, Y. (1993). “Influence of Winding Angle on the Strength and Deformation of Filament-Wound Composite Tubes

Subjected to Uniaxial and Biaxial Loads”, *Composites Science and Technology*.  
Vol. 46(4), pp.363-378.

Wang, H., Bouchard, R., Eagleson, R., Martin, P. and Tyson, W.R. (2002). “Ring Hoop Tension Test (RHTT): a Test for Transverse Tensile Properties of Tubular Materials”, *Journal of Testing and Evaluation*, JTEVA. Vol. 30(5), pp.382-391.

Yoon, S.H., Kim, C.G. and Cho, W.M. (1997). “Measurement of Tensile Properties Using Filament Wound Ring Specimens”, *Journal of Reinforced Plastics and Composites*. Vol. 16(9), pp.810-824.

Zhang, L.Q., Li, H. and Ou, J.P. (2009). “Experimental and Numerical Study of Mechanical Properties of Filament-Wound CFRP Tubes”, *Civil Engineering Journal*. Vol. 42(8), pp.50-56. (in Chinese).

**Table 3. 1 ASTM and ISO standards for FRP composite testing**

<b>Specimen form</b>	<b>Objective</b>	<b>Reference</b>	<b>Title</b>
Strip	Tensile properties	ASTM D638-14 (2014)	Standard Test Method for Tensile Properties of Plastic
		ASTM D3039/D3039M-14 (2014)	Standard Test Method for Tensile Properties of Polymer Matrix Composite Materials
		ASTM D7565/D7565 M-10 (2017)	Standard Test Method for Determining Tensile Properties of Fiber Reinforced Polymer Matrix Composites Used for Strengthening of Civil Structures
	Compressive properties	ASTM D3410/D3410M-16 (2016)	Standard Test Method for Compressive Properties of Polymer Matrix Composite Materials with Unsupported Gage Section by Shear Loading
		ASTM D6641/D6641-16e1 (2016)	Standard Test Method for Compressive Properties of Polymer Matrix Composite Materials Using a Combined Loading Compression (CLC) Test Fixture
Ring	Hoop tensile properties	ASTM D2290-16 (2016)	Standard Test Method for Apparent Hoop Tensile Strength of Plastic or Reinforced Plastic Pipe
Tube	Longitudinal compressive properties	ASTM D695-15 (2015)	Standard Test Method for Compressive Properties of Rigid Plastics
		ASTM D5449/D5449M-16 (2016)	Standard Test Method for Compressive Properties of Polymer Matrix Composite Materials with Unsupported Gage Section by Shear Loading

<b>Specimen form</b>	<b>Objective</b>	<b>Reference</b>	<b>Title</b>
Tube	Longitudinal tensile properties	ASTM D5450/D5450M-16 (2016)	Standard Test Method for Transverse Tensile Properties of Hoop Wound Polymer Matrix Composite Cylinders
		ASTM D2105-01 (2014)	Standard Test Method for Longitudinal Tensile Properties of “Fiberglass” (Glass-Fiber-Reinforced Thermosetting-Resin) Pipe and Tube
	Burst test	ISO 7509 (2015)	Plastics piping systems - Glass-reinforced thermosetting plastics (GRP) pipes-Determination of Time to Failure under Sustained Internal Pressure
Strip and tube	Longitudinal tensile properties	ISO 8513 (2016)	Plastics piping systems - Glass-reinforced thermosetting plastics (GRP) pipes - Test methods for the determination of the initial longitudinal tensile strength
Strip, ring and tube	Hoop tensile properties	ISO8521 (2009)	Plastics piping systems — Glass-reinforced thermosetting plastics (GRP) pipes -Test methods for the determination of the apparent initial circumferential tensile strength

**Table 3. 2 Results of tension tests using the strip method**

Specimen		Tensile properties	
Thickness (mm)	Notation	Strength (MPa)	Modulus (GPa)
5	G1	35.28	10.62
	G2	23.14	9.74
	G3	22.34	10.24
	G4*	NA	NA
	G5	26.18	10,70
	G6	28.51	9.860
	Average	27.09	10.23
	Standard deviation	5.20	0.43
7	F1	28.03	5.31
	F2*	NA	NA
	F3	32.72	4.83
	F4	29.55	4.88
	F5	33.29	5.20
	F6	28.05	4.86
	Average	30.33	5.02
	Standard deviation	2.52	0.22

\*Note: Specimens G4 and F2 were tested under axial compression in an attempt to investigate the influence of the effective length of specimens in a strip compression test. However the attempt was not successful, so they were not included in the discussion of tensile test results.

**Table 3. 3 Results of compression tests using the strip method**

Specimen		Compressive properties	
Thickness (mm)	Notation	Strength (MPa)	Modulus (GPa)
5	B1	NA	10.94
	B2	83.57	12.40
	B3	74.6	11.50
	B5	NA	NA
	B6	85.04	9.86
	Average	81.07	11.18
	Standard deviation	5.65	1.06
7	A1	NA	6.70
	A2	74.14	8.27
	A3	67.81	6.82
	A4	72.07	6.46
	A5	73.37	7.44
	Average	71.85	7.14
	Standard deviation	2.82	0.73

**Table 3. 4 Hoop modulus of elasticity from split disk tests (GPa)**

Tube	Position of gauge section	Specimen						Average	Standard deviation
		S1	S2	S3	S4	S5	S6		
T400-4-2	1	44.20	43.22	45.08	44.39	39.79	49.60	44.38	3.17
	2	66.12	70.38	67.77	69.56	70.69	67.71	68.71	1.79
T400-6-2	1	50.69	53.46	55.55	54.75	48.77	50.22	52.24	2.73
	2	70.07	72.08	71.50	68.75	68.21	68.33	69.82	1.67

**Table 3. 5 Longitudinal properties of filament-wound GFRP tube in compression**

<b>Tube</b>	<b>Specimen</b>	$D_{in}$ (mm)	$t_{frp}$ (mm)	$E_x$ (GPa)	$\nu_{x\theta}$	<b>Ave</b> $E_x$ (GPa)	<b>Ave</b> $\nu_{x\theta}$
T150-6-3	S1	148.8	2.93	11.91	0.114	11.82	0.113
	S2	148.4	2.88	11.72	0.112		
T200-6-3	S1	198.6	3.20	12.51	0.099	11.63	0.105
	S2	198.6	3.18	10.74	0.111		
T300-4-2	S1	299.1	1.49	11.70	0.110	11.10	0.116
	S2	298.9	1.60	11.91	0.123		
	S3	299.1	1.64	10.32	0.123		
	S4	298.3	1.70	10.69	0.112		
	S5	298.8	1.72	10.93	0.113		
	S6	299.2	1.64	11.68	0.127		
	S7	299.2	1.59	10.48	0.101		
T300-6-2	S1	298.5	2.40	9.79	0.104	10.94	0.106
	S2	298.8	2.26	10.25	0.105		
	S3	299.4	2.30	11.66	0.098		
	S4	299.1	2.35	12.04	0.116		
T300-6-3	S1	300.3	2.93	11.79	0.101	11.79	0.101
T300-8-2	S1	298.7	3.67	10.84	0.119	10.90	0.124
	S2	298.4	3.77	10.72	0.123		
	S3	300.0	3.87	11.13	0.129		
T400-4-1	S1	399.8	1.93	10.07	0.085	10.44	0.099
	S2	399.9	1.94	10.61	0.091		
	S3	402.6	1.80	10.44	0.100		
	S4	401.0	1.86	10.62	0.121		
T400-4-2	S1	401.4	1.79	10.30	0.131	10.39	0.124
	S2	399.4	1.91	10.48	0.117		
T400-6-2	S1	401.6	2.62	10.97	0.098	11.75	0.102
	S2	401.6	2.59	11.04	0.103		
	S3	398.4	2.43	12.56	0.111		
	S4	398.5	2.42	11.49	0.105		
	S5	402.7	2.52	12.68	0.094		
T400-6-3	S1	404.8	2.91	11.94	0.109	11.27	0.100
	S2	404.7	2.89	10.60	0.090		

**Table 3. 6 Hoop modulus of elasticity of filament-wound GFRP tubes**

Tube	Specimen	$D_{in}$ (mm)	$t_{frp}$ (mm)	$E_{\theta}$ (GPa)	Ave $E_{\theta}$ (GPa)
T150-6-3	S1	148.6	2.88	37.89	37.89
T200-6-3	S1	199.5	3.25	38.33	38.33
T300-4-2	S1	299.0	1.70	36.11	36.48
	S2	298.7	1.73	37.18	
	S3	298.7	1.73	35.95	
	S4	298.9	1.73	36.72	
	S5	299.0	1.77	35.98	
	S6	298.9	1.74	36.93	
T300-6-2	S1	297.9	2.49	38.73	39.62
	S2	299.0	2.51	40.19	
	S3	299.6	2.27	39.66	
	S4	299.6	2.22	41.43	
	S5	299.0	2.49	38.10	
T300-6-3	S1	300.3	2.98	42.73	42.73
T300-8-2	S1	299.0	3.69	35.26	34.82
	S2	298.5	3.76	35.15	
	S3	299.6	2.86	34.04	
T400-4-1	S1	402.8	1.95	33.41	34.43
	S2	402.8	1.95	33.30	
	S3	402.8	1.95	32.67	
	S4	401.5	1.86	36.09	
	S5	401.5	1.86	33.98	
	S6	402.0	1.90	34.94	
	S7	402.5	1.80	36.60	
T400-4-2	S1	401.8	1.80	40.41	40.55
	S2	401.0	1.79	39.70	
	S3	400.9	1.68	42.64	
	S4	401.0	1.85	39.47	
T400-6-1	S1	402.1	2.85	38.93	38.93
T400-6-2	S1	401.1	2.53	40.76	41.60
	S2	398.8	2.41	42.45	
T400-6-3	S1	404.7	3.10	40.66	39.82
	S2	403.1	3.22	38.97	

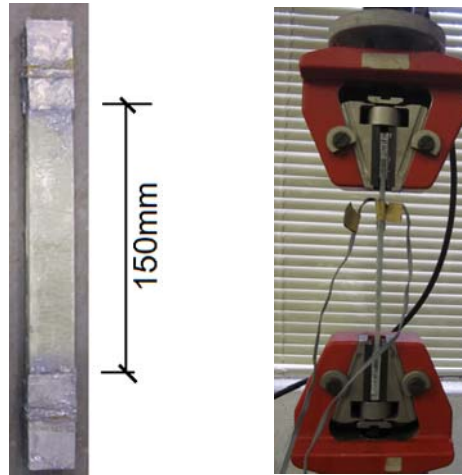
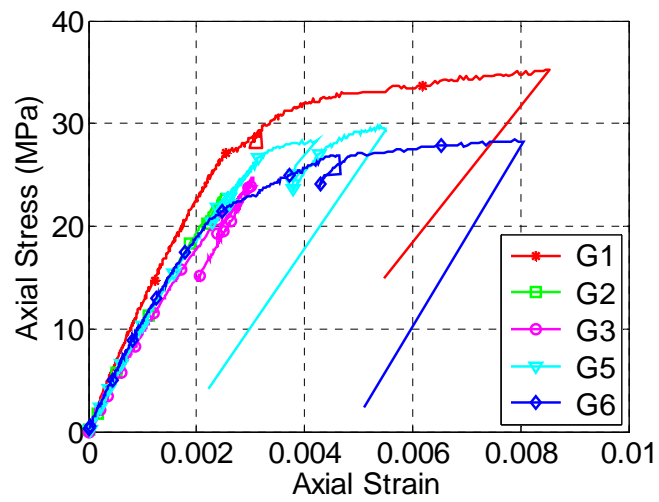
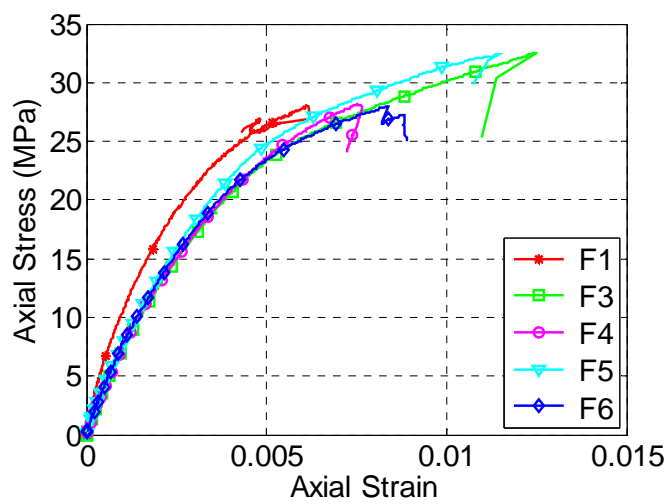


**Figure 3. 1** Strip specimen for tension test and tension test setup



(a)  $t=5\text{mm}$



(b)  $t=7\text{mm}$

**Figure 3. 2** Tensile stress-strain curves of FRP strip specimens

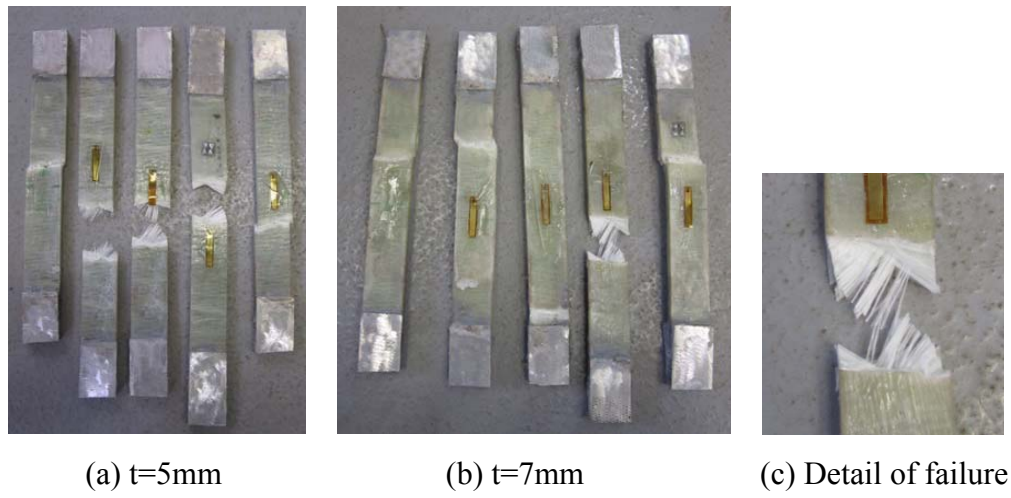
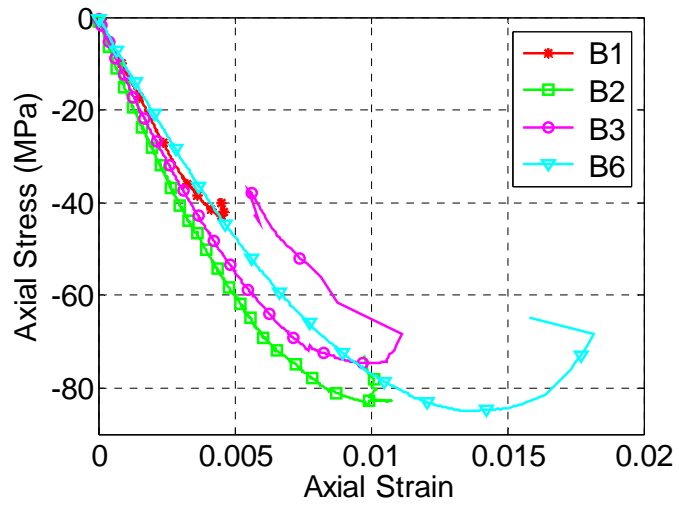


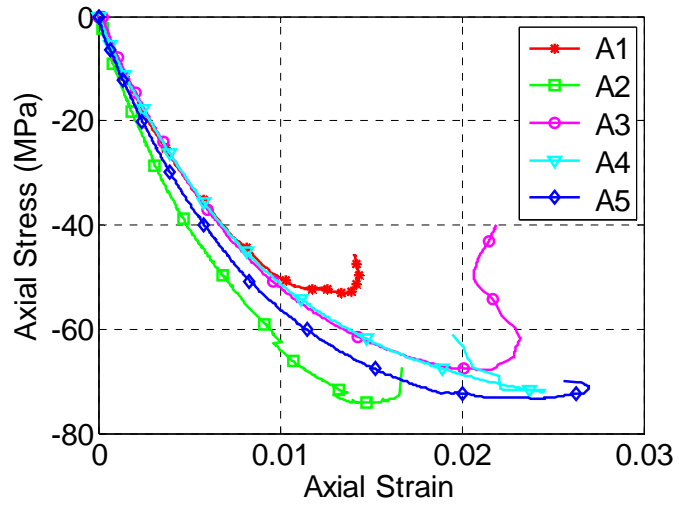
**Figure 3. 3** Failure mode of FRP strip specimens



**Figure 3. 4** Strip specimen for compression test and compression test setup



(a)  $t=5\text{mm}$



(b)  $t=7\text{mm}$

**Figure 3. 5** Results of compression test on FRP strip specimens



**Figure 3. 6** Failure mode of compression test on FRP strip specimens

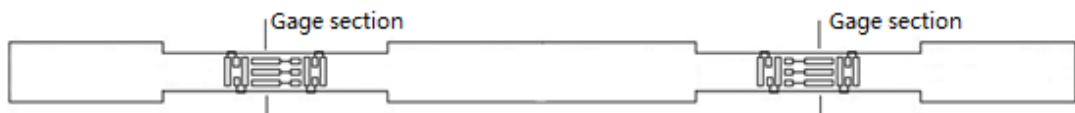


**Figure 3. 7** Development of a ring specimen



**Figure 3. 7** Setup of split disk tests



(a) Position-1

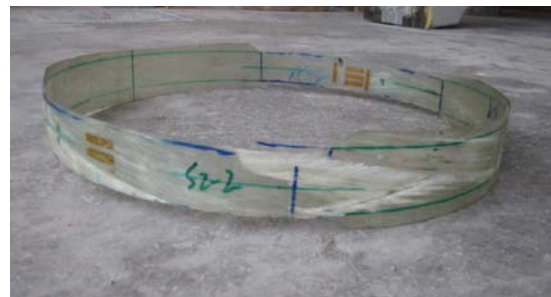


(b) Position-2

**Figure 3. 8** Location of gauge section

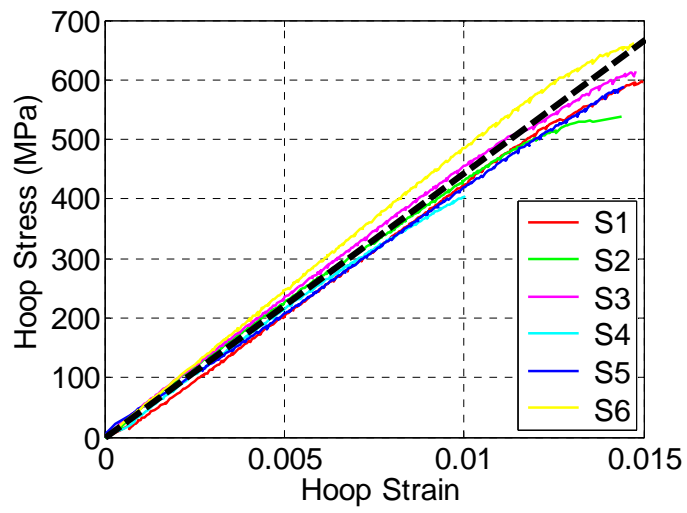


(a) Position-1

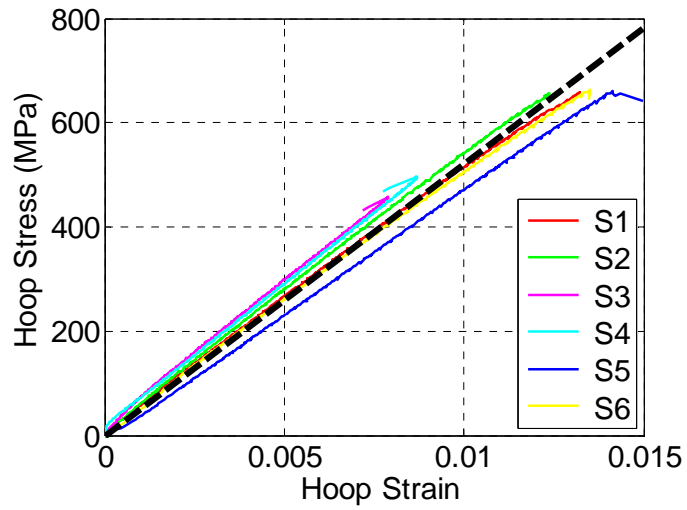


(b) Position-2

**Figure 3. 9** Location of failure section

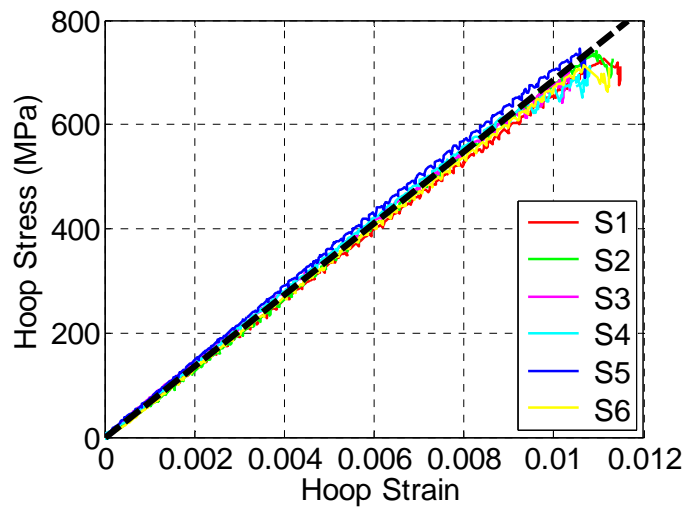


(a) Tube T400-4-2

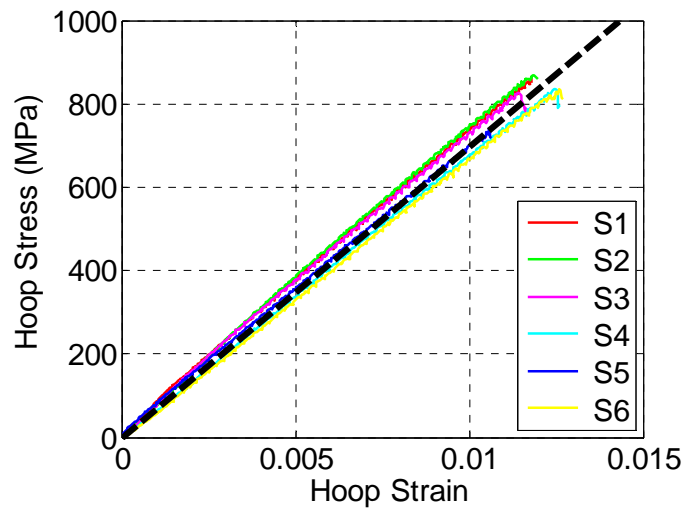


(b) Tube T400-6-2

**Figure 3. 10** Results of split disk tests (Position-1)



(a) Tube T400-4-2



(b) Tube T400-6-2

**Figure 3. 11** Results of split disk tests (Position-2)

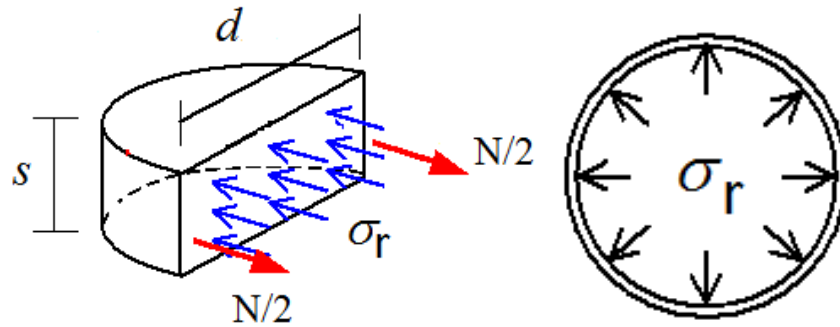


**Figure 3. 12** Relationship between pull force and radial stress

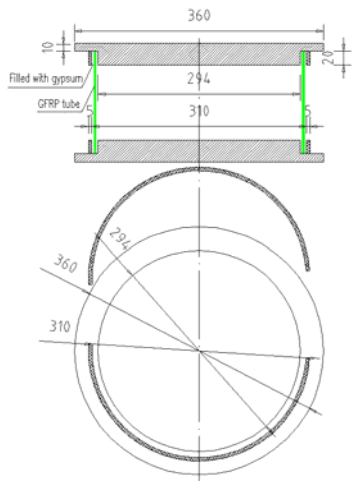


**Figure 3. 13** Loading platens with a groove to fit the ends of tube specimen

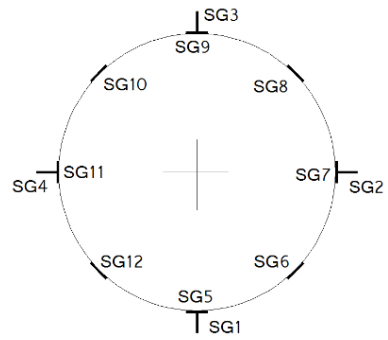


**Figure 3. 14** Compression test setup for filament-wound GFRP tubes

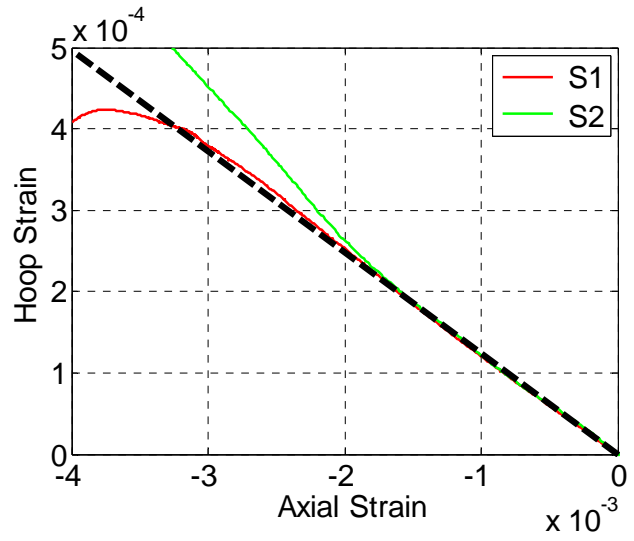
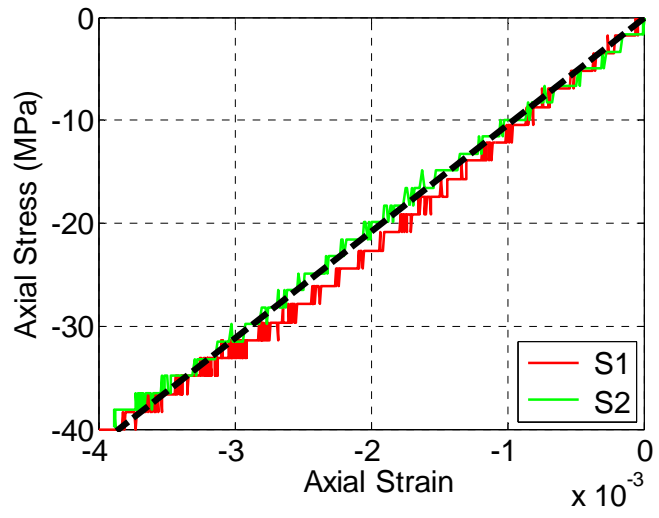


(a) Buckling of specimen

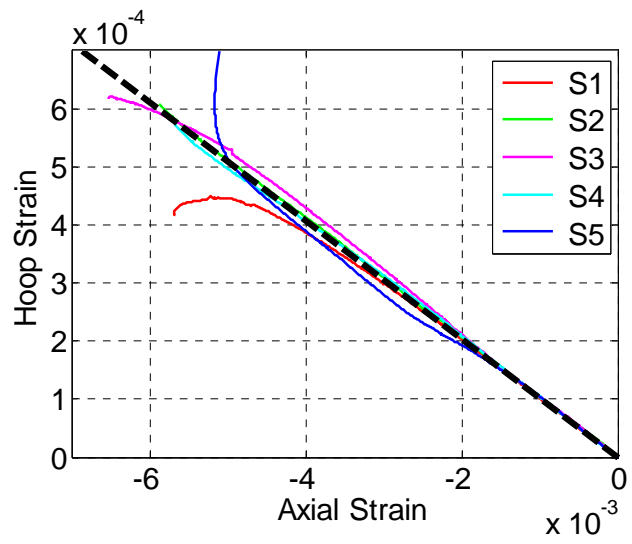
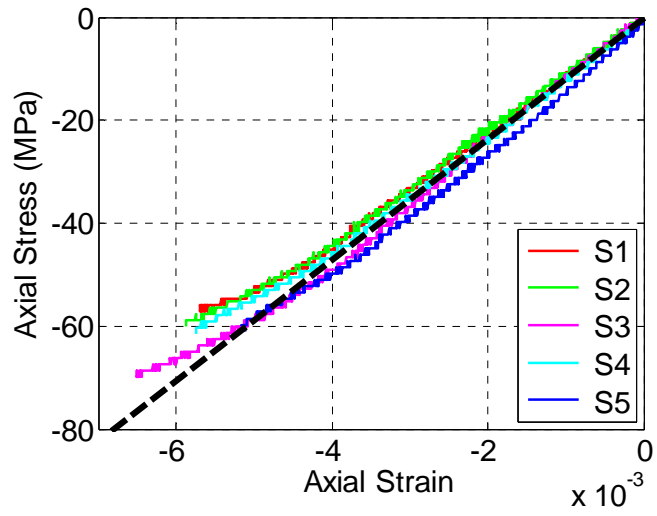


(b) Splitting of specimen

**Figure 3. 15** Failure mode of compression tests on bare GFRP tubes

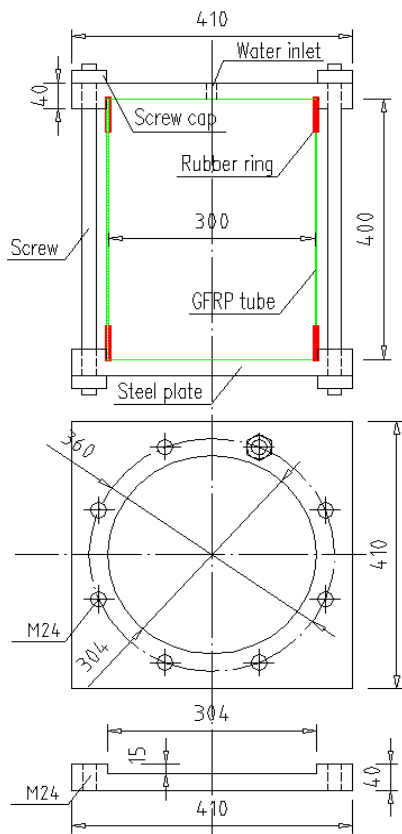


(a) Tube T400-4-2



(b) Tube T400-6-2

**Figure 3. 16** Results of compression tests on bare GFRP tubes



(a)



(b)



(c)



(d)

**Figure 3. 17** Hydraulic pressure test setup



(a) With CFRP strengthening



(b) Without CFRP strengthening

**Figure 3. 18** Failure mode of hydraulic pressure test



(a) Steel screw specimens



(b) Test setup

**Figure 3. 19** Tension tests of steel screws

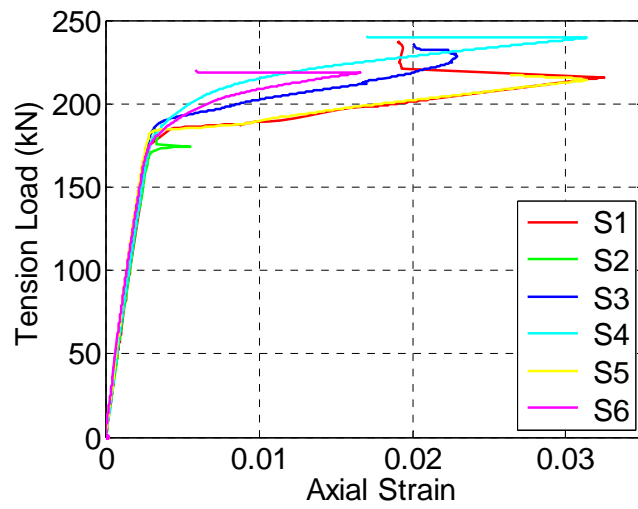
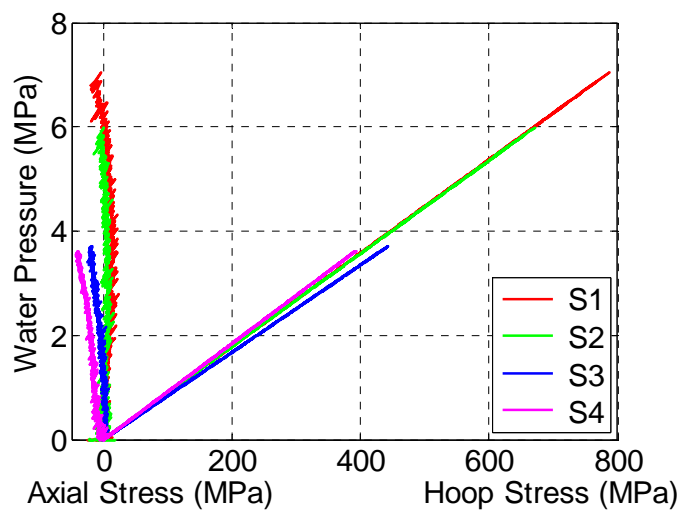
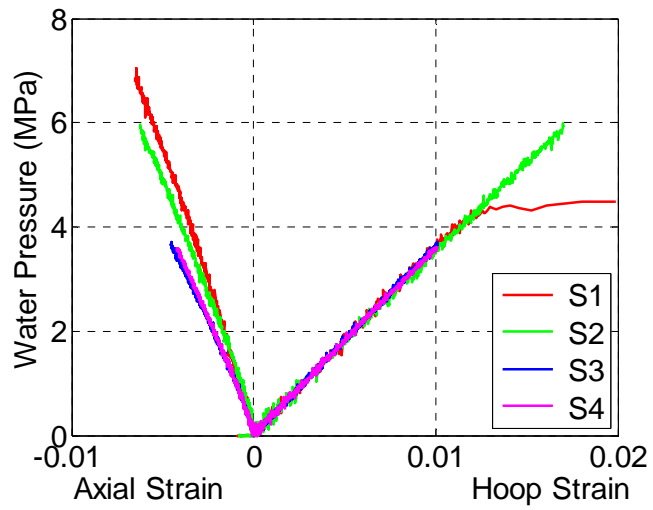
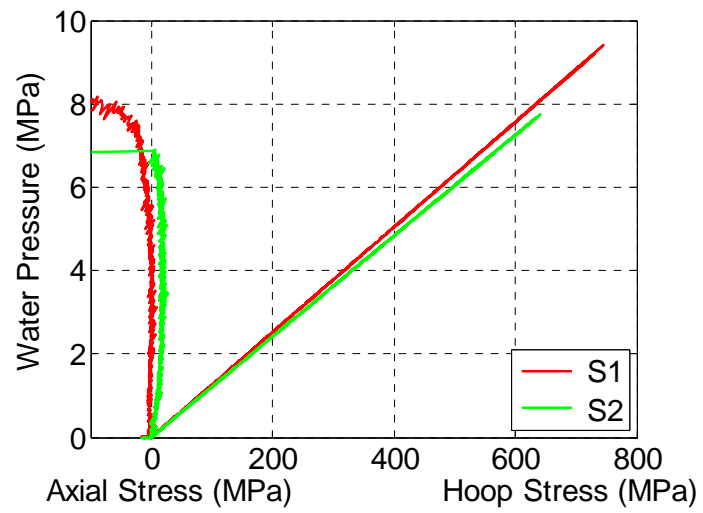
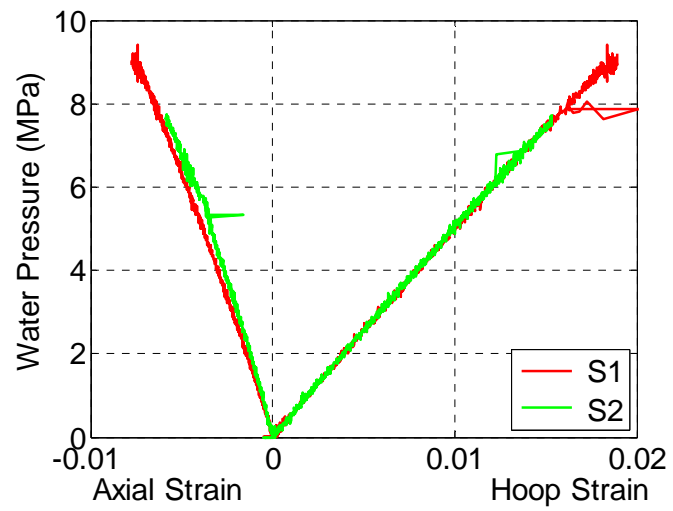


Figure 3. 20 Test results of tension test of steel screws



(a) T400-4-2



(c) T400-6-2

**Figure 3. 21** Results of hydraulic pressure tests on GFRP tubes



# CHAPTER 4

## EFFECT OF SELF-COMPACTING CONCRETE ON THE BEHAVIOR OF LARGE-SCALE CONCRETE-FILLED FRP TUBES

### 4.1 INTRODUCTION

Self-compacting concrete (SCC) is a type of concrete which can flow into place under its own weight and consolidate without using internal or external vibration (Paultre *et al.* 2005). For hybrid DSTCs, using normal concrete (NC) generally cannot ensure the integrity and uniformity of concrete in a relatively narrow space between the inner steel tube and the outer FRP tube, which adversely affects the load-bearing capacity of hybrid DSTCs. In this regard the use of SCC would be a solution. A large number of studies have been conducted on FRP tubes filled with NC (e.g., Mirmiran and Shahawy 1997; Fam and Rizkalla 2001a, b) and many stress-strain models have been proposed for FRP-confined concrete (e.g., Lam and Teng 2003; Jiang and Teng 2007). However, SCC is associated with larger shrinkage and reduced modulus of elasticity compared with NC because of the lower coarse aggregate content. It has been pointed out that the structural performance of FRP-confined SCC is different from that of FRP-confined NC under the same confinement condition (El Chabib *et al.* 2005; Yu *et al.* 2014). Yu *et al.*'s (2014) conducted axial compression tests on 24 SCC cylinders confined with post-applied FRP wraps and concluded that the behavior of FRP-confined SCC is similar to that of FRP-confined NC except that FRP-confined SCC has a larger lateral strain than FRP-confined NC under the same axial strain of concrete. El Chabib *et al.* (2005) tested several series of CFFTs made with NC or SCC with or without expansive cement. It was reported that the stress-strain curves of SCC-filled GFRP tubes are different from those of NC-filled GFRP tubes due to the shrinkage of

SCC. The difference in the stress-strain curves between NC and SCC specimens was not observed when expansive cement was used. The detrimental effect of SCC may be amplified in CFFTs or hybrid DSTCs where confinement is provided by filament-wound FRP tubes instead of post-applied FRP wraps. This is because the large shrinkage of SCC may lead to the formation of an initial gap between the concrete core and the FRP tube, causing a delay in the activation of the confinement action of the FRP tube. However, little research has been carried out on this aspect and a careful investigation into the behavior of SCC-filled FRP tubes is necessary.

On the other hand, the aforementioned tests on FRP-confined SCC were carried out on small-scale specimens about 150 mm in diameter, without considering the adverse effect of SCC in large-scale CFFTs. Only Ozbakkaloglu (2013) has conducted axial compression tests on seven circular CFFTs. In their tests, the diameter of the specimens varied from 74 mm to 300 mm. Their test results showed that the small-scale specimens exhibited slightly better performance in terms of compressive strength and ultimate axial strain than their large-scale counterparts. On the other hand, a number of experimental studies have investigated the size effect in FRP-confined NC in circular columns. While some of the studies (De Lorenzis 2002; Matthys *et al.* 2005, 2006; Thériault *et al.* 2004; Smith *et al.* 2010; Elsanadedy *et al.* 2012; Liang *et al.* 2012; Ozbakkaloglu 2013; Lim *et al.* 2016) indicated that the effect of size is insignificant, other studies (Issa *et al.* 2009; Cui *et al.* 2010; Wang and Wu 2011; Bo 2013, Zhou *et al.* 2016; Chen *et al.* 2016) suggested that the influence of size on the strength and stress-strain behavior of FRP-confined NC cannot be ignored. In summary, consensus has not been reached on the issue of size effect in FRP-confined concrete. The detrimental effect of concrete shrinkage may be amplified in large-scale columns when SCC is used.

In this Chapter, an experimental investigation into the compressive behavior of short CFFTs, which were made with NC, SCC and self-compacting expansive concrete (SCEC) and had a diameter ranging from 150 mm to 400 mm, will be presented. The following sign convention is adopted in the present chapter: in the concrete, compressive stresses and strains are positive; but in the FRP tube, tensile stresses and strains are positive.

## **4.2 EXPERIMENTAL PROGRAM**

### **4.2.1 Specimen Details**

In order to understand the effect of concrete shrinkage on the behavior of CFFTs especially for large-scale columns, a total of 23 circular specimens were prepared and tested in three series with NC, SCC and SCEC, respectively. Filament-wound GFRP tubes made with six layers of fibers oriented at a winding angle of  $\pm 80^\circ$  with respect to the longitudinal axis of the tube were used in the specimens. The GFRP tubes had a nominal inner diameter of 150 mm, 200 mm, 300 mm or 400 mm and a height-to-diameter ratio of two. Duplicated tests were performed for each test configuration to account for the large scatter of results (Xiao *et al.* 2010), except for Series N in which only one 400 mm-diameter specimen was tested because the number of GFRP tubes was inadequate.

A summary of the specimen information is given in Table 4.1, where the types and properties of concrete, the dimensions and properties of the GFRP tubes are provided. The specimens are denoted in the following manner. The beginning letter(s) “N”, “S” or “SE” denotes the type of concrete (i.e., “N” for NC, “S” for SCC and “SE” for

SCEC). The numeral “1”, “2” or “3” next to the letter(s) refers to the batch of concrete. The following number “150”, “200”, “300” or “400” represents the diameter of the concrete core in millimeter. The Roman numeral “I” or “II” represents the first or the second specimen in duplicated tests.

#### **4.2.2 Concrete Mixtures**

The concrete for Series N was proportioned with ordinary Portland cement, river sand and coarse aggregate of crushed granite with a maximum nominal size of 10 mm. Each series of specimens were prepared from two or three batches of concrete due to the limited capacity of the mixer. For Series S and SE, fly ash was used as a supplementary cementitious binder and superplasticizer was added to improve the flowability of concrete. In order to control the shrinkage of concrete, expansive cement was used to replace part of the cement and fly ash in Series SE. Details of the mix proportions for the three series of concrete are provided in Table 4.2. An image of the slump flow measurement of the Series S concrete is given in Figure 4.1, showing a slump flow of 55 cm with no segregation of the concrete.

Three standard cylinders (150 mm × 300 mm) were tested for each batch of concrete to determine the compressive strength  $f'_{co}$ , the corresponding axial strain  $\epsilon_{co}$  and the modulus of elasticity  $E_c$ , following the method described in ASTM C469/C469M-14 (2014). The setup of cylinder tests is shown in Figure 4.2 and the results are provided in Table 4.1.

#### **4.2.3 Filament-Wound GFRP tubes**

The inner diameters  $D_{in}$  and wall thicknesses  $t_{frp}$  of the filament-wound GFRP tubes given in Table 4.1 are actual measurements of the FRP tubes used in the tests.

Uniaxial compression tests and hydraulic pressure tests on bare GFRP tubes described in Chapter 3 were carried out to determine the modulus of elasticity in the longitudinal direction  $E_x$  and the circumferential direction  $E_\theta$  and the Poisson's ratio  $\nu_{x\theta}$  of the FRP tube, which are also presented in Table 4.1. The confinement stiffness ratio  $\rho_k$  defined by Teng *et al.* (2009) is calculated for each specimen from the following equation

$$\rho_k = \frac{2E_\theta \cdot t_{frp}}{\left(\frac{f'_{co}}{\varepsilon_{co}}\right) \cdot D_{in}} \quad (4.1)$$

In the calculation of  $\rho_k$ , the value of  $\varepsilon_{co}$  was taken to be 0.002 as suggested in Teng *et al.* (2009).

#### 4.2.4 Preparation of Test Specimens

In preparing the specimens, concrete was directly cast into the filament-wound GFRP tube which was fixed on a wooden bottom plate and served both as a stay-in-place formwork and as the confining jacket (Figure 4.3). The specimens were cured in the laboratory environment for 30 days before testing. For the specimens with SCEC (Series SE), strain gauges were installed on the surface of the FRP tubes to monitor the hoop and axial strains during the first three days of curing after the concrete was cast (Figure 4.4). The FRP tube in a SCEC specimen was subjected to tension in both the circumferential and longitudinal directions as a result of concrete expansion after a short period of shrinkage at the initiation of cement hydration. Cao *et al.* (2017) reported that the expansion of SCEC had a relatively fast rate in the first 24 hours and tended to stabilize after three days of curing (i.e., the expansive strain became almost constant). However, as can be seen from Figure 4.5 for the results of the present tests,

the increasing trend of expansive strains (tensile strains) did not seem to have stabilized at the age of three days. As in this study, strain monitoring did not continue after three days, the actual magnitude of concrete expansion at the day of column testing was not clear. Table 4.3 gives only the tensile strain readings at the last measurement at 3 days. It can be seen that the hoop expansive strain is smaller than the axial expansive strain because of the restraint of the FRP tube.

#### **4.2.5 Test Setup and Instrumentation**

Axial compression tests on the CFFT column specimens were initiated 30 days after concrete casting and were performed using a testing machine with a maximum capacity of 10000 kN. The test setup is shown in Figure 4.6. In order to prevent premature failure of the GFRP tubes at the top and bottom ends, additional CFRP strips were provided at the ends of each column specimen within a region of one-tenth of the specimen height to strengthen the GFRP tube (see Figure 4.6). In testing, the axial load was applied to the column using an actuator under displacement control at a constant axial strain rate of 0.0006/min.

Linear variable displacement transducers (LVDTs) were used to monitor the movement of the platen at top, and measure the shortening of the column under axial compression within two fifths of the column height at the middle (Figure 4.6). The number of LVDTs installed on each specimen to measure the axial shortening was two for the 150 mm diameter specimens and four for the other specimens (Figure 4.7). One-directional strain gauges with a gauge length of 20 mm were installed on the surface of FRP tubes at the mid height to measure the strains of concrete and FRP, assuming that there was no slip between the FRP and the concrete core. For each of the 150-mm and 200-mm diameter specimens, a total of eight strain gauges were used,

four in the longitudinal direction and four in the circumferential direction. For each of the 300-mm and 400-mm diameter specimens, the total number of strain gauges was 12, including four longitudinal and eight circumferential, as shown in Figure 4.7. The loads, strains and displacements were recorded simultaneously using a data logger.

## **4.3 TEST RESULTS AND DISCUSSIONS**

### **4.3.1 Failure Mode**

All the specimens were failed by the rupture of GFRP under hoop tension in the mid-height region, followed immediately by the crushing of concrete, as illustrated in Figure 4.8. Initial damages of FRP tubes were associated with snapping noises, which happened after the cylinder concrete strength was reached. With increasing loading, white bands on the surface of FRP tube started to develop and propagated in the direction paralleling the winding angle. The eventual rupture of the GFRP tubes was sudden and noisy, followed by a quick drop of the applied load.

It can be seen from Figure 4.8 that the failure of SCC specimens (Series S) was not much different from that of NC specimens (Series N) for the relatively small-scale specimens (i.e., 150 mm or 200 mm in diameter). In comparison, the failure of the larger SCC specimens (i.e., 300 mm or 400 mm in diameter) was relatively more localized than that of the NC specimens of the same size. This difference in failure mode between SCC and NC specimens with the diameters of 300 mm and 400 mm can be clearly seen in Figure 4.8. The more localized failure of the SCC specimens might be due to the non-uniformity of concrete deformation and the localization of the FRP rupture.

On the other hand, it is observed that the failure of large SCEC specimens (Series SE) was explosive, as demonstrated by the failure of specimen SE-3-400-II shown in Figure 4.8(1). This explosive failure, which was not observed for the other two series of specimens, was probably because the energy stored in the SCEC specimens was higher than the counterparts in the other two series as the use of expansive cement led to a more uniform expansion of the concrete, as demonstrated in the subsequent subsection.

### **4.3.2 FRP Hoop Rupture Strains**

Figure 4.9 presents a schematic illustration of the FRP hoop strains at specimen mid-height at the ultimate rupture for all specimens. For each specimen, individual strain gauge readings are represented by hollow symbols, while the average hoop strain for the specimen is denoted by a solid symbol. Strain gauge readings were unavailable at some locations because of the early damage of the gauges.

It is observed from Figure 4.9 that there is an increasing trend of the average hoop rupture strains with increasing specimen diameter. This observation agrees with Lam and Teng (2004) who suggested the FRP hoop rupture strain increases with a decrease in curvature. On the other hand, the FRP hoop rupture strain data are less scattered for the SCEC specimens (Series SE), indicating a more uniform FRP confinement for the specimens, as a consequence of the concrete expansion or the absence of shrinkage due to the use of expansive cement. In contrast, a large scatter of the hoop rupture strains was observed for the large SCC specimens (S-2-400-I and S-3-400-II), which could be attributed to the non-uniformity of concrete deformation and weak FRP confinement.

### 4.3.3 Load Capacity and Ultimate Axial Strain

The key test results are summarized in Table 4.4. In Table 4.4,  $P_{total}$  is the maximum applied load for each specimen from the test,  $P_{frp}$  is the axial load resisted by the FRP tube corresponding to  $P_{total}$ , and  $P_c$  is the difference between  $P_{total}$  and  $P_{frp}$  and represents the axial load carried by the concrete core.  $P_{co}$  is equal to the unconfined concrete strength times the area of the concrete section. The calculation of the axial load carried by the FRP tube ( $P_{frp}$ ) will be described in detail in Chapter 5 considering the biaxial nonlinear behavior of the FRP tube based on the model of Jones and Nelson (1975). Other key test results listed in Table 4.4 include the ultimate axial strain ( $\epsilon_{cu}$ ), which is the axial strain at the rupture of the FRP tube and was found from the average readings of LVDTs installed at the mid-height region of specimens, and the hoop rupture strain of FRP tube ( $\epsilon_{h,rup}$ ), which was averaged from readings of the hoop strain gauges. Table 4.4 suggests that among the three series of specimens, the SCEC specimens with a diameter of 150 mm, 200 mm or 300 mm had the lowest enhancement in compressive strength and ultimate axial strain under the same test configuration. This is probably because their unconfined concrete strength ( $f'_{co}$ ) for specimens of this range of diameter was the highest among the three series (see Table 4.1). The axial load-axial strain curves (referred to as “load-strain curves” hereafter) obtained from the compression tests are shown in Figure 4.10. All the load-strain curves feature a bilinear shape, although for the two 400-mm diameter SCC specimens (S-2-400-I and S-3-400-II) the responses are less stable. It can be noticed in Table 4.4 that the use of SCC in CFFTs had little effect on the load capacity, but reduced the ultimate axial strain by some extent for specimens with a diameter up to 300 mm. However, it led to a significant reduction in both the load capacity and the ultimate axial strain for specimens with a diameter of 400 mm. This is due to the limited

confinement level in the 400 mm-diameter specimens and the large shrinkage of SCC which will be discussed in the following sections. In comparison, the use of SCEC did not change much the load capacity and the ultimate axial strain of specimens in all sizes. It should be noted that in the above discussion, the difference in cylinder compressive strength of the unconfined concrete has been taken into account.

#### **4.3.4 Stress-Strain Responses**

Figure 4.11 shows the stress-strain responses of the confined concrete core in the three series of specimens, where the axial stresses are normalized using the cylinder compressive strength ( $f'_{co}$ ), and the axial and the lateral strains are normalized using the axial strain at the cylinder strength ( $\epsilon_{co}$ ) which is assumed to be equal to 0.002 according to GB-50010 (2010). The axial stress of concrete was obtained by dividing the axial load carried by the concrete (obtained by subtracting the axial load carried by the FRP tube from the total axial load) by its cross-sectional area. The calculation of the axial load carried by the FRP tube will be described in detail in Chapter 5. The lateral strain was averaged from the readings of the hoop strain gauges. It should be mentioned that the axial strain of specimen N-1-200-I was obtained from only three LVDTs beyond the point corresponding to two-third of the ultimate load, because one of the four LVDTs was no longer working beyond this point.

It is observed from Figure 4.11 that for most specimens, the normalized axial stress-axial strain curves have a bilinear shape typical of FRP-confined concrete, and those from duplicated tests match well each other, indicating a good reproducibility of the results. Exceptions are found for the two 300-mm diameter NC specimens (i.e. N-1-300-I and N-1-300-II) and the two 400-mm diameter SCC specimens (i.e. S-2-400-I and S-3-400-II). For the 300-mm diameter NC specimens, the responses of concrete

deviated from each other, which might be attributed to experimental errors. For the 400-mm diameter SCC specimens, the stress-strain responses were not stable after the cylinder strength of unconfined concrete was reached.

It is noticed from Figure 4.11(a) that for the 150-mm diameter specimens, the lateral strain and axial stress at a certain axial strain are larger for SCC specimens than for the counterparts in the other two series, although the ultimate axial stresses are not so different. Similar observations were reported in studies on SCC columns confined with FRP wraps, and were attributed to the lower coarse aggregate content of SCC (Domone 2007, Yu *et al.* 2014). It should also be noted that, the responses of SCEC specimens are on the lower side in the normalized stress-strain plots in Figure 4.11, which is probably due to the higher cylinder compressive strength that has been used to normalize the stresses.

#### **4.3.5 Lateral Strain and Dilation Properties of Confined Concrete**

In order to better understand the behavior of CFFTs with different types of concrete, the lateral strain and dilation properties of FRP-confined concrete are explored. In Figure 4.12 the absolute values of the lateral-to-axial strain ratios ( $|\varepsilon_l/\varepsilon_c|$ ) are plotted against the normalized axial strains ( $\varepsilon_c/\varepsilon_{co}$ ). In Figure 4.13, the normalized axial stresses in concrete ( $\sigma_c/f'_{co}$ ) are plotted against the volumetric strains ( $\varepsilon_v$ ). The latter is calculated from  $\varepsilon_v = \varepsilon_c + 2\varepsilon_l$ , where  $\varepsilon_c$  and  $\varepsilon_l$  are the axial compressive strain and the lateral strain of concrete respectively. Negative values of  $\varepsilon_v$  denote concrete dilation while positive values correspond to concrete compaction.

Teng and Lam (2004) compared the lateral-to-axial strain ratio and dilation properties of unconfined, actively confined and FRP-confined concrete based on experimental

observations. For unconfined concrete and concrete under a constant active confinement, the absolute value of the lateral-to-axial strain ratio is monotonically increasing with increasing axial strain, leading to unstable dilation after initial compaction (Teng and Lam 2004). In contrast, the lateral-to-axial strain ratio of FRP-confined concrete, after rapid increases during the initial period of loading, stabilizes at values depending on the relative stiffness of the confining FRP jacket (i.e., confinement stiffness ratio  $\rho_k$ , see Table 4.1). With increasing axial compression loading, the dilation tendency may be taken over by compaction in FRP-confined concrete when the confining FRP jacket is sufficiently stiff due to the linear elastic behavior of FRP (Teng and Lam 2004).

Figure 4.12 shows that for almost all the specimens except the two 400-mm diameter SCC specimens (i.e., S-2-400-I and S-3-400-II), the lateral-to-axial strain ratio, given in absolute values, stabilizes at certain levels below unity. This level of stabilization is found to depend not only on the relative stiffness of FRP confinement, but also on the type of concrete. First, when comparison is made for the same concrete, the level of lateral-to-axial strain ratio at stabilization was higher for the specimen with a larger diameter which corresponded to a lower confinement stiffness ratio  $\rho_k$ . Second, when comparison is made for the same diameter, the level of lateral-to-axial strain ratio at stabilization was higher for the specimen prepared with SCC than for the others. The two 400-mm diameter SCC specimens were the extreme cases that the lateral-to-axial strain ratio was continuously increasing and did not stabilize, indicating unstable dilation of the concrete at that level of FRP confinement. On the other hand, it is noticed from Figure 4.12 that at the same diameter, the lateral-to-axial strain ratio of the SCEC specimens stabilized at a level in between those of the SCC specimens and NC specimens. Considering the fact that the SCEC specimens had higher cylinder

strength than the NC specimens and consequently lower confinement stiffness ratios, it is believed that the lateral strain behavior of the SCEC specimens is not much different from that of the NC specimens.

Figure 4.13 shows that the dilation properties of the specimens are also dependent on the concrete properties and the confinement stiffness. It can be seen from Figure 4.13(a) that for the NC specimens of 150 mm in diameter, the dilation tendency was taken over by compaction at a normalized axial stress about 1.5 times the cylinder strength  $f'_{co}$ . However, for the SCC specimens of the same diameter and similar confinement stiffness ratio to the NC specimens (see Table 4.1), the dilation tendency remained unchanged until failure. This observation indicates that CFFT specimens prepared with SCC has a stronger tendency of dilation than those prepared with NC at the same level of FRP confinement. Stronger dilation tendency was also observed for the SCC specimens with larger diameters [Figures 4.13(b) and (c)], although the confinement stiffness at these levels was still able to maintain stable ascending axial stress-axial strain responses until failure. Unstable dilation was observed for the 400-mm diameter SCC specimens at confinement stiffness ratios of 0.0235 and 0.0250, at which the lateral-to-axial strain ratio was not convergent [see Figure 4.12(d)] and the second portion of the axial stress-axial strain curves lost stability [Figure 4.11(d)].

#### **4.3.6 Effect of SCC on the Behavior of CFFT Specimens**

It is clear from the above discussion that under axial compression the specimens prepared with SCC have stronger dilation tendency than those prepared with NC and SCEC, leading to a larger lateral-to-axial strain ratio and an unstable axial stress-axial strain response if the stiffness of the confining FRP tube does not exceed a certain threshold value. Because of the stronger dilation tendency of SCC-filled FRP tubes in

axial compression, this threshold value of confinement stiffness ratio must be larger than that for FRP-confined NC for which a threshold value of  $\rho_k = 0.01$  has been suggested by Teng *et al.* (2009). The exact value of  $\rho_k$  for SCC-filled FRP tubes should be determined when more tests are available.

Demone (2007) and Yu *et al.* (2014) attributed the stronger dilation tendency of SCC-filled FRP tubes to the lower coarse aggregate content of SCC. Considering that the specimens with SCEC did not show the same dilation tendency, it is reasonable to assume that the stronger dilation tendency of the specimens with SCC is resulted from the large shrinkage. The only difference between the mix details of SCEC and SCC was the use of expansive cement in the former. However, it is still not clear how the large shrinkage of SCC connects to the stronger tendency of dilation under axial compression. Nevertheless, when used in CFFTs, SCC should be better proportioned with expansive cement to reduce the shrinkage and enhance the volumetric stability.

#### **4.4 CONCLUSIONS**

This chapter has presented the results of an experimental program consisting of 23 CFFT specimens subjected to axial compression. The specimens were divided into three series in terms of the type of concrete used (i.e., NC, SCC and SCEC). The diameter of the specimens in each series covered 150 mm, 200 mm, 300 mm and 400 mm. The test results and discussions presented in this chapter allow the following conclusions to be drawn:

- (1) For all three series of specimens, the average hoop rupture strain of the FRP tube generally increases as the diameter increases. However, under a weak confinement level, SCC-filled FRP tubes exhibit more pronounced non-uniformity in the

distribution of the hoop rupture strains, leading to the localized failure mode different from the NC- and SCEC-filled FRP tubes.

- (2) The axial stress-axial strain curves of the concrete in the three series of specimens feature a similar bilinear shape typical of FRP-confined concrete. The level of confinement plays a similar role in the three types of confined concrete.
- (3) Compared with NC- and SCEC-filled FRP tubes, SCC-filled FRP tubes show stronger dilation tendency under axial compression which lead to a larger lateral-to-axial strain ratio, and an unstable axial stress-axial strain response of the confined concrete when the confinement stiffness is lower than a certain threshold.
- (4) The unstable performance of SCC-filled FRP tubes under a weak confinement level due to the large shrinkage can be improved by adding an appropriate amount of shrinkage-reducing admixture or increasing the confinement level.

## **4.5 REFERENCES**

- ASTM C469/469M-14. (2014). "Standard Test Method for Static Modulus of Elasticity and Poisson's Ratio of Concrete in Compression", American Society for Testing and Materials (ASTM), Philadelphia, USA.
- Bo, H. (2013). "An Improved Criterion for Sufficiently Insufficiently FRP-Confined Concrete Derived from Ultimate Axial Stress", *Engineering Structures*. Vol. 46, pp.431-446.
- Cao, Q., Tao, J.J., Wu, Z.M. and Ma, Z.G.J. (2017). "Behavior of FRP-Steel Confined Concrete Tubular Columns Made of Expansive Self-Consolidating Concrete under Axial Compression", *Journal of Composites for Construction*. Vol. 21(5):

04017037.

- Chen, Y., Visintin, P. and Oehlers, D. J. (2016). “Extracting Size-Dependent Stress-Strain Relationships from FRP-Confined Concrete Cylinders for Varying Diameters and Heights”, *Journal of Materials in Civil Engineering*, ASTM. Vol. 28(5): 04015182.
- Cui, C. and Sheikh, S.A. (2010). “Experimental Study of Normal- and High-Strength Concrete Confined with Fiber-Reinforced Polymers”, *Journal of composite Construction*. Vol. 14(5), pp.553-561.
- De Lorenzis, L., Micelli, F. and La Tegola, A. (2002). “Influence of Specimen Size and Resin Type on the Behaviour of FRP-Confined Concrete Cylinders”, *Proceedings of ACIC-2002: Advanced Polymer Composites for Structural Applications in Construction*. Southampton, UK, on 15-17 April 2002, pp.231-239.
- Domone, P. L. (2007). “A Review of the Hardened Mechanical Properties of Self-Compacting Concrete”, *Cement & Concrete Composites*. Vol. 29(1), pp.1–12.
- El Chabib, H., Nehdi, M. and El Naggar, M.H. (2005). “Behavior of SCC Confined in Short GFRP Tubes”, *Cement & Concrete Composites*. Vol. 27(1):55-64.
- Elsanadedy, H.M., Al-Salloum, Y.A., Alsayed, S.H. and Iqbal, R.A. (2012) “Experimental and Numerical Investigation of Size Effects in FRP-Wrapped Concrete Columns”, *Construction and Building Materials*. Vol. 29, pp.56-72.
- Fam, A.Z. and Rizkalla, S.H. (2001a). “Confinement Model for Axially Loaded Concrete Confined by Circular Fiber-Reinforced Polymer Tubes”, *ACI Structural Journal*. Vol. 98(4), pp.451-461.
- Fam, A. Z. and Rizkalla, S.H. (2001b). “Behavior of Axially Loaded Concrete-Filled Circular Fiber-Reinforced Polymer Tubes”, *ACI Structural Journal*. Vol. 98(3), pp.280–289.

- Issa, M.A., Alrousan, R.Z. and Issa, M.A. (2009). “Experimental and Parametric Study of Circular Short Columns Confined with CFRP Composites”, *Journal of Composites for Construction*. Vol. 13(2), pp.135-147.
- Jiang, T. and Teng, J. G. (2007). “Analysis-Oriented Stress-Strain Models for FRP-Confined Concrete”, *Engineering Structures*. Vol. 29(11), pp.2968-2986.
- Jones, R.M. and Nelson JR, D.A.N. (1975). “A New Material Model for the Nonlinear Biaxial Behavior of ATJ-S Graphite”, *Journal of Composite Materials*. Vol. 9, pp.10-27.
- Lam, L. and Teng, J.G. (2003). “Design-oriented Stress-Strain Model for FRP-Confined Concrete”, *Construction and Building Material*. Vol. 17, pp.471-489.
- Lam, L. and Teng, J. G. (2004). “Ultimate Condition of FRP-Confined Concrete”, *Journal of Composites for Construction*. Vol. 8(6), pp.539-548.
- Liang, M., Wu, Z.M., Ueda, T., Zheng, J.J. and Akogbe, R. (2012). “Experiment and Modeling on Axial Behavior of Carbon Fiber Reinforced Polymer Confined Concrete Cylinders with Different Sizes”, *Journal of Reinforced Plastics and Composites*. Vol. 31(6), pp.389-403.
- Lim, J.C., Karakus, M. and Ozbakkaloglu, T. (2016). “Evaluation of Ultimate Conditions of FRP-Confined Concrete Columns Using Genetic Programming”, *Computers & Structures*. Vol. 162, pp.28-37.
- Matthys, S., Toutanji, H., Audenaert, K. and Taerwe, L. (2005). “Axial Load Behavior of Large-Scale Columns Confined with Fiber-Reinforced Polymer Composites”, *ACI Structural Journal*. Vol. 102(2), pp.258-267.
- Matthys, S., Toutanji, H. and Taerwe, L. (2006). “Stress-Strain Behavior of Large-Scale Circular Columns Confined with FRP Composites”, *Journal of Structural Engineering*, ASCE. Vol. 132(1), pp.123-133.
- Mirmiran, A. and Shahawy, M. (1997). “Behavior of Concrete Columns Confined by

- Fiber Composites”, *Journal of Structural Engineering*, ASCE. Vol. 123(5), pp.583-590.
- Ozbakkaloglu, T. (2013). “Compressive Behavior of Concrete-Filled FRP Tube Columns: Assessment of Critical Column Parameters”, *Engineering Structures*. Vol. 51, pp.188-199.
- Paultre, P., Khayat, K.H., Cusson, D. and Tremblay, S. (2005). “Structural Performance of Self-Consolidating Concrete Used in Confined Concrete Columns”, *ACI Structural Journal*. Vol. 102(4), pp.560-568.
- Smith, S.T., Kim, S.J. and Zhang, H.W. (2010). “Behavior and Effectiveness of FRP Wrap in the Confinement of Large Concrete Cylinders”, *Journal of Composites for Construction*, ASTM. Vol. 14 (5), pp.573-582.
- Teng, J.G. and Lam L. (2004). “Behavior and Modeling of Fiber Reinforced Polymer-Confined Concrete”, *Journal of Structural Engineering*, ASCE. Vol. 130(11), pp.1713-1723.
- Teng, J. G., Jiang, T., Lam, L., and Luo, Y. Z. (2009). “Refinement of A Design-Oriented Stress-Strain Model for FRP-Confined Concrete”, *Journal of Composites for Construction*. Vol. 13(4), pp.269–278.
- Thériault, M, Neale, K.W. and Claude, S. (2004). “Fiber-Reinforced Polymer-Confined Circular Concrete Columns: Investigation of Size and Slenderness Effects”, *Journal of Composites for Construction*. Vol. 8(4), pp.323-331.
- Wang, Y.F. and Wu, H.L. (2011). “Size Effect of Concrete Short Columns Confined with Aramid FRP Jackets”, *Journal of Composites for Construction*. Vol. 15(4), pp.535-544.
- Xiao, Q. G., Teng, J. G., and Yu, T. (2010). “Behavior and Modeling of Confined High-Strength Concrete”, *Journal of Composites for Construction*. Vol. 14(3), pp.249-259.

Yu, T., Fang, X.L. and Teng, J.G. (2014). “FRP-Confined Self-Compacting Concrete under Axial Compression”, *Journal of Materials in Civil Engineering*. Vol. 26(11), 04014082.

Zhou, J.K, Bi, F.T., Wang, Z.Q. and Zhang, J. (2016). “Experimental Investigation of Size Effect on Mechanical Properties of Carbon Fiber Reinforced Polymer (CFRP) Confined Concrete Circular Specimens”, *Construction and Building Materials*. Vol. 127, pp. 643-652.

**Table 4. 1 Geometric and material properties of specimens**

Specimen		Concrete				GFRP tube					$\rho_k$
No.	Notation	Type	$f_{co}$ (MPa)	$\epsilon_{co}$ (%)	$E_c$ (GPa)	$D_{in}$ (mm)	$t_{frp}$ (mm)	$E_x$ (GPa)	$E_\theta$ (GPa)	$\nu_{x,\theta}$	
1	N-2-150-I	NC	37.82	0.245	31.85	148.6	2.90	11.82	37.89	0.113	0.0790
2	N-2-150-II					148.4	2.88				0.0786
3	N-1-200-I		35.41	0.242	32.76	199.2	3.20	11.63	38.33	0.105	0.0696
4	N-1-200-II					200.0	3.30				0.0714
5	N-1-300-I					300.0	2.99	11.79	42.73	0.101	0.0481
6	N-1-300-II		301.7	3.07	0.0491						
7	N-2-400-I		37.82	0.245	31.85	404.1	3.18	11.27	39.82	0.100	0.0331
8	S-1-150-I	SCC	38.11	0.219	34.19	148.6	2.92	11.82	38.29	0.113	0.0790
9	S-1-150-II					148.3	2.88				0.0781
10	S-1-200-I					199.7	3.01	11.63	38.33	0.105	0.0655
11	S-1-200-II		199.1	2.93	0.0645						
12	S-1-300-I		300.5	2.89	11.79	42.73	0.101	0.0499			
13	S-1-300-II		300.1	2.90				0.0486			
14	S-2-400-I		44.06	0.247	35.34	402.8	3.08	11.27	39.82	0.100	0.0235
15	S-3-400-II	45.90	0.233	34.62	404.6	3.20	0.0250				
16	SE-1-150-I	SCEC	47.98	0.290	32.72	148.5	2.91	11.82	38.29	0.113	0.0625
17	SE-1-150-II					148.2	2.86				0.0616
18	SE-1-200-I					198.8	3.10	11.63	38.33	0.105	0.0498
19	SE-1-200-II		199.2	3.21	0.0515						
20	SE-1-300-I		299.7	2.89	11.79	42.73	0.101	0.0413			
21	SE-1-300-II		299.7	2.90				0.0415			
22	SE-2-400-I		42.52	0.290	31.92	404.1	3.18	11.27	39.82	0.100	0.0271
23	SE-3-400-II	41.51	0.289	31.01	404.2	3.17	0.0265				

**Table 4. 2 Proportions of concrete mixtures**

Series	N	S		SE
Concrete type	NC	SCC		SCEC
Batch No.	1, 2, 3	1	2, 3	1, 2, 3
Ordinary Portland cement ( $kg/m^3$ )	350	237	237	213
Fly ash ( $kg/m^3$ )	0	201	201	181
Expansive cement ( $kg/m^3$ )	0	0	0	44
River sand ( $kg/m^3$ )	711	736	736	736
10 mm coarse aggregate ( $kg/m^3$ )	1067	976	976	976
Water ( $kg/m^3$ )	210	192	188	188
Superplasticizer ( $l/m^3$ )	0	3	7	7
Water/Cementitious	0.60	0.44		
Aggregate/Cementitious	5.08	3.91		

**Table 4. 3 Expansive strains in FRP tubes for Series SE specimens at final measurement**

Specimen	Axial strain	Hoop strain	Specimen	Axial strain	Hoop strain
SE-1-150-I	0.000159	0.000081	SE-1-300-I	0.000160	0.000101
SE-1-150-II	0.000182	0.000089	SE-1-300-II	0.000158	0.000098
SE-1-200-I	0.000132	0.000076	SE-2-400-I	0.000166	0.000079
SE-1-200-II	0.000160	0.000099	SE-3-400-II	0.000232	0.000124

**Table 4. 4 Key test results**

Specimen		$P_{total}$ (kN)	$P_{frp}$ (kN)	$P_c$ (kN)	$P_{co}$ (kN)	$P_c/P_{co}$	Average $\epsilon_{cu}$	Average $\epsilon_{cu}/\epsilon_{co}$	Average $\epsilon_{h,rup}$
No.	Notation								
1	N-2-150-I	1969	228	1741	656	2.66	0.0331	13.53	0.0144
2	N-2-150-II	1937	226	1710	654	2.61	0.0341	13.91	0.0155
3	N-1-200-I	3666	259	3407	1103	3.09	0.0362	14.78	0.0220
4	N-1-200-II	3519	314	3205	1112	2.88	0.0385	15.72	0.0202
5	N-1-300-I	6047	313	5734	2502	2.29	0.0300	12.40	0.0189
6	N-1-300-II	5664	365	5299	2150	2.46	0.0322	13.31	0.0190
7	N-2-400-I	8844	451	8393	4219	1.99	0.0267	10.89	0.0212
8	S-1-150-I	1877	142	1736	659	2.63	0.0217	9.90	0.0118
9	S-1-150-II	2031	154	1877	657	2.86	0.0253	11.53	0.0142
10	S-1-200-I	3697	272	3425	1193	2.87	0.0338	15.39	0.0181
11	S-1-200-II	3606	192	3414	1186	2.88	0.0280	12.75	0.0186
12	S-1-300-I	5957	189	5768	2431	2.37	0.0244	11.14	0.0198
13	S-1-300-II	6102	257	5850	2425	2.41	0.0277	12.65	0.0193
14	S-2-400-I	8876	143	8733	5613	1.56	0.0153	6.96	0.0212
15	S-3-400-II	8026	133	7893	5898	1.35	0.00953	4.34	0.0154
16	SE-1-150-I	2147	210	1937	831	2.33	0.0313	10.81	0.0146
17	SE-1-150-II	2098	192	1906	828	2.30	0.0304	10.47	0.0153
18	SE-1-200-I	3782	278	3504	1489	2.35	0.0365	12.59	0.0194
19	SE-1-200-II	3290	203	3087	1494	2.07	0.0251	8.65	0.0143
20	SE-1-300-I	5795	271	5524	2808	1.96	0.0277	9.56	0.0181
21	SE-1-300-II	5870	315	5555	2808	1.98	0.0290	9.99	0.0170
22	SE-2-400-I	8947	373	8574	5452	1.57	0.0236	8.15	0.0206
23	SE-3-400-II	9397	411	8986	5323	1.69	0.0265	9.13	0.0224

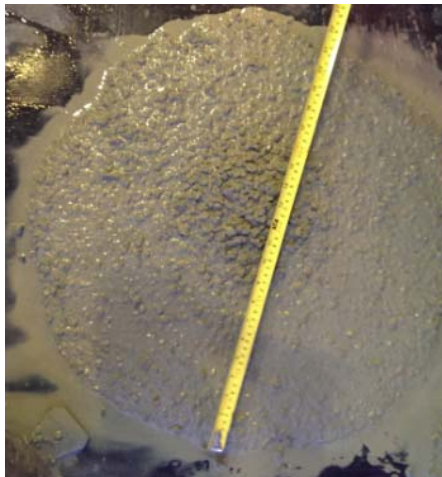


**Figure 4. 1** Slump flow of SCC



**Figure 4. 2** Control cylinder test



**Figure 4. 3** Preparation of filament-wound GFRP tubes



**Figure 4. 4** Strain measurement of specimens filled with SCEC

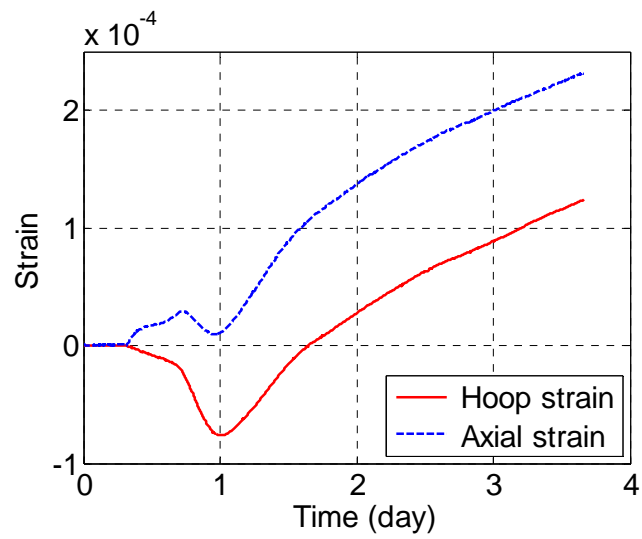


**Figure 4. 5** Expansive strains of Specimen SE-3-400-II



**Figure 4. 6** Test setup of large-scale specimens

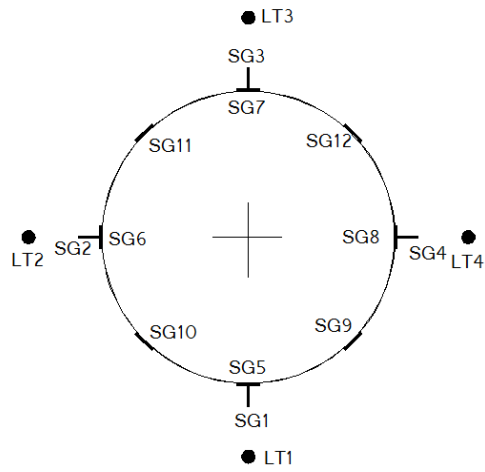


**Figure 4. 7** LVDT and strain gauge layout for 300-mm and 400-mm diameter specimens



(a) N-2-150-I, II

(b) S-1-150-I, II

(c) SE-1-150-I, II



(d) N-1-200-I



(e) S-1-200-I



(f) SE-1-200-I



(g) N-1-300-I

(h) S-1-300-I

(i) SE-1-300-I



(j) N-2-400-I

(k) S-3-400-II

(l) SE-3-400-II

**Figure 4. 8** Failure mode of CFFT specimens

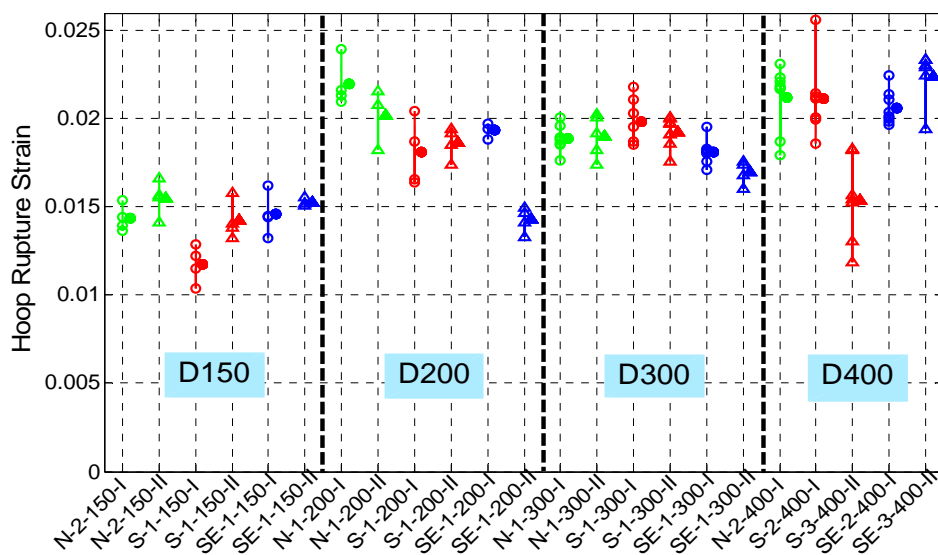
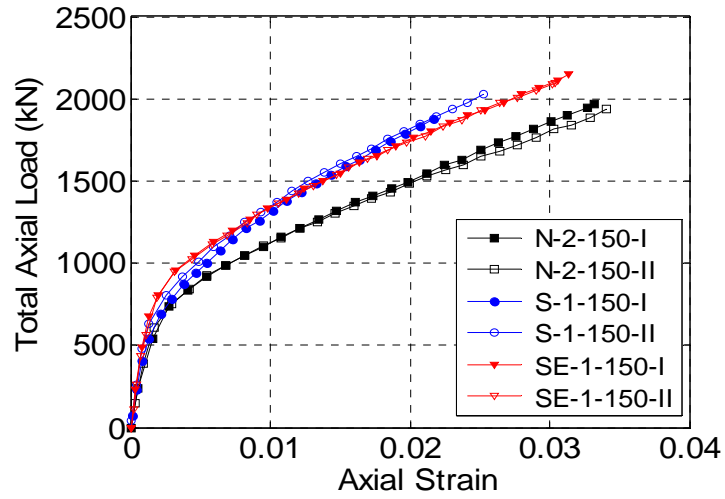
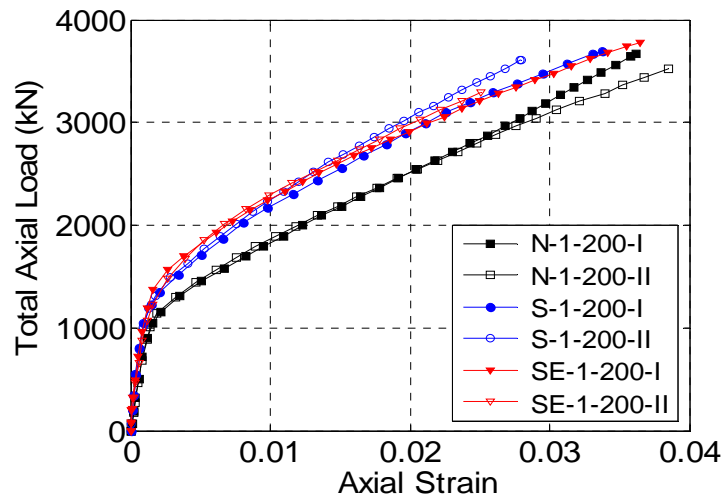


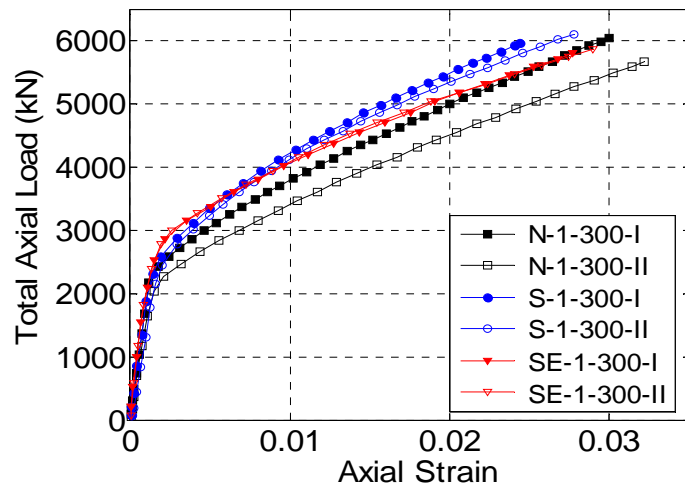
**Figure 4. 9** FRP hoop rupture strains



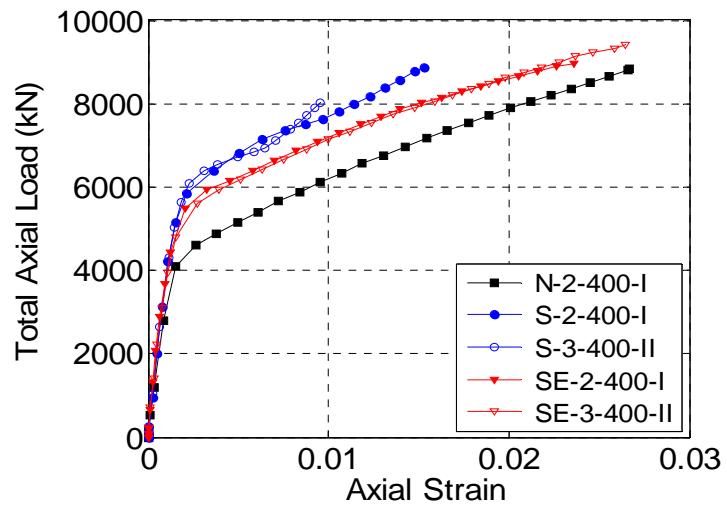
(a) 150-mm diameter specimens



(b) 200-mm diameter specimens

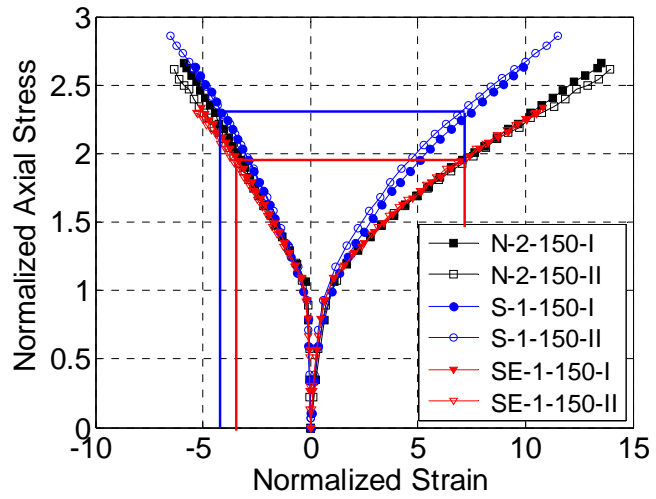


(c) 300-mm diameter specimens

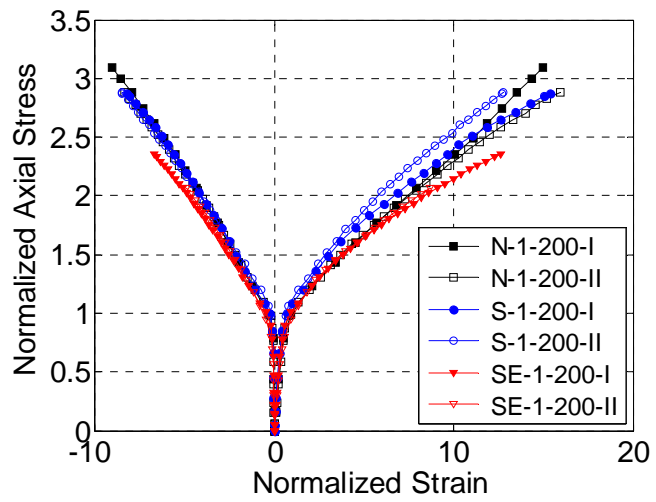


(d) 400-mm diameter specimens

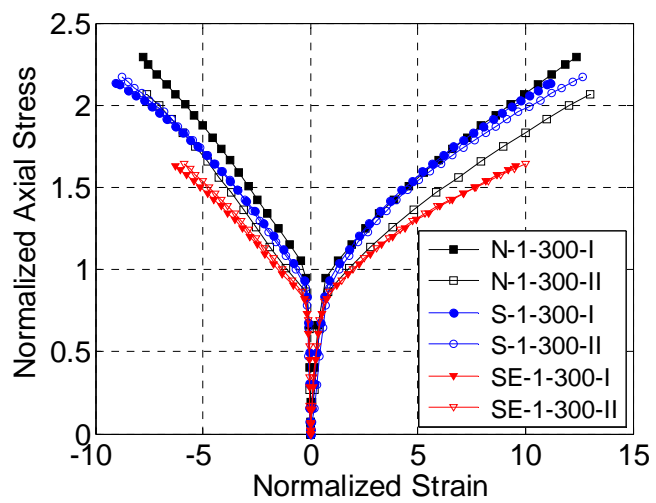
**Figure 4. 10** Load-axial strain curves



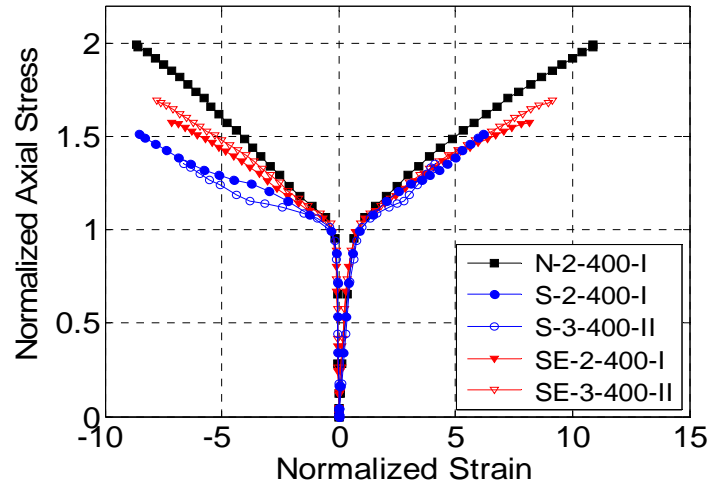
(a) 150-mm diameter specimens



(b) 200-mm diameter specimens

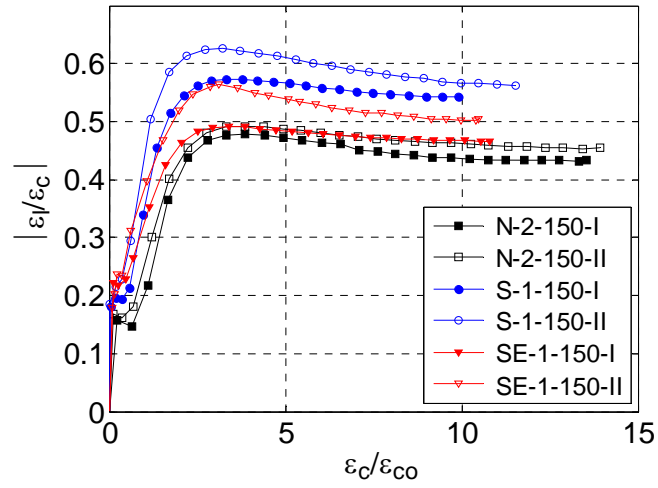


(c) 300-mm diameter specimens

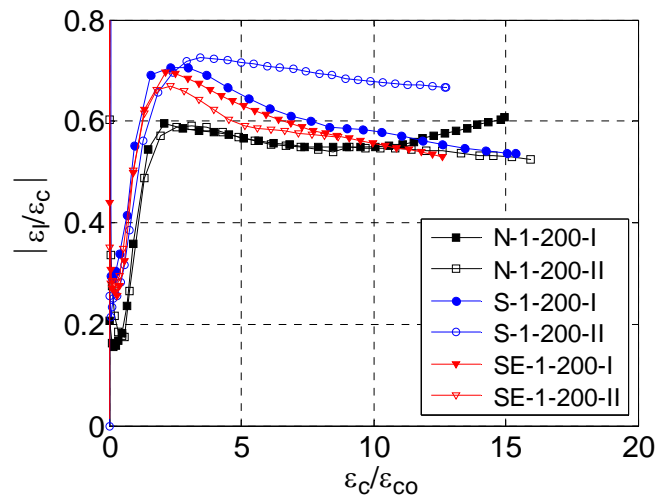


(d) 400-mm diameter specimens

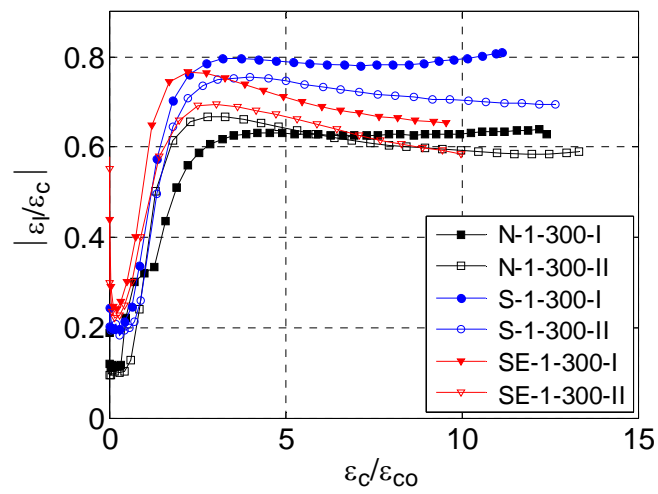
**Figure 4. 11** Normalized axial stress-strain curves



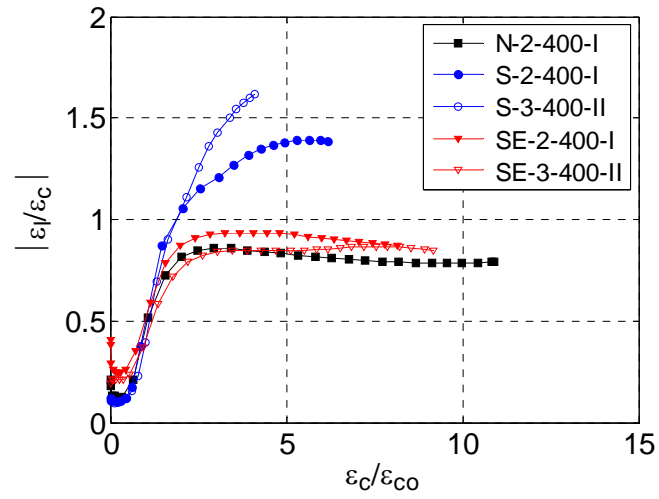
(a) 150-mm diameter specimens



(b) 200-mm diameter specimens

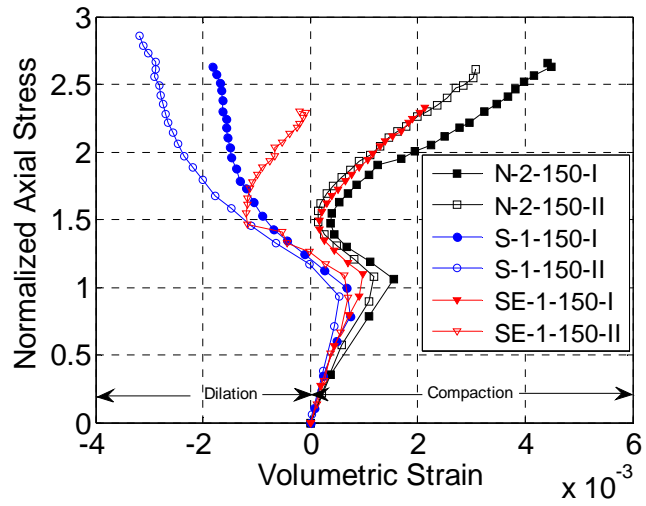


(c) 300-mm diameter specimens

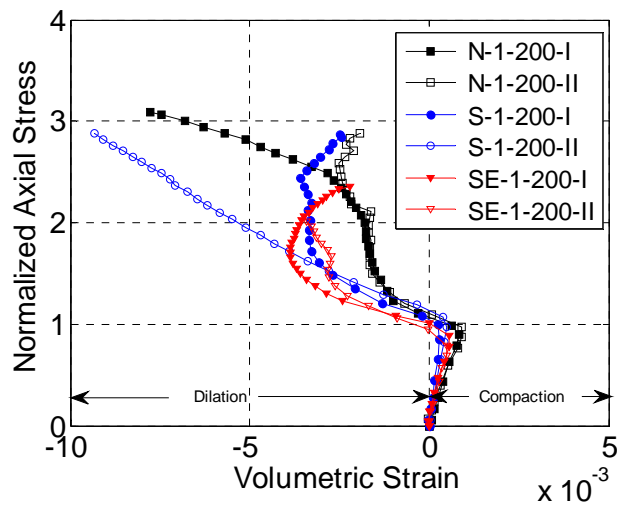


(d) 400-mm diameter specimens

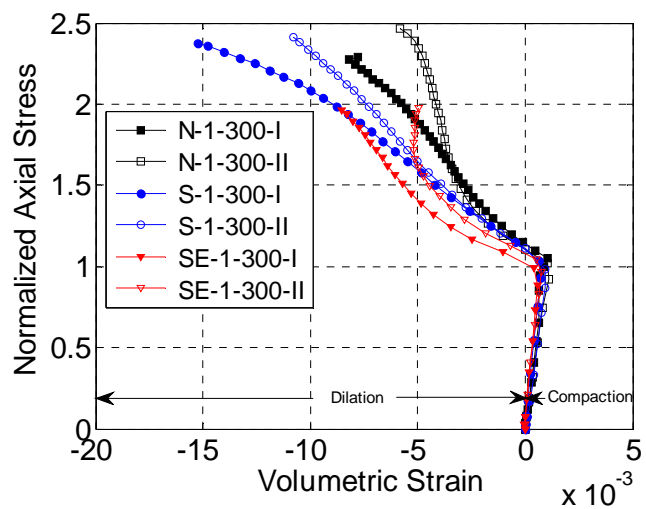
**Figure 4. 12** Normalized lateral strain-axial strain curves



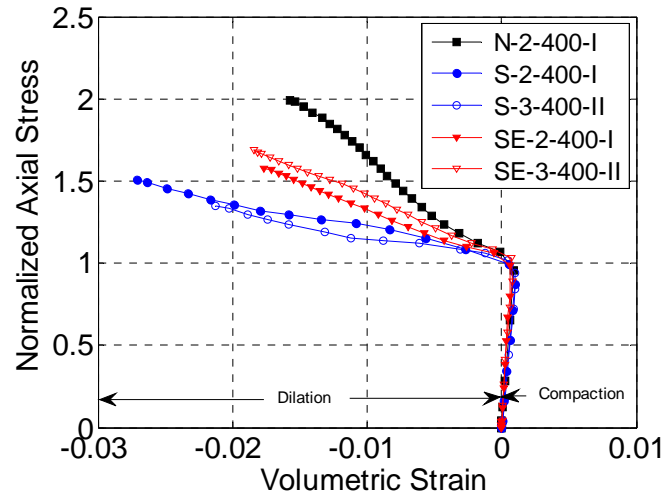
(a) 150-mm diameter specimens



(b) 200-mm diameter specimens



(c) 300-mm diameter specimens



(d) 400-mm diameter specimens

**Figure 4. 13** Normalized axial stress-volumetric strain curves

## CHAPTER 5

# MODELING OF CONCRETE-FILLED FRP TUBES CONSIDERING NONLINEAR BIAXIAL TUBE BEHAVIOR

### 5.1 INTRODUCTION

Many experimental studies have been conducted on CFFTs under axial compression over the past two decades (e.g., Mirmiran and Shahawy 1997; Fam and Rizkalla 2001a, b; Ozbakkaloglu and Oehlers 2008; Park *et al.* 2011; Teng *et al.* 2016), but only a limited amount of work has been devoted to the theoretical analysis of CFFTs. As pointed out in Chapter 1, the existing theoretical studies on CFFTs suffer from two main deficiencies, that is, the negligence of the effect of biaxial stress state and the effect of nonlinear tube behavior.

The first deficiency is discussed below. Although the fibers in a filament-wound FRP tube are typically oriented close to the hoop direction (or at an angle close to  $90^\circ$  with respect to the axis of the tube, such as  $\pm 80^\circ$ ), the tube still possesses a significant axial stiffness. As a result, significant axial stresses can develop in a filament-wound FRP tube for confining concrete and the effect of biaxial stresses (i.e., axial compression in combination with hoop tension) should be taken into account in the modelling of CFFTs under axial compression. However, to the best knowledge of the author, only Fam and Rizkalla (2001a, 2003) took the biaxial behavior of FRP tubes into account in their analysis of the behavior of CFFTs. As reviewed in Chapter 2, the rest of the theoretical studies generally treated the direct axial load contribution of the FRP tube in one of the three following ways: (1) ignoring the axial load contribution of the FRP tube (Mirmiran and Shahawy 1997; Park *et al.* 2011; Teng *et al.* 2016); (2) considering

the axial stiffness of the FRP tube without considering the Poisson's effect (Saafi *et al.* 1999; Mohamed and Masmoudi 2010; Li *et al.* 2010, 2011); and (3) extrapolating the axial load resisted by the FRP tube from the axial load-axial strain curves obtained from uniaxial compression tests on bare FRP tubes (Fam and Rizkalla 2001b; El Chabib *et al.* 2005; Zhang *et al.* 2015).

The second deficiency is discussed below. In most existing theoretical studies on CFFTs (e.g. Saafi *et al.* 1999; Fam and Rizkalla 2001a, 2003; Mohamed and Masmoudi 2010; Li *et al.* 2010, 2011), the FRP tube has been assumed to be linear elastic and the modulus of elasticity of filament-wound FRP tube along the longitudinal direction was obtained from the corresponding strip tests or provided by manufacturers. However, FRP laminae are known to exhibit a certain degree of nonlinear behavior especially in the direction perpendicular to the orientation of the fibers (Jones and Morgon 1977). The nonlinear behavior of FRP laminae mainly stems from the nonlinear matrix material. For example, an obvious nonlinear response of the filament-wound GFRP tubes was observed in Zhang *et al.*'s (2015) tests on CFFTs under axial compression. As a result, a reliable model that can accurately describe the nonlinear behavior of composite laminae is desired in the modeling of CFFTs under axial compression. Many models of this type have been proposed (e.g., Hahn 1973; Hahn and Tsai 1973; Jones and Nelson 1975; Jones and Morgon 1977; Jones 1980; Haj-Ali and Kilic 2002; Zindel and Bakis 2011). Among these models, Hahn and Tsai's (1973) model and Jones and Nelson's (1975) model were proposed based on abundant test data and have been widely adopted by other researchers due to their simplicity and accuracy (e.g., Ishikawa and Chou 1983; Xia *et al.* 1986; Xiao *et al.* 2009).

This chapter will formulate a theoretical model for axially-compressed CFFTs in

which the nonlinear biaxial tube behavior is properly accounted for. The proposed model is a combination of Jiang and Teng's (2007) stress-strain model for FRP-confined concrete and a nonlinear biaxial model for the FRP tube based on Hahn and Tsai's model (1973) or Jones and Nelson's model (1975). The following sign convention is adopted in the present chapter: in the concrete compressive stresses and strains are positive while in the FRP tube tensile stresses and strains are positive.

## 5.2 BIAXIAL BEHAVIOR OF FRP TUBE

The proposed analytical approach is based on the framework of Jiang and Teng's (2007) analysis-oriented model for FRP-confined concrete. Jiang and Teng's (2007) model has been shown to be among the most successful models for FRP-confined concrete (Ozbakkaloglu *et al.* 2013). This model has been reviewed in Section 2.6.3 of Chapter 2. In Jiang and Teng's (2007) model, the FRP jacket is assumed to have hoop stresses and strains only and to be linear elastic, that is,  $\sigma_\theta = E_{frp}\varepsilon_\theta$ , where  $E_{frp}$  and  $\varepsilon_\theta$  are the modulus of elasticity and the hoop strain of the FRP jacket, respectively. Jiang and Teng's (2007) model was originally developed based on the results of concrete columns confined with an FRP jacket with fibers oriented solely or predominantly in the hoop direction, for which the axial stiffness and the Poisson's effect of the FRP jacket can be ignored.

For a CFFT, the FRP tube can be approximated as an orthotropic elastic membrane and the following equation can be used to calculate  $\sigma_\theta$  to properly consider the biaxial behavior of the FRP tube:

$$\begin{bmatrix} \varepsilon_x \\ \varepsilon_\theta \end{bmatrix} = \begin{bmatrix} 1/E_x & -\nu_{x\theta}/E_x \\ -\nu_{x\theta}/E_x & 1/E_\theta \end{bmatrix} \begin{bmatrix} \sigma_x \\ \sigma_\theta \end{bmatrix} \quad (5.1)$$

where  $E_x$  and  $E_\theta$  are the elastic moduli of the FRP tube in the axial and the hoop directions, respectively;  $\nu_{x\theta}$  is the Poisson's ratio for the strain in the hoop direction when stressed in the axial direction; and  $(\sigma_x, \varepsilon_x)$  and  $(\sigma_\theta, \varepsilon_\theta)$  are the stresses and the strains in the axial and the hoop directions of the FRP tube, respectively.

### 5.3 NONLINEAR ANALYSIS OF FRP LAMINAE

To consider the nonlinear behavior of FRP tubes, both Hahn and Tsai's (1973) model and Jones and Nelson's (1975) model were used and incorporated into Jiang and Teng's (2007) stress-strain model for FRP-confined concrete in the present study. The two models are briefly described in the following two sub-sections, respectively.

#### 5.3.1 Hahn and Tsai's (1973) model

Hahn and Tsai (1973) derived a general stress-strain relation of composite laminae based on the theory of complementary elastic energy density. For a typical composite lamina with the same compressive and tensile elastic properties, a polynomial expansion up to fourth-order for the complementary energy density is given by (Hahn and Tsai 1973)

$$\begin{aligned} \bar{W}^* = & \frac{1}{2}S_{11}\sigma_1^2 + \frac{1}{2}S_{22}\sigma_2^2 + \frac{1}{2}S_{66}\sigma_6^2 + S_{12}\sigma_1\sigma_2 + \frac{1}{4}S_{1111}\sigma_1^4 + \frac{1}{4}S_{2222}\sigma_2^4 + \\ & \frac{1}{4}S_{6666}\sigma_6^4 + S_{1112}\sigma_1^3\sigma_2 + S_{1122}\sigma_1^2\sigma_2^2 + S_{1222}\sigma_1\sigma_2^3 \end{aligned} \quad (5.2)$$

where  $\sigma_1$  and  $\sigma_2$  are the stresses in the two principal material axes of the composite lamina respectively (Figure 5.1);  $\sigma_6$  is the shear stress; and  $S_{11}$ ,  $S_{22}$ ,  $S_{66}$ ,  $S_{12}$ ,  $S_{1111}$ ,

$S_{2222}$ ,  $S_{6666}$ ,  $S_{1122}$ ,  $S_{1112}$ ,  $S_{1222}$  are coefficients which can be determined by test results of the composite lamina under simple stress states (e.g., uniaxial tension/compression, biaxial tension/compression, pure shear).

According to the definition of complementary energy, the strains  $\varepsilon_i$  ( $i = 1, 2, 6$ ) can be determined by

$$\begin{bmatrix} \varepsilon_1 \\ \varepsilon_2 \\ \varepsilon_6 \end{bmatrix} = \begin{bmatrix} \frac{\partial \bar{W}^*}{\partial \sigma_1} \\ \frac{\partial \bar{W}^*}{\partial \sigma_2} \\ \frac{\partial \bar{W}^*}{\partial \sigma_6} \end{bmatrix} = \begin{bmatrix} S_{11}\sigma_1 + S_{12}\sigma_2 + S_{1111}\sigma_1^3 + 3S_{1112}\sigma_1^2\sigma_2 + 2S_{1122}\sigma_1\sigma_2^2 + S_{1222}\sigma_2^3 \\ S_{12}\sigma_1 + S_{22}\sigma_2 + S_{1112}\sigma_1^3 + 3S_{1222}\sigma_1\sigma_2^2 + 2S_{1122}\sigma_1^2\sigma_2 + S_{2222}\sigma_2^3 \\ S_{66}\sigma_6 + S_{6666}\sigma_6^3 \end{bmatrix} \quad (5.3)$$

Most composite materials exhibit linear behavior ( $\sigma_1 \sim \varepsilon_1$  and  $\sigma_1 \sim \varepsilon_2$ ) under pure tension in the 1 direction (fiber direction) (i.e.,  $\sigma_2 = \sigma_6 = 0$ ) which suggests that  $S_{1111} = 0$  and  $S_{1112} = 0$  in Eq. (5.3) (Jones and Morgan 1977; Xia *et al.* 1986). Under pure tension in the 2 direction (transverse direction),  $\sigma_2 \sim \varepsilon_1$  generally exhibits linear relation, but  $\sigma_2 \sim \varepsilon_2$  exhibits nonlinear relation, which suggests that  $S_{1222} = 0$  and  $S_{2222} \neq 0$  in Eq. (5.3) (Jones and Morgan 1977; Xia *et al.* 1986). Xia *et al.* (1986) tested a glass/unsaturated polyester composite lamina and a glass/epoxy composite lamina under biaxial tension (i.e.,  $\sigma_1 = 2\sigma_2$ ,  $\sigma_6 = 0$ ), and found that the relations,  $\sigma_1 \sim \varepsilon_1$ , for both laminae are linear and thus  $S_{1122}$  equals zero. Therefore, Eq. (5.3) can be simplified to become

$$\begin{bmatrix} \varepsilon_1 \\ \varepsilon_2 \\ \varepsilon_6 \end{bmatrix} = \begin{bmatrix} S_{11} & S_{12} & 0 \\ S_{12} & S_{22} & 0 \\ 0 & 0 & S_{66} \end{bmatrix} \begin{bmatrix} \sigma_1 \\ \sigma_2 \\ \sigma_6 \end{bmatrix} + S_{2222}\sigma_2^2 \begin{bmatrix} 0 \\ \sigma_2 \\ 0 \end{bmatrix} + S_{6666}\sigma_6^2 \begin{bmatrix} 0 \\ 0 \\ \sigma_6 \end{bmatrix} \quad (5.4)$$

When the loading direction of an FRP lamina is not along either of the principal material axes [i.e., the reference coordinate system orients from the principal material coordinate (1-2) by an angle  $\alpha$ ] (see Figure 5.1), the stresses/strains in the principal material coordinate system need to transform to those in the reference coordinate system. Considering that no shear stresses/strains exist in an FRP tube subjected to uniaxial compression in the reference coordinate system, Eq. (5.4) transforms to

$$\begin{bmatrix} \varepsilon_x \\ \varepsilon_y \end{bmatrix} = \begin{bmatrix} \overline{S}_{11} & \overline{S}_{12} \\ \overline{S}_{12} & \overline{S}_{22} \end{bmatrix} \begin{bmatrix} \sigma_x \\ \sigma_y \end{bmatrix} + S_{2222} \sigma_2^3 \begin{bmatrix} \sin^2 \alpha \\ \cos^2 \alpha \end{bmatrix} + S_{6666} \sigma_6^3 \begin{bmatrix} -\cos \alpha \cdot \sin \alpha \\ \cos \alpha \cdot \sin \alpha \end{bmatrix} \quad (5.5a)$$

$$\sigma_2 = \sigma_x \sin^2 \alpha + \sigma_y \cos^2 \alpha \quad (5.5b)$$

$$\sigma_6 = -\sigma_x \cos \alpha \cdot \sin \alpha + \sigma_y \cos \alpha \cdot \sin \alpha \quad (5.5c)$$

where  $(\sigma_x, \varepsilon_x)$  and  $(\sigma_y, \varepsilon_y)$  are respectively the stress and strain of the FRP lamina in  $x$  and  $y$  directions which correspond to the longitudinal and circumferential directions of an FRP tube;  $\overline{S}_{11} = 1/E_x$ ;  $\overline{S}_{22} = 1/E_\theta$ ; and  $\overline{S}_{12} = -\nu_{x\theta}/E_x$ .

### 5.3.2 Jones and Nelson's (1975) model

Jones and Nelson's (1975) model is based on an approach that can be broadly classified as a deformation theory of plasticity approach, in which the total strains are related directly to the total stresses using secant values of moduli and Poisson's ratios (Jones 2009). In this model, the secant value of a nonlinear mechanical property of a composite lamina (e.g., the secant moduli  $E_{x,sec}$ ,  $E_{\theta,sec}$ , or the secant Poisson's ratio  $\nu_{x\theta,sec}$ ) is described as a function of the strain energy density,  $U$

$$\text{Mechanical property}_i = A_i[1 - B_i U^{C_i}] \quad (5.6)$$

where  $A_i$  is the initial value for the  $i$ th material property;  $B_i$  and  $C_i$  are constants to be determined; and  $U$  is the strain energy density of the equivalent linear elastic system (referred to as “the strain energy density” directly hereafter) with the same stresses and strains as those of the nonlinear system (Jones and Nelson 1975). Therefore, for a tube assumed to be in a plane stress state, the strain energy density is given by

$$U = (\sigma_x \varepsilon_x + \sigma_\theta \varepsilon_\theta + \tau_{x\theta} \gamma_{x\theta})/2 \quad (5.7)$$

According to Jones and Nelson (1975),  $B_i$  and  $C_i$  can first be determined by fitting Eq. (5.6) to the material property-versus- $U$  curve obtained from the uniaxial stress-strain data of the lamina in a simple stress state.

## 5.4 TEST SPECIMENS

### 5.4.1 Concrete-Filled GFRP Tubes

The results of tests on CFFTs presented in Chapter 4 are used in this chapter to verify the proposed theoretical model. A total of 23 CFFTs were tested in Chapter 4. These columns all had the same height-to-diameter ratio of two and covered four values of diameter (i.e., an inner diameter of the tubes of 150 mm, 200 mm, 300 mm or 400 mm). The columns were filled with NC, SCC or SCEC.

## 5.4.2 Nonlinear Properties of GFRP tubes

In order to obtain the material properties of the GFRP tubes, axial compression tests (Figure 5.2) and hydraulic pressure tests (Figure 5.3) on bare GFRP tubes were carried out in Chapter 3. Figures 5.2 (b) and 5.3 (b) show typical experimental stress-strain curves from the tests. The nonlinear behavior of the filament-wound GFRP tubes can be observed in the axial stress-axial strain curve from axial compression tests [Figure 5.2 (b)]. Based on these test results, the constants in Hahn and Tsai's (1973) model and Jones and Nelson's (1975) model correlated to the nonlinear behavior of GFRP tubes can be determined, as shown in the following sub-sections.

### 5.4.2.1 Hahn and Tsai's (1973) model

Using the stress-strain curves from axial compression tests on bare GFRP tubes (Figure 5.2 (b)), the following constants in Hahn and Tsai's (1973) model [Eq. (5.5)] can be calculated for GFRP tubes based on the test results of 150 mm-diameter tubes (Table 3.5)

$$E_x = 11820 \text{ MPa}, \overline{S_{11}} = \frac{1}{E_x} = 8.396 \times 10^{-5} (\text{MPa})^{-1} \quad (5.8a)$$

$$\nu_{x\theta} = 0.113, \overline{S_{12}} = -\frac{\nu_{x\theta}}{E_x} = -9.572 \times 10^{-6} (\text{MPa})^{-1} \quad (5.8b)$$

$$S_{2222} = 1.107 \times 10^{-9} (\text{MPa})^{-3}, S_{6666} = 1.228 \times 10^{-8} (\text{MPa})^{-3} \quad (5.8c)$$

The remaining constants in Eq. (5.5) can be obtained using the results of the hydraulic pressure tests on the same batch of tubes (Table 3.6)

$$E_{\theta} = 37893MPa, \overline{S_{22}} = \frac{1}{E_{\theta}} = 2.639 \times 10^{-5}(MPa)^{-1} \quad (5.9)$$

The values of  $S_{2222}$  and  $S_{6666}$  are highly sensitive to the test errors probably associated with the issues of specimen centering and loading platen leveling which are especially difficult to control for large-scale tube specimens. Therefore the values of  $S_{2222}$  and  $S_{6666}$  for GFRP tubes with a diameter of 200 mm, 300 mm or 400 mm are assumed to be equal to those of the 150 mm-diameter tubes. It should be noted that for Hahn and Tai's (1973) model, the relevant parameters are difficult to obtain and this imposes a limitation on the applicability of the model. This problem can be solved by exploring more suitable test methods.

#### 5.4.2.2 Jones and Nelson's (1975) model

The stress-strain curves from the axial compression tests on bare GFRP tubes were used to generate material property-versus- $U$  curves in Jones and Nelson's (1975) model. Figure 5.4 shows such curves for the secant modulus  $E_{x,sec}$  and the secant Poisson's ratio  $\nu_{x\theta,sec}$  for GFRP tubes with a diameter of 150 mm, 200 mm and 400 mm, respectively. The constants in Eq. (5.6) were obtained utilizing a least-square fit of the curves and are summarized in Table 5.1 for  $E_{x,sec}$  and  $\nu_{x\theta,sec}$  respectively. However, it should be noted that the strain energy density of the FRP tube in a CFFT under axial compression can significantly exceed the maximum strain energy density ( $U^*$ ) experienced in compression tests on bare FRP tubes (Jones and Morgan 1977). Eq. (5.6) will lead to a negative value for  $E_{x,sec}$  or  $\nu_{x\theta,sec}$  when  $U$  is relatively large, which is obviously not reasonable. To avoid such a problem, Jones and Morgan (1977) proposed that as  $U$  approaches infinity, the secant value of a material property as

employed in Eq. (5.6) should be assumed to approach asymptotically its tangent value at  $U^*$ . Therefore, in the present study, a fractional expression with an asymptote [Eqs. (5.10) and (5.11) ] is used for the extrapolation of the material property-versus- $U$  curve beyond  $U^*$ . That is, the material property-versus- $U$  curves for the secant modulus and the secant Poisson's ratio are depicted by the following equations respectively

$$E_{x,sec} = \begin{cases} A(1 - BU^c) & U \leq U^* \\ E_{x,tan}^* + \frac{a}{b+U} & U > U^* \end{cases} \quad (5.10)$$

$$\nu_{x\theta,sec} = \begin{cases} A(1 - BU^c) & U \leq U^* \\ \nu_{x\theta,tan}^* + \frac{a}{b+U} & U > U^* \end{cases} \quad (5.11)$$

where  $U^*$  is the maximum strain energy density from the bare FRP tube tests;  $E_{x,tan}^*$  and  $\nu_{x\theta,tan}^*$  are the tangent modulus and tangent Poisson's ratio at  $U^*$ ;  $a$  and  $b$  are constants determined by the condition that the second segment connects to the first segment smoothly at  $U^*$ . Note that the second segments ( $U > U^*$ ) in Eqs. (5.10) and (5.11) approach asymptotically  $E_{x,tan}^*(= d\sigma_x/d\varepsilon_x, U = U^*)$  and  $\nu_{x\theta,tan}^*(= |d\varepsilon_\theta/d\varepsilon_x|, U = U^*)$  respectively when  $U$  approaches infinity (Jones and Morgan 1977). Figure 5.4 shows the material property-versus- $U$  curves from Eqs. (5.10) and (5.11) for the test GFRP tubes; the constants obtained for Eqs. (5.10) and (5.11) for each tube are also listed in Table 5.1. It should be noted that the constants of 300 mm-diameter FRP tubes were assumed to be the same as those of 150 mm-diameter tubes as there was no available test data to generate their material property-versus- $U$  curves. To justify the validity of this assumption, comparisons were made between the predicted behavior of 200 mm-diameter and 400 mm-diameter CFFTs based on the

constants of the 150 mm-diameter tubes and their own. The comparisons indicated very small differences between the predicted results based on the two approaches.

The hoop secant modulus of the GFRP tubes,  $E_{\theta,sec}$ , was assumed to be constant and equal to the hoop modulus of elasticity of the GFRP tube,  $E_{\theta}$ , obtained from the hydraulic pressure tests on GFRP tubes (see Table 4.1).

## **5.5 COMPARISON FOR NC-FILLED FRP TUBES BASED ON JIANG AND TENG’S (2007) MODEL**

### **5.5.1 Analysis Procedure**

Comparisons between the predictions of the proposed theoretical model and the test results of seven NC-filled FRP tubes presented in Chapter 4 are shown in Figure 5.5. The experimental axial load-strain curves are compared with the theoretical curves produced by Jiang and Teng’s (2007) model with the separate incorporation of three biaxial models for FRP laminae: (1) the nonlinear behavior of the GFRP tube is ignored (“2D analysis” in Figure 5.5); (2) the nonlinear behavior of the GFRP tube is considered using Hahn and Tsai’s (1973) model [“2D analysis (H&T)” in Figure 5.5]; and (3) the nonlinear behavior of the GFRP tube is considered using Jones and Nelson’s (1975) model [“2D analysis (J&N)” in Figure 5.5]. In the calculation, full composite action between the FRP tube and the concrete core was assumed (i.e. the axial strain and the hoop strain of the FRP tube were assumed to be equal to those of the concrete core). The total axial load taken by a CFFT is the sum of the axial load taken by the concrete core and that taken by the FRP tube

$$P_{sum} = \sigma_c A_c + (-\sigma_x) A_{frp} \quad (5.12)$$

where  $\sigma_c$  is the axial stress of the confined concrete;  $\sigma_x$  is the axial stress of the GFRP tube;  $A_c$  and  $A_{frp}$  are the section areas of the GFRP tube and the concrete, respectively.

The analysis procedure for predicting the axial load-strain curves using Jiang and Teng's (2007) model with the incorporation of Jones and Nelson's (1975) model is summarized in a flowchart (Figure 5.6). The full curve is generated by specifying successively increasing values of the hoop strain  $\varepsilon_\theta$  until the value reaches the experimental FRP rupture strain  $\varepsilon_{h,rupt}$  via a double iteration process. For each increment of the hoop strain, the solution is sought via a double iteration process consisting of the following steps:

- (1) construct the compliance matrix in Eq. (5.1) with the initial values of material properties of FRP tube  $E_\theta$ ,  $(E_x)_1$ ,  $(\nu_{x\theta})_1$  obtained from material tests presented in Chapter 3;
- (2) specify a hoop strain value  $\varepsilon_{\theta,i}$  for the current incremental step where  $i$  is the index of the current incremental step;
- (3) assume an initial value for the axial strain of the FRP tube  $\varepsilon_{x,i}$ , which should be negative to represent the compression state of the FRP tube;
- (4) calculate the corresponding axial and hoop stresses of the FRP tube,  $(\sigma_{x,i})_1$  and  $(\sigma_{\theta,i})_1$ , using Eq. (5.1);
- (5) calculate the strain energy density,  $(U_i)_1$ , defined by Eq. (5.7) using the resulting stresses and strains;
- (6) obtain new material properties at  $(U_i)_1$  via Eqs. (5.10) and (5.11);
- (7) recalculate the axial and the hoop stresses of the FRP tube,  $(\sigma_{x,i})_2$  and  $(\sigma_{\theta,i})_2$ , for the new material properties;

- (8) calculate the new strain energy density,  $(U_i)_2$ , defined by Eq. (5.7) using the new stresses;
- (9) if  $|(U_i)_2 - (U_i)_1|/(U_i)_1 \leq 10^{-6}$  [where  $(U_i)_2$  and  $(U_i)_1$  are the strain energy densities calculated in Step (8) and Step (5), respectively], continue with step (10); otherwise,  $(U_i)_1$  is replaced by  $(U_i)_2$  and go back to step (6) until the criterion in step (9) is satisfied;
- (10) input the hoop stresses  $\sigma_{\theta,i}$  into Jiang and Teng's model (2007) [Eqs. (2.14) to (2.20)] to obtain the axial strain and the axial stress of the confined concrete,  $\sigma_{c,i}$  and  $\varepsilon_{c,i}$  and;
- (11) if  $|( |\varepsilon_{c,i}| - |\varepsilon_{x,i}| ) / \varepsilon_{x,i}| \leq 10^{-6}$  [ $\varepsilon_{x,i}$  and  $\varepsilon_{c,i}$  should be the same in magnitude according to the assumption of full composite action], continue with step (12); otherwise, go back to step (3) with the assumed value of  $\varepsilon_{x,i}$  being updated by the value of  $-\varepsilon_{c,i}$  and obtained in step (10) until the criterion in step (11) is satisfied; and
- (12) finally obtain the axial load using Eq. (5.12).

The analysis procedure using Jiang and Teng's (2007) model with the incorporation of Hahn and Tsai's (1973) model is simpler as it only involves a single iteration process. This is because the compliance matrix can be directly constructed using Eq. (5.5) so the loop of iteration associated with the construction of the compliance matrix in Jones and Nelson's (1975) model is avoided. The flowchart of the analysis procedure is shown in Figure 5.7. The "2D analysis" procedure is similar to the "2D analysis (H&T)" procedure. The only difference is that the compliance matrix does not consider the nonlinear behavior of the FRP tube and can thus be constructed using Eq. (5.1).

### 5.5.2 Comparison and Discussions

In the existing analyses of CFFTs under axial compression with fibers oriented close

to the hoop direction, two factors are generally ignored: (1) the biaxial stress state of the FRP tube (i.e., the Poisson's effect on tube behavior); and (2) the contribution of the FRP tube to the axial load resisted by the CFFT. The former leads to an overestimation of the lateral confining pressure provided by the FRP tube and thus an overestimation of the axial load enhancement of the concrete core due to FRP confinement, while the latter leads to an underestimation of the axial load capacity of a CFFT. The two factors compensate for each other, at least partially, and may sometimes lead to close predictions for the response of CFFTs (e.g., Saafi *et al.* 1999). The predicted axial load-strain curves with the above two factors ignored for specimen N2-150-I and N2-150-II are respectively shown in Figures 5.5(a) and (b) (labeled "1D analysis"). It can be seen that such a simplified approach leads to a noticeable underestimation in the axial load for a given axial strain. The predicted axial load is even lower if the Poisson's effect of the FRP tube is considered as an additional factor [labeled "1D analysis with Poisson's effect" in Figures 5.5(a) and (b), where the Poisson's effect of the FRP tube is taken into account but the axial load contribution of the FRP tube is ignored].

Figure 5.5 clearly shows that the axial load at a given axial strain of the test specimen is significantly overestimated if the nonlinear behavior of the GFRP tube is ignored. The predictions obtained with the nonlinear behavior of the GFRP tube accounted for agree much better with the test results. The analysis using Hahn and Tsai's (1973) model generally predicts a larger axial load than that using Jones and Nelson's (1975) model for the same axial strain, with the latter providing more accurate predictions for the test results than the former.

Note that for specimen N-1-200-I, the abnormal increase of axial strain beyond the

point at two-third of the ultimate load is attributed to the reading of one LVDT being unavailable as presented in Section 4.3.4. Additionally it is significant that the unconfined concrete strength of specimen N-1-300-II and N-2-400-I are overestimated which are represented by the control cylinder compressive strength as shown in Figure 5.5 (f) and (h) separately. When the unconfined concrete strength are respectively reduced to 85% and 87% of control cylinder compressive strength, Jiang and Teng's (2007) model combining with Jones and Nelson's (1975) model can provide good prediction on the behavior of NC-filled FRP tube columns under axial compression [Figure 5.5 (g) and (i)].

Furthermore, the axial load carried by FRP tube is derived from the total axial load of specimen as shown in Figure 5.8. Note that the axial load undertaken by the FRP tube was obtained on the basis of the measured axial strain and hoop strain of tube. It can be seen that the initial axial stiffness of FRP tube keep almost linear. This is consistent with the suggestions provided by some researchers (e.g., Saafi *et al.* 1999; Fam and Rizkalla 2001a, 2003; Mohamed and Masmoudi 2010; Li *et al.* 2010, 2011). After the axial strain reached to about 0.005 (i.e., the ultimate axial strain of the bare FRP tube under axial compression), the axial load carried by FRP tube under the combination of axial compression and lateral tension due to the expansion of concrete still keep increasing, but the increase speed remarkably drop. This feature can be defined as nonlinear behavior of filament-wound FRP tube. Additionally, it can be seen from Figure 5.8 that the contributions of FRP tube to the axial load occupy a smaller proportion in the total axial load with the increase of the dimension of the specimen. So the error due to ignoring the contribution of FRP tube to axial load has a smaller influence for a large-scale CFFT.

## **5.6 COMPARISON WITH JIANG AND TENG'S (2007) MODEL FOR NC, SCC AND SCEC-FILLED FRP TUBES**

In this section, Jiang and Teng's (2007) model incorporating Jones and Nelson's (1975) model to consider the nonlinear biaxial tube behavior is employed to analyze the behavior of all CFFT specimens presented in Chapter 4.

Figure 5.9 shows the comparisons between test results and theoretical predictions for axial stress-strain curves and axial strain-lateral strain curves of the confined concrete. In Figure 5.9, only one predicted curve is produced for each pair of duplicated specimens with the FRP hoop rupture strain input into the theoretical model being average from the two duplicated specimens. The only exception is that for the pair of Specimens N-1-300-I and N-1-300-II, two separate predicted curves are provided. This is because the compressive strength of unconfined concrete of Specimen N-1-300-II was taken to be 85% of that of the control cylinder as explained earlier.

For specimens with a diameter of 150 mm, 200 mm or 300 mm, two main observations can be made in Figure 5.9: (1) the predicted curves match well with the test curves for NC- and SCEC-filled FRP tubes in general; and (2) for the SCC specimens, the predicted axial stress-strain curves appear lower than the test curves (i.e. the axial stresses are underestimated). The good prediction for the SCEC specimens is because the tight interface between the FRP tube and the concrete core as a result of using expansive cement made the behavior of the SCEC specimens similar to that of the NC specimens. In contrast, the SCC specimens, as reported in Chapter 4, showed a stronger dilation tendency under axial compression. This leads to a larger lateral expansion of concrete and thus a larger confining pressure under the same axial strain

(Domone 2007; Yu *et al.* 2014). As a result, the axial stresses of the SCC specimens are underestimated.

For the 400 mm-diameter specimens, the prediction for the NC specimen is still good. However, the axial stresses of the SCC and the SCEC specimens are overestimated, especially for the SCC specimens. Yu *et al.* (2014) reported that the axial stress of SCC is smaller than that of NC under the same axial strain and confining pressure. Similarly, the reduced confinement level in the 400 mm-diameter specimens due to their large size may be the cause of the overestimation of axial stresses of SCC and SCEC specimens in the present tests.

## **5.7 CONCLUSIONS**

This chapter has presented the formulation of a theoretical model for CFFTs subjected to axial compression, in which the FRP tube is assumed to be an orthotropic elastic membrane. The proposed model combines Jiang and Teng's (2007) stress-strain model for FRP-confined concrete and a nonlinear biaxial model for the FRP tube. For the latter, both Hahn and Tsai's (1973) model and Jones and Nelson's (1975) model were examined with regard to their accuracy in depicting the nonlinear biaxial behavior of filament-wound GFRP tubes. For comparison purposes, less sophisticated modeling approaches which ignore the axial stiffness or the material nonlinearity of the FRP tube were also performed. The predictions by different modeling approaches were compared with the results of tests on CFFTs presented in Chapter 4. The following conclusions regarding the theoretical model for CFFTs can be drawn from the results and discussions presented in this chapter:

- (1) If the FRP tube is assumed to be linear elastic and possess only stiffness in the

hoop direction (1D analysis), the theoretical model may significantly underestimate the axial load resisted by the CFFT.

- (2) If the FRP tube is assumed to be linear elastic and in a biaxial stress state (2D analysis), the theoretical model may overestimate the axial load resisted by the CFFT.
- (3) If the nonlinear biaxial behavior of the FRP tube is properly accounted for, the theoretical model leads to accurate predictions of the axial compressive behavior of CFFTs;
- (4) Compression tests and hydraulic tests on bare FRP tubes are needed to obtain constants in Hahn and Tsai's (1973) model and Jones and Nelson's (1975) model to describe the nonlinear behavior of FRP tubes in a biaxial stress state;
- (5) The use of Jones and Nelson's (1975) model in the proposed theoretical model for CFFTs leads to more accurate predictions than the use of Hahn and Tsai's (1973) model, and therefore Jones and Nelson's (1975) model is recommended for future use in the proposal theoretical model.
- (6) Jiang and Teng's (2007) model incorporating Jones and Nelson's (1975) model generally provides accurate predictions for NC- and SCEC-filled FRP tubes. However, it underestimates the axial stresses of SCC-filled FRP tubes with a diameter of 150 mm, 200 mm or 300 mm and overestimates the axial stresses of SCC-filled FRP tubes with a diameter of 400 mm. The former is due to the stronger dilation tendency of SCC-filled FRP tubes while the latter may be due to

the relatively weak confinement level the 400 mm-diameter specimens.

## 5.8 REFERENCES

- Chabib, H.E., Nehdi, M. and Naggar, M.H.E. (2005). "Behavior of SCC Confined in Short GFRP Tubes", *Cement & Concrete Composites*. Vol. 27, pp.55-64.
- Domone, P. L. (2007). "A Review of the Hardened Mechanical Properties of Self-Compacting Concrete." *Cement & Concrete Composites*. Vol. 29(1), pp.1-12.
- Fam, A.Z. and Rizkalla, S.H. (2001a). "Confinement Model for Axially Loaded Concrete Confined by Circular Fiber-Reinforced Polymer Tubes", *ACI Structural Journal*. Vol. 98(4), pp.451-461.
- Fam, A. Z., and Rizkalla, S.H. (2001b). "Behavior of Axially Loaded Concrete-Filled Circular Fiber-Reinforced Polymer Tubes", *ACI Structural Journal*. Vol. 98(3), pp.280–289.
- Fam, A. and Rizkalla, S. (2003). "Large Scale Testing and Analysis of Hybrid Concrete/Composite Tubes for Circular Beam-Column Applications", *Construction and Building Materials*. Vol. 17, pp.507-516.
- Hahn, H.T. (1973). "Nonlinear Behavior of Laminated Composites", *Journal of Composite Materials*. Vol. 7, pp.257-271.
- Hahn, H.T. and Tsai, S.W. (1973). "Nonlinear Elastic Behavior of Unidirectional Composite Laminae", *Journal of Composite Materials*. Vol. 7, pp.102-118.
- Haj-Ali, R. and Kilic, H. (2002). "Nonlinear Behavior of Pultruded FRP Composite", *Composite Part B*. Vol. 33(3), pp.173-191.
- Ishikawa, T. and Chou, T.W. (1983). "Nonlinear Behavior of Woven Fabric Composites", *Journal of Composite Materials*. Vol. 17, pp.399-413.
- Jiang, T. and Teng, J. G. (2007). "Analysis-Oriented Stress-Strain Models for FRP-Confined Concrete", *Engineering Structures*. Vol. 29(11), pp.2968-2986.

- Jones, R.M. and Nelson JR, D.A.N. (1975). “A New Material Model for the Nonlinear Biaxial Behavior of ATJ-S Graphite”, *Journal of Composite Materials*. Vol. 9, pp.10-27.
- Jones, R.M. and Morgon, H.S. (1977). “Analysis of Nonlinear Stress-Strain Behavior of Fiber-Reinforced Composite Material”, *AIAA Journal*. Vol. 15(12), pp.1669-1676.
- Jones, R.M. (1980). “Modeling Nonlinear Deformation of Carbon-Carbon Composite Materials”, *Journal of Composite Materials*. Vol. 18(8), pp.995-1001.
- Li, G.Q., Torres,S., Alaywan, W. and Abadie, C. (2010). “Experimental Study of FRP Tube-Encased Concrete Columns”, *Journal of Composites Materials*. Vol. 39(13), pp.1131-1145.
- Li, G.Q., Pang, S.S., Ibekwe, S.I. (2011). “FRP Tube Encased Rubberized Concrete Cylinders”, *Materials and Structures*. Vol. 44, pp.233-243.
- Mirmiran, A. and Shahawy, R. (1997). “Behavior of Concrete Columns Confined by Fiber Composites”, *Journal of Structural Engineering*. Vol. 5(583), pp.583-590.
- Mohamed, H.M. and Masmoudi, R. (2010). “Axial Load Capacity of Concrete-Filled FRP Tube Columns: Experimental Versus Theoretical Predictions”, *Journal of Composites for Construction*, ASCE. Vol. 14(2), pp.231-243.
- Ozbakkaloglu, T., Lim, J. C. and Vincent, T. (2013). “FRP-Confined Concrete in Circular Sections: Review and Assessment of Stress-Strain Models”, *Engineering Structures*. Vol. 49, pp.1068-1088.
- Ozbakkaloglu, T. and Oehlers, D.J. (2008). “Concrete-Filled Square and Rectangular FRP Tubes under Axial Compression”, *Journal of Composites for Construction*, ASCE. Vol. 12(4), pp.469-477.
- Park, J.H., Jo, B.W, Yoon, S.J. and Park, S.K. (2011). “Experimental Investigation on the Structural Behavior of Concrete Filled FRP Tubes with/without Steel Re-Bar”,

- KSCE *Journal of Civil Engineering*. Vol. 15(2), pp.337-345.
- Saafi, M., Toutanji, H.A. and Li, Z.J. (1999). "Behavior of Concrete Confined with Fiber-Reinforced Polymer Tubes", *ACI Material Journal*. Vol. 96(4), pp.500-509.
- Teng, J.G., Zhao, J.L., Yu, T., Li, L.J. and Guo, Y.C. (2016). "Behavior of FRP-Confined Compound Concrete Containing Recycled Concrete Lumps", *Journal of Composites for Construction*. Vol. 20(1): 04015038.
- Xia, Y.M., Yang, B.C. and Xu, Z. (1986). "Nonlinear Constitutive Relation of Unidirectional Composite Laminae", *Acta Materiae Compositae Sinica*. Vol. 3(4), pp.44-50. (in Chinese)
- Xiao, Q., Jiang, S. and Ružička, M. (2009). "Experimental Verification and Theory Analysis of Nonlinear Behavior of Filament Wound Composite Products", *Proceedings of the 3rd ICMEM, International Conference on Mechanical Engineering and Mechanics*, 21-23 Oct, 2009, Beijing, China.
- Yu, T., Fang, X.L. and Teng, J.G. (2014). "FRP-Confined Self-Compacting Concrete under Axial Compression", *Journal of Materials in Civil Engineering*. Vol. 26(11): 04014082.
- Zhang, B., Yu, T., J. G. Teng, J.G. (2015). "Behavior of Concrete-Filled FRP Tubes under Cyclic Axial Compression", *Journal of Composites for Construction*, ASCE. Vol. 19(3): 04014060.
- Zindel, D. and Bakis, Ch.E. (2011). "Nonlinear Micromechanical Model of Filament-Wound Composite Considering Fiber Undulation", *Mechanics of Composite Materials*. Vol. 47(1), pp.73-94.

**Table 5. 1 Constants in Jones and Nelson's model**

<b>Tube</b>	<b>Constants</b>	<b><math>U^*</math></b>	<b><math>A</math></b>	<b><math>B</math></b>	<b><math>C</math></b>	<b><math>E_{x,tan}^*</math> or <math>\nu_{x\theta,tan}^*</math></b>	<b><math>a</math></b>	<b><math>b</math></b>
D150	$E_{x,sec}$	0.2518	12889	0.5648	0.7188	6135	2130	0.2737
	$\nu_{x\theta,sec}$		0.1217	0.0890	0.1828	0.1125	1.0611	-0.1200
D200	$E_{x,sec}$	0.2573	14420	2.2927	2.1660	5307	2523	0.1093
	$\nu_{x\theta,sec}$		0.1195	0.2464	0.2195	0.0967	0.0049	-0.2063
D400	$E_{x,sec}$	0.2484	12450	0.1739	0.5332	5870	13926	2.2610
	$\nu_{x\theta,sec}$		0.1200	0.2346	0.2405	0.0987	0.0069	-0.1889

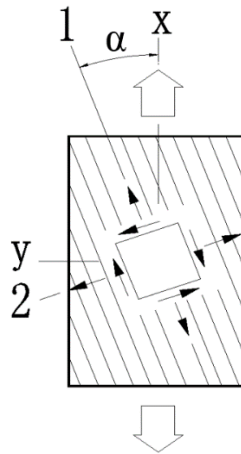
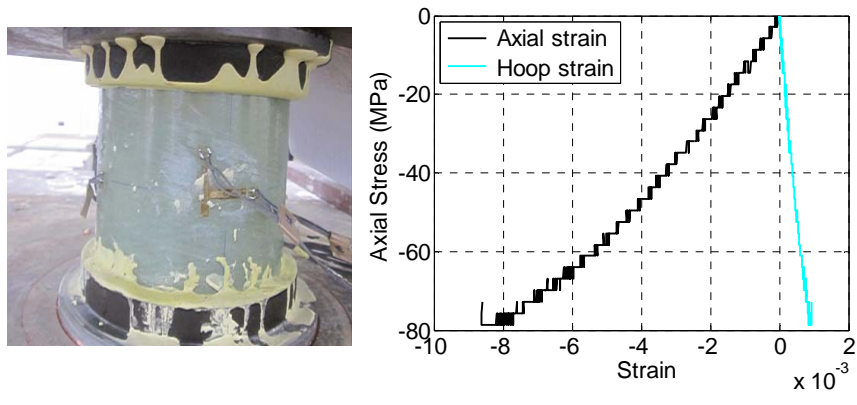
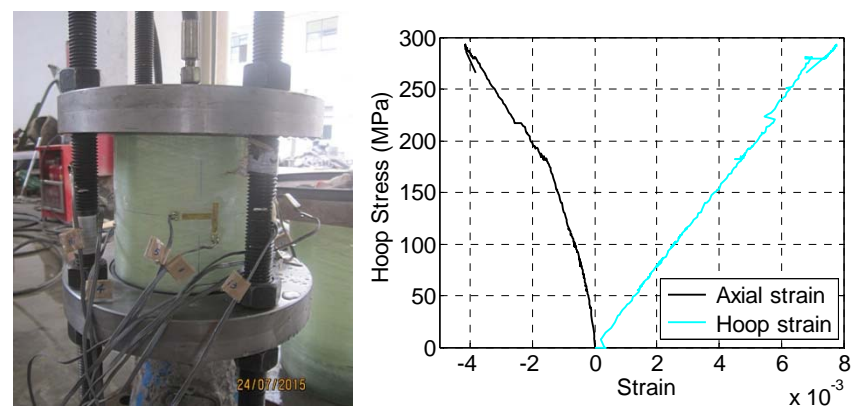


**Figure 5. 1** Principal material axes of a composite lamina



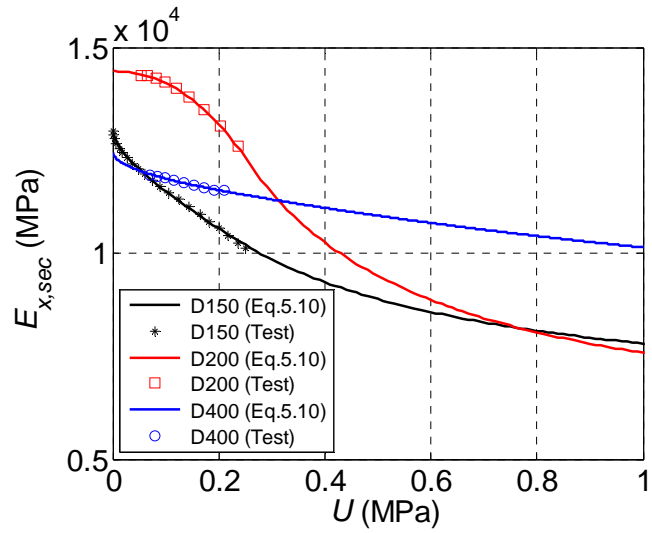
(a) Test specimen (b) Axial stress-strain curves

**Figure 5. 2** Compression test of a bare GFRP tube

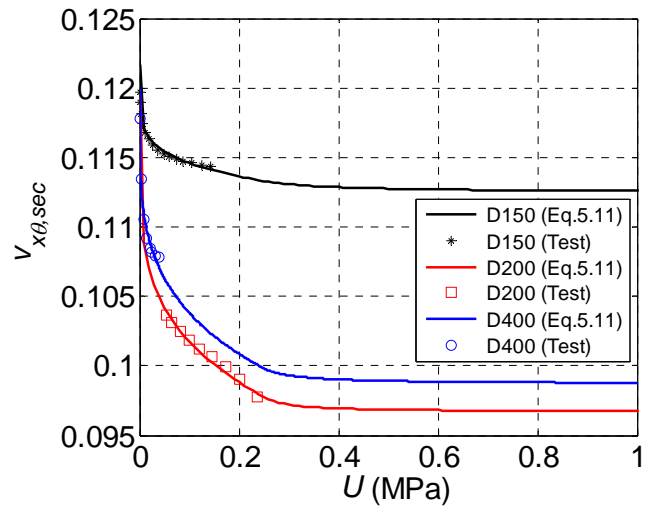


(a) Test specimen (b) Hoop stress-strain curves

**Figure 5. 3** Hydraulic test of a bare GFRP tube

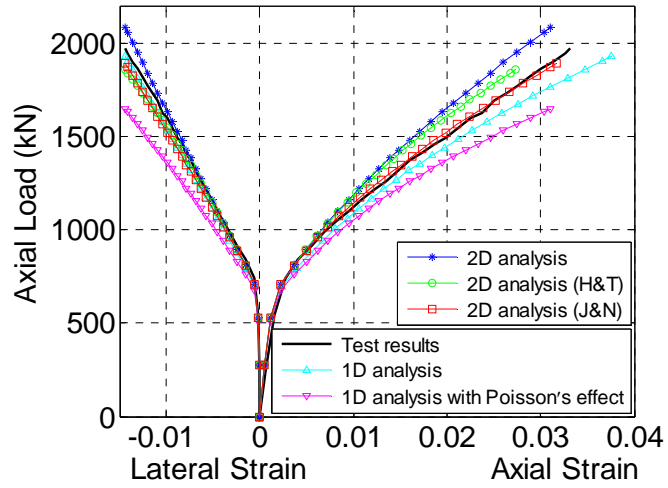


(a)  $E_{x,sec}$ -versus- $U$  curves

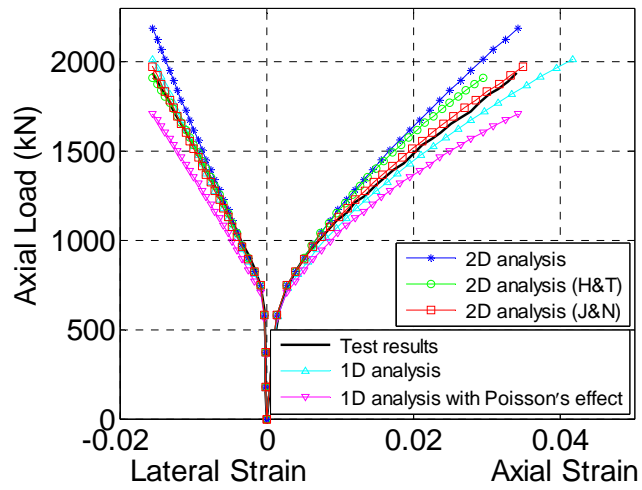


(b)  $\nu_{x\theta,sec}$ -versus- $U$  curves

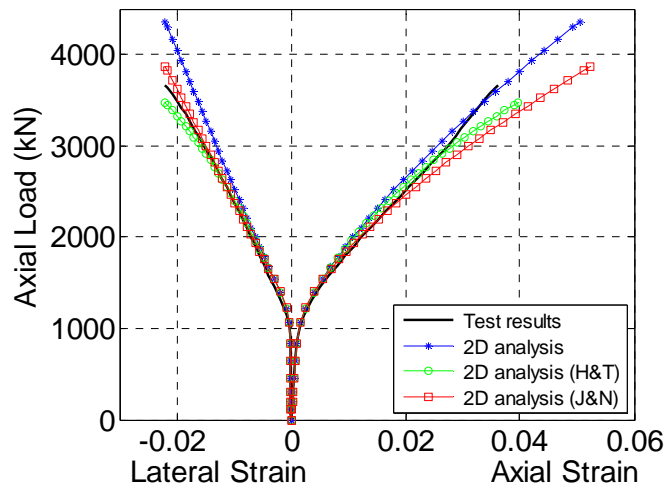
**Figure 5. 4** Material property-versus-strain energy density curves



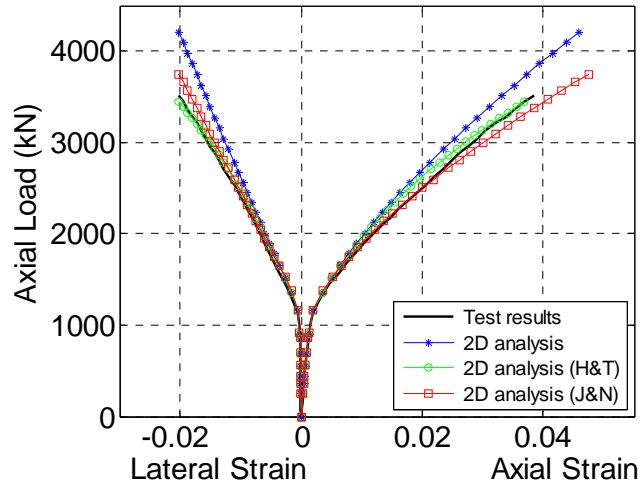
(a) Specimen N-2-150-I



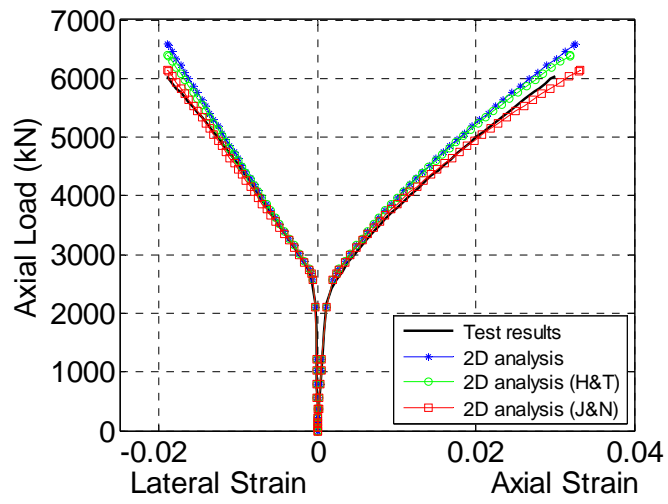
(b) Specimen N-2-150-II



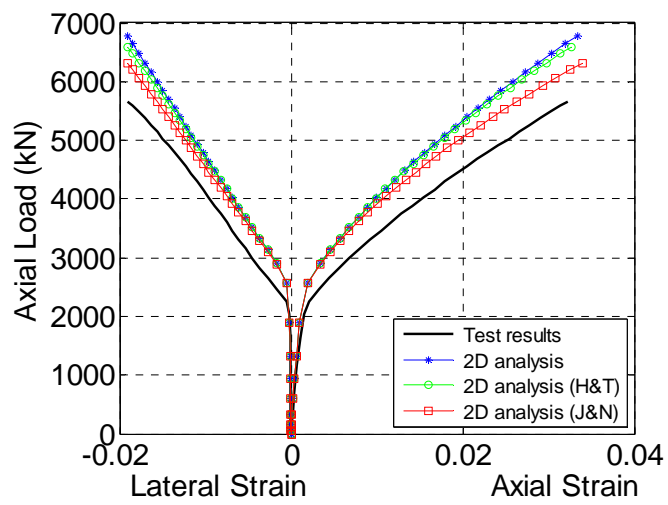
(c) Specimen N-1-200-I



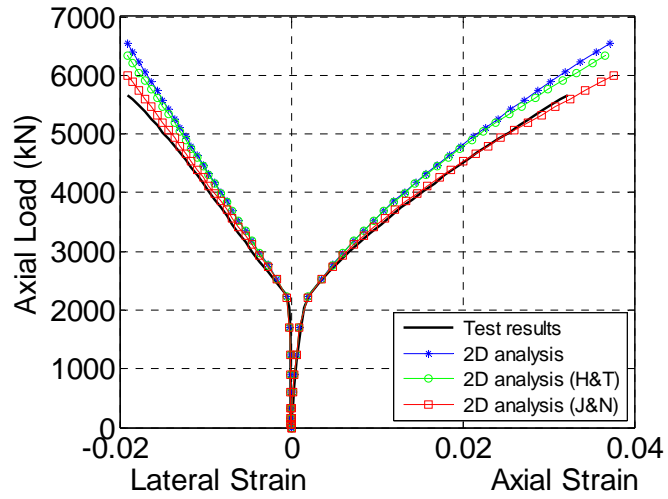
(d) Specimen N-1-200-II



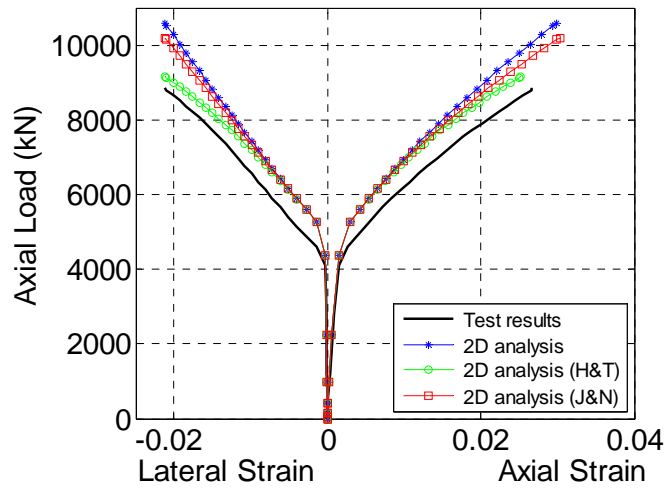
(e) Specimen N-1-300-I



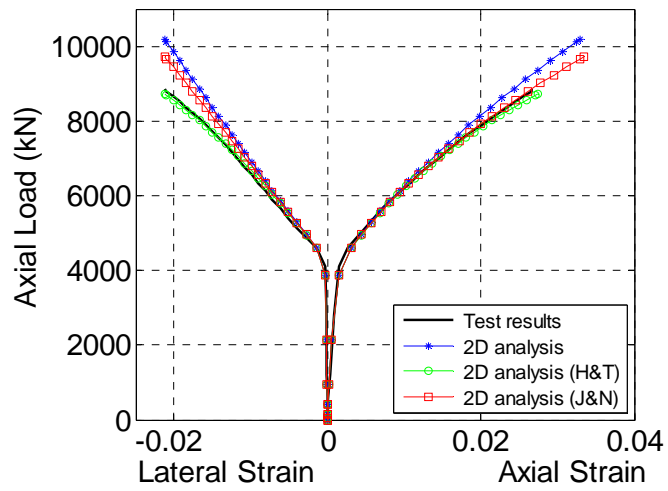
(f) Specimen N-1-300-II



(g) Specimen N-1-300-II (unconfined concrete strength being reduced)



(h) Specimen N-2-400-I



(i) Specimen N-2-400-I (unconfined concrete strength being reduced)

**Figure 5.5** Comparison of Axial load-strain curves of NC-filled FRP tube specimens

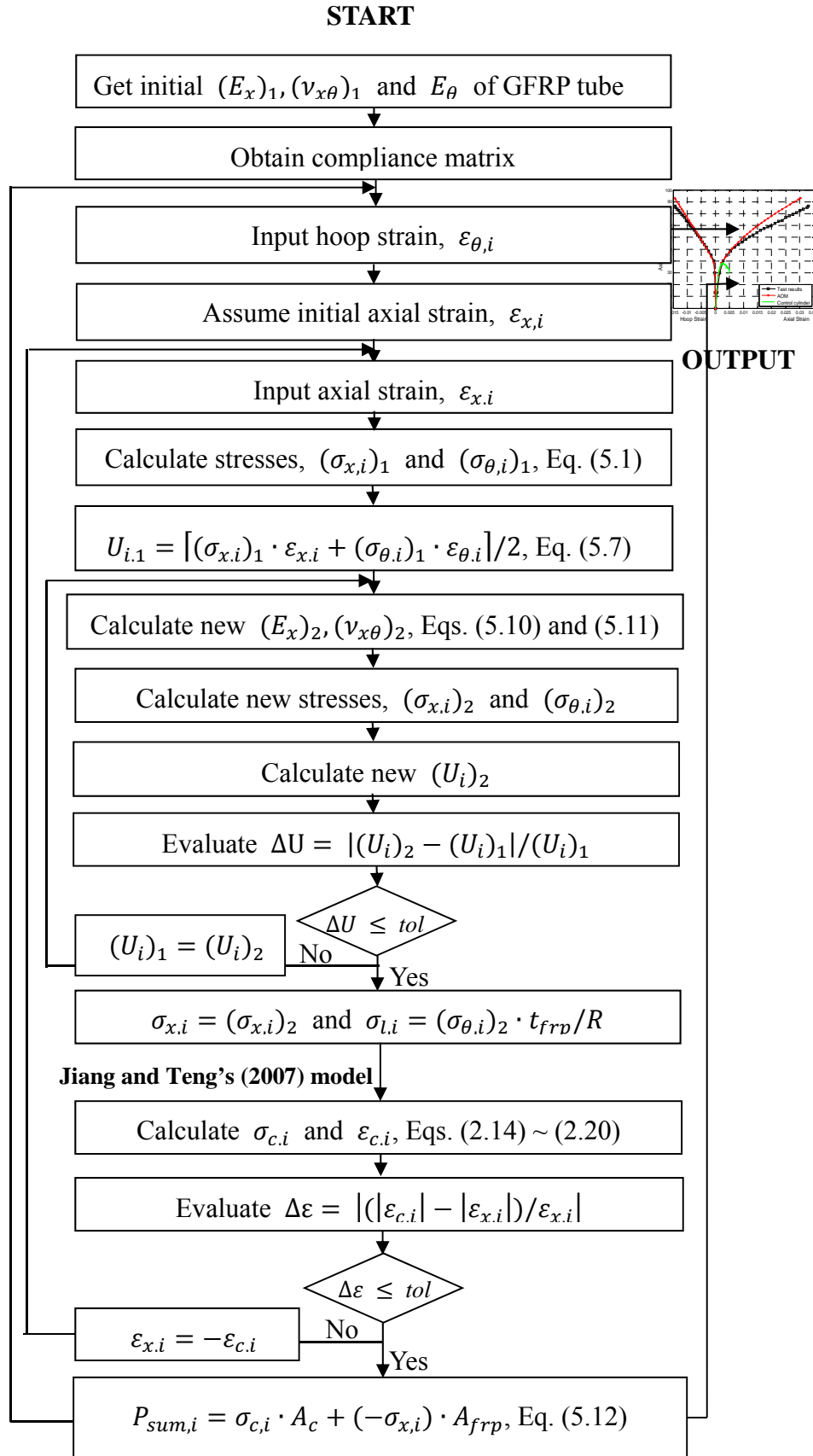


**Figure 5. 6** Flowchart of generation of axial load-strain curves of CFFTs considering nonlinear biaxial tube behavior based on Jones and Nelson's (1975) model

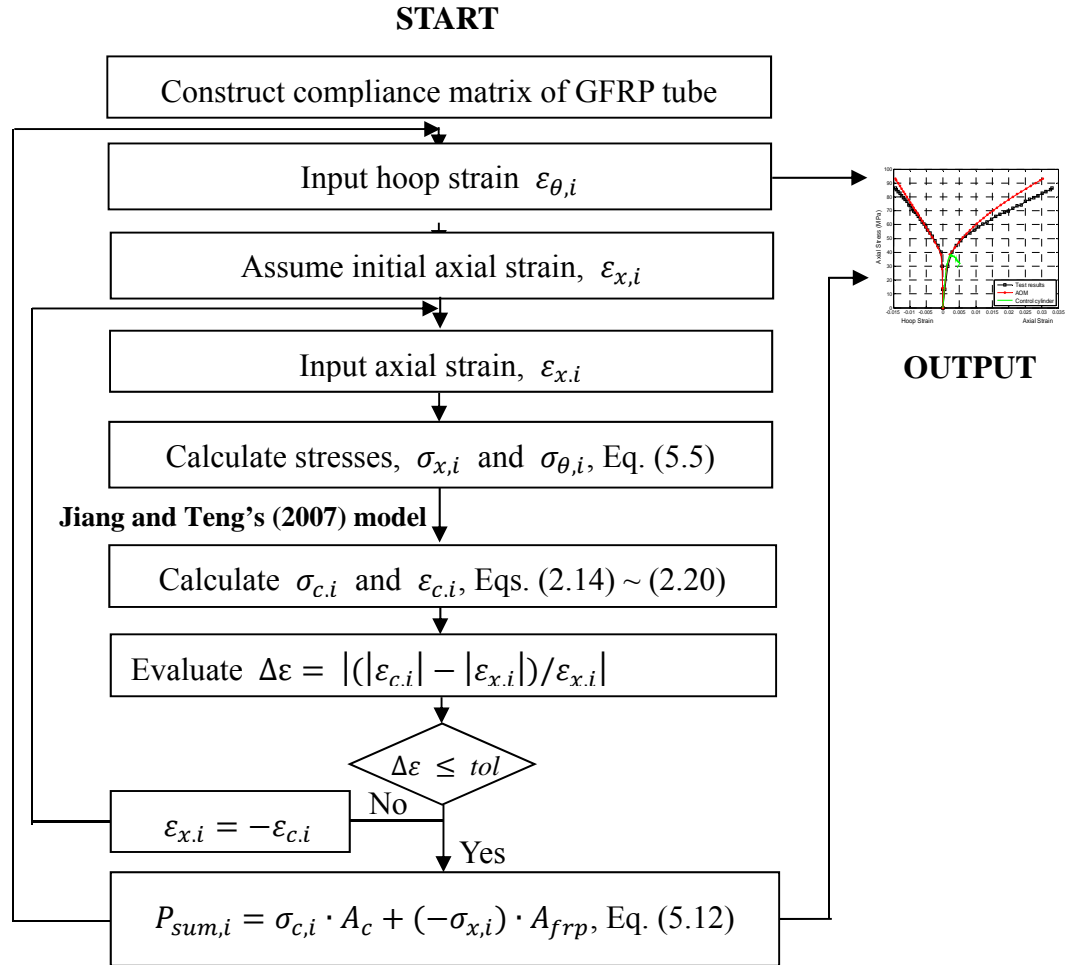
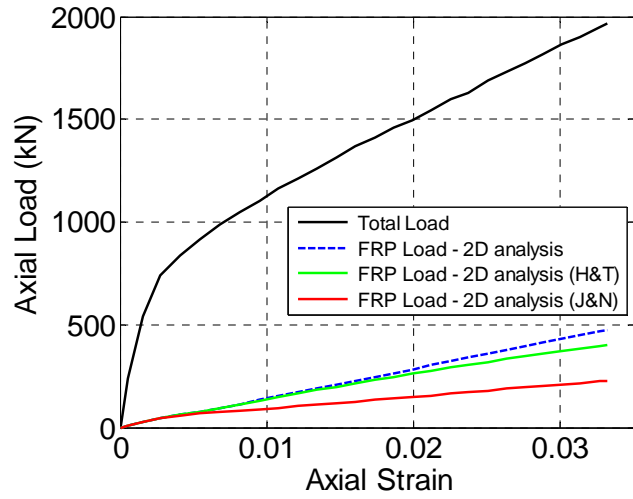
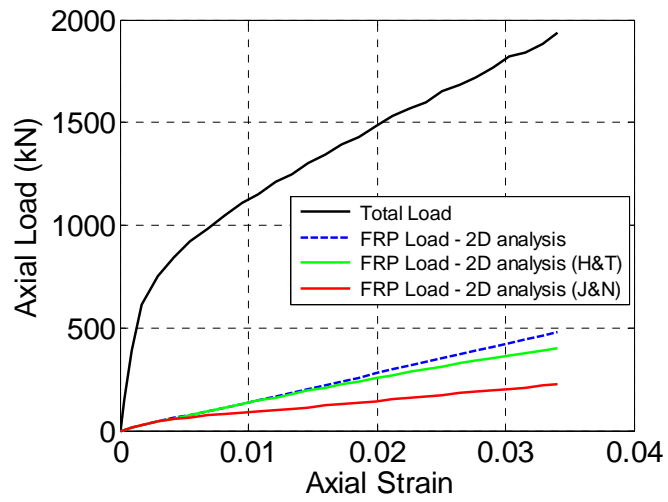


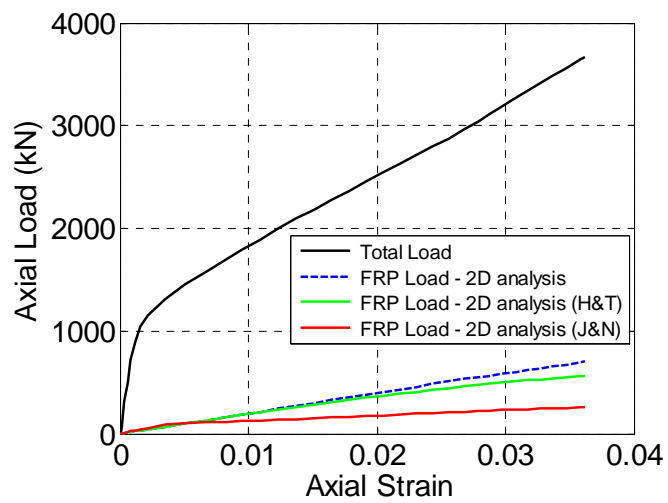
**Figure 5. 7** Flowchart of generation of axial load-strain curves of CFFTs considering nonlinear biaxial tube behavior based on Hahn and Tsai's (1973) model



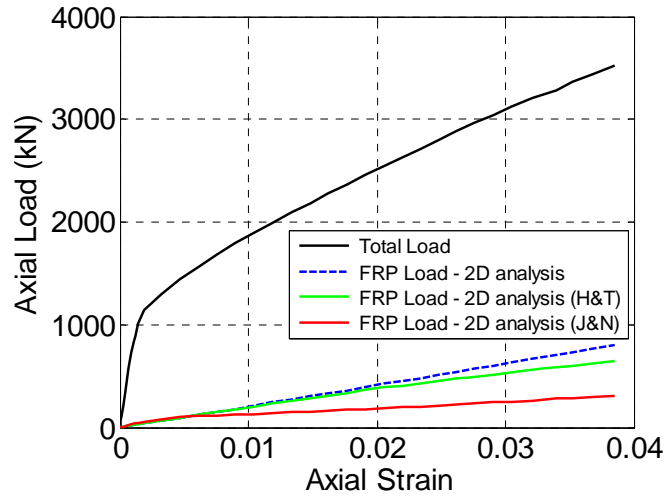
(a) N-2-150-I



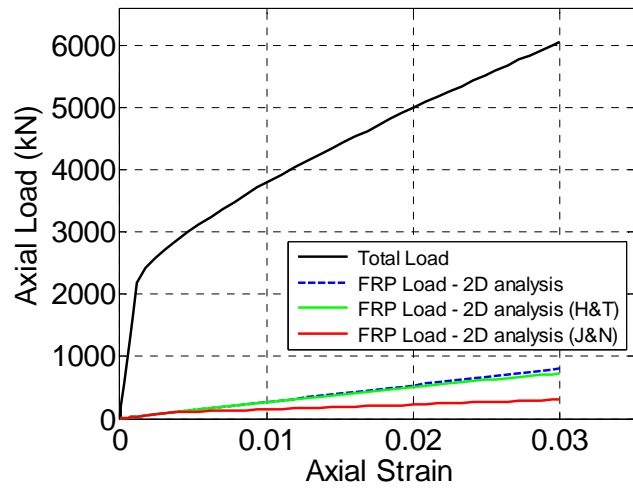
(b) N-2-150-II



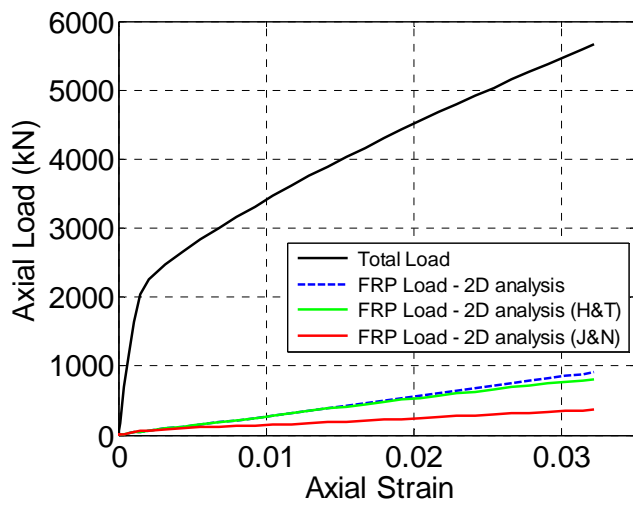
(c) N-1-200-I



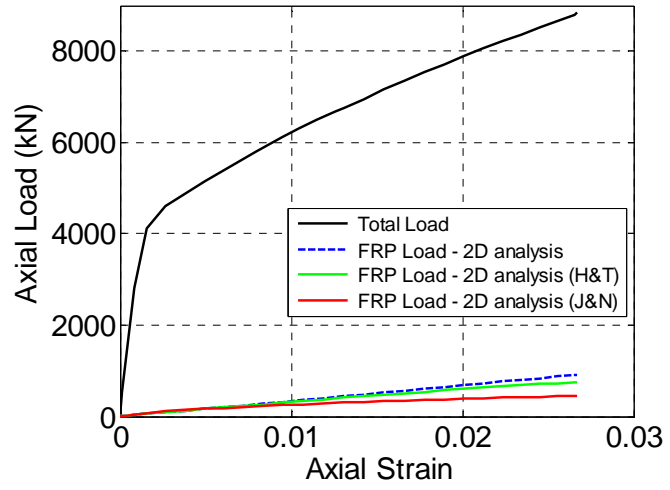
(d) N-1-200-II



(e) N-1-300-I

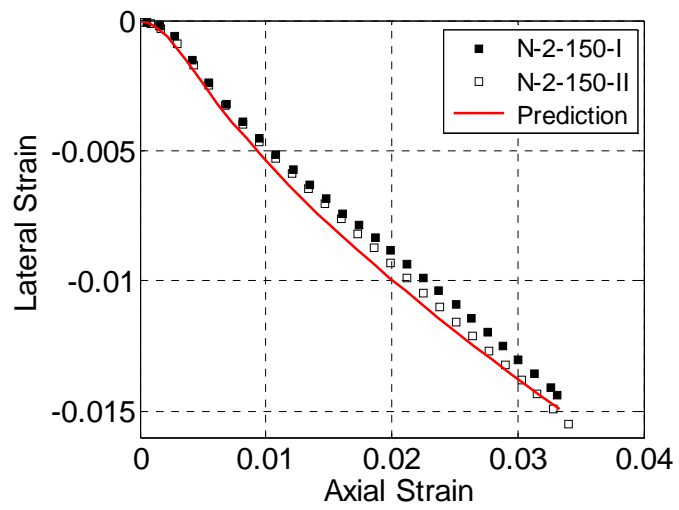
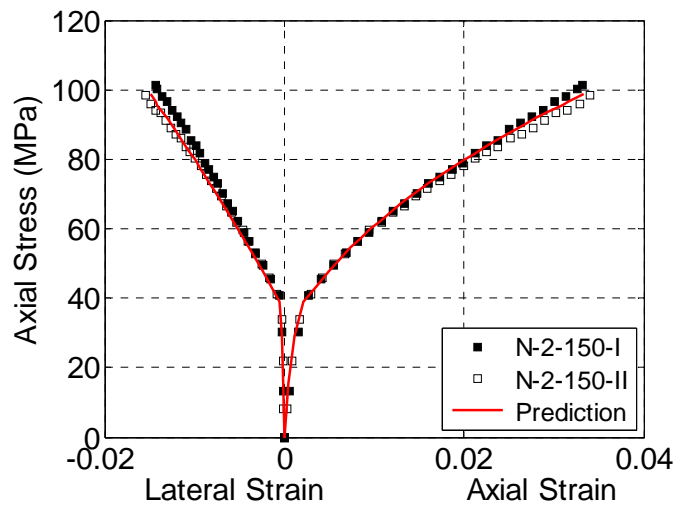


(f) N-1-300-II

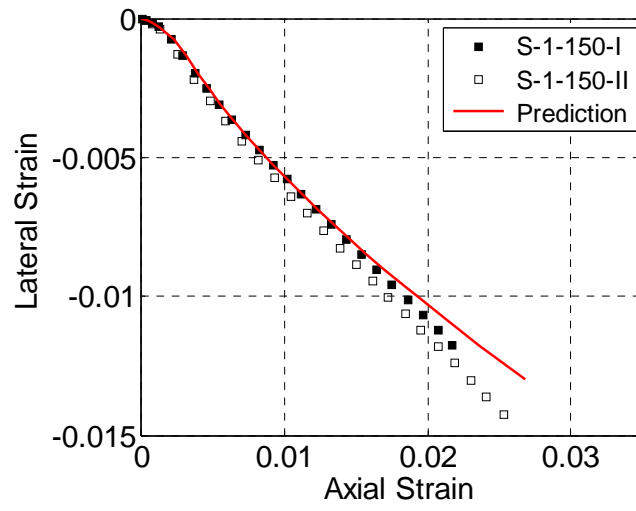
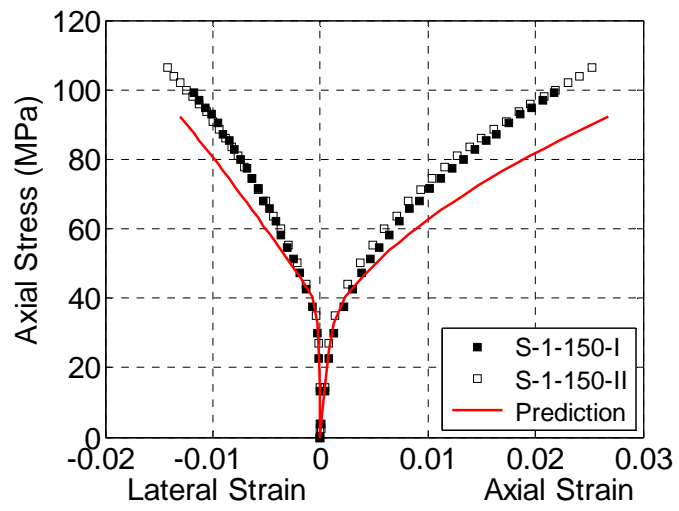


(g) N-2-400-I

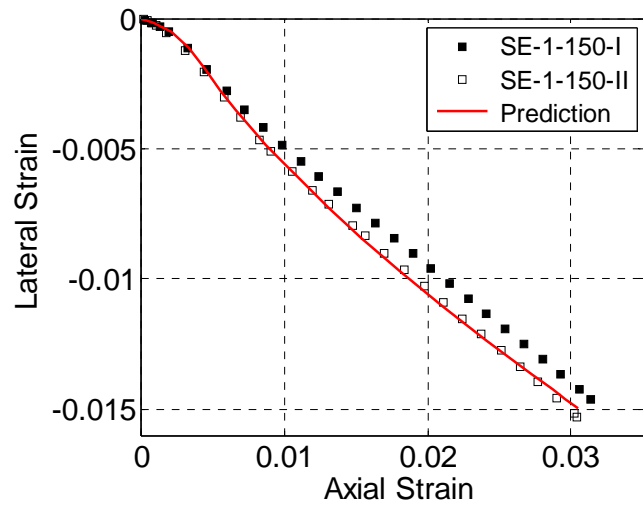
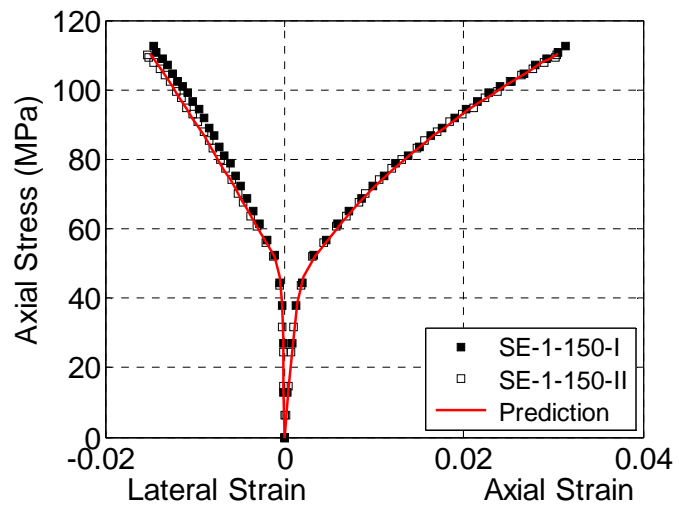
**Figure 5. 8** Contribution of FRP tube to total axial load



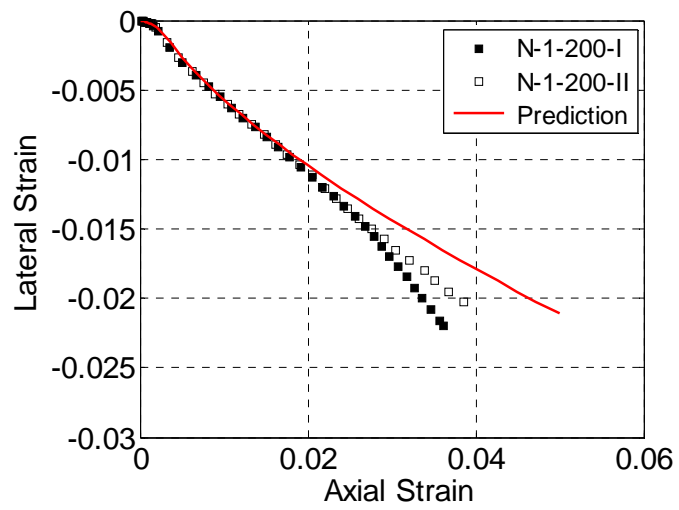
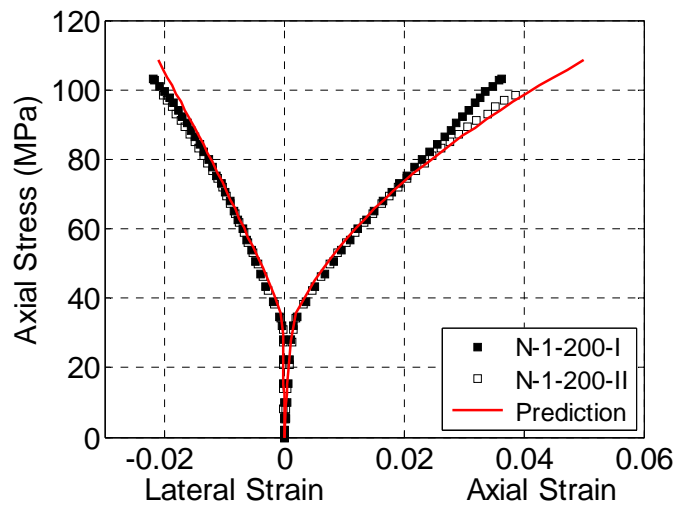
(a) Specimens N-2-150-I and N-2-150-II



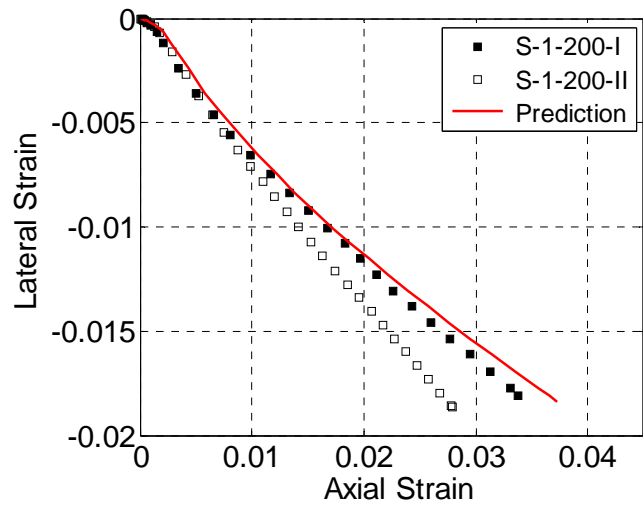
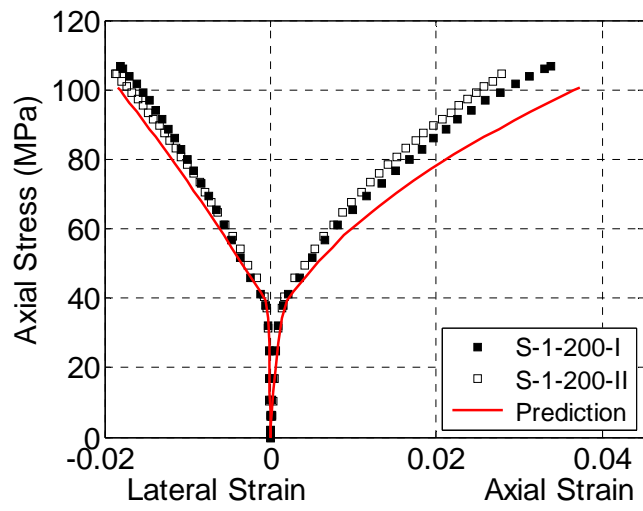
(b) Specimens S-1-150-I and S-1-150-II



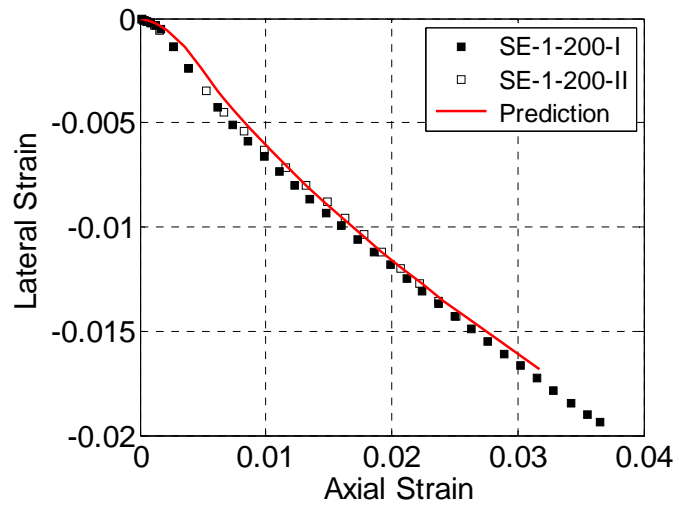
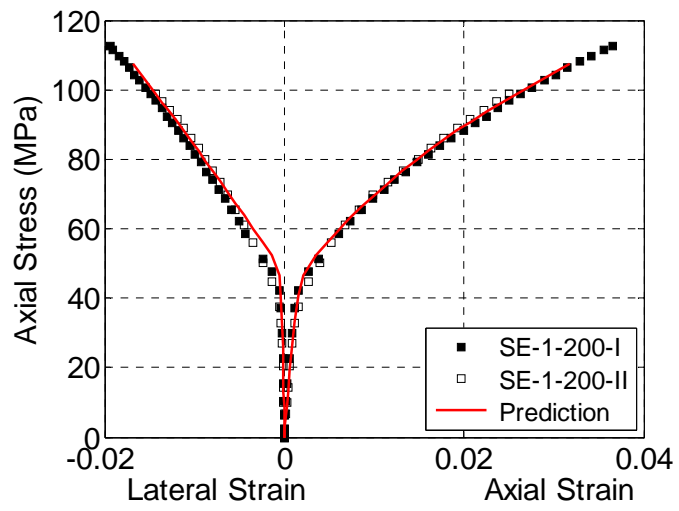
(c) Specimens SE-1-150-I and SE-1-150-II



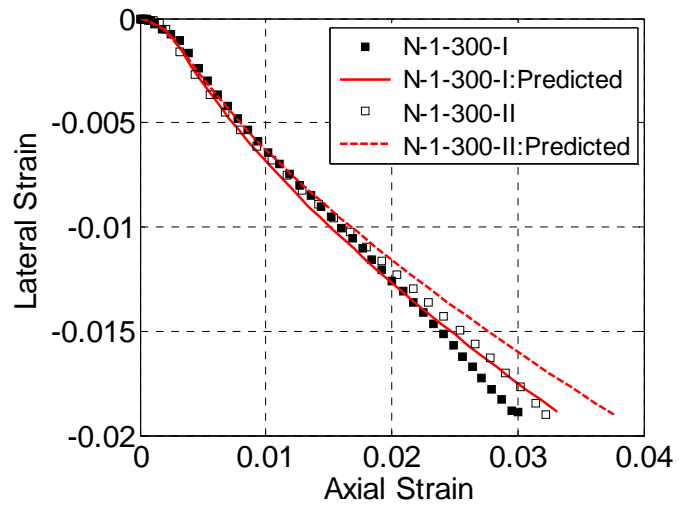
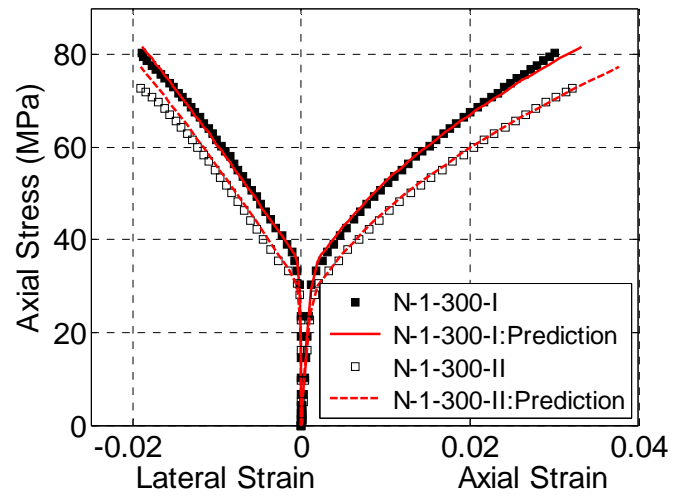
(d) Specimens N-1-200-I and N-1-200-II



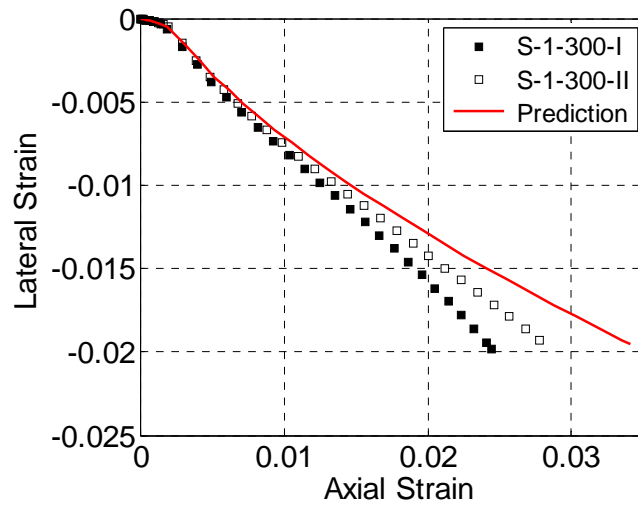
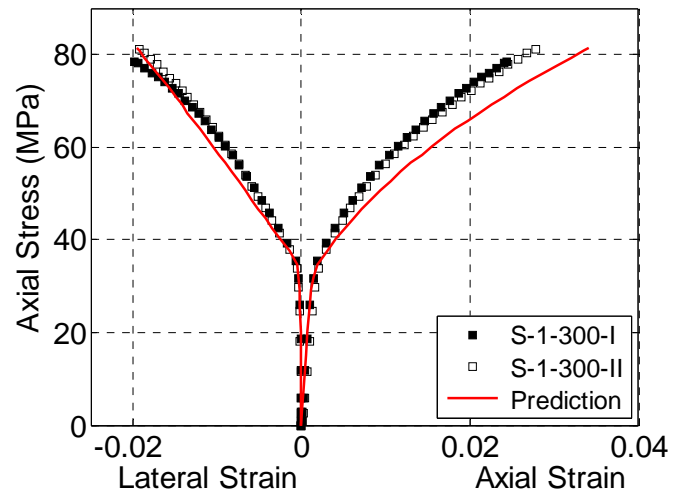
(e) Specimens S-1-200-I and S-1-200-II



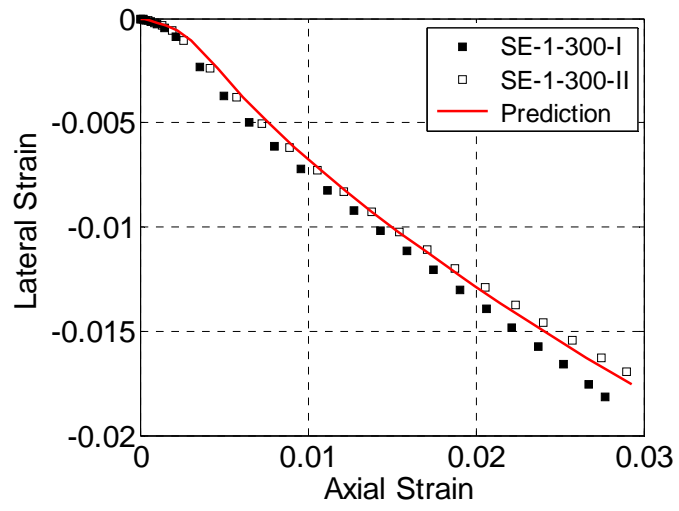
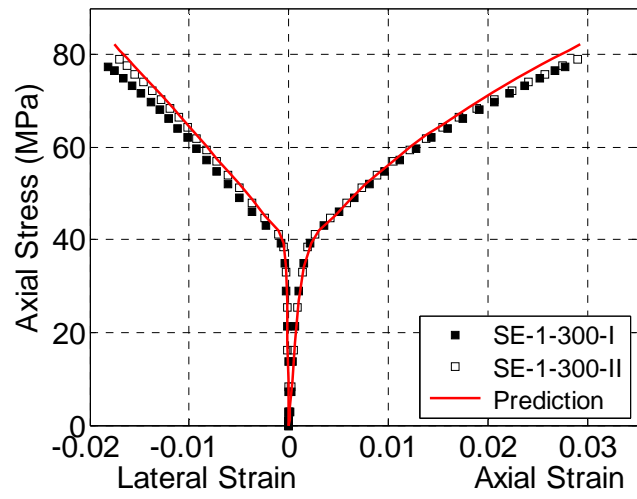
(f) Specimens SE-1-200-I and SE-1-200-II



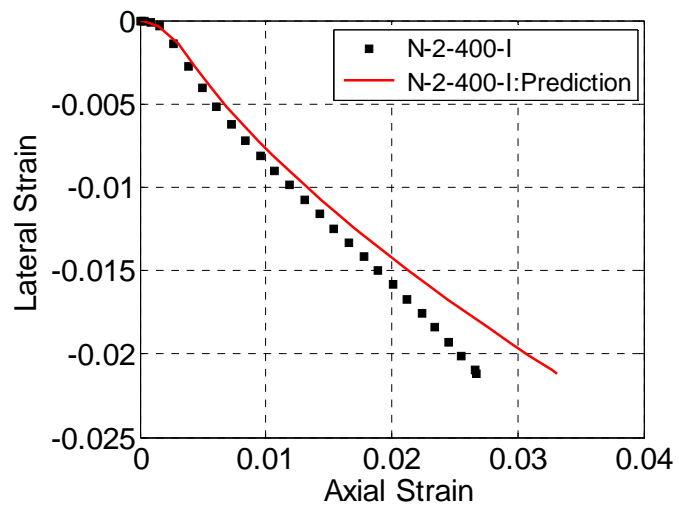
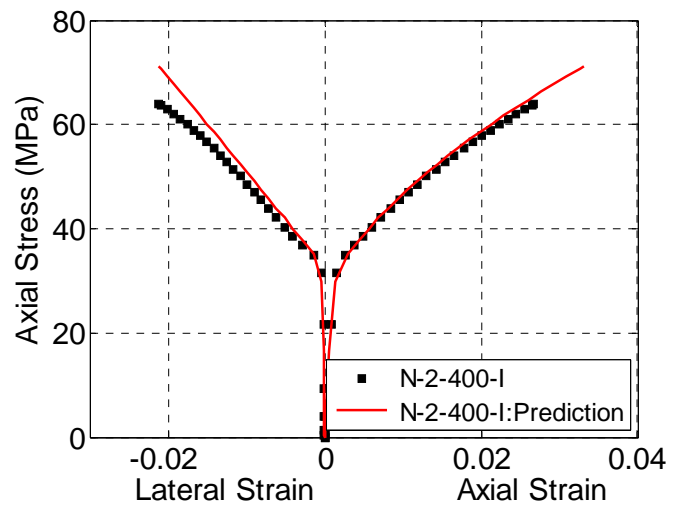
(g) Specimens N-1-300-I and N-1-300-II



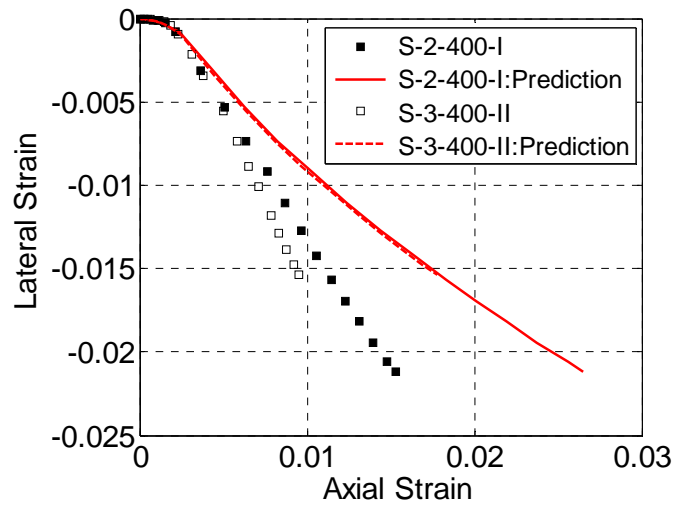
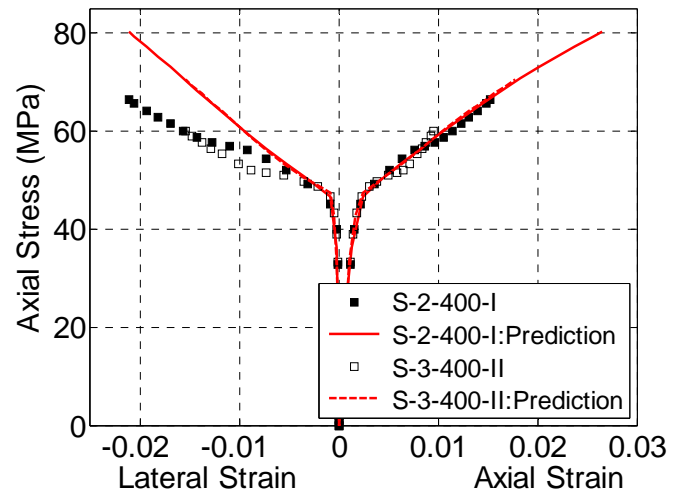
(h) Specimens S-1-300-I and S-1-300-II



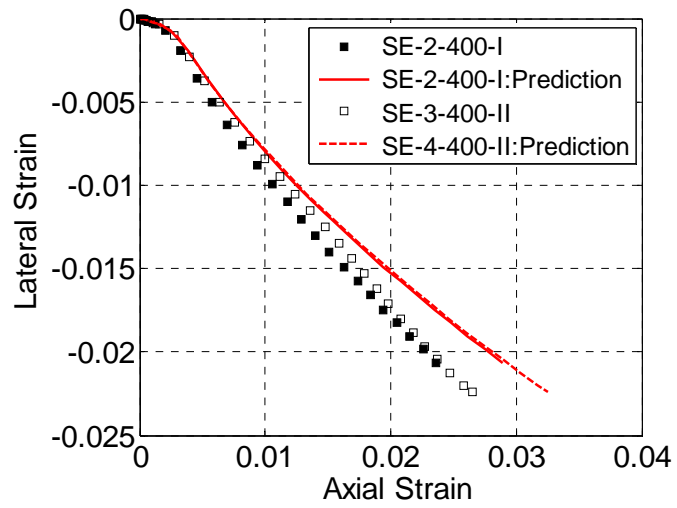
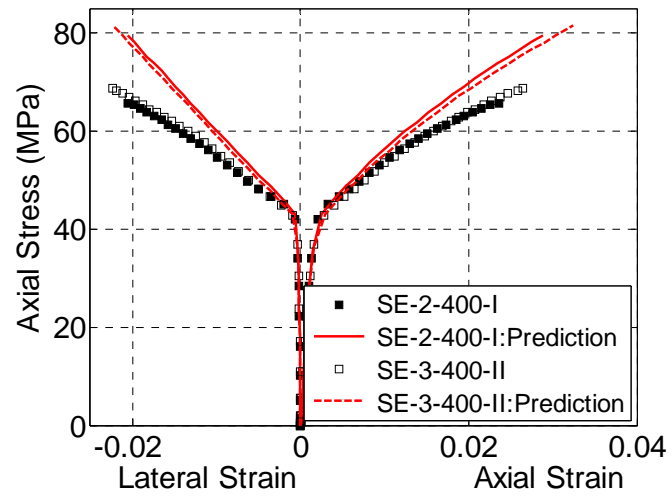
(i) Specimens SE-1-300-I and SE-1-300-II



(j) Specimens N-2-400-I



(k) Specimens S-2-400-I and S-3-400-II



(l) Specimens SE-2-400-I and SE-3-400-II

**Figure 5. 9** Performance of Jiang and Teng's (2007) model

## CHAPTER 6

# LARGE-SCALE HYBRID DSTCS SUBJECTED TO CONCENTRIC COMPRESSION

### 6.1 INTRODUCTION

Hybrid DSTCs are a new form of hybrid columns developed at the Hong Kong Polytechnic University (PolyU) and it possess many important advantages over conventional structural members, including the excellent corrosion resistance as well as excellent ductility (Teng *et al.* 2004, 2007). A large amount of experimental research has been conducted on hybrid DSTCs to study their axial compression behavior at PolyU (e.g., Teng *et al.* 2007; Yu 2007; Wong *et al.* 2008; Xie *et al.* 2011; Zhang *et al.* 2011, 2014, 2017; Yu and Teng 2013) and elsewhere (e.g., Qian and Liu 2006, 2008; Wang *et al.* 2011, 2012; Fanggi and Ozbakkaloglu 2013, 2015a, 2015b; Ozbakkaloglu and Fanggi 2014, 2015; Hu and Yao 2016; Yu *et al.* 2017; Zhou *et al.* 2017; Cao *et al.* 2017).

As reviewed in Chapter 2, existing studies have confirmed the excellent structural performance of hybrid DSTCs under axial compression. Nevertheless, these studies are subjected to a number of deficiencies. First, these studies have been limited to small-scale specimens with a diameter less than 200 mm; the only exception is Zhang *et al.* (2017) in which the specimens had a diameter of 300 mm. For the confident use of hybrid DSTCs in practice, axial compression tests on large-scale hybrid DSTCs are urgently needed. Second, although SCC is attractive for use as the infill in the relatively thin concrete layer of hybrid DSTCs due to its segregation resistance and excellent flowability, few studies have investigated the use of SCC in hybrid DSTCs (Cao *et al.* 2017). Finally, hybrid DSTCs are intended for use in new construction, so

the use of prefabricated FRP tubes, preferably filament-wound FRP tubes because of their automated manufacture process, would be predominant in practice as they can serve as stay-in-place formwork. However, in some studies, the inner steel tube and the surrounding annular concrete are first made and FRP wraps are then applied along the hoop direction via a wet-layup process to form the outer tube (post-applied FRP wraps). It should be noted that when post-applied wraps are used, the formation of an initial gap between the concrete and the FRP wraps due to shrinkage of concrete (especially when SCC is used) is much less likely because the wraps are applied after the hardening of concrete and interfacial adhesive bonding exists between the concrete and the FRP wraps.

Against this background, this chapter presents a test program on large-scale hybrid DSTCs under axial compression aimed to address the above deficiencies. A comparison was also made between the test results and the predictions of Yu *et al.*'s (2010a) design-oriented stress-strain model for confined concrete in hybrid DSTCs.

## **6.2 EXPERIMENTAL PROGRAM**

### **6.2.1 Specimen Details**

In total, 11 hybrid DSTC specimens were tested. The specimens all had a nominal outer diameter of 400 mm (excluding the FRP tube) and a height of 800 mm. Detailed geometric and material properties of the specimens are summarized in Table 6.1. It should be noted that the dimensions of FRP tubes and steel tubes in Table 6.1 are the actual measured values which slightly differ from the nominal values. The specimens were fabricated in three series. In Series 1, the outer FRP tubes were formed by wet-layup wrapping of uni-directional glass fiber sheets around hardened concrete in the

hoop direction (i.e., post-applied wraps) while those used for Series 2 and 3 were prefabricated filament-wound FRP tubes with a winding angle of  $\pm 80^\circ$  with respect to the tube axis. The major difference between Series 2 and 3 is the type of concrete being NC or SCC. Each series of specimens covered two void ratios (i.e., ratio of the inner diameter to the outer diameter of the annular concrete section) (0.61 and 0.81) and two different thicknesses of FRP tubes (4 and 6 plies of fibers). The only exception is that Series 3 covered three void ratios (0.55, 0.61 and 0.81) as this series contained an additional specimen (CC219-6-P6S), which was originally designed to serve as a reference for eccentrically-loaded slender hybrid DSTCs with the same test configurations except slenderness. However, an outer diameter of 300 mm instead of 400 mm was finally adopted in the tests on slender hybrid DSTCs (see Chapter 8) as otherwise the length of the slender hybrid DSTCs would exceed the maximum allowable length of the testing machine. It should be noted that the diameter-to-thickness ratio of steel tube  $D_{o,s}/t_s$  and the void ratio  $\phi$  in Table 6.1 are based on the nominal geometric values. The cross section of hybrid DSTCs with a void ratio of 0.61 and 0.81 are shown in Figures 6.1 (a) and (b), respectively.

Each specimen is given a name which starts with two letters “CC” to indicate the loading condition of concentric compression, followed by a three-digit number (i.e., 219, 245 or 325) and a number (i.e., 6, 8, 9 or 10) to respectively represent the nominal outer diameter and nominal thickness of the inner steel tube in millimeter, and then a letter “W” or “P” to indicate the form of FRP tube (W for post-applied wraps and P for prefabricated filament-wound FRP tubes) and together with a number (i.e., 4 or 6) to represent the number of fiber plies, and ends with a letter “N” or “S” to differentiate specimens filled with NC or SCC.

## 6.2.2 Material Properties

### 6.2.2.1 Properties of GFRP tubes

The GFRP wraps used in Series 1 had a tensile strength of 1825.5 MPa and a modulus of elasticity of 80.1 GPa (Table 6.1) according to the results of six tensile coupon tests conducted by Teng *et al.* (2007) on the same type of GFRP. The tensile strength and the modulus of elasticity were both based on a nominal thickness of 0.17 mm per ply. The axial stiffness of the wraps was ignored as the fibers were oriented in the hoop direction only. For convenience of presentation and discussion, Series 1 is also referred to as Series W hereafter. The mechanical properties of the filament-wound GFRP tubes used in Series 2 and 3 were obtained from axial compression bare tube tests and hydraulic pressure tests presented in Chapter 3 and are also summarized in Table 6.1. Series 2 and 3 are also referred to as Series P as a whole hereafter.

### 6.2.2.2 Properties of concrete

The specimens of Series 1 and 2 were cast in five batches of concrete with the same mix proportion and the same maximum aggregate size of 10 mm while commercial SCC was used for Series 3. Three plain concrete cylinders (150 mm × 300 mm) were tested for each batch of concrete to determine their material properties, including the modulus of elasticity ( $E_c$ ), the peak stress ( $f'_{co}$ ) (i.e., the control cylinder compressive strength) and the axial strain at peak stress ( $\epsilon_{co}$ ), as given in Table 6.1.

### 6.2.2.3 Properties of steel tubes

Tension tests on three steel coupons were conducted for each type of steel tubes. The coupons were cut along the longitudinal direction of the steel tubes and were tested

following BS 18 (1987). The average values of the modulus of elasticity ( $E_s$ ), yield strength ( $f_y$ ), and tensile strength ( $f_u$ ) for each type of steel tubes are also listed in Table 6.1.

In addition, two bare steel tubes belonging to the same batch of tubes used in the hybrid DSTC specimens were tested under axial compression (Figure 6.2). The bare steel tube specimens had the same height as those in the hybrid DSTC specimens (i.e., 800 mm). All these steel tubes showed large plastic deformation until local buckling occurred in the elephant's foot mode, as shown in Figure 6.2. Four bi-directional strain gauges with a gauge length of 10 mm were attached at the mid-height of steel tube and four LVDTs were used to measure the axial shortening of the whole tube.

Two axial stress-axial strain curves of the bare steel tubes with an outer diameter of 325 mm and a thickness of 10 mm, in which the axial strains were respectively averaged from the readings of four strain gauges and four LVDTs, are displayed in Figure 6.3. It is evident that the axial strain from LVDTs is larger than that from strain gauges at a given axial load mainly due to the occurrence of local deformation near the two ends and local buckling of the steel tubes.

### **6.2.3 Specimen Preparation**

The most important step of specimen construction was to fix up the outer GFRP tube and the inner steel tube on a wooden platform using four vertical screws and keep uniform distances between the two tubes using four horizontal screws. For Series W, an outer GFRP tube and an inner steel tube were used as formwork to cast the annular concrete. After the concrete hardened, the GFRP tube was demolded and the specimen was applied with continuous FRP wraps via a wet-layup process. The starting end of

the FRP wraps overlapped with the finishing end by a length of approximately 100 mm. To prevent premature local failure, the region near the top and the bottom ends of each specimen was strengthened with an additional CFRP strip 60 mm in width.

#### **6.2.4 Test Setup and Instrumentation**

The layout of the strain gauges is shown in Figure 6.4. For Series W, four bi-directional strain rosettes (SR1 to SR4, for measuring axial and hoop strains) and four unidirectional strain gauges (SG9 to SG12, for measuring hoop strains), all with a gauge length of 20 mm, were installed at the mid-height of the FRP tube. Eight unidirectional strain gauges with a gauge length of 5 mm were attached at the mid-height of the inner steel tube, among which four (SG1 to SG4) were installed for measuring axial strains while the other four (SG5 to SG8) were for measuring hoop strains. At the same time, ten LVDTs in three groups were respectively employed to measure the axial deformation of the whole column (LT 9 to LT10), that of the 320-mm middle region (LT1 to LT4), and that of the 120-mm middle region [LT5 to LT8) in Figure 6.4 (a)]. The differences between Series P and Series W are that four bi-directional strain rosettes (SR1 to SR4) with a gauge length of 10mm displaced eight unidirectional strain gauges [SG1 to SG 8 in Figure 6.4 (a)], and four LVDTs covering the 120 mm middle region (LT5 to LT8) were cancelled as shown in Figure 6.4(b).

Concentric compression tests were carried out using a 10,000 kN servo-hydraulic testing machine with displacement control at a constant rate of 0.48 mm/minute as shown in Figure 6.5. All test data, including strains, loads, and displacements, were recorded simultaneously by a data logger.

## 6.3 TEST RESULTS AND DISCUSSIONS

### 6.3.1 Test Observations

Similar to the small-scale specimens tested by Wong *et al.* (2008), all large-scale concentrically-loaded hybrid DSTCs failed by the rupture of the FRP tube as a result of hoop tension and crushing of concrete. All specimens after test are shown in Figure 6.6. For Series P, white patches were observed on the FRP tubes in later loading stages. In contrast, no white patches were observed in specimens of Series W until failure due to the firm bonding between the FRP wraps and the concrete. Series 1 and 2 failed with drastic rupture of fiber accompanied with loud explosion, whereas Series 3 experienced a relatively mild failure process with a more narrow rupture area. For all the specimens, global buckling of the inner steel tube featuring a continuous concave-convex shape can be observed in Figure 6.7 instead of local buckling with ripples which occurred in the axial compression tests on small-scale hybrid DSTCs by Wong *et al.* (2008).

### 6.3.2 Axial Strain

There are four ways to interpret the axial strain for Series 1: (1) the average reading of the four axial strain gauges with a length of 20 mm attached at the mid-height of column (Figure 6.4); (2) and (3) the average reading of the four LVDTs covering 120-mm and 320-mm middle region respectively where the former was adopted by Wong *et al.* (2008) as the gauge length for their 305 mm tall hybrid DSTCs and the latter was proportionally magnified according to the height of specimens in the present tests (800 mm); (4) the average reading of the two LVDTs over the whole height of the specimen. Figure 6.8 displays the axial load-axial strain curves of Specimen CC325-9-W6N obtained in the above four ways to clarify the effect of the gauge length on the

measured axial strain. In the initial stage of loading, axial strains obtained in the first three ways are close to each other while the axial strain representing the overall axial shortening of columns is the largest due to the development of localized deformation near the two ends of specimen. After the unconfined concrete strength was reached, the axial strain from LVDTs covering 320-mm middle region became the largest, indicating that the localized deformation occurred outside of the 120-mm middle region. Therefore, the axial strain from LVDTs covering 320-mm middle region was considered more representative of the strain state of concrete and was adopted in the remainder of this chapter.

### **6.3.3 Hoop Rupture Strain**

The hoop strain distributions at ultimate condition (i.e., when the FRP tube ruptured and the ultimate axial strain was reached) found from the readings of the hoop strain gauges attached at the mid-height of specimens are shown in Figure 6.9. The solid points close to each of distribution lines represent the corresponding values of average hoop rupture strain. For Series W, strain gauge readings in the overlapping zone were excluded.

Except Specimen CC325-9-W4N whose hoop rupture strain is much smaller due to premature failure caused by a defect arising from the preparation of the specimen, it is evident that the average hoop rupture strains of Series W are larger than those of Series P because of the intimate contact between the concrete and the FRP wraps. Additionally, for the specimens with 6 plies of fibers, those with a smaller void ratio failed at a higher average hoop rupture strain. This phenomenon is opposite to the observation in small-scale hybrid DSTC tests reported by Ozbakkaloglu and Fanggi (2014) and Cao *et al.* (2017), where the specimens all had a diameter of about 150 mm

and were confined with wet-layup FRP tubes. This may be attributed to the thicker annular concrete generally featuring more uniform hoop strain distribution for large-scale specimens. Except Specimen CC219-6-P6S, the scatter in the hoop rupture strain appears to be less pronounced for hybrid DSTCs with a smaller void ratio due to the thicker annular concrete when confined with the same FRP tube. For specimens with the same test configurations but a different FRP tube thickness, the average hoop rupture strain and its scatter generally increase with increasing tube thickness (number of fiber plies) with the only exception being the companion pair of Specimens CC325-8-P4S and CC325-8-P6S. Another noteworthy point is that Specimen CC245-8-P6S had a much smaller average hoop rupture strain than CC245-8-P6N although the two specimens had similar test configurations. The major difference between the two specimens is the type of concrete used, so it is believed that this phenomenon is attributed to the less uniform dilation of SCC which caused the premature rupture of FRP.

#### **6.3.4 Total Axial Load-Axial Strain Curves**

The total axial load-axial strain curves of all hybrid DSTC specimens are shown in Figure 6.10. It is evident that significant differences exist between the curves of Series 1, 2 and 3. So the curves of the three series are discussed separately below.

For Series 1, the total axial load-axial strain curves of large-scale hybrid DSTCs with NC and post-applied FRP wraps typically have a bilinear shape and terminate at a large ultimate axial strain, similar to those found from tests on small-scale hybrid DSTCs (Wong *et al.*, 2008). The axial load of Specimen CC325-9-W4N terminated at a relatively small value caused by a defect mentioned earlier. The slope of the second linear portion of the curve is seen to increase significantly with the thickness of the

FRP tube, but the void ratio does not appear to affect this slope significantly.

For Series 2 in which the hybrid DSTCs were made with NC and a filament-wound FRP tube, the total axial load-axial strain curves also exhibit the monotonically ascending shape, but the second linear portion of the curves appears more curvilinear than that observed for Series 1.

Of interest is that for Series 3, the axial load reached a peak value and then suddenly dropped due to the local damage of concrete. After this stage, the axial load gradually rose again and might terminate at a value lower than the previous peak load. This phenomenon was also observed in axial compression tests on hybrid DSTCs with high-strength concrete (HSC) in the tests conducted by Fanggi and Ozbakkaloglu (2013), Ozbakkaloglu and Fanggi (2014), and Zhang *et al.* (2017) where prefabricated FRP tubes were used. They attributed this to the brittle nature of HSC. For Series 3, however, the SCC used only had a compressive strength of 49.24 MPa, not high enough to be categorized as HSC. It is believed that the drop of the axial load in the present tests was attributed to a gap between the annular concrete and the wall of the outer FRP tube due to the large shrinkage of SCC. It should be noted that HSC also generally has a larger shrinkage than normal concrete as it generally has higher amount of cementitious materials. The axial load only started to rise again until the gap was closed by the accelerated concrete dilation after reaching the compressive strength of unconfined concrete. In other words, the activation of the confinement action is postponed. In contrast to the present test results, the same phenomenon was not observed in Cao *et al.*'s (2017) axial compression tests on small-scale hybrid DSTCs though SCC and prefabricated FRP tubes were also used. This is probably because the confinement level in Cao *et al.*'s (2017) tests was high enough to prevent the axial load

drop from occurring.

To better understand the different behavior of the three series of specimens, the development of axial and hoop strains of steel tube and FRP tube of three representative specimens, one from each series, with the same steel tube and the same number of fiber plies (i.e., Specimens CC245-8-W6N, CC245-8-P6N and CC245-8-P6S) is shown and compared in Figure 6.11. The axial strains of FRP tube were averaged from the readings of four LVDTs while other strains were all found from the corresponding strain gauges (see Figure 6.4). For Series 3 [e.g., CC245-8-P6S, see Figure 6.11 (c)], when the sudden load drop occurred, the axial and hoop strain of FRP tube became quite unstable compared with specimens of Series 1 and 2 [e.g., CC245-8-W6N and CC245-8-P6N, see Figure 6.11 (a) and (b)]. This indicates that when SCC in hybrid DSTCs is crushed, their lateral expansion and axial deformation are highly non-uniform due to the high shrinkage. The pronounced non-uniform deformation of SCC caused the local damage of specimens with an axial load drop. At the same time, the steel tube was heavily loaded for maintaining the balance of the whole loading system. So the readings of the four axial strain gauges installed on the surface of steel tube deviated from each other, as can be observed in Figure 6.11(c). For hybrid DSTCs of Series 1, the instability of strains of steel tube was the slightest, because they were hardly affected by the shrinkage of concrete as a result of use of post-applied FRP wraps [see Figure 6.11(a)].

To further study the behavior of concrete in hybrid DSTCs under axial compression, the load carried by concrete is derived from the total load of specimens, as shown in Figure 6.12. For Series P, the total axial load is assumed to be equal to the sum of load resisted by the three constituent materials (i.e., the outer FRP tube, the inner steel tube

and the annular concrete). The nonlinearity of FRP tube was taken into account based on Jones and Nelson's (1975) model presented in Chapter 5. For Series W, the contribution of FRP tube to axial load was ignored due to its small axial stiffness as the FRP tube was formed with uni-directional fiber sheets wrapped in the hoop direction only, so the load undertaken by concrete was assumed to be equal to the difference between resistances of hybrid DSTC specimen and steel tube. The axial load resisted by steel tube was respectively found from the axial load-axial strain curves of the corresponding bare tubes subjected to axial compression at the same axial strain. Note that the axial strain of steel tube was averaged from the readings of four strain gauges installed at the mid-height of steel tube along the longitudinal direction. For Series 1, there were no available axial load-axial strain curves of bare steel tubes with a diameter of 325 mm, so the modified curve of 245-mm diameter bare steel tubes accounting for the small difference in the geometric properties of the tube was used in the analysis of Specimens CC325-9-W4N and CC325-9-W6N.

Of interest is that, for Specimen CC325-10-P4N, the axial load carried by concrete experienced a drop in the transition zone between the two approximately linear portions of axial load-axial strain curve although the total axial load-axial strain curve keeps monotonically increasing. This is because in this specimen the axial load resisted by the concrete was much smaller than that resisted by the steel tube due to the large void ratio, the weak confinement level and the large thickness of steel tube. As a result, the axial load drop of the concrete was compensated by the continuously increasing axial load of the steel tube.

### **6.3.5 Key Test Results**

The key test results of all eleven specimens are summarized in Table 6.2. In this table,

$P_{total}$  is the axial load of a hybrid DSTC from test at ultimate condition (i.e., when the FRP tube ruptured and the ultimate axial strain was reached),  $P_s$  and  $P_{frp}$  are respectively the axial load carried by the inner steel tube and the outer GFRP tube when  $P_{total}$  is reached,  $P_c$  is the axial load resisted by concrete which is equal to the difference between  $P_{total}$  and the sum of  $P_s$  and  $P_{frp}$ .  $P_{co}$  is equal to the unconfined concrete strength times the area of the annular concrete section, and  $(P_{co} + P_s + P_{frp})$  represents the axial load of the hybrid DSTC at ultimate condition if the constituent parts do not interact and the confinement effect of the FRP tube is ignored. It is worth noting that for Specimen CC325-8-P4S, the axial load at ultimate condition is lower than the first peak load because of the sudden load drop in the transition zone of the axial load-axial strain curves. Additionally, for Specimens CC245-8-P6S and CC325-8-P6S, the first peak load is slightly smaller than the axial load at ultimate condition, but the axial load resisted by concrete corresponding to the former is larger than that corresponding to the latter. For these specimens, the bracketed numbers in Table 6.2 refer to the values at the first peak load. Other key test results listed in Table 6.2 include the ultimate axial strain ( $\epsilon_{cu}$ ), the hoop rupture strain of FRP tube ( $\epsilon_{h,rup}$ ) and the corresponding hoop stress of FRP tube ( $\sigma_{\theta u}$ ). For specimens of Series P, the hoop stress of FRP tube at ultimate condition was calculated according to the measured hoop rupture strain of FRP tube and the ultimate axial strain with the nonlinear tube behavior presented in Chapter 5 being taken into account. The nominal hoop rupture strain of the filament-wound FRP tubes ( $\epsilon'_{h,rup}$ ) can then be obtained by dividing the hoop stress of FRP tube at ultimate condition by the hoop modulus of elasticity of FRP tube (i.e.,  $\epsilon'_{h,rup} = \sigma_{\theta u}/E_{\theta}$ ) and was used in the subsequent theoretical analyses.

For Specimen CC325-9-W4N, the much smaller axial load  $P_c$  at ultimate condition

and the much smaller ultimate axial strain  $\varepsilon_{cu}$  (see Table 6.2) were partially caused by an unexpected premature failure of FRP tube as a result of a specimen defect. It is evident that the use of SCC, larger void ratio or lower confinement level has an adverse effect on the load bearing capacity of hybrid DSTCs. For example, the axial load of Specimens CC325-10-P4N, CC245-8-P6S, CC325-8-P4S and CC325-8-P6S at ultimate condition are almost comparable to the simple addition of loads undertaken by unconfined concrete, inner steel tube and outer FRP tube. Especially for Specimen CC325-8-P4S, as shown in Table 6.2,  $P_{total}/(P_{co} + P_s + P_{frp})$  is less than 1.0 due to the resultant from the three aforementioned factors. This issue was also discussed by Wong *et al.* (2008). On the contrary, for Specimen CC219-6-P6S, the thicker annular concrete and the more substantial level of lateral confinement led to the relatively larger enhancement factor in the axial load at ultimate condition, 1.18, though the value evidently has been reduced by the effect of SCC whose large shrinkage resulted in the suddenly drop in the transition region of axial load-axial strain curve as shown in Figure 6.10(h). For Specimen CC325-9-W6N, the relatively low enhancement factor, 1.14, can be attributed to the overestimation of axial load carried by steel tube. The enhancement factor in the axial load of other specimens at ultimate condition (i.e., CC245-8-W6N, CC245-8-P4N, CC245-8-P6N and CC325-10-P6N) is up to about 20%. At the same time, as expected, the ultimate axial strain was greatly increased (by up to around 250% to 1111%) for all specimens, indicating the significant beneficial effect arising from the interaction of the three components in a hybrid DSTC. It should be noted that the hoop rupture strain of the FRP tubes (0.00658 to 0.0154) are significantly smaller than those found from small-scale hybrid DSTC tests [ranging from 0.017 to 0.019, see Wong *et al.* (2008)]. The premature rupture of FRP may be due to greater non-uniformity in the lateral expansion of concrete for a large-scale column.

### 6.3.6 Axial Stress-Axial Strain Behavior of Concrete in Hybrid DSTCs

The normalized axial stress-strain curves of the concrete in all hybrid DSTCs are shown in Figures 6.13 to 6.15. The axial stress of the concrete is defined as the load carried by the annular concrete section divided by its cross-sectional area. The axial stress and axial strain are normalized by the unconfined concrete strength  $f'_{co}$  and the corresponding compressive strain  $\epsilon_{co}$ , respectively.

#### 6.3.6.1 Effects of type of concrete and FRP tube

The effects of type of concrete and FRP tubes on the behavior of concrete in hybrid DSTCs are investigated in Figure 6.13. The curves of specimens with the same number of FRP plies and the same void ratio are grouped together for comparison. It is evident that Series 1 with post-applied FRP tubes and NC have a relatively smooth curve featuring an approximately bilinear shape due to the intimate interfacial contact between concrete and the wall of FRP tube. For Series 3 with filament-wound FRP tubes and SCC, however, a sudden drop in the axial stress occurred led by the large shrinkage of SCC. For Series 2 with filament-wound FRP tubes and NC, Specimens CC245-8-P4N, CC245-8-P6N and CC325-10-P6N have a smooth curve, but the second portion of curve does not exhibit clear linearity. It is believed that the axial strain averaged from the readings of LVDTs attached on the external surface of FRP tube underestimated the axial strain state of concrete due to the deformation incompatibility between FRP tubes and concrete. The same issue was reported by Lim and Ozbakkaloglu (2014) and Teng *et al.* (2016). To some extent, the deformation incompatibility was caused by the shrinkage of NC. The effect of shrinkage of NC in hybrid DSTCs can be proved by the stress-strain behavior of Specimen CC325-10-P4N, which was filled with NC and also experienced a sudden drop in axial stress as

all hybrid DSTC specimens filled with SCC, because the influence of shrinkage of NC emerged under the combination of a limited confinement level and a large void ratio.

#### *6.3.6.2 Effect of number of fiber layers*

Figure 6.14 presents the stress-strain response of hybrid DSTCs with a different number of fiber layers. It is evident that an increase in the number of fiber layers leads to an increase of strength and ductility of hybrid DSTCs when the other parameters are the same. In general terms, the second branch of the stress-strain curves of concrete becomes stiffer with the increase of number of fiber layers (Lam and Teng 2003; Teng *et al.* 2009; Wong *et al.* 2008; Yu *et al.* 2010a), even for small-scale hybrid DSTCs with SCC (Cao *et al.* 2017). But large-scale hybrid DSTCs with SCC are more likely to experience a load drop caused by the large shrinkage of SCC, and thus the effect of number of fiber layers on the slope of the second linear portion appears not so significant. [e.g., comparing Specimens CC325-8-P4S and CC325-8-P6S in Figure 6.15 (d)].

#### *6.3.6.3 Effect of void ratio*

The effect of void ratio is shown in Figure 6.15. Based on the test results of small-scale hybrid DSTCs with NC, Wong *et al.* (2008) reported that a larger void ratio generally results in a stiffer second linear portion in the stress-strain curve of the annular concrete. This is however inconsistent with the observations about the axial compression tests on small-scale hybrid DSTCs conducted by Cao *et al.* (2017). In the present tests on large-scale hybrid DSTCs, the effect of void ratio on the slope of second linear portion appears not significant. Additionally, except Specimen CC219-6-P6S, specimens of Series P with a larger void ratio had a larger axial strain enhancement ratio than their counterparts. This is consistent with the observations in

Wong *et al.*'s (2008) tests. Specimen CC219-6-P6S had the largest axial strain enhancement ratio in Series 3 due to the fact that the detrimental effect of the smallest void ratio was compensated by the beneficial effect of the largest hoop rupture strain. On the other hand, according to Tsai-Wu failure criterion (Daniel and Ishai 2006), for a composite lamina under a biaxial state of compression-tension, a larger compressive stress will cause a smaller tensile stress at ultimate condition. So Specimens CC325-10-P4N, CC325-10-P6N and CC325-8-P6S had a lower hoop stress of FRP tube at ultimate condition ( $\sigma_{\theta u}$ ) than their counterparts due to their larger axial stress as a result of larger axial strain (see Table 6.2).

## **6.4 COMPARISON WITH A STRESS-STRAIN MODEL**

In this section, the experimental axial stress-axial strain curves of concrete in hybrid DSTCs are compared with those predicted by the stress-strain model proposed by Yu *et al.* (2010a).

### **6.4.1 Yu *et al.*'s (2010a) Model for Hybrid DSTCs**

On the basis of an FE model (Yu *et al.* 2010 b, c) validated by experimental results of hybrid DSTCs under axial compression (Wong *et al.* 2008), Yu *et al.* (2010a) conducted a parametric study on the stiffness of the FRP tube, the stiffness of the steel tube, and the size of the inner void and developed a design-oriented stress-strain model for concrete in hybrid DSTCs. The model was modified from the design-oriented model proposed by Teng *et al.* (2009) for FRP-confined concrete. Teng *et al.*'s (2009) model has two versions, differentiated by the second linear portion of a stress-strain curve being represented by a horizontal line (Version I) or descending line (Version II) in situation of insufficient confinement. Yu *et al.* (2010a) adopted Version I with a modification to reflect the effect of void ratio on the ultimate axial strain of concrete

in hybrid DSTCs. Teng *et al.*'s (2009) model consisting of a parabolic first portion and linear second portion is described as follows

$$\sigma_c = E_c \varepsilon_c - \frac{(E_c - E_2)^2}{4f'_{co}} \varepsilon_c^2 \quad \text{for } 0 \leq \varepsilon_c < \varepsilon_t \quad (6.1)$$

and

$$\sigma_c = f'_{co} + E_2 \varepsilon_c \quad \text{for } \varepsilon_t \leq \varepsilon_c \leq \varepsilon_{cu} \quad (6.2)$$

where  $\sigma_c$  and  $\varepsilon_c$  are axial stress and axial strain of confined concrete respectively;  $E_c$  is modulus of elasticity of unconfined concrete cylinder compressive strength;  $f'_{co}$  is the compressive strength of unconfined concrete;  $\varepsilon_{cu}$  is the ultimate axial strain of confined concrete.  $\varepsilon_t$  is the axial strain at the smooth transition point where the linear first portion connect with the parabolic first portion given by:

$$\varepsilon_t = \frac{2f'_{co}}{(E_c - E_2)} \quad (6.3)$$

$E_2$  is slope of the linear second portion given by

$$E_2 = \frac{f'_{cc} - f'_{co}}{\varepsilon_{cu}} \quad (6.4)$$

where  $f'_{cc}$  is compressive strength of confined concrete.

The ultimate axial strain ( $\varepsilon_{cu}$ ) and compressive strength ( $f'_{cc}$ ) of FRP-confined concrete are predicted using the following equations:

$$\frac{f'_{cc}}{f'_{co}} = \begin{cases} 1 + 3.5(\rho_k - 0.01)\rho_\varepsilon & \text{if } \rho_k \geq 0.01 \\ 1 & \text{if } \rho_k < 0.01 \end{cases} \quad (6.5)$$

$$\frac{\varepsilon_{cu}}{\varepsilon_{co}} = 1.75 + 6.5\rho_K^{0.8}\rho_\varepsilon^{1.45} \quad (6.6)$$

where  $\rho_k$  and  $\rho_\varepsilon$  are respectively the confinement stiffness ratio and the strain ratio and given by

$$\rho_K = \frac{E_{frp}t_{frp}}{E_{seco}R} \quad (6.7)$$

$$\rho_\varepsilon = \frac{\varepsilon_{h,rup}}{\varepsilon_{co}} \quad (6.8)$$

where  $E_{frp}$  and  $t_{frp}$  are modulus of elasticity in hoop direction and thickness of FRP tube;  $R$  is the radius of the confined concrete core;  $E_{seco}$  is secant modulus of unconfined concrete, with  $E_{seco} = f'_{co}/\varepsilon_{co}$ ; and,  $\varepsilon_{co}$  is the axial strain corresponding to cylinder compressive strength, respectively.

Considering the effect of void ratio on the ultimate axial strain of concrete in hybrid DSTCs ( $\phi$ ), Yu *et al.* (2010a) modified Eq. (6.6) as follows

$$\frac{\varepsilon_{cu}}{\varepsilon_{co}} = 1.75 + 6.5\rho_K^{0.8}\rho_\varepsilon^{1.45}(1 - \phi)^{-0.22} \quad (6.9)$$

It should be noted that when calculating  $\rho_K$  in Eq. (6.9),  $R$  in Eq. (6.7) should be replaced by the outer radius of the annular concrete section ( $R_o$ ).

#### 6.4.2 Comparison with Yu *et al.*'s (2010a) model

The comparisons between test results and predictions of Yu. *et al.*'s (2010a) model are shown in Figure 6.16. It should be noted that for specimens of Series P, the nominal FRP hoop rupture strain ( $\epsilon'_{h,rupt}$ ) was used in Eq. (6.8) to produce the predicted curves. For Specimens of Series 1, Yu *et al.*'s (2010a) model provides close predictions for the test results of Specimen CC245-8-W6N, but is in appreciable error for the other two specimens (i.e., Specimens CC325-9-W4N and CC325-9-W6N). The error may be led by the fact that the load carried by steel tube was obtained from the modified test results of bare steel tube with a diameter of 245 mm. For Specimens CC245-8-P4N, CC245-8-P6N and CC325-10-P6N of Series 2, Yu *et al.*'s (2010a) model underestimates the axial stresses. The three main causes are believed to be: (1) in later stages of loading, the steel tube and the concrete may contact with each other, providing enhancement of the concrete resistance which is ignored in Yu *et al.*'s (2010a) model; (2) Yu *et al.*'s (2010a) model generally provides conservative predictions for axial stresses even for small-scale specimens; (3) Yu *et al.*'s (2010a) model was developed on the test results of hybrid DSTCs with post-applied FRP wraps rather than filament-wound FRP tubes. In addition, the much steeper slope of the second portion of test curves than the predicted curves is partly due to the measurement error of axial strain of concrete presented earlier. For Specimen CC325-10-P6N of Series 2 and specimens of Series 3, Yu *et al.*'s (2010a) model fails to predict the sudden drop in axial stress, but it reasonably well predicts the slope of the portion of stress-strain curve succeeding the occurrence of axial stress drop.

### 6.5 CONCLUSIONS

This chapter has presented the results of a series of concentric compression tests on

large-scale hybrid DSTCs. The effects of different types of concrete and FRP tubes, void ratio, thickness of FRP tubes on the compressive behavior of hybrid DSTCs were investigated. The test results were also compared with an existing stress-strain model for concrete in hybrid DSTCs originally developed based on results of small-scale tests. Based on the test results and comparisons with theoretical predictions, the following conclusions can be drawn:

- (1) The test results confirmed that similar to small-scale hybrid DSTCs, large-scale hybrid DSTCs possess excellent ductility under axial compression and their axial load capacity and ductility increase with the thickness of FRP tubes.
- (2) The enhancement of axial load capacity of a hybrid DSTC due to the interaction between the constituent materials (i.e., confinement action) is limited for cases with a large void ratio and a relatively weak confinement level. This suggests that hybrid DSTCs with a large void ratio should be provided with relatively stiff FRP tubes to ensure the beneficial effect of the confinement action.
- (3) A drop in axial load undertaken by the concrete in hybrid DSTCs may occur once the unconfined concrete strength is reached when the confinement is provided by filament-wound FRP tubes instead of post-applied FRP wraps. It is believed that the axial load drop is attributed to a gap between the annular concrete and the wall of the outer FRP tube due to concrete shrinkage, which delays the activation of the confinement action of the filament-wound FRP tube. The axial load drop is more substantial for SCC and may translate into a drop in the total axial load of the hybrid DSTCs.

- (4) Yu *et al.*'s (2010a) stress-strain model can provide reasonably accurate predictions for the stress-strain behavior of concrete in large-scale hybrid DSTCs for cases without axial stress drop of concrete. Yu *et al.*'s (2010a) model is unable to predict the axial stress drop of concrete due to its simple nature and thus overestimates the axial stress of concrete for cases with axial stress drop of concrete.
- (5) For taking full advantage of three constituent materials (i.e., steel tube, concrete and FRP tube) of hybrid DSTCs, SCEC is a good choice especially for large-scale hybrid DSTCs. More tests on large-scale hybrid DSTCs with SCEC are needed to verify the applicability of conclusions drawn from tests on small-scale hybrid DSTCs to large-scale hybrid DSTCs.

## 6.6 REFERENCES

- BS 18. (1987). "Tensile Testing of Metals (Including Aerospace Materials)", British Standards Institution, UK.
- Cao, Q., Tao, J.J., Wu, Z.M. and Ma, Z.G.J. (2017). "Behavior of FRP-Steel Confined Concrete Tubular Columns Made of Expansive Self-Consolidating Concrete under Axial Compression", *Journal of Composites for Construction*. Vol. 21(5), 04017037.
- Daniel, I. M., and Ishai, O. (2006). "Engineering Mechanics of Composite Materials", Oxford University Press, New York.
- Fanggi, B.A.L. and Ozbakkaloglu, T. (2013). "Compressive Behavior of Aramid FRP-HSC-Steel Double-Skin Tubular Columns", *Construction and Building Materials*. Vol. 48, pp.554-565.
- Fanggi, B.A.L. and Ozbakkaloglu, T. (2015a). "Behavior of Hollow and Concrete-Filled FRP-HSC and FRP-HSC-Steel Composite Columns Subjected to

- Concentric Compression”, *Advances in Structural Engineering*. Vol. 18(5), pp. 715-738.
- Fanggi, B.A.L. and Ozbakkaloglu, T. (2015b). “Square FRP-HSC-Steel Composite Columns: Behavior under Axial Compression”, *Engineering Structures*. Vol. 92, pp.156-171.
- Hu, F. and Yao, J. (2016). “Experimental Study of FRP-Concrete-Steel Double-Skin Tubular Long Columns Subjected to Axial Compression”, *Industrial Construction*. Vol. 46(9), pp.130-139. (in Chinese)
- Jones, R.M. and Nelson JR, D.A.N. (1975). “A New Material Model for the Nonlinear Biaxial Behavior of ATJ-S Graphite”, *Journal of Composite Materials*. Vol. 9, pp.10-27.
- Lam, L. and Teng, J.G. (2003). “Design-Oriented Stress-Strain Model for FRP-Confined Concrete in Rectangular Columns”, *Journal of Reinforced Plastics and Composites*. Vol. 22(13), pp.1149-1186.
- Lim, J. C., and Ozbakkaloglu, T. (2014). “Influence of Silica Fume on Stress-Strain Behavior of FRP Confined HSC”, *Construction and Building Materials*. Vol. 63, pp.11-24.
- Ozbakkaloglu, T. and Fanggi, B. L. (2014). “Axial Compressive Behavior of FRP-Concrete- Steel Double-Skin Tubular Columns Made of Normal- and High-Strength Concrete”, *Journal of Composites for Construction*. Vol. 18(1): 04013027.
- Ozbakkaloglu, T. and Fanggi, B.A.L. (2015). “FRP-HSC-Steel Composite Columns: Behavior under Monotonic and Cyclic Axial Compression”, *Material and Structures*. Vol. 48(4), pp.1075-1093.
- Qian, J.R. and Liu, M.X. (2006). “Experiment of FRP-Concrete-Steel Double-Skin Tubular Long Columns under Axial Compressive Load”, *Journal of Concrete*

- (*Theoretical Research*). Vol. 203, pp.31-34. (in Chinese).
- Qian, J.R. and Liu, M.X. (2008). “Experimental Investigation of FRP-Concrete-Steel Double-Skin Tubular Stubs under Axial Compressive Loading”, *Journal of Building Structures*. Vol. 29(2), pp.104-113. (in Chinese).
- Teng, J.G., Yu, T. and Wong, Y.L. (2004). “Behaviour of Hybrid FRP-Concrete-Steel Double-Skin Tubular Columns”, *Proceedings, 2<sup>nd</sup> International Conference on FRP Composites in Civil Engineering*. Adelaide, Australia, 2004, pp. 811-818.
- Teng, J.G., Yu, T., Wong, Y.L. and Dong, S.L. (2007). “Hybrid FRP-Concrete-Steel Tubular Columns: Concept and Behavior”, *Construction and Building Materials*. Vol. 21(4), pp. 846-854.
- Teng, J.G., Jiang, T., Lam, L. and Luo, Y.Z. (2009). “Refinement of a Design-Oriented Stress-Strain Model for FRP-Confined Concrete”, *Journal of Composites for Construction*, ASCE. Vol.13(4), pp.269-278.
- Teng, J.G., Zhao, J.L., Yu, T., Li, L.J. and Guo, Y.C. (2016). “Behavior of FRP-Confined Compound Concrete Containing Recycled Concrete Lumps”, *Journal of Composites for Construction*. Vol. 20(1), 04015038.
- Wang, J., Zhao, J.H., Zhu, Q., Zhang, Z.C. and Liu, Q. (2011). “Axial Bearing Capacity of FRP-Concrete-Steel Double-Skin Tubular Short Columns”, *Industrial Construction*. Vol. 41(11), pp.130-133. (in Chinese).
- Wang, J., Liu, W.Q., Fang, H. and Zhu, L. (2012). “Experiment and Capacity Calculation Theory Research of Hybrid GFRP-Concrete-Steel Double Skin Tubular Columns under Axial Compression”, *Building structure*. Vol. 42(2), pp.133-138. (in Chinese).
- Wong, Y.L., Yu, T., Teng, J.G. and Dong, S.L. (2008). “Behavior of FRP-Confined Concrete in Annular Section Columns”, *Composites Part B-Engineering*. Vol. 39(3), pp. 451-466.

- Xie, P., Yu, T., Wong, Y.L. and Teng J.G. (2011). “Compression Behavior of Large-Scale Hybrid FRP-Concrete-Steel Double-Skin Tubular Columns”, *International Conference on Civil Engineering, Architecture and Building Materials, CEABM2011*, 18-20 June, Haikou, China.
- Yu, T. (2007). “Behavior of Hybrid FRP-Concrete-steel Double-Skin Tubular Columns”, Ph. D. Thesis, The Hong Kong Polytechnic University.
- Yu, T., Teng, J.G. and Wong, Y.L. (2010a). “Stress-Strain Behavior of Concrete in Hybrid Double-Skin Tubular Columns”, *Journal of Structural Engineering*, ASCE. Vol. 136(4), pp.379-389.
- Yu, T., Teng, J.G., Wong, Y.L. and Dong, S.L. (2010b). “Finite Element Modeling of Confined Concrete-I: Drucker-Prager Type Plasticity Model”, *Engineering Structures*. Vol. 32, pp. 665-679.
- Yu, T., Teng, J.G., Wong, Y.L. and Dong, S.L. (2010c). “Finite Element Modeling of Confined Concrete-II: Plastic-Damage Model”, *Engineering Structures*. Vol. 32, pp. 680-691.
- Yu, T. and Teng, J.G. (2013). “Behavior of Hybrid FRP-Concrete-Steel Double-Skin Tubular Columns with a Square Outer Tube and a Circular Inner Tube Subjected to Axial Compression”, *Journal of Composites for Construction*. Vol. 17, pp.271-279.
- Yu, T., Zhang, S.S., Huang, L. and Chan, C. (2017). “Compressive Behavior of Hybrid Double-Skin Tubular Columns with a Large Rupture Strain FRP Tube”, *Composite Structures*. Vol. 171, pp.10-18.
- Zhang, B., Yu, T. and Teng, J.G. (2011). “Axial Compression Tests on Hybrid Double-Skin Tubular Columns Filled with High Strength Concrete”, *Proceedings, Third International Postgraduate Conference on Infrastructure and Environment*, 11-12 July, Hong Kong, China, pp.171-176.

Zhang, B. (2014). “Hybrid FRP-Concrete-Steel Double-Skin Tubular Columns under Static and Cyclic Loading”, Ph.D. Thesis, The Hong Kong Polytechnic University.

Zhang, B., Teng, J.G. and Yu, T. (2017). “Compressive Behavior of Double-Skin Tubular Columns with High-Strength Concrete and a Filament-Wound FRP Tube”, *Journal of Composites for Construction*, ASCE. Vol. 21(5): 04017029.

Zhou, Y.W., Liu, X.M., Xing, F., Li, D.W., Wang, Y.C. and Sui, L.L. (2017). “Behavior and Modeling of FRP-Concrete-Steel Double-Skin Tubular Columns Made of Full Lightweight Aggregate Concrete”, *Constructions and Building Materials*. Vol. 139, pp.52-63.

**Table 6. 1 Geometrical and material properties of DSTC specimens**

	Specimen	GFRP tube					Steel tube					Concrete			Void ratio $\phi$	
		$D_{in}$ (mm)	$t_{frp}$ (mm)	$E_x$ (GPa)	$\nu_{x\theta}$	$E_\theta$ (GPa)	$D_{o,s}$ (mm)	$t_s$ (mm)	$E_s$ (GPa)	$f_y$ (MPa)	$f_u$ (MPa)	$E_c$ (GPa)	$\epsilon_{co}$	$f'_{co}$ (MPa)		$D_{o,s}/t_s$
1	CC245-8-W6N	401.9	1.02	-	-	80.1	245.8	8.00	209.8	307.2	457.8	24.02	0.00258	25.79	30.63	0.61
	CC325-9-W4N	402.6	0.68	-	-	80.1	323.6	9.30	218.7	316.3	508.0	26.46	0.00335	31.30	36.11	0.81
	CC325-9-W6N	401.7	1.02	-	-	80.1						28.90	0.00310	37.34		
2	CC245-8-P4N	402.9	1.95	10.44	0.099	34.43	245.5	8.17	202.2	280.5	481.6	27.61	0.00333	34.07	30.63	0.61
	CC245-8-P6N	403.8	2.85	10.53	0.104	38.93										
	CC325-10-P4N	401.7	1.89	10.44	0.099	34.43	325.0	10.13	218.2	289.1	414.0	24.26	0.00338	26.31	32.50	0.81
	CC325-10-P6N	404.5	2.85	10.53	0.104	38.93										
3	CC219-6-P6S	401.1	2.53	11.75	0.102	41.60	219.0	6.38	215.0	309.0	385.0	33.19	0.00277	49.24	36.50	0.55
	CC245-8-P6S	398.8	2.41				245.5	8.17	202.2	280.5	481.6				30.63	0.61
	CC325-8-P4S	401.1	1.80	10.39	0.124	40.55	325.0	8.0	206.0	261.0	314.0				40.63	0.81
	CC325-8-P6S	399.1	2.42	11.75	0.102	41.60										

**Table 6. 2 Key test results of concentrically-loaded DSTCs**

Series	Specimen	$P_{total}$	$P_s$	$P_{frp}$	$P_c$	Average	Average	Average	Average	Average	$\sigma_{\theta u}$	$\epsilon'_{h,rup}$
		(kN)	(kN)	(kN)	(kN)	$P_{co}$ (kN)	$P_{total} / (P_{co} + P_s + P_{frp})$	$\epsilon_{cu}$	$\epsilon_{cu} / \epsilon_{co}$	$\epsilon_{h,rup}$	(kN)	
1	CC245-8-W6N	6378	2703	0	3675	2080	1.33	0.0287	11.11	0.0154	1237.20	0.0154
	CC325-9-W4N <sup>c</sup>	4812	3299	0	1513	1432	1.02	0.0105	3.14	0.00658	526.92	0.00658
	CC325-9-W6N	6487	3952	0	2535	1715	1.14	0.0255	8.24	0.0150	1200.10	0.0150
2	CC245-8-P4N	5870	1876	77	3917	2730	1.25	0.00834	2.50	0.00843	265.79	0.00772
	CC245-8-P6N	7264	2191	202	4871	2749	1.41	0.0157	4.70	0.0122	439.86	0.0113
	CC325-10-P4N <sup>b</sup>	5174	3768	215	1191	1152	1.01	0.0172	5.09	0.00894	258.51	0.00751
	CC325-10-P6N	7153	4187	446	2521	1198	1.23	0.0255	7.55	0.0111	400.92	0.0103
3	CC219-6-P6S <sup>b</sup>	7272	1618	181	5472	4366	1.18	0.0170	6.14	0.0133	500.43	0.0120
	CC245-8-P6S <sup>a b</sup>	5842 (6254)	1724 (2221)	82 (156)	4036 (3805)	3817	1.04	0.0137	4.96	0.00980	382.44	0.00919
	CC325-8-P4S <sup>a b</sup>	4049 (3895)	1876 (1954)	64 (143)	2109 (1797)	2136	0.99	0.0149	5.39	0.00981	352.49	0.00869

Series	Specimen	$P_{total}$ (kN)	$P_s$ (kN)	$P_{frp}$ (kN)	$P_c$ (kN)	Average $P_{co}$ (kN)	Average $P_{total} / (P_{co} + P_s + P_{frp})$	Average $\epsilon_{cu}$	Average $\epsilon_{cu} / \epsilon_{co}$	Average $\epsilon_{h,rup}$	$\sigma_{\theta u}$ (kN)	$\epsilon'_{h,rup}$
3	CC325-8-P6S <sup>a b</sup>	4223 (4298)	1889 (2116)	100 (205)	2233 (1977)	2073	1.03	0.0143	5.16	0.00807	297.52	0.00715

<sup>a</sup>  $P_{total}$  is assigned to the first peak load of specimen;

<sup>b</sup> The axial load carried by concrete experienced a drop and then increased again;

<sup>c</sup> Premature failure.



(a) Void ratio  $\phi = 0.61$

(b) Void ratio  $\phi = 0.81$

**Figure 6. 1** Cross section of hybrid DSTCs



**Figure 6. 2** Test setup and buckling of bare steel tubes under axial compression

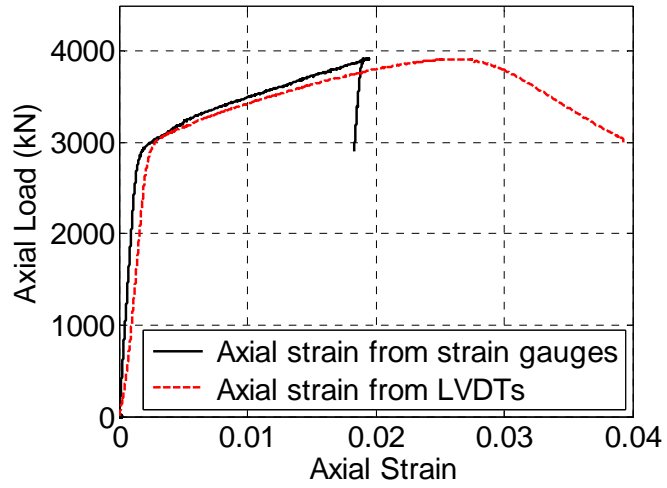


**Figure 6.3** Axial load-axial strain curves of bare steel tubes

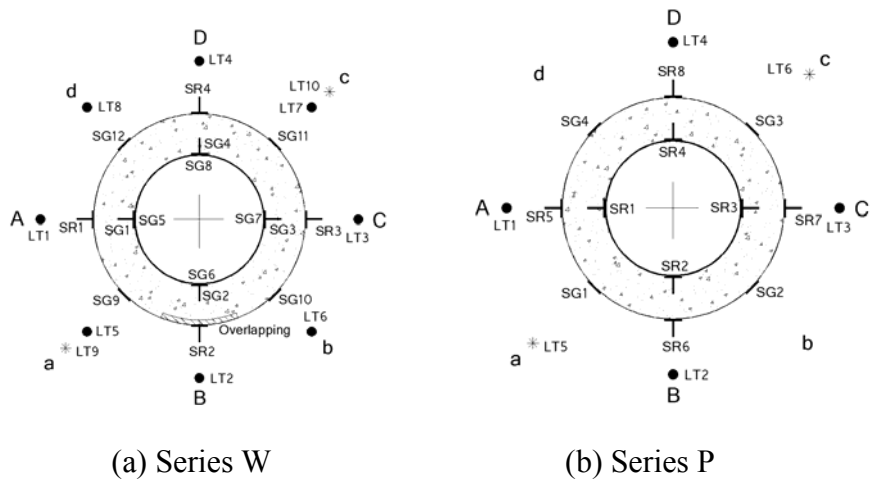


**Figure 6.4** Layout of strain gauges and LVDTs



(a) Series W (b) Series P

**Figure 6.5** Setup for concentric compression tests on DSTCs



(a) CC245-8-W6N



(b) CC325-9-W4N



(c) CC325-9-W6N



(d) CC245-8-P4N



(e) CC245-8-P6N



(f) CC325-10-P4N



(g) CC325-10-P6N



(h) CC219-6-P6S



(i) CC245-8-P6S



(j) CC325-8-P4S



(k) CC325-8-P6S

**Figure 6. 6** Failure mode of hybrid DSTCs under axial compression



**Figure 6.7** Global buckling of the inner steel tube of hybrid DSTCs

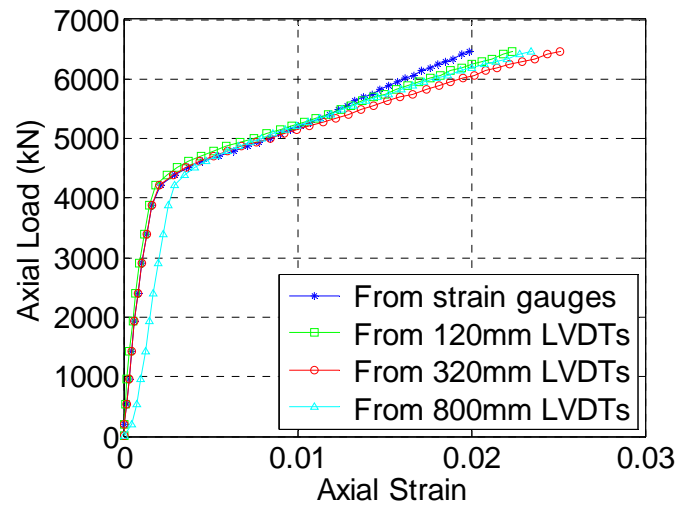


**Figure 6.8** Comparison of axial strains obtained by different ways

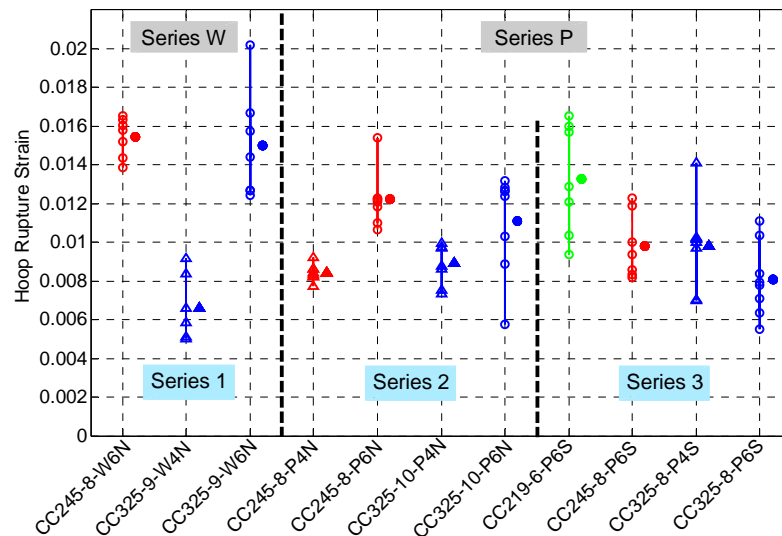
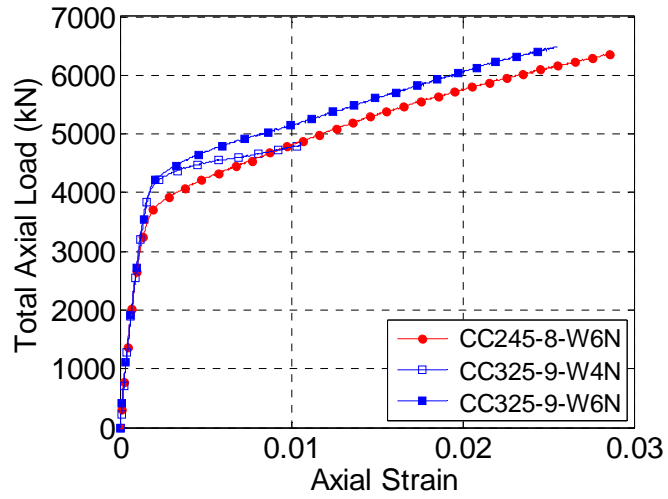
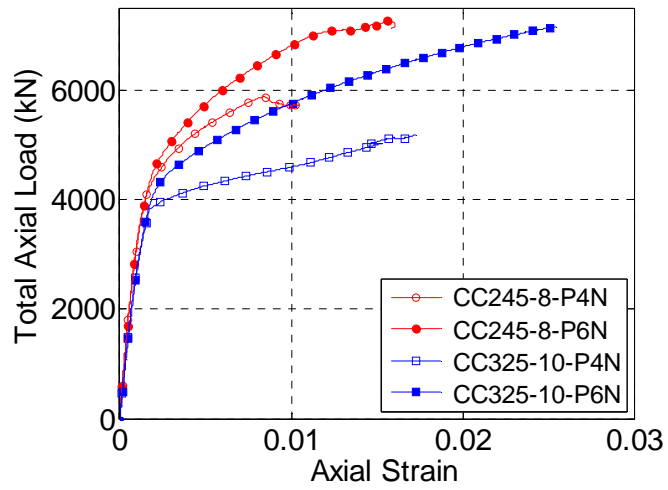


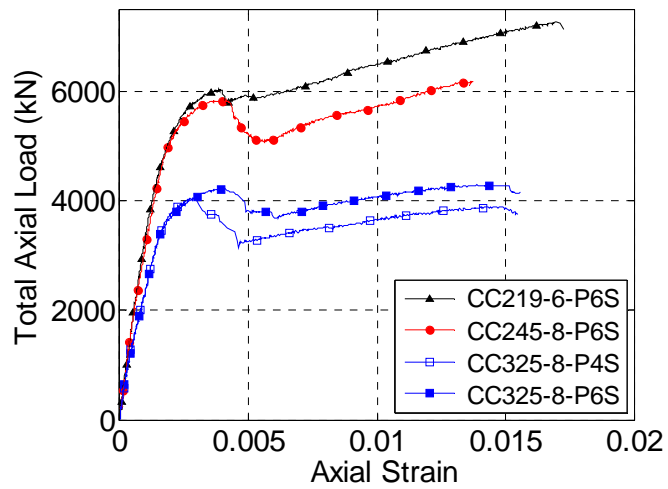
**Figure 6.9** Distribution of hoop rupture strains



(a) Series 1

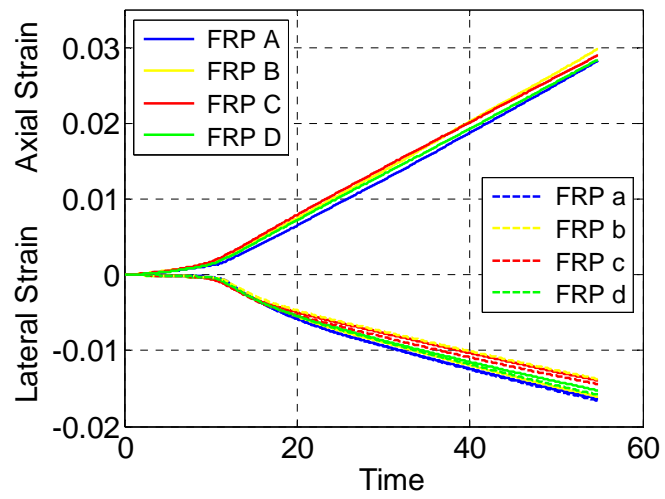
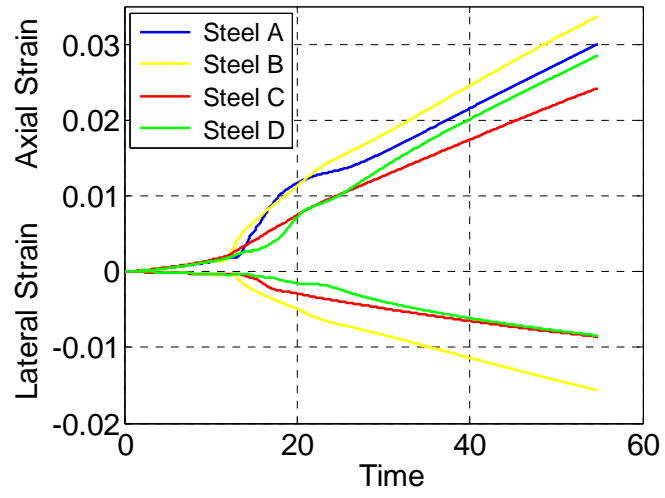


(b) Series 2

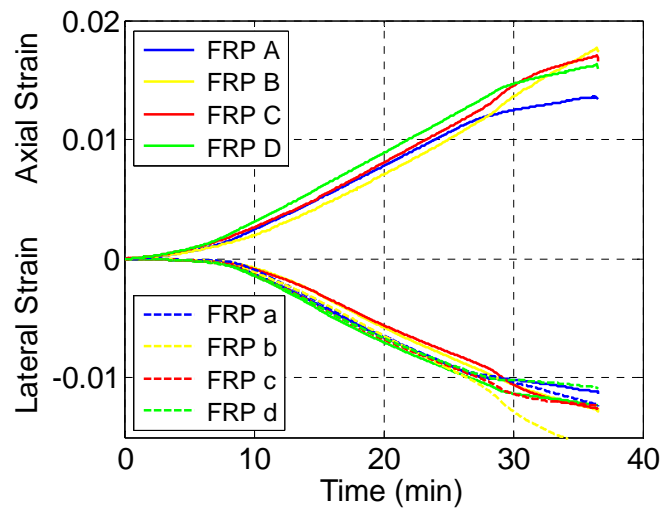
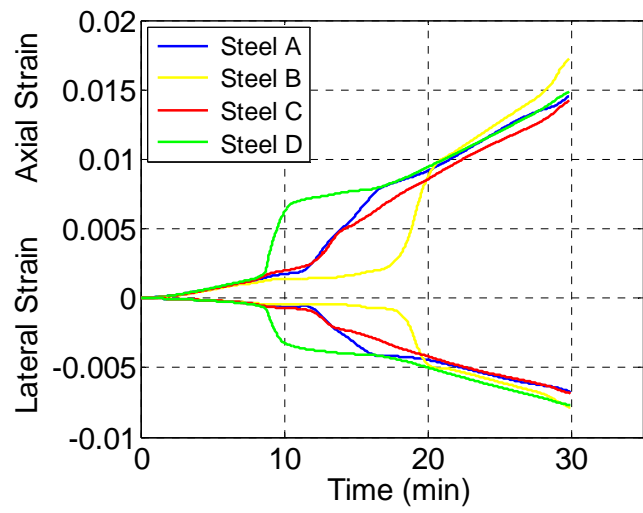


(c) Series 3

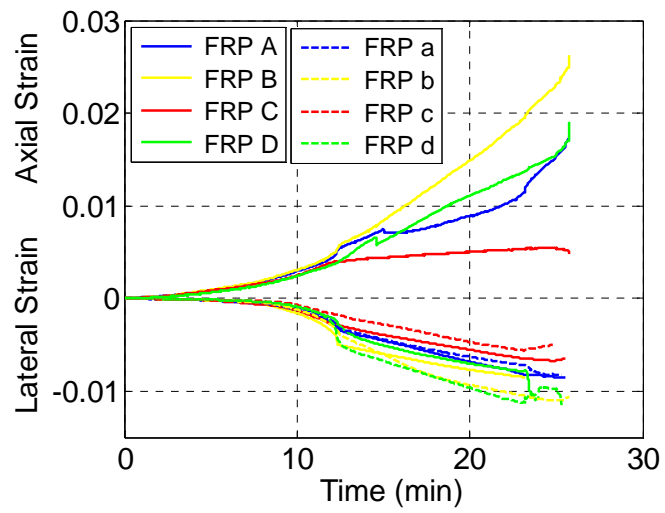
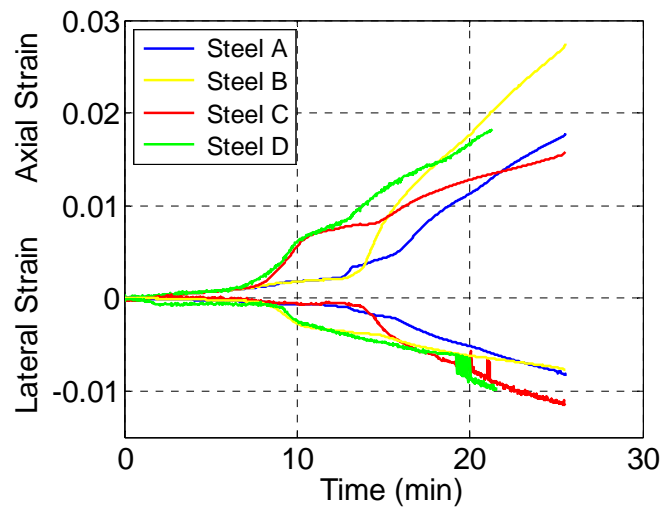
**Figure 6. 10** Total axial load-axial strain curves



(a) CC245-8-W6N

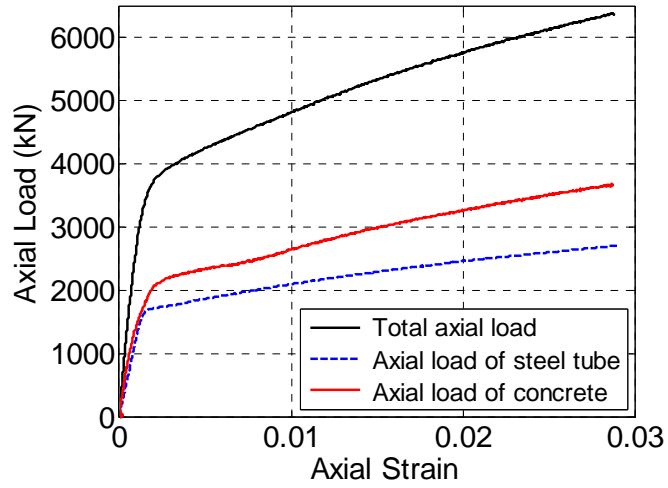


(b) CC245-8-P6N

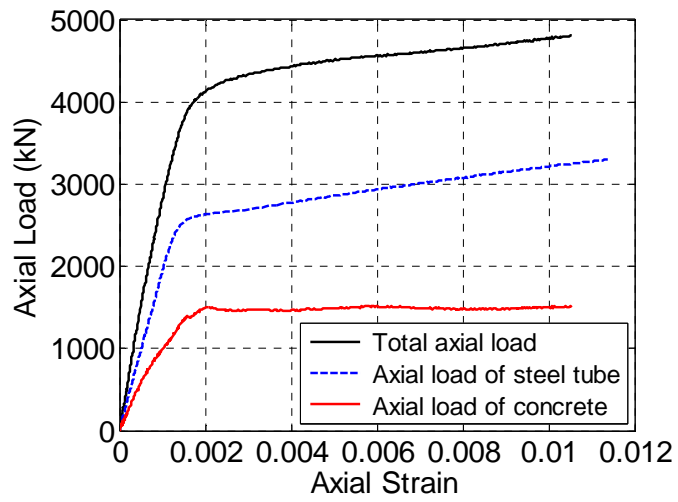


(c) CC245-8-P6S

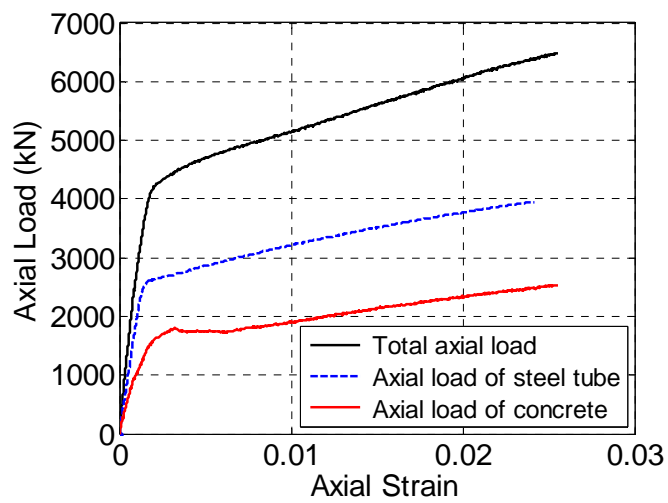
**Figure 6. 11** Development of strains during tests



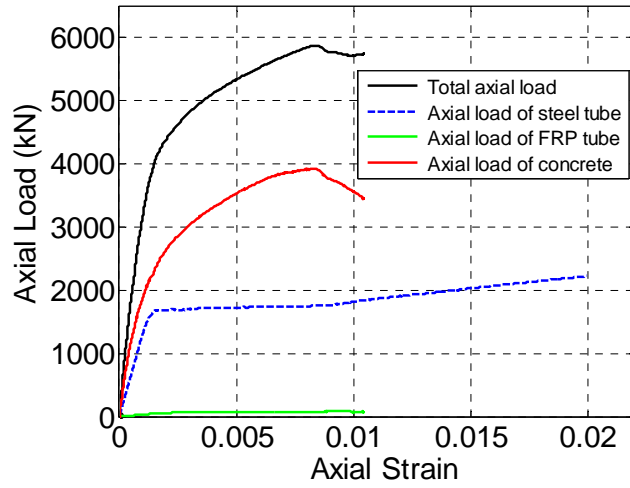
(a) CC245-8-W6N



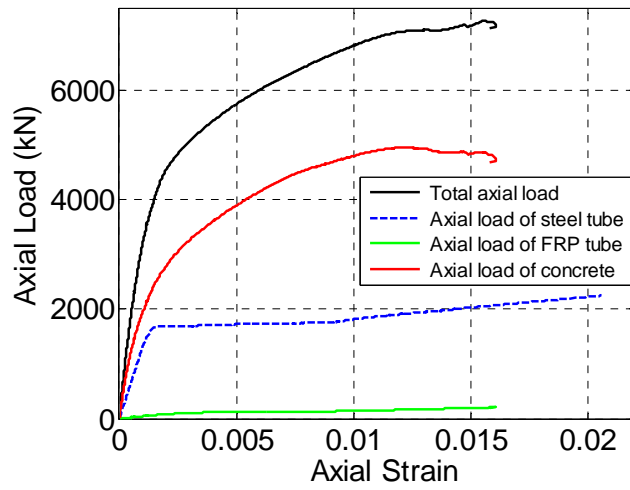
(b) CC 325-9-W4N



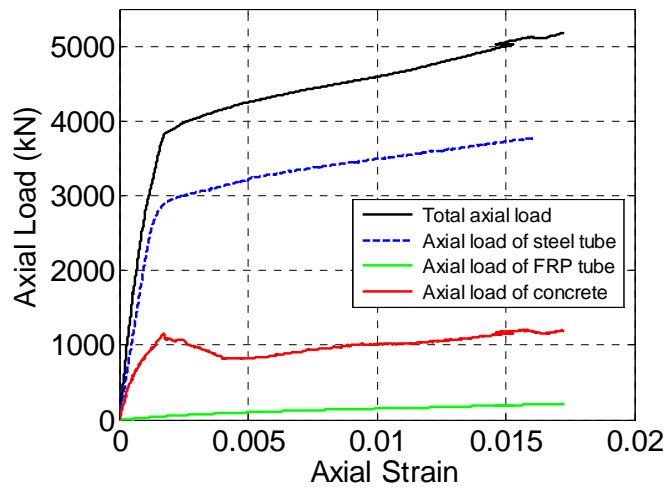
(c) CC325-9-W6 N



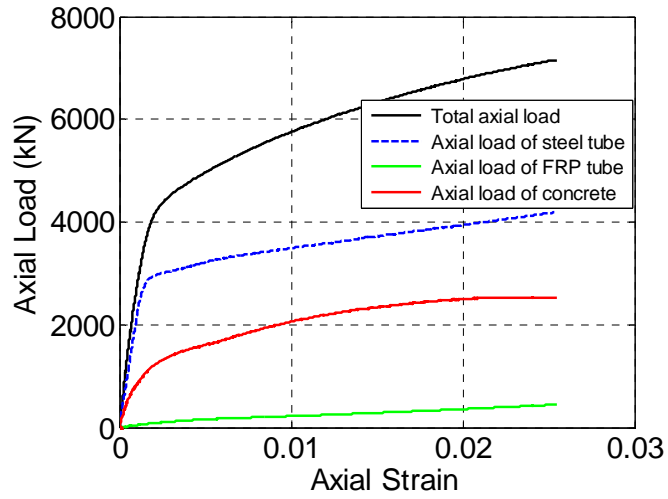
(d) CC245-8-P4 N



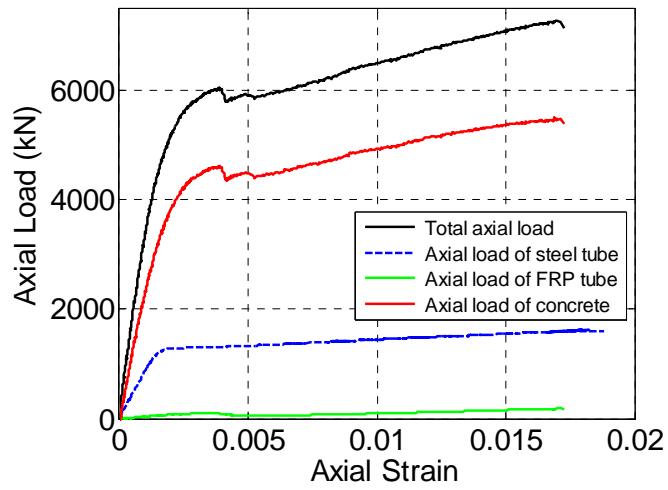
(e) CC245-8-P6 N



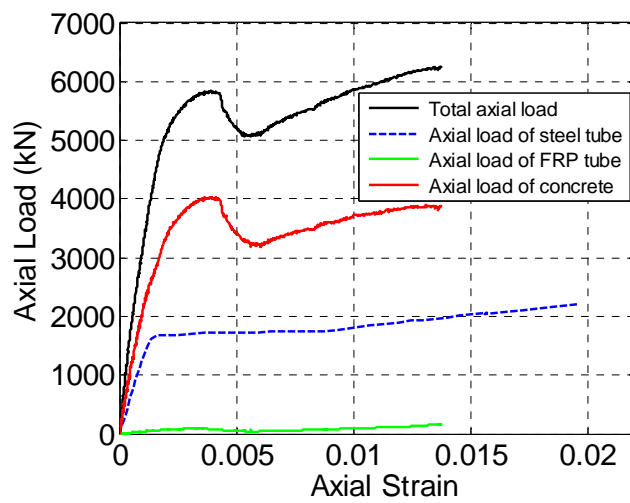
(f) CC325-10-P4 N



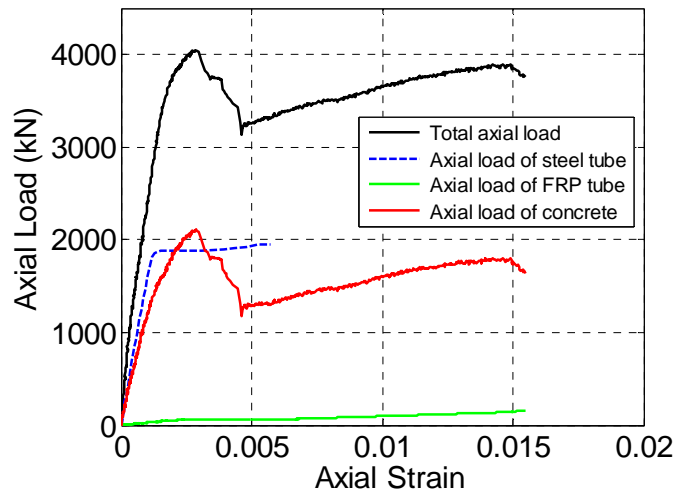
(g) CC325-10-P6 N



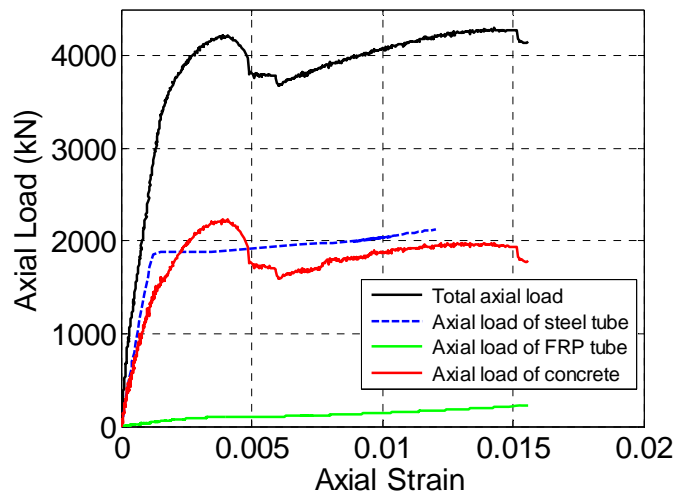
(h) CC219-6-P6S



(i) CC245-8-P6S

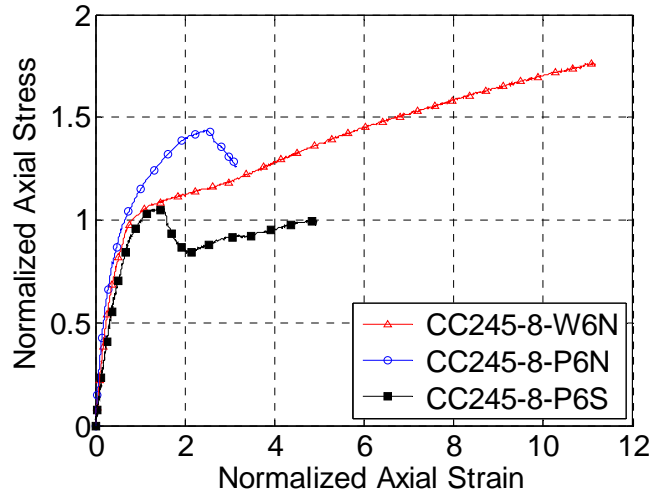


(j) CC325-8-P4S

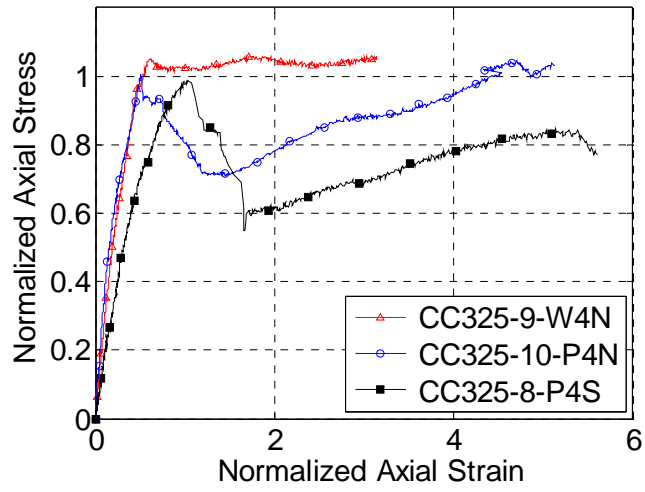


(k) CC325-8-P6S

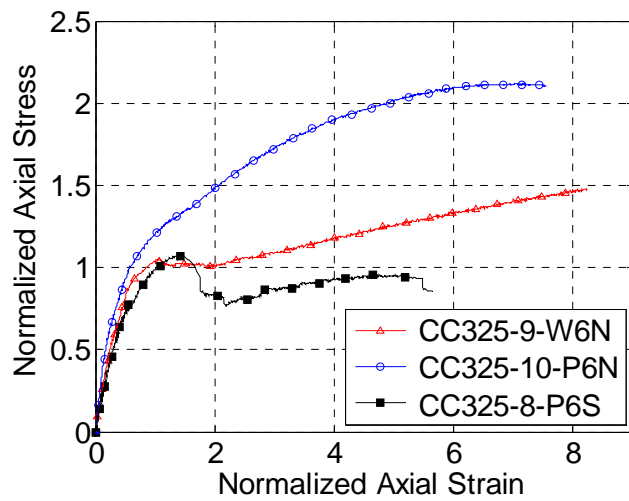
**Figure 6. 12** Contribution of FRP tube, concrete and steel tube to total axial load



(a)

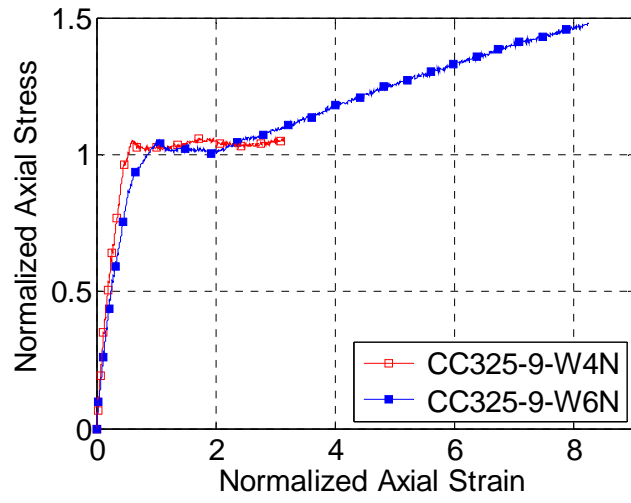


(b)

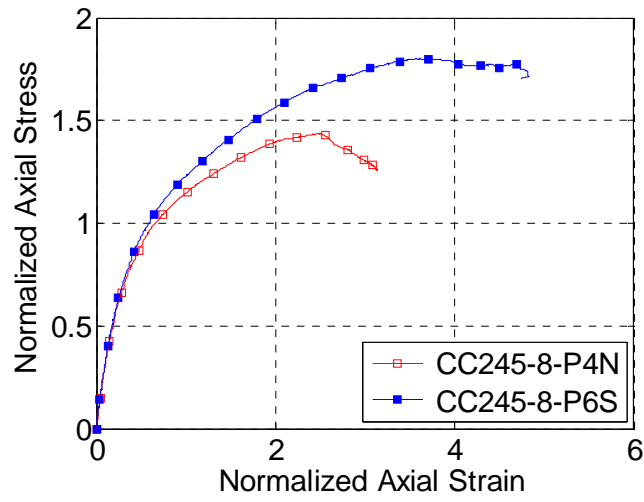


(c)

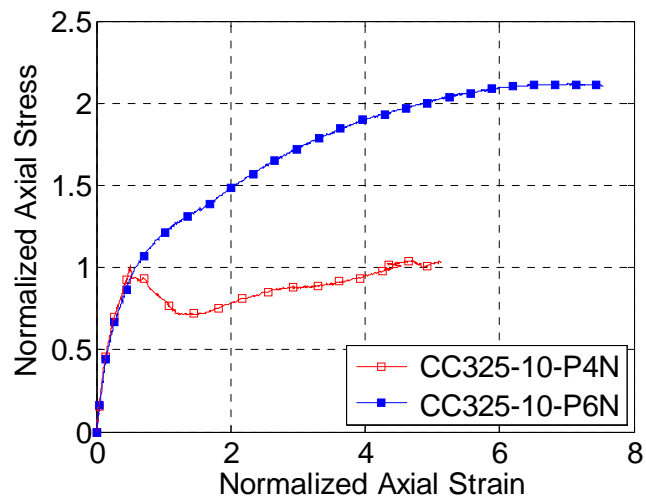
**Figure 6. 13** Effects of type of concrete and FRP tube



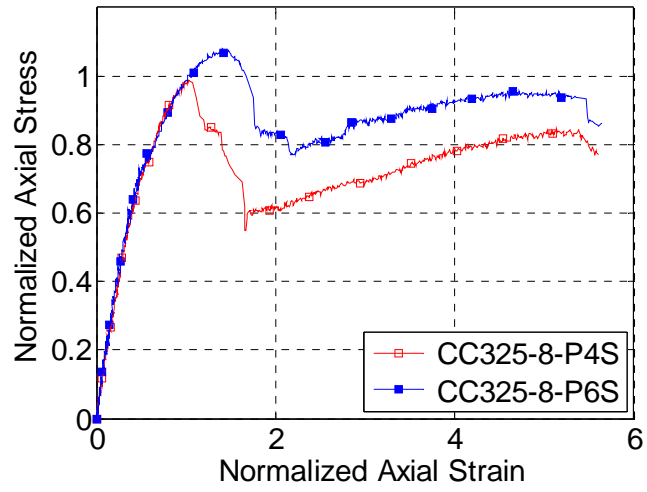
(a)



(b)

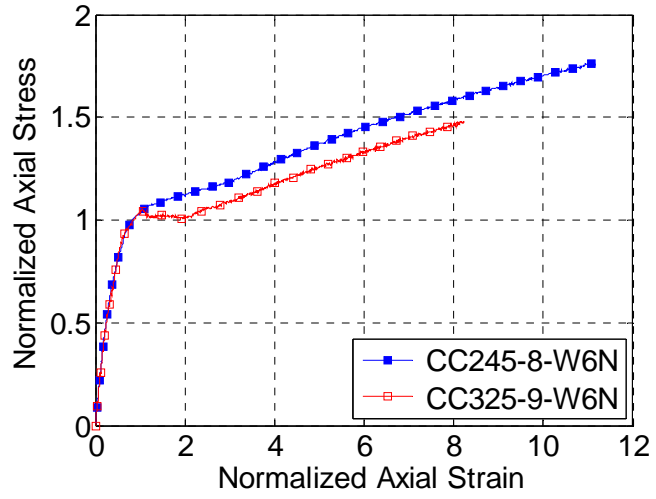


(c)

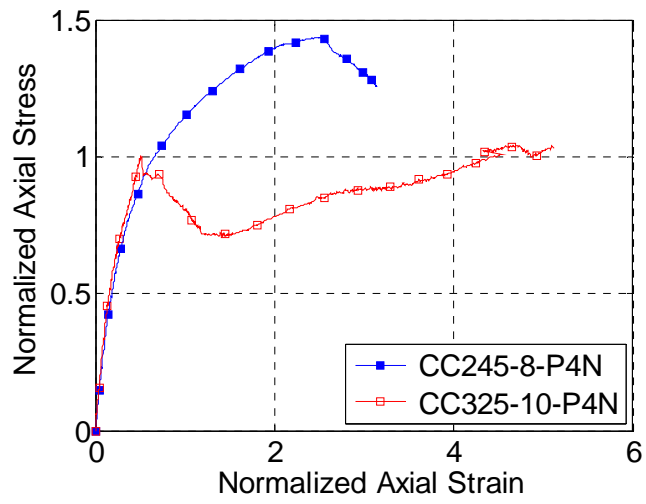


(d)

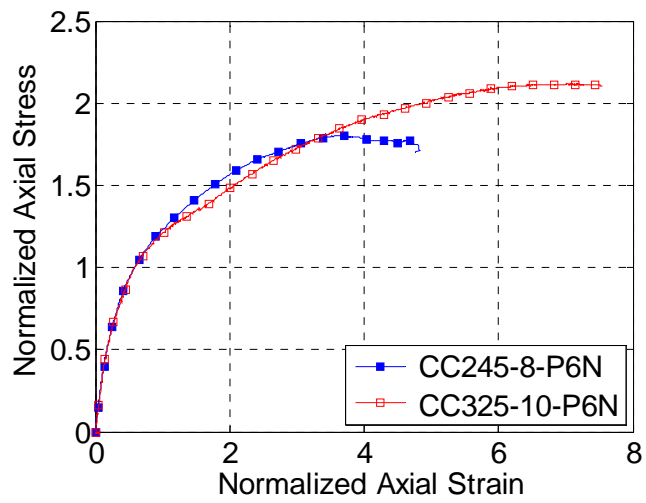
**Figure 6. 14** Effect of FRP thickness



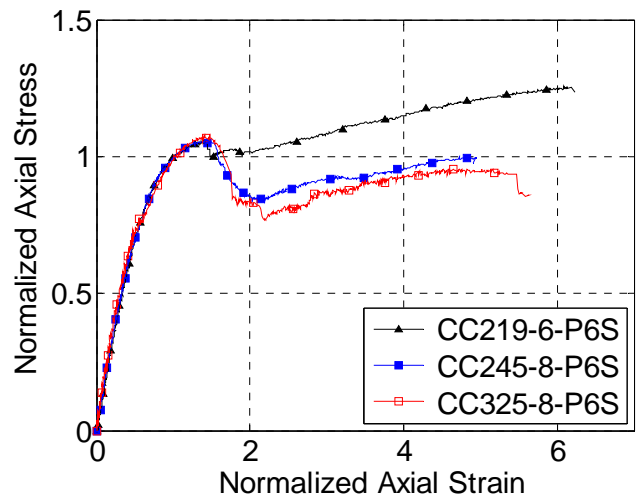
(a)



(b)

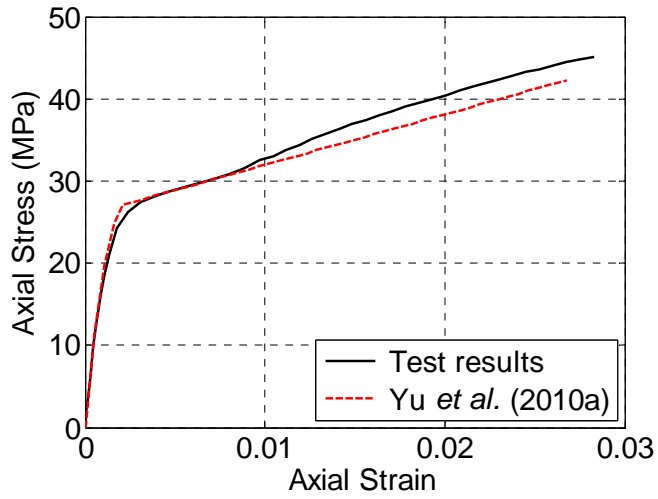


(c)

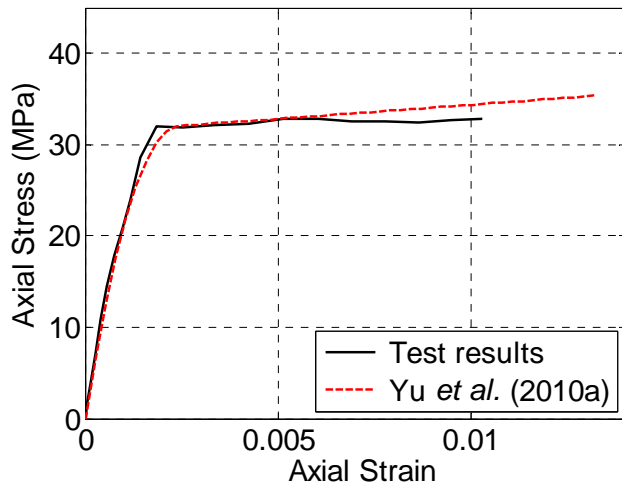


(d)

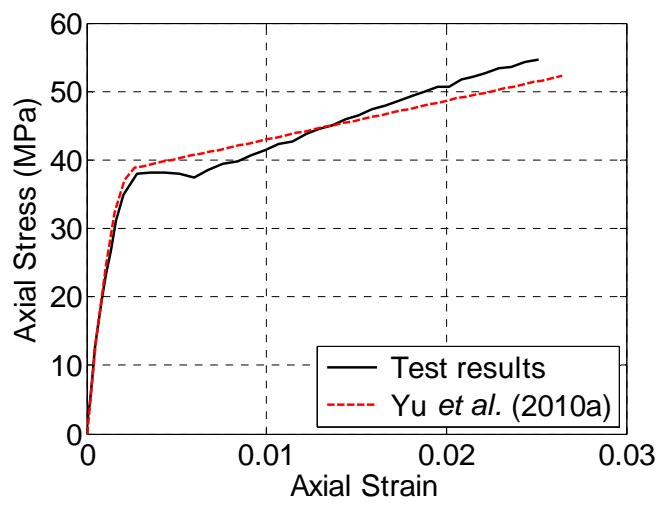
**Figure 6. 15** Effect of void ratio



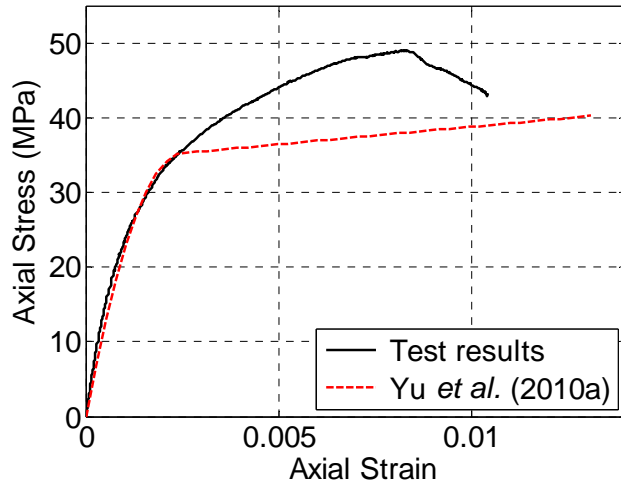
(a) CC245-8-W6N



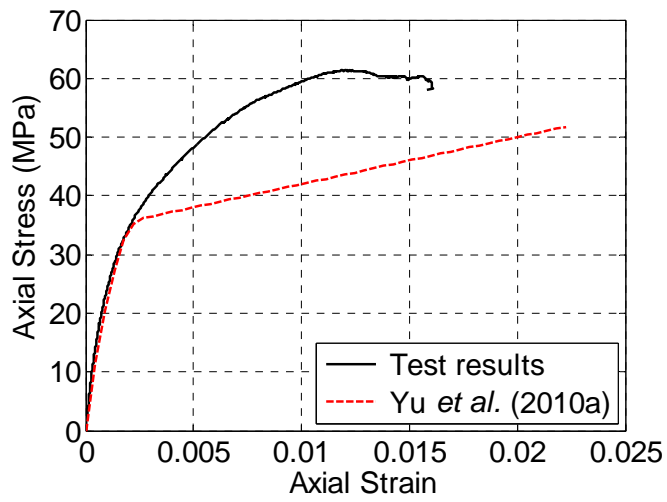
(b) CC 325-9-W4N



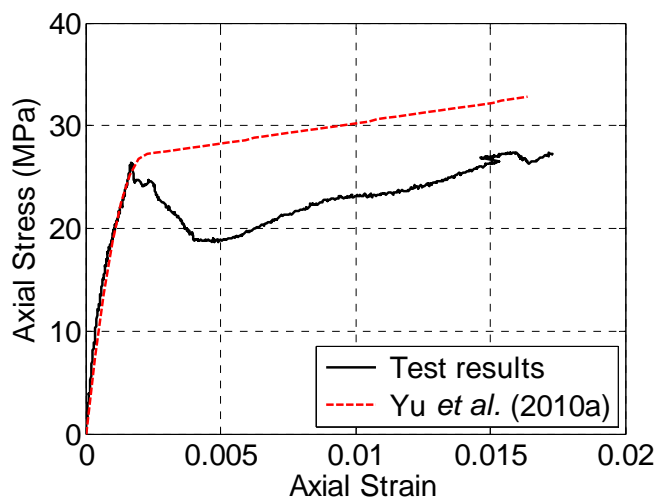
(c) CC325-9-W6N



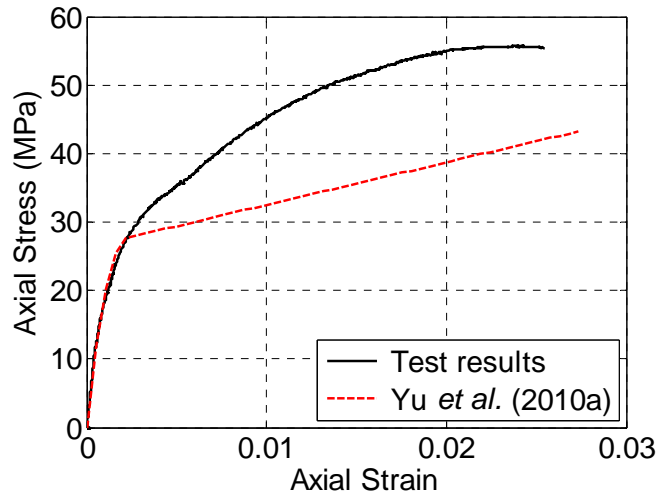
(d) CC245-8-P4N



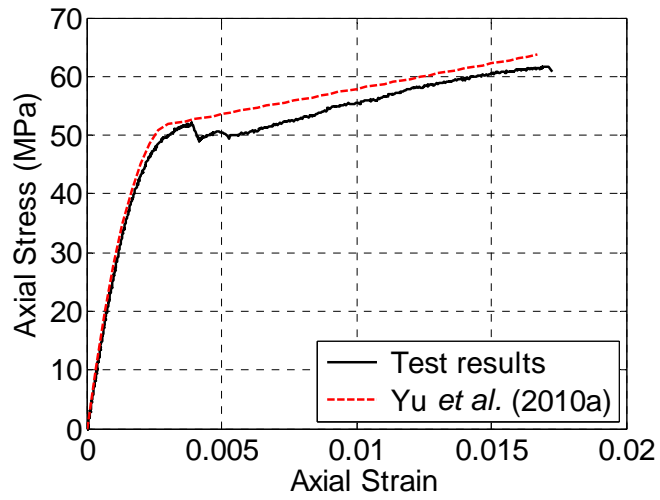
(e) CC245-8-P6N



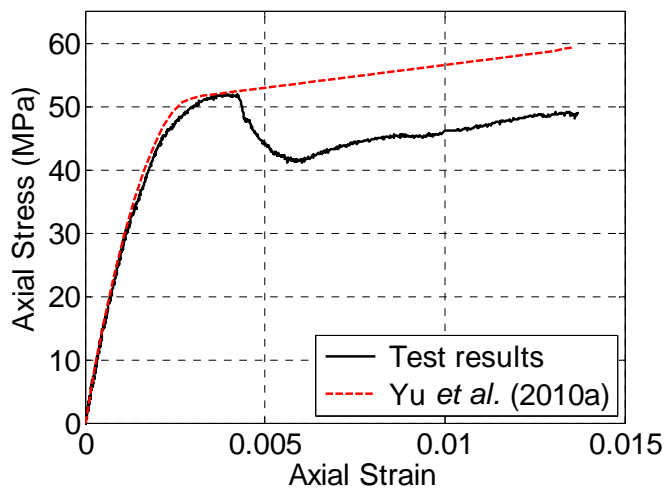
(f) CC325-10-P4N



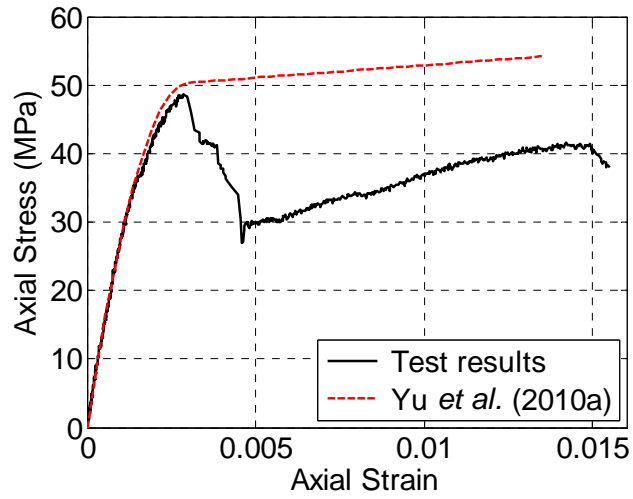
(g) CC325-10-P6N



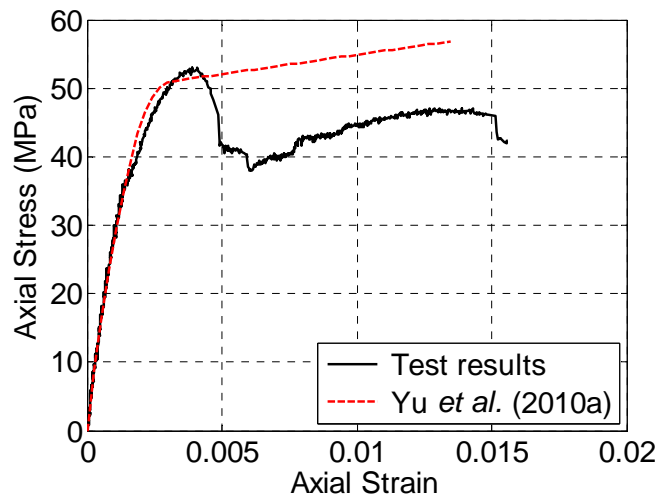
(h) CC219-6-P6S



(i) CC245-8-P6S



(j) CC325-8-P4S



(k) CC325-8-P6S

**Figure 6. 16** Comparison of axial stress-axial strain curves of concrete in hybrid DSTCs



# CHAPTER 7

## LARGE-SCALE SHORT HYBRID DSTCS SUBJECTED TO ECCENTRIC COMPRESSION

### 7.1 INTRODUCTION

Chapter 6 has been concerned with the behavior of large-scale hybrid DSTCs subjected to concentric compression. In real structures, however, the perfect concentric loading is impossible considering the unintended load eccentricity as a result of geometric and material imperfections and accidental load eccentricity. For this reason, an additional eccentricity is required to be imposed on all hybrid DSTCs in the Chinese Technical Code for Infrastructure Application of FRP Composites (GB50608 2010). Therefore, all hybrid DSTCs should be designed as columns subjected to the combination of compression and bending (i.e., eccentric compression of the section). The existing research on the eccentric compression behavior of hybrid DSTCs has been rather limited.

Yu *et al.* (2010b) conducted eccentric compression tests on six identical hybrid DSTCs confined with post-applied CFRP wraps. All specimens had a diameter of 155 mm and a height of 465 mm and were made with an inner steel tube which had a diameter of 76 mm and a thickness of 3.7 mm. Every two identical specimens were imposed with the an eccentricity of 0 mm, 9 mm or 18 mm. Considering the effect of strain gradient on the effectiveness of confinement, a so-called “variable confinement model” for the concrete in the hybrid DSTCs was proposed and provided reasonably accurate prediction for the small-scale specimens. Ma (2013) tested nine square hybrid DSTCs subjected to eccentric compression where all specimens had a side length of 150 mm and a height of 500 mm and proposed an expression for the axial bearing capacity of

eccentrically-loaded square hybrid DSTCs.

In comparison, a greater number of experimental and theoretical studies have been carried out on eccentrically-loaded FRP-confined concrete columns (Fam *et al.* 2003; Tao 2004; Hadi 2006a, 2006b, 2007; El Maaddawy 2008; Bisby and Ranger 2010; El Sayed and El Maaddawy 2011; Wu and Jiang 2013; Jiang and Teng 2012a, 2012b, 2013; Jiang *et al.* 2014). The findings of these studies provide beneficial reference for the investigation of hybrid DSTCs subjected to eccentric compression. In particular, the axial strain enhancement effect (i.e., the ultimate axial strain at the extreme compression concrete fiber increases with the eccentricity) has been observed in both eccentrically-loaded hybrid DSTCs (Yu *et al.* 2010b) and FRP-confined concrete columns (e.g., Fam *et al.* 2003; Ranger 2007; Fitzwilliam and Bisby 2010; Csuka and Kollár 2012; Zhang 2014). The feature owned by the concrete in eccentrically-loaded FRP-confined concrete columns can be described by eccentricity-dependent (EccD) stress-strain models (Fam *et al.* 2003; Lin 2016).

Zhang (2014) tested 20 circular FRP-confined concrete specimens 150 mm in diameter and 300 mm in height with varying load eccentricity up to 40 mm and revealed that the presence of eccentricity decreases the slope of the second linear portion of stress-strain curves of the confined concrete while increases the ultimate axial strain of the confined concrete. Lin (2016) developed a robust EccD stress-strain model for the concrete in FRP-confined RC columns under eccentric compression based on the results of a parametric study using a 3D FE model. The FE model has been verified by the test results of FRP-confined concrete columns under combined bending and axial compression performed by Fitzwilliam (2006), Ranger (2007), Mosalam *et al.* (2007), Fitzwilliam and Bisby (2010), Bisby and Ranger (2010) and Zhang (2014). In Lin's

(2016) model, the axial strain enhancement effect is accounted for.

To better understand the behavior of hybrid DSTCs under eccentric compression, this chapter will present an experimental study on large-scale short hybrid DSTCs subjected to eccentric compression where the eccentricity and the thickness of filament-wound GFRP tube are the major research variables. Moreover, the test results are compared with a theoretical column model in which the stress-strain relationship of the confined concrete is separately described using the following three stress-strain models: (1) Yu *et al.*'s (2010a) stress-strain model for concrete in hybrid DSTCs under concentric compression; (2) Yu *et al.*'s (2010b) stress-strain model for concrete in hybrid DSTCs under eccentric compression; and (3) Lin's (2016) stress-strain model for concrete in FRP-confined concrete columns under eccentric compression.

## **7.2 EXPERIMENTAL PROGRAM**

### **7.2.1 Specimen Details**

Totally two series of short hybrid DSTC specimens were fabricated and tested under eccentric compression. All hybrid DSTC specimens had a nominal outer diameter of 400 mm (excluding the FRP tube), a height of 1200 mm and a void ratio of 0.81. The filament-wound GFRP tubes used in these specimens were the same with those used in concentrically-loaded hybrid DSTCs in Chapter 6. The first test series included two specimens with NC infill while the second series included four specimens filled with SCC. Table 7.1 provides the geometric and material properties of the specimens. Specimen naming is based on the following convention: each specimen name starts with two letters "CE" to indicate the loading condition of eccentric compression, followed by a three-digit number (i.e., 325) and a number (i.e., 8 or 10) to respectively

represent the nominal outer diameter and the nominal thickness of steel tube in millimeter, and then a letter “P” to indicate the use of prefabricated filament-wound FRP tubes and together with a number (i.e., 4 or 6) to represent the number of fiber layers, followed by a letter “N” or “S” to differentiate specimens filled with NC or SCC, and ends with a two- or three-digit number (i.e., 50, 80, 100 or 150) to indicate the load eccentricity in millimeter. Note that Specimens CC325-10-P4N, CC325-8-P4S and CC325-8-P6S, which were tested under concentric compression in Chapter 6, are also included in Table 7.1 as specimens with a zero eccentricity for comparison purposes.

### **7.2.2 Material Properties**

Ancillary material tests, including axial compression tests on standard concrete control cylinders, bare steel tubes and bare FRP tubes, tensile tests on coupons cut from steel tubes, and hydraulic pressure tests on FRP tubes, were conducted to determine the properties of the three constituent materials. A summary of the material properties is given in Table 7.1. The dimensions of FRP and steel tubes listed in Table 7.1 are the actual measured values which slightly differ from the nominal values, but the diameter-to-thickness ratio of the steel tubes ( $\phi$ ) is based on the nominal values.

### **7.2.3 Specimen Preparation**

The construction of eccentrically-loaded specimen was also in accord with that of concentrically-loaded specimens using an outer filament-wound GFRP tube and an inner steel tube as stay-in-place formwork. The width of CFRP reinforcing strips near the top and the bottom ends of each eccentrically-loaded specimen was proportionally enlarged to 90 mm because of the increase of the specimen height.

#### 7.2.4 Test Setup and Instrumentation

Figure 7.1 illustrates the layout of strain gauges and LVDTs of the eccentrically-loaded specimens. In total, 16 bi-directional strain rosettes with a gauge length of 20 mm were evenly distributed around specimen circumference at the mid-height (i.e., Section A). Of the 16 strain rosettes, eight (SR1 to SR8) were attached at the outer surface of the steel tube and the other eight (SR9 to SR16) were mounted at the outer surface of the GFRP tube, to measure the axial and the hoop strains at different locations during loading (Figure 7.1). In addition, two groups of eight unidirectional strain gauges with a gauge length of 20 mm (i.e., SG1 to SG8 and SG9 to SG16) were respectively installed along Section B and Section C, 300 mm above or below Section A, to measure the strains of the GFRP tube (Figure 7.1). Four LVDTs (LT1 to LT4) covering the 320-mm middle region of the specimen were located at different distances from the applied load to record axial shortenings while five LVDTs (LT5 to LT9) were installed at different heights to monitor lateral deflection of the specimens in the bending direction. In addition, four LVDTs (LT10 to LT13) were fixed on the top and the bottom ends of the specimens to monitor end rotation.

For creating pinned-end conditions, an end loading assembly consisting of a set of loading plates and a roller was designed to ensure accurate control of load eccentricity. At each specimen end, a rigid steel cap plate with a central hole was welded at the end of the inner steel tube. A detachable steel plate was bolted with the steel cap at the designated location to ensure the desired eccentricity (see Figure 7.2). The detachable steel plate was machined with an 8 mm deep semi-circular groove to nest a steel roller whose opposite side was welded with a fixed steel plate to receive the force from the loading machine and transfer it to the detachable plate. The distance between the

centers of the two steel rollers is the sum of the specimen clear length of 1200 mm and the height of the end loading assembly of 180 mm. Before testing, the groove of the detachable plates and the steel rollers were carefully lubricated.

Originally, the diameter of the hole on the steel caps was designed to be larger than the outer diameter of the steel tube, so the connection between the steel tube and the steel cap completely depended on the welds. The design was proved unsuccessful in the testing of Specimen CE325-10-P4N-100 (damaged) as an obvious separation between the steel tube and the steel cap was observed after test due to the destroy of the welds on the compression side of the column as shown in Figure 7.3. The separation caused unloading of the steel tube and thus a sudden increase of compressive load in the concrete, leading to unexpected rupture of the FRP tube near the upper quarter region instead of the middle-height region due to the local crushing of concrete at the corresponding position (see Figure 7.3). For avoiding this undesirable failure mode, the diameter of the hole in the steel cap on the compression side was modified to be equal to the inner diameter of the steel tube as shown in Figure 7.4. Thus, the steel caps could rest on the ends of the steel tube on the compression side to directly deliver the compressive load from the steel caps to the steel tube. The subsequent test results proved that this modification was successful. The test on Specimen CE325-10-P4N-100 was conducted again using a new specimen with the new design. The test results of Specimen CE325-10-P4N-100 in Table 7.1 are for this new specimen rather than the damaged one.

All eccentric compression tests were also carried out using a 10,000 kN servo-hydraulic testing machine with displacement control at a constant rate of 0.60mm/minute as shown in Figure 7.5. All test data, including loads, strains and

displacements, were recorded simultaneously by a data logger.

## **7.3 TEST RESULTS AND DISCUSSIONS**

### **7.3.1 Test Observations**

Figure 7.6 displays the failure mode of all eccentrically-loaded hybrid DSTC specimens. Three photos are provided from left to right for each specimen to show the compression side, the profile and the tension side of the same failed specimen, respectively.

All specimens failed by the rupture of the outer GFRP tube at the compression side at or near specimen mid-height while tensile cracks of the GFRP tube developed along the fiber direction on the tension side due to the damage of resin (Figure 7.6). For specimens with the same FRP tube, those loaded under a larger eccentricity experienced a larger rotation and exhibited more noticeable tensile cracks on the tension side because of the larger bending. The inner steel tube buckled due to the combined effect of axial shortening and bending, as revealed by the removal of the surrounding concrete after test (see Figure 7.7).

### **7.3.2 Axial Strain Distribution over Mid-height Section**

Figure 7.8 shows the distribution of axial strains over the mid-height section under different load levels. In Figure 7.8, the hollow symbols represent the axial strains of the GFRP tube at five different positions relative to the centerline of the section and the solid ones represent the axial strains of the steel tube also at five different positions relative to the centerline of the section. The axial strains at the middle three positions were averaged from the axial strain readings of the pair of strain rosettes with the same

horizontal distance from the centerline. The following observations can be made from Figure 7.8: (1) in the initial stages of loading, the axial strains of the steel tube and the GFRP tube generally distribute along the same line. The only exception is Specimen CE325-8-P4S-50 whose axial strain at the extreme compression fiber is not large enough to satisfy the plane section assumption; (2) when the maximum axial strain of the steel tube reaches about 0.0015 (approximately the yield strain of steel), some axial strain values of the steel tube start to deviate from the linear strain distribution due to the non-uniform local plastic deformation of the steel tube; (3) when the maximum axial strain of the FRP tube exceeds about 0.0025 (approximately the axial strain at the compressive strength of unconfined concrete), the axial strain distribution of the FRP tube in some specimens begin to exhibit noticeable nonlinearity as a result of the local damage of concrete; and (4) the neutral axis sustains movement towards the center of the section with the increase of compressive load (i.e. the compression zone becomes smaller) due to the formation of tensile cracks at the tension side of specimen. The trend of neutral axis movement is clearer in specimens with a larger eccentricity.

### **7.3.3 Column Lateral Deflection**

Figure 7.9 shows the development of lateral deflection along the height of columns during the tests. The lateral deflections were obtained from the readings of five LVDTs installed at different heights of the columns (LT5 to LT9 in Figure 7.1). In each sub-figure of Figure 7.9, each curve represents the lateral deflection of a specific column under a specific axial load level. After the peak load is reached, the deflection curves are related to different axial strain levels at the extreme compression fiber of concrete instead. It can be seen from Figure 7.9 that the lateral deflection was relatively small in the initial loading stage; indeed, the readings of some LVDTs of Specimen CE325-10-P4N-80 were even negative due to geometric and material imperfections. The

development of the lateral deflection was rapidly accelerated as the axial load increased especially after the peak axial load was reached. In the later loading stages, the lateral deflection curves become approximately symmetrical.

#### **7.3.4 Axial Load-Axial Strain Response**

The concrete at the extreme compression fiber was most heavily stressed over the entire section, so its response plays a key role in the determination of the response of the whole section. The axial load-axial strain curves at the extreme compression fiber of concrete are shown in Figures 7.10 and 7.11. The corresponding concentrically-loaded specimens were also included for comparison. For the concentrically-loaded specimens, the axial strains were averaged from the readings of four LVDTs covering the 320 mm middle-height region of columns while those of the eccentrically-loaded specimens were obtained from the readings of the LVDT installed near the most compression fiber of concrete (i.e., LT1 in Figure 7.1). Of interest is that except CE325-8-P6S-150, all eccentrically-loaded specimens experienced a sudden axial load drop in the transition zone of the axial load-axial strain curves, a phenomenon similar to that observed in concentrically-load DSTC specimens with SCC presented in Chapter 6, but to a much less significant extent. Subsequently, the load rose again and the first peak load was gradually recovered. This process is reflected by a portion of flat and approximately linear axial load-axial strain curve in Figures 7.10 and 7.11. After the outer FRP tube ruptured (i.e., ultimate condition being reached), the eccentrically-loaded DSTCs still experienced a period of increasing deflection with a slow decrease of load, indicating excellent ductility. It is worth noting that for Specimens CE325-8-P4S-50 and CE325-8-P6S-100, the axial load experienced several small falls and rises after reaching the peak load.

The effect of load eccentricity on the axial load-axial strain responses is examined in Figure 7.10 where specimens with the same steel tube and the same GFRP tube are grouped together. It can be seen that the specimens with a larger eccentricity have a smaller initial stiffness and a lower axial load capacity due to the larger moment. Similar findings have also been reported by Yu *et al.* (2010a) based on their eccentric compression tests on small-scale hybrid DSTCs. In addition, the axial strain of hybrid DSTCs at the extreme compression fiber at ultimate condition (i.e., FRP rupture) increases with increasing load eccentricity. For example, the axial strain at ultimate condition of Specimen CE325-8-P4S-50 with an eccentricity of 50 mm is about 130% higher than that of the corresponding specimen subjected to concentric compression (i.e., Specimens CC325-8-P4S). This phenomenon is termed “axial strain enhancement effect” and has also been observed in RC columns (Scott et al. 1982) and FRP-confined RC columns (Bisby and Ranger 2010; Csuka and Kollár 2012; Zhang 2014). It is believed that this phenomenon occurs because an axial strain gradient exists as a result of eccentric compression. Therefore, the concrete at the more compressed region has a tendency to dilate to the less compressed region.

Figure 7.11 examines the effect of FRP tube thickness on the axial load-axial strain responses by comparing the responses of Specimens CE325-8-P4S-50 and CE325-8-P6S-50. The only difference between these two specimens was the thickness of the FRP tubes. It can be seen that Specimen CE325-8-P6S-50 had a higher first peak axial load due to its thicker FRP tube; however, the two specimens exhibited very similar responses after the occurrence of the axial load drop. This is because the role of FRP confinement becomes less significant once a drop in the axial load occurs due to the local damage of concrete.

### 7.3.5 Key Test Results

The key test results of the eccentrically-loaded and the corresponding concentrically-loaded DSTCs are summarized in Table 7.2. In this table,  $N_u$  is the axial load of a hybrid DSTCs from test at ultimate condition, and  $M_u$  and  $\varepsilon_{cu}$  are the corresponding moment and the corresponding axial strain of the extreme compression fiber at the mid-height section.  $M_u$  is composed of the first-order moment due to the initial eccentricity  $e$  and the second-order moment due to lateral deflection  $e'_u$  at ultimate condition. It is evident that the axial load at ultimate condition decreases but the corresponding moment increases with the load eccentricity.  $\varepsilon_{cu}$  also increases with the load eccentricity due to the axial strain enhancement effect mentioned earlier. It should be noted that  $N_u$  is not the peak axial load for Specimens CE325-8-P4S-50, CE325-8-P6S-100 and CE325-8-P6S-150 as the peak axial load was reached prior to reaching the ultimate condition due to the sudden drop in the axial load in these specimens. The bracketed numbers in Table 7.2 represent the peak axial load of these specimens and the corresponding values of moment, lateral deflection, and axial strain at extreme compression fiber at the mid-height section.

## 7.4 THEORETICAL ANALYSIS

### 7.4.1 Eccentricity-Dependent (EccD) Stress-Strain Models

Eccentricity-dependent (EccD) stress-strain models for FRP-confined concrete subjected to eccentric compression were generally developed by modifying concentric-loading stress-strain models known as “eccentricity-independent (EccI) stress-strain models”. In the process, the ratios between the parameters subjected to concentric compression and those subjected to eccentric compression were directly or indirectly related to the load eccentricity. Lin (2016) developed an EccD stress-strain

model for FRP-confined concrete based on Teng *et al.*'s (2009) design-oriented stress-strain model. Yu *et al.* (2010b) proposed an EccD stress-strain model for confined concrete in hybrid DSTCs based on a previous EccI stress-strain model developed by the same research group (Yu *et al.* 2010a). Yu *et al.*'s (2010a) EccI stress-strain model has been presented in Chapter 6 and is referred to as Yu *et al.*'s EccI model hereafter. The above two EccD models are described in detail below.

#### 7.4.1.1 Yu *et al.*'s (2010b) EccD Model

Considering the reduced effectiveness of FRP confinement on concrete as a result of the existence of the strain gradient under eccentric compression, a so-called “variable confinement model” for confined concrete in hybrid DSTCs was proposed by Yu *et al.* (2010b) (referred to as “Yu *et al.*'s EccD model” hereafter) where only the second-portion slope is dependent on the load eccentricity adopting an expression proposed by Fam *et al.* (2003)

$$E_{2,ecc} = E_{2,con} \frac{D_o}{D_o + e_{sum}} \quad (7.1)$$

where  $E_{2,con}$  and  $E_{2,ecc}$  are the second-portion slope for concentric and eccentric compression cases, respectively;  $D_o$  is the outer diameter of annular concrete section;  $e_{sum}$  is the total eccentricity which is the sum of the initial eccentricity  $e$  and the lateral deflection  $e'$ .  $E_{2,con}$  can be calculated using Eq. (6.4). Yu *et al.*'s EccD model does not consider the axial strain enhancement effect, so the ultimate axial strain predicted by Yu *et al.*'s EccD is the same as that predicted by Yu *et al.*'s EccI model [see Eq. (6.9)]. As a result, the only difference between the two models is that the former suggests a reduction in axial stress of confined concrete in hybrid DSTCs due to eccentricity through decreasing the second-portion slope of axial stress-axial strain

curve. Note that  $E_2$  in Eqs. (6.1), (6.2) and (6.3) should be replaced by  $E_{2,ecc}$  when a stress-strain curve is generated using the EccD stress-strain model.

#### 7.4.1.2 Lin's (2016) EccD Model

Lin (2016) suggested that both the second-portion slope and the ultimate axial strain of confined concrete at the extreme compression fiber are a function of the outer diameter-to-compression depth ratio ( $D_o/c$ ), where  $D_o$  is the outer diameter of concrete and  $c$  is the depth of the compression region (i.e. depth of neutral axis).

$$E_{2,ecc} = E_{2,con} \left( 1 - 0.00808 \frac{D_o}{c} \right), \frac{D_o}{c} \leq 12.4 \quad (7.2)$$

$$\varepsilon_{cu,ecc} = \varepsilon_{cu,con} \left[ 1 + 0.263 \frac{D_o}{c} + 0.0227 \left( \frac{D_o}{c} \right)^2 \right], \frac{D_o}{c} \leq 12.4 \quad (7.3)$$

where  $\varepsilon_{cu,con}$  and  $\varepsilon_{cu,ecc}$  are respectively the ultimate axial strain of confined concrete for concentric and eccentric compression cases.  $\varepsilon_{cu,con}$  can be calculated using Eq. (6.9). For simplicity, the model is referred to as “Lin’s EccD model” hereafter. Lin’s EccD model employs the same axial stress-axial strain equations as Yu *et al.*’s EccI model.

To illustrate the difference between Yu *et al.*’s EccD model and Lin’s EccD model, the non-dimensional axial stress-axial strain curves generated by the two models are displayed in Figure 7.12. It is evident that the stress-strain curves of the EccD stress-strain models have a lower second-portion slope than the EccI stress-strain model. The main difference between Yu *et al.*’s EccD model and Lin’s EccD model is that the ultimate axial strain ( $\varepsilon_{cu}$ ) is eccentricity-independent for the former while  $\varepsilon_{cu}$

increases with the eccentricity for the latter. In this aspect, Lin's EccD model is more reasonable because it catches the axial strain enhancement effect of confined concrete in eccentrically-loaded hybrid DSTCs described in Sub-sections 7.3.4 and 7.3.5. Lin's EccD model suggests a small increase of ultimate axial stress of confined concrete under eccentric compression compared with the corresponding concentric compression case due to the combined effect of second-portion slope decreasing and ultimate axial strain increasing with the load eccentricity (Lin 2016). Yu *et al.*'s EccI model", Yu *et al.*'s EccD model and Lin's EccD model are employed to represent the stress-strain response of confined concrete over the whole column section and incorporated into a theoretical column model to model the behavior of hybrid DSTCs under eccentric compression. The theoretical column model is presented in the following Sub-section.

#### **7.4.2 Theoretical Column Model**

The theoretical column model was modified from Jiang and Teng's (2012a) column model for FRP-confined RC columns which can capture the slenderness effect in columns. The use of a column model instead of simple section analysis for short hybrid DSTCs is intended to achieve higher accuracy of analysis since a certain slenderness effect existed in the tested columns despite their short length, as indicated by the noticeable lateral deflection of columns (see Figure 7.9). Jiang and Teng's (2012a) column model employs the well-known numerical integration method to generate the full-range axial load-lateral deflection curve (referred to as the load-deflection curve for brevity) of a column. In the analysis procedure, the column is divided into a desirable number of segments and the column section at each grid point is divided into a desirable number of horizontal layers. Section analysis is carried out at each grid point to construct the axial load-moment-curvature relationship. The lateral

displacement at each grid point at a particular loading stage is sought in an iterative manner by making use of the axial load-moment-curvature relationship of the column section and the numerical integration function of the column. The full-range load-deflection curve can then be traced in an incremental manner using either a force-control or deflection-control technique. Jiang and Teng's (2012a) column model incorporates Teng *et al.*'s (2009) stress-strain model for FRP-confined concrete for carrying out section analysis at each grid point without considering the effect of eccentricity on the stress-strain relationship of FRP-confined concrete. Details of this column model can be found in Jiang and Teng (2012a).

In the present theoretical column model for hybrid DSTCs, the framework of Jiang and Teng's (2012a) column model is retained; the main modification is the employment of a stress-strain model for confined concrete in hybrid DSTCs instead of Teng *et al.*'s (2009) stress-strain model for FRP-confined concrete. In the analysis procedure without considering the effect of eccentricity on the stress-strain relationship of the confined concrete in eccentrically-loaded hybrid DSTCs, Yu *et al.*'s EccI model was directly used. In the analysis procedure considering the effect of eccentricity, Yu *et al.*'s EccD model and Lin's EccD model were respectively employed. Note that the position of the neutral axis which varies during the analysis procedure using Lin's EccD model should be determined through an iterative process to reach the force equilibrium for each axial strain value. On the other hand, it should also be noted that the actual eccentricity is the sum of the initial load eccentricity and the lateral deflection varied at each grid point along the height of the column [see Eq. (7.1)], thus the analysis procedure using Yu *et al.*'s EccD model needs to update the stress-strain curve of concrete at each grid point for each lateral deflection value. The inner steel tube was assumed to have an elastic-perfectly plastic stress-strain behavior

in the longitudinal direction and its lateral confinement effect on the concrete was ignored.

For the outer FRP tube, based on Jones and Nelson's (1975) model presented in Chapter 5, a simple axial stress-axial strain model (see Figure 7.13) (referred to as "simple model" hereafter for brevity) was established to consider its progressive reduction of axial stiffness and used to calculate the axial load resisted by the FRP tube in the theoretical analysis. The simple model features a bilinear shape in both compression and tension conditions and can be represented by the following equations

$$\begin{cases} \sigma_x = E_x \varepsilon_x & \text{if } \varepsilon_x \leq 0.004 \\ \sigma_x = 0.004E_x + \frac{(0.04E_{x,tan}^* - 0.004E_x)(\varepsilon_x - 0.004)}{0.036} & \text{if } \varepsilon_x > 0.004 \end{cases} \quad (7.4)$$

where  $\sigma_x$  and  $\varepsilon_x$  are the axial stress and the axial strain of the FRP tube, respectively;  $E_x$  is the axial modulus of elasticity of the FRP tube obtained from the axial compression tests on bare FRP tubes presented in Chapter 3;  $E_{x,tan}^*$  is the tangent axial modulus of elasticity at the peak load of the bare FRP tube under axial compression. The values of both  $E_x$  and  $E_{x,tan}^*$  are listed in Table 7.1. For a composite lamina under a biaxial stress state, Jones and Morgan (1977) suggested that the secant value of a material property should decrease with its strain energy density ( $U$ ) and reach asymptotically its tangent value at the peak load when its strain energy density ( $U$ ) approaches infinity. Due to the 1D nature of the analytical approach, it was not possible to calculate the hoop strain of the FRP tube, so it was not possible to calculate the strain energy density ( $U$ ) of FRP tube either [see Eq. (5.7)]. Thus the simple model assumes that the axial modulus of elasticity of the FRP tube keeps constant  $E_x$  before the axial strain reaches 0.004 while it gradually decreases from

$E_x$  to  $E_{x,tan}^*$  when the axial strain increases from 0.004 to 0.04 as shown in Figure 7.13. Normally the ultimate axial strain of the GFRP tube would not exceed 0.04 even under a biaxial stress state.

It is worth noting that the axial strain  $\varepsilon_x$  in the simple model is solely caused by uniaxial compression, that is to say the axial strain caused by the Poisson's effect should be removed from the total axial strain when using the simple model for FRP tubes under a biaxial stress state. To demonstrate the effect of the Poisson's ratio, an example is given in Figure 7.13 for a CFFT specimen (Specimens N2-400-I) presented in Chapter 5. Two experimental axial stress-axial strain curves of the GFRP tube of that specimen are shown, either with or without considering the Poisson's effect. The predicted curve of the simple model is also shown for comparison. It can be seen that the predicted curve agrees well with the experimental curve with considering the Poisson's effect (i.e., the axial strain caused by the Poisson's effect is removed from the measured axial strain), while it appears noticeably higher than the experimental curve without considering the Poisson's effect (i.e., the axial strain caused by the Poisson's effect is not removed from the measured axial strain). In other words, the axial load undertaken by the FRP tube is overestimated by the simple model if the measured axial strain is directly used.

It should be pointed out that the true hoop rupture strains of FRP tubes  $\varepsilon_{h,rupt}$  were not captured in the present tests as almost all strain gauges were damaged before specimen failure. So the nominal FRP hoop rupture strains  $\varepsilon'_{h,rupt}$  obtained from the concentrically-loaded specimens presented in Chapter 6 were directly used in the analysis of the corresponding eccentrically-loaded specimens. The values of the nominal hoop rupture strains are also given in Table 7.2.

### 7.4.3 Comparison with Test Results

The experimental and the predicted axial load-axial strain at extreme compression fiber curves are compared in Figure 7.14 for all six eccentrically-loaded hybrid DSTCs. In Figure 7.14, two experimental curves with the axial strain being respectively obtained from the readings of strain gauge (i.e., SR9 in Figure 7.1) and LVDTs installed near the extreme compression fiber (i.e., LT1 in Figure 7.1) are shown for each specimen for comparison. The two experimental curves are very close to each other before the strain gauges were damaged, suggesting the acceptability of using the readings of LVDT to represent the axial strain at the extreme compression fiber. On the other hand, the solid circular points on the experimental curves are used to represent the ultimate condition of the corresponding specimens (i.e., FRP rupture).

The analysis procedure terminates as the hoop strain at the extreme compression fiber of FRP tube reaches its nominal hoop rupture strain ( $\epsilon'_{h,rupt}$ ). The curves predicted respectively using Yu *et al.*'s EccI model, Yu *et al.*'s EccD model and Lin's EccD model were produced in the following two ways: (1) ignoring the axial load carried by the outer FRP tube; the so-obtained curves are labeled as "Yu *et al.*'s EccI model-1", "Yu *et al.*'s EccD model-1" and "Lin's EccD model-1" in Figure 7.14; (2) axial load taken by FRP tube being identified using the simple model presented above; the so-obtained curves are labeled as "Yu *et al.*'s EccI model-2", "Yu *et al.*'s EccD model-2" and "Lin's EccD model-2" in Figure 7.14. In the latter, it was not possible to consider the Poisson's effect due to the 1D nature of the analytical approach, so the axial load resisted by the FRP tube was overestimated by the simple model. On the other hand, the total axial load predicted by the former must be smaller than that by the latter. Nevertheless, the two predicted curves are very close to each other in all cases. Thus,

the theoretical analysis with the contribution of the FRP tube to the total axial load ignored is considered acceptable due to its simplicity.

Furthermore, Figure 7.15 compares the experimental and the predicted load-deflection curves of the column mid-height. The experimental lateral deflection was obtained from the readings of the LVDT installed horizontally at the column mid-height (i.e., LT5 in Figure 7.1). For Specimens CE325-10-P4N-80, CE325-8-P4S-50 and CE325-P6S-50, the predicted curves evidently deviate from the experimental ones before the curves bend over. This may be due to the errors arising from the unstable pinned-end condition in the initial loading stages. Specifically, the steel rollers were not completely nested in the semi-circular grooves on the detachable plates when the applied axial load was respectively small. Indeed, the lateral deflection over the column height for these three specimens was less symmetrical than the others, as shown in Figure 7.9 (a), (c) and (e). The unstable condition was gradually mitigated as the axial load increased.

It can be seen from Figure 7.14 that the theoretical results produced by the column model with the separate incorporation of the three stress-strain models all underestimate the axial strain at extreme compression fiber at ultimate condition with Lin's EccD model performing better than the other two as a result of taking the axial strain enhancement effect into account. For the same reason, Lin's EccD model is also more accurate than the other two models in predicting the lateral deflection at ultimate condition, as can be seen from Figure 7.15. For the prediction of the axial load at ultimate condition, although all three models fail to predict the sudden drop in the axial load, all of them provide rather accurate predictions. This is because the drop in the axial load was not significant and the such-induced overestimation is partially

compensated by ignoring the axial load contribution of FRP tube in the analysis procedure. The overestimation is further compensated by considering compressive strength reduction of confined concrete due to eccentricity in Yu *et al.*'s EccD model. As a result, Yu *et al.*'s EccD model appears to be more accurate in predicting the axial load capacity of the specimens. The predicted values of  $N_u$ ,  $M_u$ ,  $\epsilon_{cu}$  and  $e'$  are summarized in Table 7.2.

#### 7.4.4 Axial Load-Bending Moment Interaction Diagrams

The axial load-bending moment ( $N$ - $M$ ) interaction diagrams constructed by the results of section analysis are shown in Figure 7.16, with each sub-figure showing three  $N$ - $M$  curves respectively produced using Yu *et al.*'s EccI model, Yu *et al.*'s EccD model and Lin's EccD model, for hybrid DSTCs with the same test configurations except the load eccentricity. In the section analysis, the contribution of FRP tube to the total axial load was ignored. It can be seen that the interaction curves generated by the three models are very close to each other, indicating that the compressive strength reduction and the axial strain enhancement behavior of the confined concrete due to eccentricity only have a small influence on the section strength of hybrid DSTCs.

In Figure 7.16, the experimental  $N$ - $M$  paths radiating from the origin are also shown for comparison. The solid symbol on each experimental  $N$ - $M$  path represents the ultimate condition of the corresponding specimen. All solid symbols lie in the neighborhood of the theoretical interaction curves, indicating that the ultimate condition of specimens was fairly well predicted. In Figure, 7.16, each experimental  $N$ - $M$  path is accompanied with a straight line representing the  $N$ - $M$  path in the absence of slenderness effect (i.e., the height of the column is reduced to zero). The interception of the straight line with the section interaction curve represents the axial load capacity

of the zero-height column. It can be seen that the experimental  $N-M$  paths closely follow the accompanying straight line till an axial load level close to the axial load at ultimate condition and then gradually bend over and deviate from the straight line till the axial load at ultimate condition is reached. This indicates that the slenderness effect in the specimens tested was not significant because it can be inferred that the reduction of axial load capacity due to the slenderness effect was small.

## 7.5 CONCLUSIONS

This chapter has presented a test program on six large-scale short hybrid DSTCs under eccentric compression. A theoretical column model instead of simple section analysis is employed as the analytical tool to achieve higher accuracy of analysis. In the column model, Yu *et al.*'s EccI model, Yu *et al.*'s EccD model and Lin's EccD model are respectively incorporated to describe the stress-strain behavior of confined concrete in hybrid DSTCs. On the basis of the test results and their comparisons with the theoretical results presented in the chapter, the following conclusions can be drawn:

- (1) The failure mode of eccentrically-loaded short hybrid DSTCs is the rupture of the outer FRP tube at the compression side at or near specimen mid-height. Buckling of the inner steel tube may occur due to the combined effect of axial shortening and bending.
- (2) The axial load capacity of eccentrically-loaded short hybrid DSTCs decreases with load eccentricity and increases with thickness of FRP tubes. Short hybrid DSTCs may experience a sudden drop in axial load once the unconfined concrete strength is reached, a phenomenon similar to that observed in the concentric compression tests on hybrid DSTCs presented in Chapter 6, but to a much less significant extent.

- (3) When a hybrid DSTC is loaded under eccentric compression, an axial strain gradient exists over its section with the distribution of axial strains generally conforming to the plane section assumption. The axial strain gradient causes the concrete at the more compressed region to have a tendency to dilate to the less compressed region. As a result, the same concrete in a hybrid DSTC features a larger axial strain at ultimate condition under eccentric compression than under concentric compression. This phenomenon is termed “axial strain enhancement effect” and indicates that the eccentricity has a certain effect on the stress-strain behavior of confined concrete in hybrid DSTCs.
- (4) When incorporated into the theoretical column model, Yu *et al.*'s EccI model, Yu *et al.*'s EccD model and Lin's EccD model all provide fairly accurate predictions for the axial load capacity of eccentrically-loaded hybrid DSTCs. However, Lin's EccD model performs much better in predicting the axial strain and the lateral deflection of eccentrically-loaded hybrid DSTCs because it takes the axial strain enhancement effect into consideration. Therefore, Lin's EccD model is recommended for future use.
- (5) The contribution of the FRP tube to the axial load resistance of hybrid DSTCs is shown to be small enough to be neglected in the analysis procedure. This treatment is conservative and simplifies the analysis procedure.

## **7.6 REFERENCES**

- Bisby, L. and Ranger, M. (2010). “Axial-Flexural Interaction in Circular FRP-Confined Reinforced Concrete Columns”, *Construction and Building Materials*. Vol. 24(9), pp.1672-1681.

- Csuka, B. and Kollár, L.P. (2012). "Analysis of FRP Confined Columns under Eccentric Loading", *Composite Structures*. Vol. 94(3), pp.1106-1116.
- El Maaddawy, T. (2008). "Behavior of Corrosion-Damaged RC Columns Wrapped with FRP under Combined Flexural and Axial Loading", *Cement and Concrete Composites*. Vol. 30(6), pp.524-534.
- El Sayed, M. and El Maaddawy, T. (2011). "Analytical Model for Prediction of Load Capacity of RC Columns Confined with CFRP under Uniaxial and Biaxial Eccentric Loading", *Materials and Structures*. Vol. 44(1), pp.299-311.
- Fam, A., Flisak, B. and Rizkalla, S. (2003). "Experimental and Analytical Modeling of Concrete-Filled Fiber-Reinforced Polymer Tubes Subjected to Combined Bending and Axial Loads", *ACI Structural Journal*. Vol. 100(4), pp.499-509.
- Fitzwilliam, J. (2006). "Fibre-Reinforced Polymer Wraps for Slender Eccentrically-Loaded Reinforced Concrete Columns", M.Sc. thesis, Queen's University, Kingston, Ontario, Canada.
- Fitzwilliam, J. and Bisby, L.A. (2010). "Slenderness Effects on Circular CFRP Confined Reinforced Concrete Columns", *Journal of Composites for Construction*, ASCE. Vol. 14(3), pp. 280-288.
- GB50608 (2010). "Technical Code for Infrastructure Application of FRP Composites", China Planning Press, Beijing, China. (in Chinese)
- Hadi, M.N.S. (2006a). "Behaviour of FRP Wrapped Normal Strength Concrete Columns under Eccentric Loading", *Composite Structures*. Vol. 72(4), pp.503-511.
- Hadi, M.N.S. (2006b). "Comparative Study of Eccentrically Loaded FRP Wrapped Columns", *Composite Structures*. Vol. 74(2), pp.127-135.
- Hadi, M.N.S. (2007). "The Behaviour of FRP Wrapped HSC Columns under Different Eccentric Loads", *Composite Structures*. Vol. 78(4), pp.560-566.

- Jiang, T. and Teng, J.G. (2012a). “Theoretical Model for Slender FRP-Confined Circular RC Columns”, *Construction and Building Materials*. Vol. 32(4), pp.66-76.
- Jiang, T. and Teng, J.G. (2012b). “Slenderness Limit for Short FRP-Confined Circular RC Columns”, *Journal of Composites for Construction*, ASCE. Vol. 16(6), pp.650-661.
- Jiang, T. and Teng, J.G. (2013). “Behavior and Design of Slender FRP-Confined Circular RC Columns”, *Journal of Composites for Construction*, ASCE. Vol. 17(4), pp.443-453.
- Jiang, T., Zhang, X.Q., Yao, J. and Luo, Y.Z. (2014). “Stress-Strain Behaviour of FRP-Confined Concrete Subjected to Eccentric Compression”, *Proceedings, 13th International Symposium on Structural Engineering (ISSE-13)*, pp.441-449.
- Jones, R.M. and Nelson JR, D.A.N. (1975). “A New Material Model for the Nonlinear Biaxial Behavior of ATJ-S Graphite”, *Journal of Composite Materials*. Vol. 9, pp.10-27.
- Jones, R.M. and Morgon, H.S. (1977). “Analysis of Nonlinear Stress-Strain Behavior of Fiber-Reinforced Composite Material”, *AIAA Journal*. Vol.15(12), pp. 1669-1676.
- Lin, G. (2016). “Seismic Performance of FRP-Confined RC Columns: Stress-Strain Models and Numerical Simulation”, Ph.D. thesis, The Hong Kong Polytechnic University, Hong Kong, China.
- Ma, Z.Q. (2013). “Performance Investigation of FRP-Concrete-Steel Double-Skin Square Columns under Eccentric Compressive Loading”, M.Sc. thesis, Zhengzhou University, Zhengzhou, China. (in Chinese)
- Mosalam, K.M., Talaat, M. and Binici, B. (2007). “A Computational Model for Reinforced Concrete Members Confined with Fiber Reinforced Polymer Lamina:

- Implementation and Experimental Validation”, *Composites Part B: Engineering*. Vol. 38(5), pp.598-613.
- Ranger, M. (2007). Fibre-Reinforced Polymer Wraps for Strengthening Eccentrically-Loaded Reinforced Concrete Columns, M.Sc. thesis, Queen's University, Kingston, Ontario, Canada.
- Scott, B.D., Park, R. and Priestley, M.J.N. (1982). “Stress-Strain Behavior of Concrete Confined by Overlapping Hoops at Low and High Strain Rates”, *ACI Journal*. Vol. 79(2), pp.13-27.
- Tao, Z., Teng, J.G., Han, L.H. and Lam, L. (2004). “Experimental Behaviour of FRP-Confined Slender RC Columns under Eccentric Loading”, *Proceedings, Advanced Polymer Composites for Structural Applications in Construction (ACIC 2004)*, University of Surrey, Guildford, UK, pp.203-212.
- Teng, J.G., Jiang, T., Lam, L. and Luo, Y.Z. (2009). “Refinement of a Design-Oriented Stress-Strain Model for FRP-Confined Concrete”, *Journal of Composites for Construction*, ASCE. Vol. 13(4), pp.269-278.
- Wu, Y.F. and Jiang, C. (2013). “Effect of Load Eccentricity on the Stress-Strain Relationship of FRP-Confined Concrete Columns”, *Composite Structures*. Vol. 98, pp.228-241.
- Yu, T., Teng, J.G. and Wong, Y.L. (2010a). “Stress-Strain Behavior of Concrete in Hybrid Double-Skin Tubular Columns”, *Journal of Structural Engineering*, ASCE. Vol. 136(4), pp.379-389.
- Yu, T., Wong, Y.L. and Teng, J.G. (2010b). “Behavior of Hybrid FRP-Concrete-Steel Double-Skin Tubular Columns Subjected to Eccentric Compression”, *Advanced in Structural Engineering*. Vol. 13(5), pp.961-974.
- Zhang, X.Q. (2014). “Experimental Study of Stress-Strain Behavior of FRP-Confined Concrete Subjected to Eccentric Compression”, M.Sc. thesis, College of Civil

Engineering and Architecture, Zhejiang University, Hangzhou, China. (in Chinese)

**Table 7. 1 Geometric and material properties of DSTC specimens**

	Specimen	GFRP tube						Steel tube					Concrete			$D_{o,s}/t_s$	Void ratio $\phi$
		$D_{in}$ (mm)	$t_{frp}$ (mm)	$E_x$ (GPa)	$E_{x,tan}^*$ (GPa)	$\nu_{x\theta}$	$E_\theta$ (GPa)	$D_{o,s}$ (mm)	$t_s$ (mm)	$E_s$ (GPa)	$f_y$ (MPa)	$f_u$ (MPa)	$E_c$ (GPa)	$\epsilon_{co}$	$f'_{co}$ (MPa)		
1	CC325-10-P4N	401.7	1.89	10.44	5.67	0.099	34.43	325.0	10.13	218.2	289.1	414.0	24.26	0.00338	26.31	32.50	
	CE325-10-P4N-80	402.8	1.90										32.35	0.00268	46.12		
	CE325-10-P4N-100	401.8	1.95										32.47	0.00238	47.12		
2	CC325-8-P4S	401.1	1.80	10.39	6.25	0.124	40.55	325.0	8.0	206.0	261.0	314.0	33.19	0.00277	49.24	40.63	0.81
	CE325-8-P4S-50	401.6	1.80														
	CC325-8-P6S	399.1	2.42	11.75	6.24	0.102	41.60										
	CE325-8-P6S-50	401.2	2.52														
	CE325-8-P6S-100	401.1	2.65														
	CE325-8-P6S-150	399.2	2.58														

**Table 7. 2 Key test results of eccentrically-loaded DSTCs**

	Specimen	Experiment				Prediction <sup>b</sup>				<i>e</i> (mm)	$\epsilon'_{h,rupt}$
		$N_u$ (kN)	$\epsilon_{cu}$	$e'_u$ (mm)	$M_u$ (kN·m)	$N_u$ (kN)	$\epsilon_{cu}$	$e'_u$ (mm)	$M_u$ (kN·m)		
1	CC325-10-P4N	5174	0.0172	NA	NA	-	-	NA	NA	NA	0.00751
	CE325-10-P4N-80	3097	0.0181	8.72	274.77	3179/ 3164/ 3187	0.0113/ 0.0112/ 0.0151	7.42/ 7.38/ 9.58	277.89/ 276.45/ 285.50	80	0.00751
	CE325-10-P4N-100	2951	0.0322	11.12	327.92	2905/ 2892/ 2905	0.0103/ 0.0103/ 0.0132	7.33/ 7.26/ 8.76	311.78/ 310.21/ 315.92	100	0.00751
2	CC325-8-P4S	4049	0.0149	NA	NA	-	-	NA	NA	NA	0.00869
	CE325-8-P4S-50 <sup>a</sup>	3144 (3199)	0.0341 (0.0229)	10.71 (7.55)	190.87 (184.10)	3209/ 3197/ 3203	0.0103/ 0.0103/ 0.0131/	6.60/ 6.51/ 8.11	181.62/ 180.64/ 186.14	50	0.00869

	Specimen	Experiment				Prediction <sup>b</sup>				<i>e</i> (mm)	$\varepsilon'_{h,rupt}$
		$N_u$ (kN)	$\varepsilon_{cu}$	$e'_u$ (mm)	$M_u$ (kN·m)	$N_u$ (kN)	$\varepsilon_{cu}$	$e'_u$ (mm)	$M_u$ (kN·m)		
2	CC325-8-P6S	4298	0.0143	NA	NA	-	-	NA	NA	NA	0.00715
	CE325-8-P6S-50 <sup>a</sup>	3176	0.0234	13.11	200.44	3261/	0.0125/	7.97/	189.03/	50	0.00715
						3237/	0.0124/	7.77/	187.00/		
						3273	0.0169	10.84	199.12		
CE325-8-P6S-100 <sup>a</sup>	2378 (2429)	0.0376 (0.0212)	11.62 (7.12)	265.43 (260.19)	2546/	0.0129/	9.02/	277.62/	100	0.00715	
					2515/	0.0128/	8.90/	273.87/			
					2551	0.0178	11.87	285.33			
CE325-8-P6S-150 <sup>a</sup>	1916 (1942)	0.0420 (0.0222)	13.44 (8.79)	313.15 (308.37)	1984/	0.0128/	10.10/	317.68/	150	0.00715	
					1952/	0.0118/	8.79/	309.94/			
					1980	0.0176	13.08	322.89			

<sup>a</sup> Axial load at ultimate condition and peak axial load were not reached simultaneously;

<sup>b</sup> Yu *et al.*'s EccI model/ Yu *et al.*'s EccD model/ Lin's EccD model, the contribution of FRP tube to axial load being ignored.

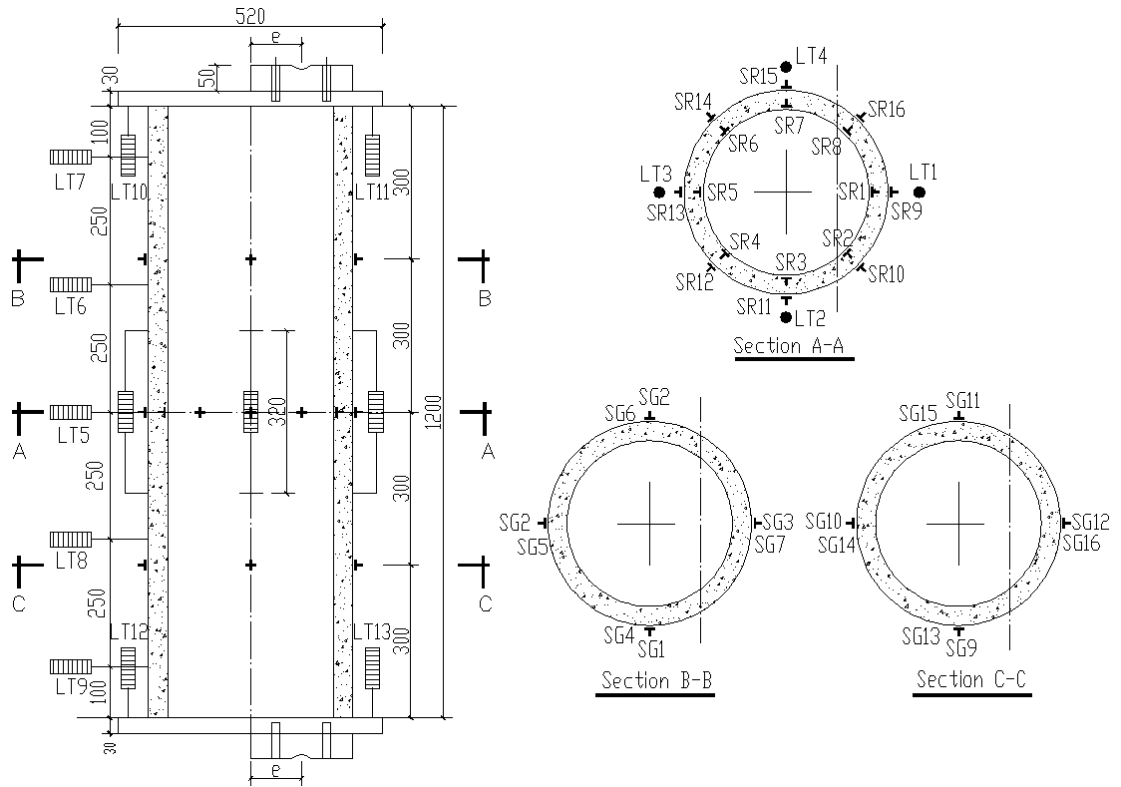
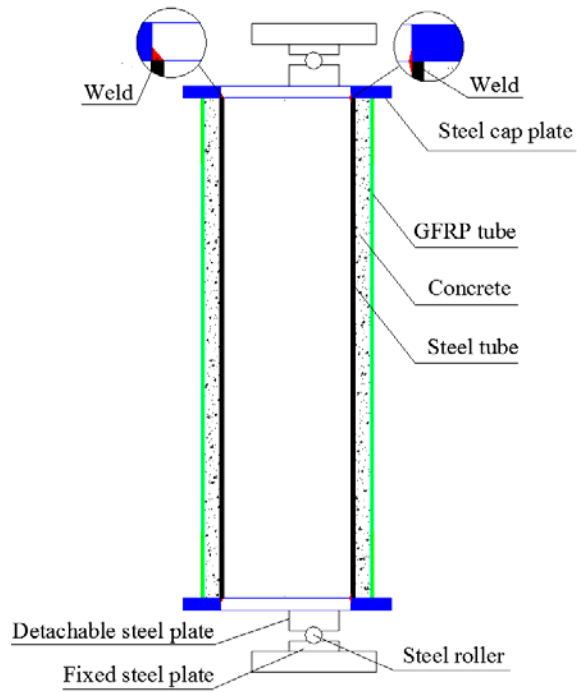


**Figure 7. 1** Layout of strain gauges and LVDTs



(a) Schematic diagram

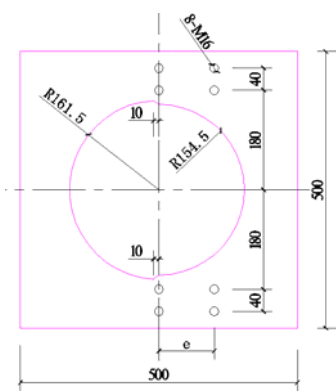


(b) Installation

**Figure 7. 2** End loading assembly



**Figure 7. 3** Local failure of specimen CE325-10-P4N-100 (damaged)



(a) Details of steel cap



(b) Steel cap

**Figure 7. 4** Steel cap of eccentrically-loaded DSTCs



**Figure 7. 5** Setup of eccentric compression tests on DSTCs



(a) CE325-10-P4N-80



(b) CE325-10-P4N-100



(c) CE325-8-P4S-50



(d) CE325-8-P6S-50



(e) CE325-8-P6S-100

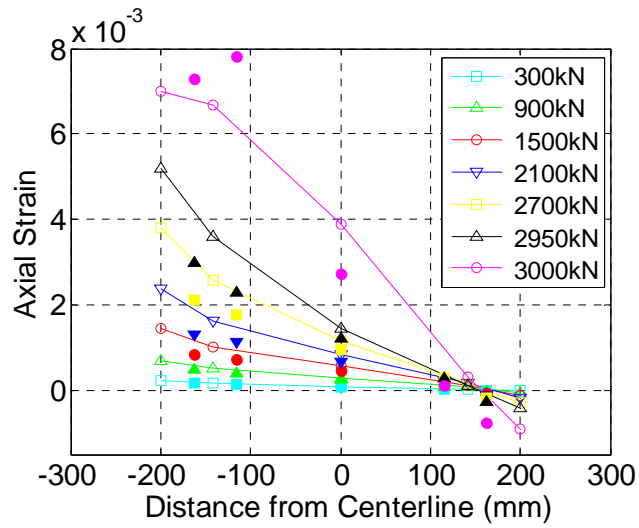


(f) CE325-8-P6S-150

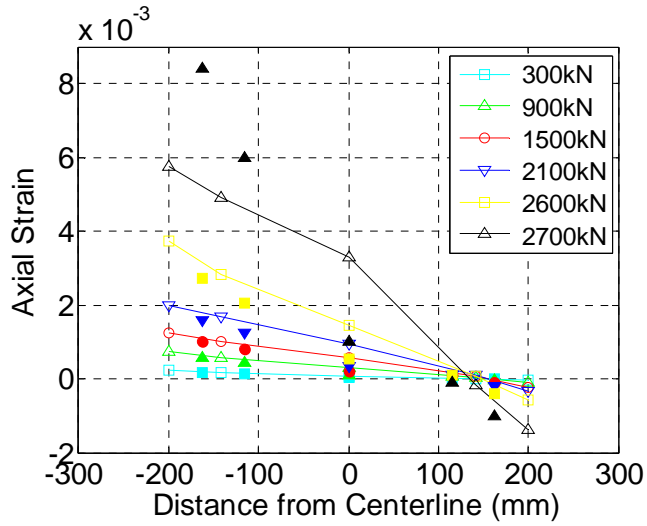
**Figure 7. 6** Failure mode of eccentrically-loaded DSTCs



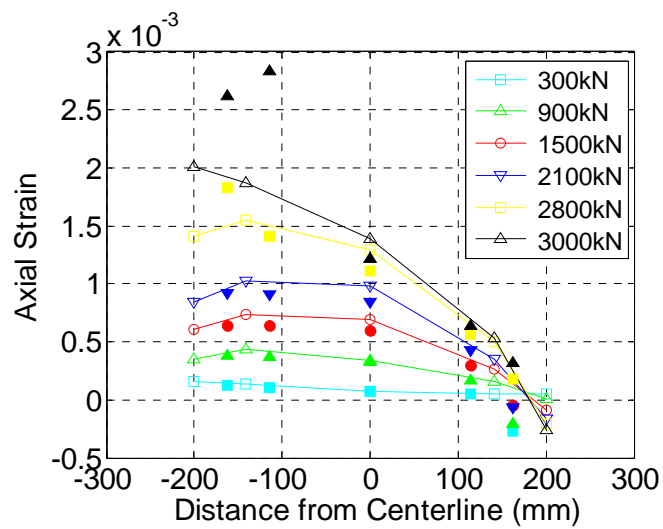
**Figure 7. 7** Buckling of inner steel tube



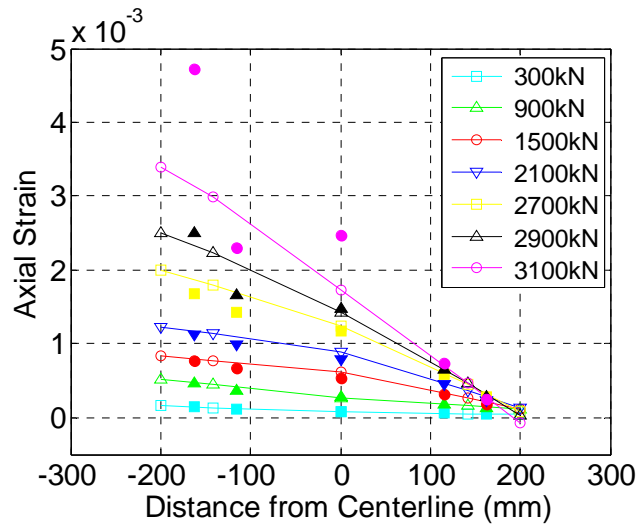
(a) CE325-10-P4N-80



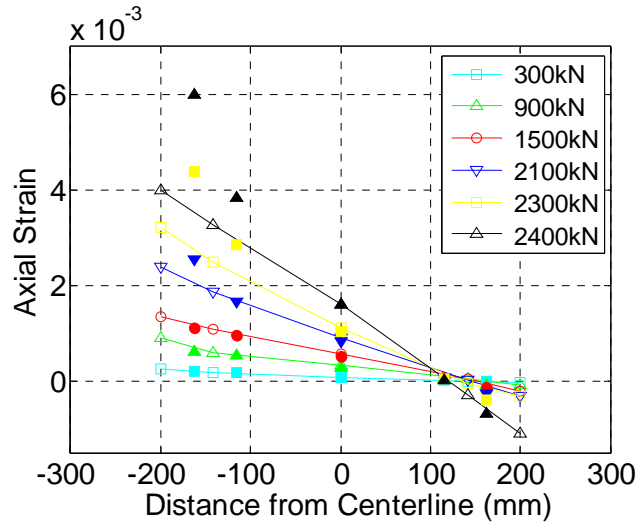
(b) CE325-10-P4N-100



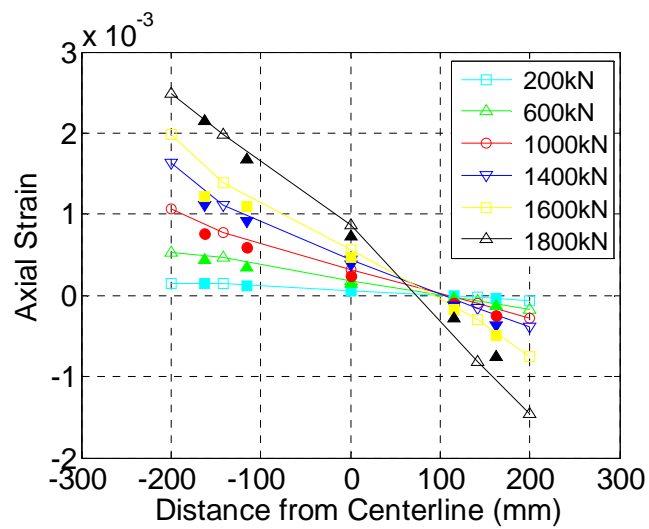
(c) CE325-8-P4S-50



(d) CE325-8-P6S-50

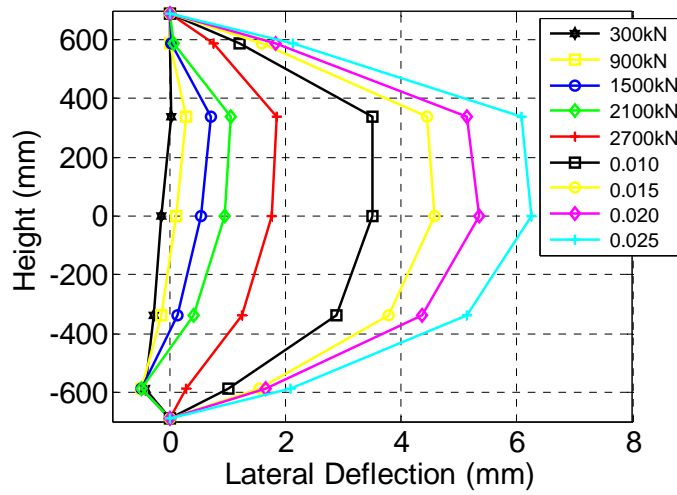


(e) CE325-8-P6S-100

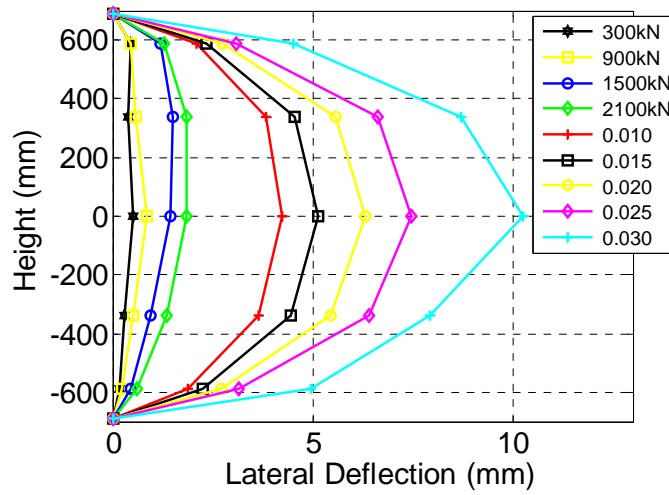


(f) CE325-8-P6S-150

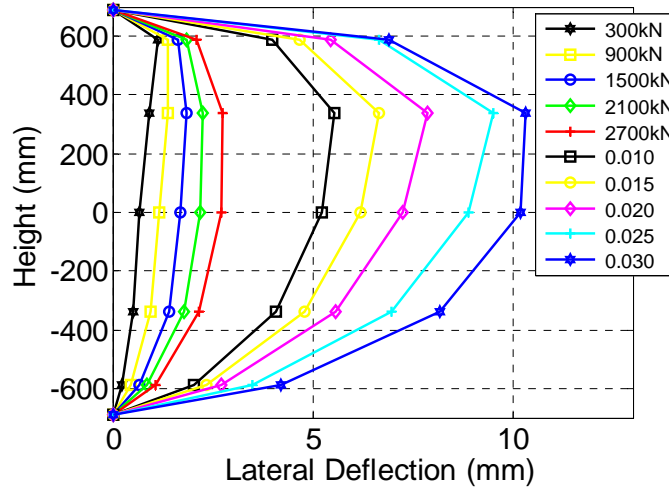
**Figure 7.8** Axial strain distributions over the mid-height section



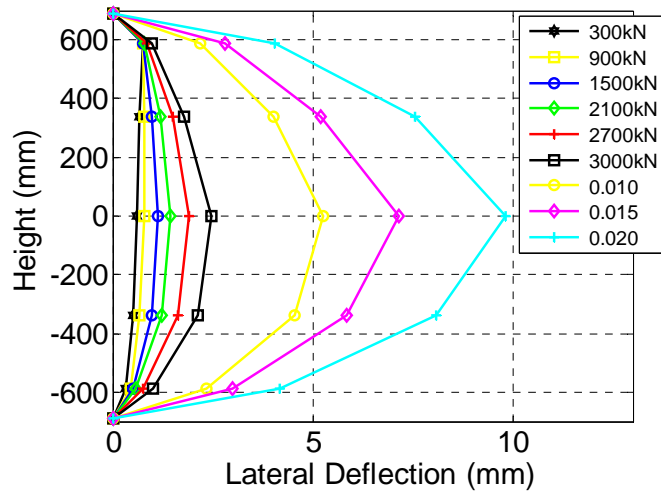
(a) CE325-10-P4N-80



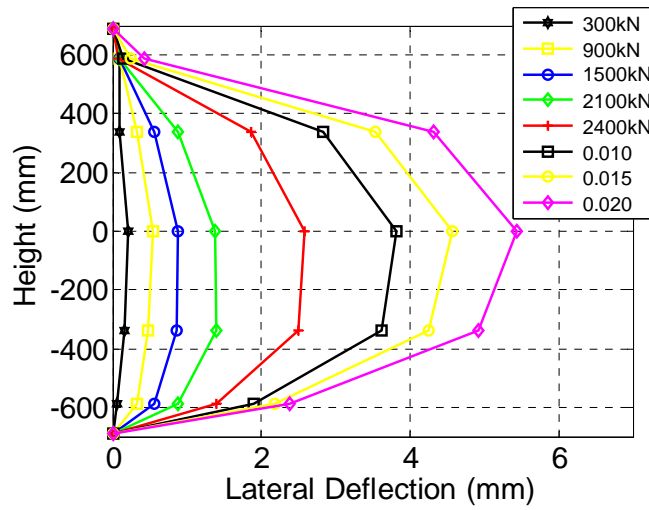
(b) CE325-10- P4N-100



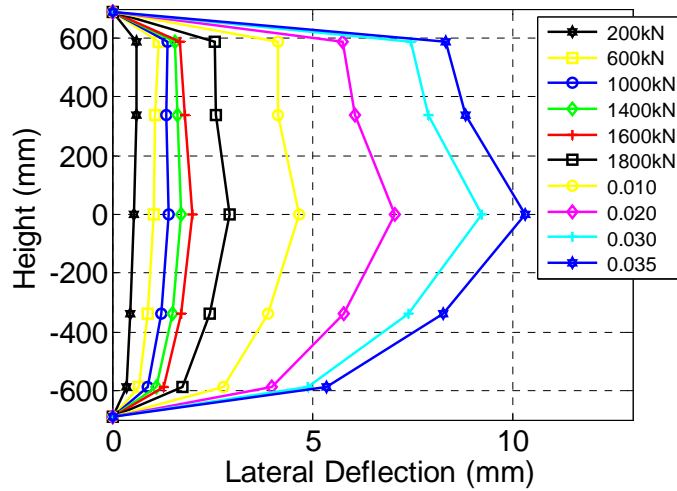
(c) CE325-8- P4S-50



(e) CE325-8- P6S-50

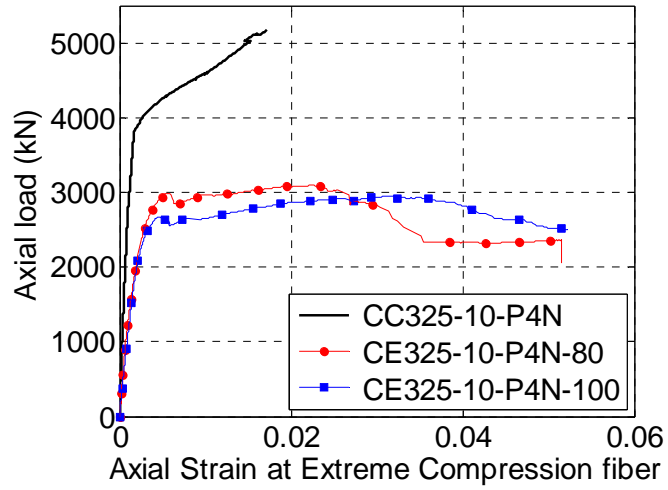


(d) CE325-8-P6S-100

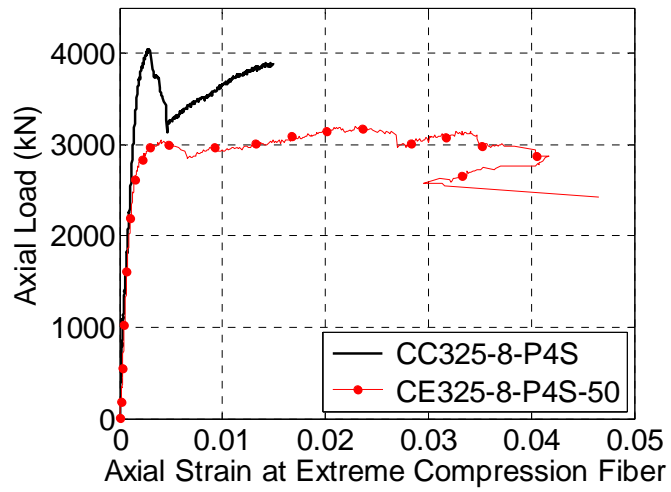


(e) CE325-8-P6S-150

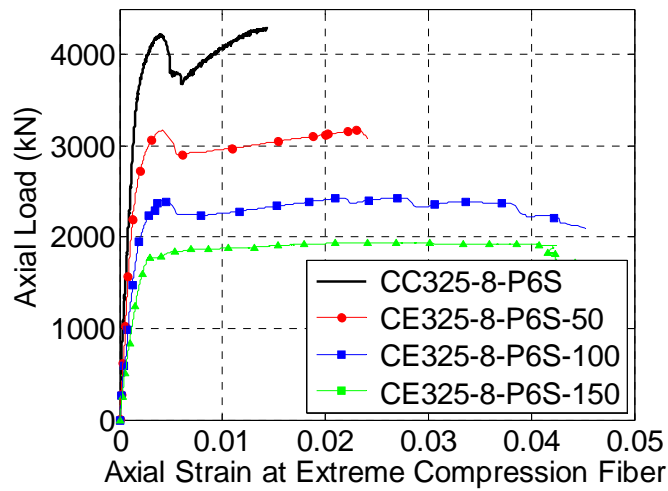
Figure 7. 9 Lateral deflections along column height



(a)



(b)



(c)

**Figure 7. 10** Effect of eccentricity on axial load-axial strain response

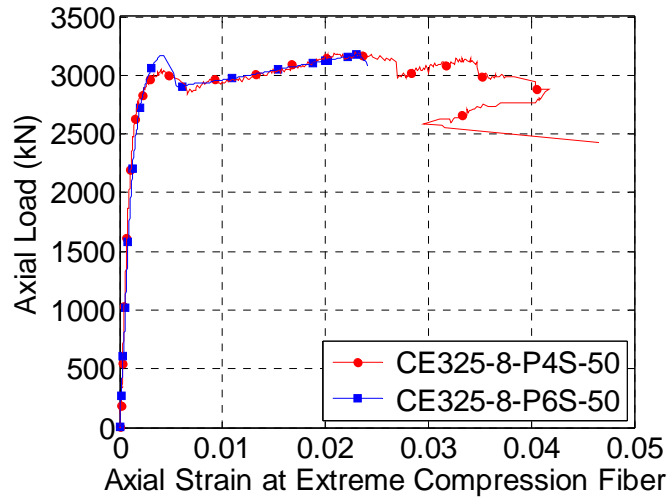
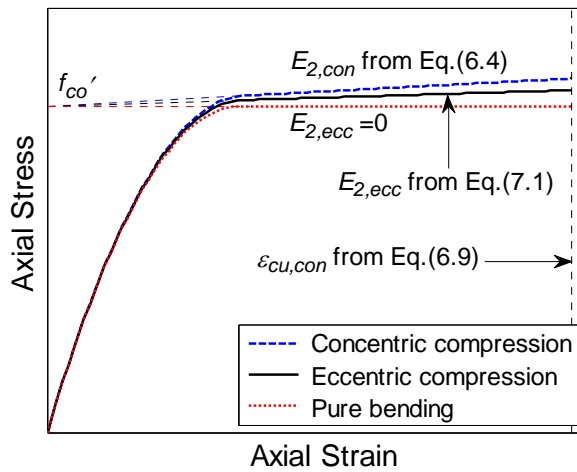
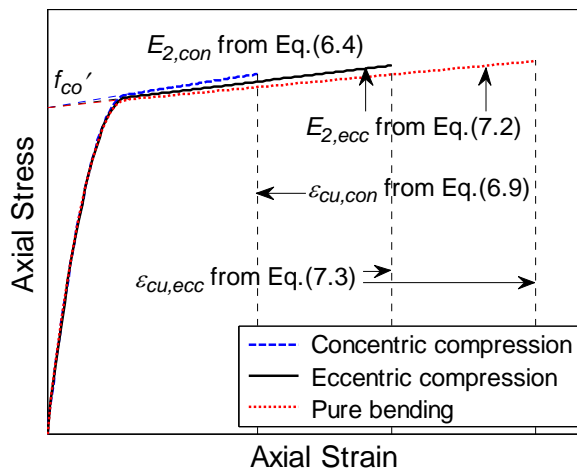


**Figure 7.11** Effect of thickness of FRP tube on axial load-axial strain response



(a) Yu *et al.*'s (2010b) EccD model



(b) Lin's (2016) EccD model

**Figure 7.12** Diagram of EccD stress-strain model

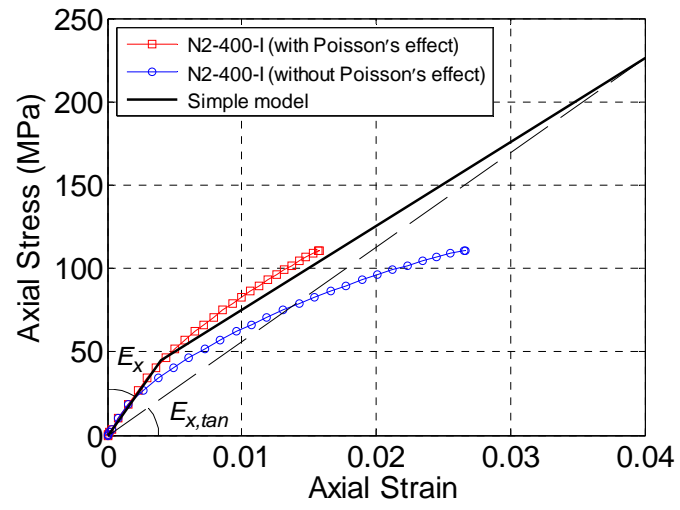
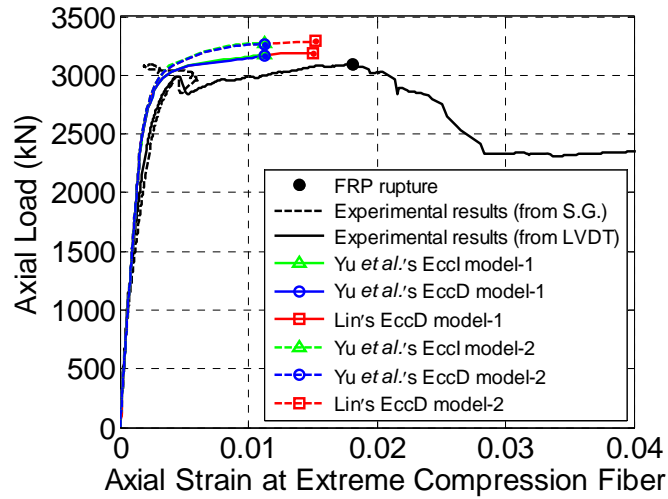
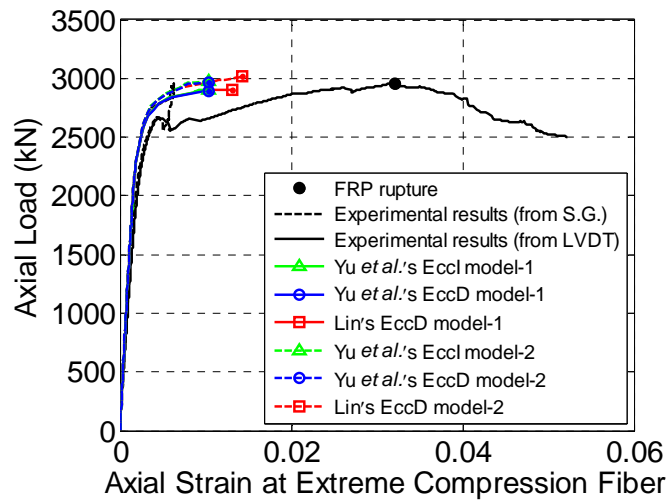


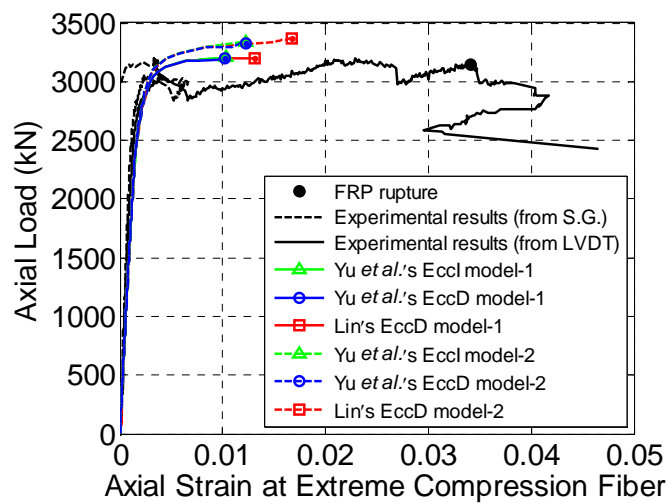
**Figure 7. 13** Axial stress-axial strain curve of the simple model for FRP tubes



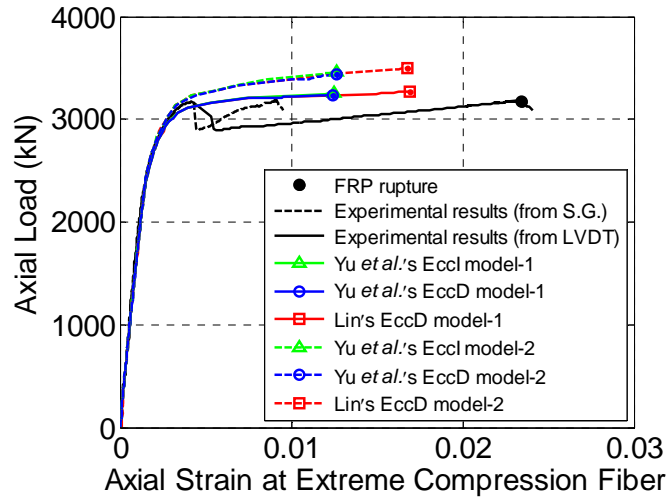
(a) CE325-10-P4N-80



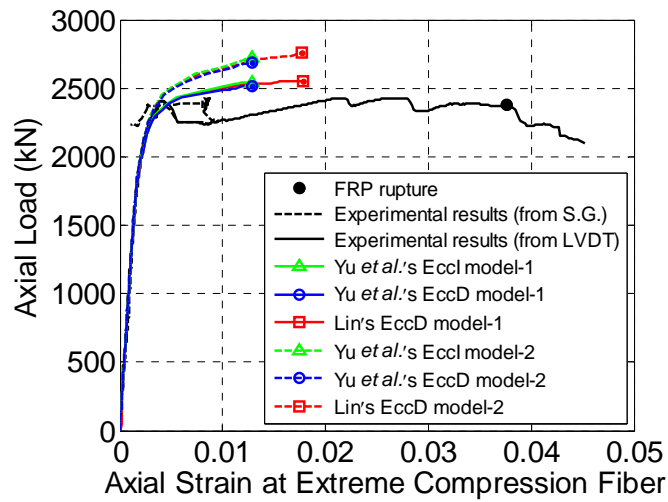
(b) CE325-10-P4N-100



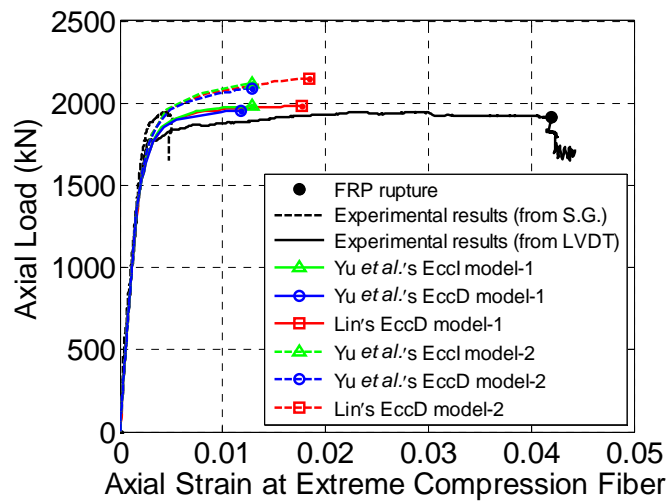
(c) CE325-8-P4S-50



(d) CE325-8-P6S-50

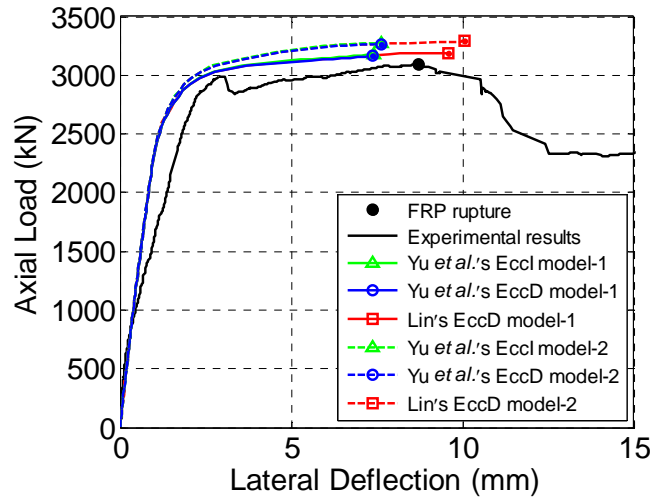


(e) CE325-8-P6S-100

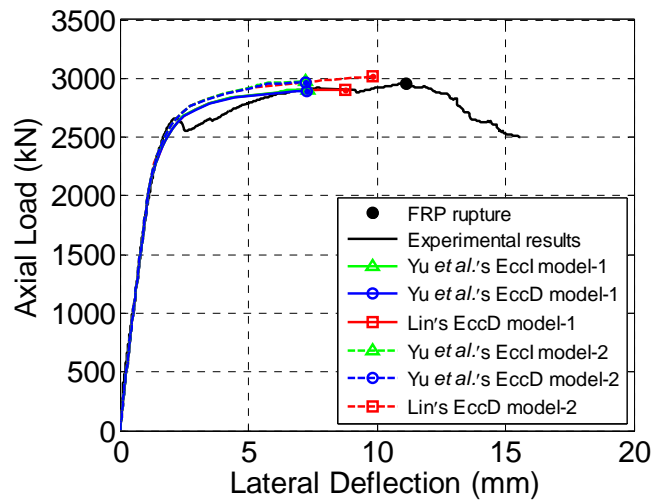


(f) CE325-8-P6S-150

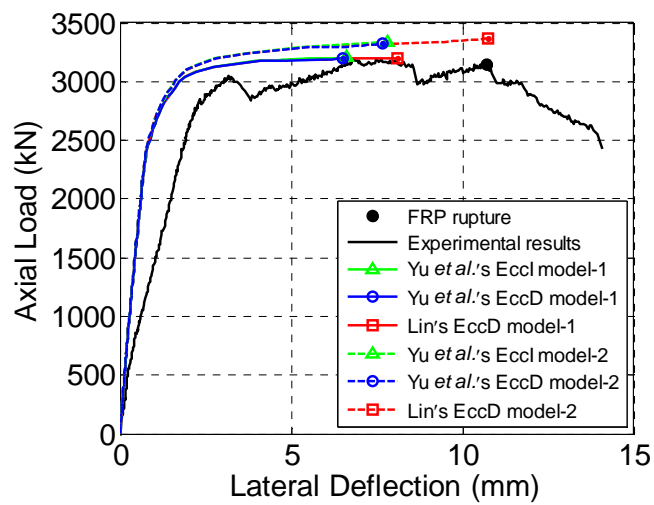
**Figure 7. 14** Axial load-axial strain at extreme compression fiber curves



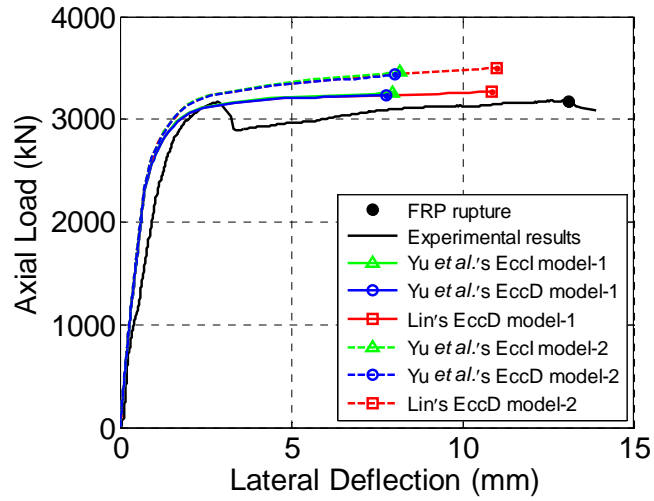
(a) CE325-10-P4N-80



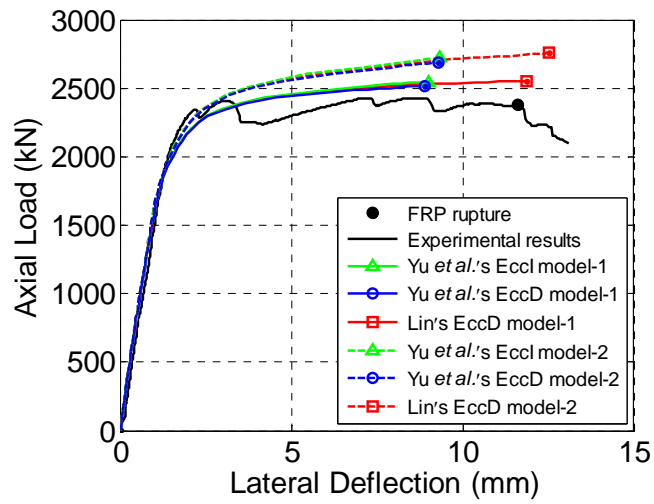
(b) CE325-10-P4N-100



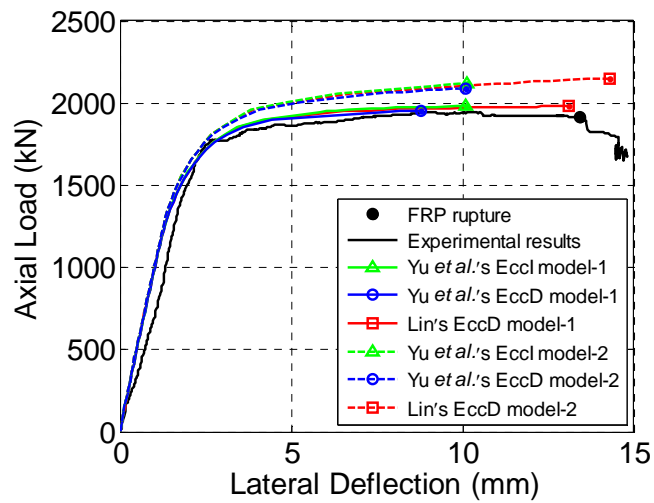
(c) CE325-8-P4S-50



(d) CE325-8-P6S-50

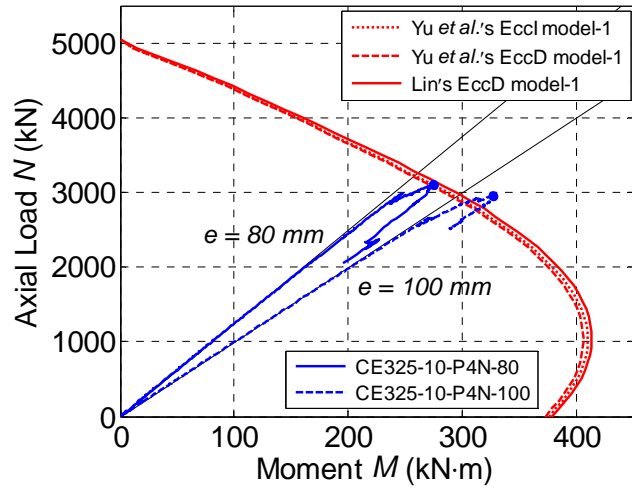


(e) CE325-8-P6S-100

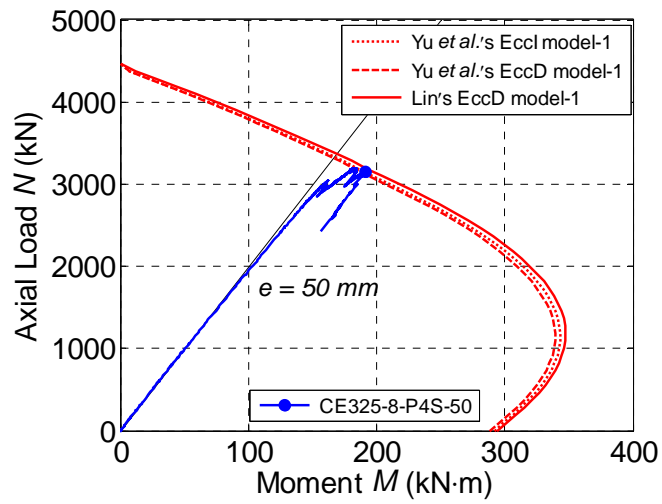


(f) CE325-8-P6S-150

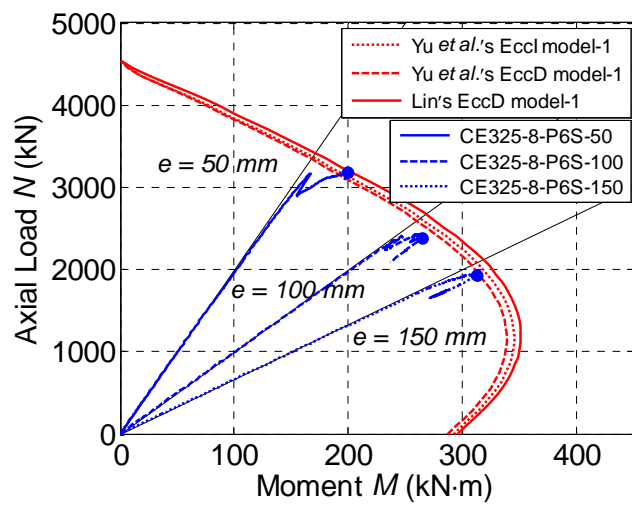
**Figure 7. 15** Axial load-lateral deflection curves



(a) CE325-10-P4N



(b) CE 325-8-P4S



(c) CE325-8-P6S

**Figure 7. 16** Axial load-moment interaction diagrams



## CHAPTER 8

# LARGE-SCALE SLENDER HYBRID DSTCS SUBJECTED TO ECCENTRIC COMPRESSION

### 8.1 INTRODUCTION

Further to the eccentric compression tests on short hybrid DSTCs presented in Chapter 7, this chapter will present a test program on large-scale slender hybrid DSTCs subjected to eccentric compression. Most of the existing tests on hybrid DSTCs have been concerned with small-scale, short columns with height-to-diameters ratios less than three, tested under axial compression (Wong *et al.* 2008; Qian and Liu 2008; Zhang *et al.* 2017; Fanggi and Ozbakkaloglu 2013). In practice, however, the majority of columns are subjected to combined compression and bending and their height-to-diameter ratios are generally larger than three. Very limited experimental research has been conducted to investigate the behavior of slender hybrid DSTCs and yet no rational analytical approach to account for the slenderness effect in hybrid DSTCs is available to date.

The existing studies on slender FRP-confined RC columns can serve as a good reference for slender hybrid DSTCs. These studies have confirmed that the column slenderness has an adverse influence on the effectiveness of FRP confinement for not only concentrically-loaded columns (Mirmiran *et al.* 1998, 2001; Thériault *et al.* 2004; Silva and Rodrigues 2006; Mohamed *et al.* 2010; Ata El-kareim 2011; Vincent and Ozbakkaloglu 2015) but also eccentrically-loaded columns (Ghali *et al.* 2003; Tao *et al.* 2004; Jiang and Teng 2012a, 2012b; Fitzwilliam and Bisby 2010). Ghali *et al.* (2003) conducted a systematic series of eccentric compression tests on small-scale circular FRP-confined RC columns and revealed that an increase in the height-to-diameter

(H/D) ratio of the columns from 4 to 8 caused an increase in the strength reduction from 26% to 70%. Fitzwilliam and Bisby (2010) conducted the eccentric compression tests on small-scale FRP confined RC columns with a diameter of 152 mm, a constant load eccentricity of 20 mm and various lengths from 300 mm to 1200 mm. They found that the axial load capacity decreased while the ultimate lateral deformation increased with increasing column slenderness, and the axial load capacity enhancement due to FRP confinement decreased with column slenderness. The findings of these studies suggests that, similarly, the effect of slenderness in hybrid DSTCs needs to be properly quantified and modeled to understand the behavior of slender hybrid DSTCs.

Qian and Liu (2006) and Hu and Yao (2016) studied slender hybrid DSTCs under concentric compression with various slenderness ratios ( $L_{eff}/r_g$ ) between 11.6 and 54.2, where  $L_{eff}$  is the effective length of columns and  $r_g$  is the gyration radius of the cross section of columns. All specimens failed due to instability and the axial load capacity and the deformation capacity of the specimens decreased with an increasing slenderness ratio.

Yao *et al.* (2015) conducted the first series of eccentric compression tests on slender hybrid DSTCs. They tested a total of five specimens 300 mm in diameter and 1800 mm in height, and had a steel tube with an outer diameter of 219 mm and a thickness of 6 mm. Two columns were confined with a filament-wound FRP tube 10 mm in thickness and were tested with an eccentricity of 30 mm and 60 mm, respectively. The other three columns were confined with a filament-wound FRP tube 6 mm in thickness and were tested with an eccentricity of 30 mm, 60 mm and 90 mm, respectively. The experimental results indicated that, with the increase of the load eccentricity, the axial load capacity of the columns decreased while the ultimate lateral deflection increased;

with the increase of FRP tube thickness, the axial load capacity and the ultimate lateral deflection both increased.

The above studies on slender hybrid DSTCs under eccentric compression suffer from the following shortcomings: (1) the thickness of FRP tubes is too large to be deemed realistic for practical applications of hybrid DSTCs; (2) the range of load eccentricity studied is not wide enough; and (3) the effect of slenderness is not well interpreted.

Against this background, this chapter will present a systematic test program on large-scale slender hybrid DSTCs. The effects of column slenderness, load eccentricity and FRP confinement stiffness will be investigated. The theoretical column model presented in Chapter 7 will be employed to compare with the test results. Again, the three stress-strain models used in Chapter 7 (i.e., Yu *et al.*'s (2010a) EccI model, Yu *et al.*'s (2010b) EccD model and Lin's (2016) EccD model) will be separately incorporated into the column model.

## **8.2 EXPERIMENTAL PROGRAM**

### **8.2.1 Specimen Details**

A total of nine slender hybrid DSTCs, which all had a nominal outer diameter of 300 mm (excluding the thickness of GFRP tube) and the same type of steel tube (an outer diameter of 219 mm and a thickness of 6.12 mm), were tested under eccentric compression. The nine columns covered four values of slenderness, four values of eccentricity and three values of confinement stiffness, as summarized in Table 8.1. Each specimen was given with a name which starts with a number (3, 6, 9 or 11) to indicate the clear length of column-to-nominal outer diameter of concrete ratio ( $L/D_o$ ),

followed by a number (0, 50, 100 or 150) to indicate the load eccentricity in millimeter, and ends with a number (4, 6 or 8) to indicate the number of fiber layers of the filament-wound GFRP tube. Specimen C6-50-6 was designed as the reference column and the remaining eight columns were designed to have only one of the three main test variables (column slenderness, load eccentricity and confinement stiffness of FRP tube) varied from the reference column so that the effects of the three main test variables can be separately examined.

### **8.2.2 Material Properties**

A variety of material tests were performed including compression tests on concrete control cylinders, bare steel tubes and FRP tubes, tensile tests on coupons cut from steel tubes along the longitudinal direction, and hydraulic tests on FRP tubes. The properties of the three constituent materials are summarized in Table 8.1.

### **8.2.3 Specimen Preparation**

A wide range of load eccentricity varying from zero to half the column diameter (i.e., 150 mm) was employed in the tests. To ensure the reliable transfer of axial load from the testing machine to the specimens especially for cases involving a large eccentricity, corbel ends were fabricated for all hybrid DSTC specimens except Specimen C6-0-6 which was tested under concentric compression. As shown in Figure 8.1, at each end of the inner steel tube, a rigid steel cap with a thickness of 24 mm was welded to the steel tube. The top steel cap was cut with three holes for grouting concrete. Four additional pieces of vertical steel plates were welded with the steel tube and the steel cap to form the frame of the corbel. It should be noted that the clear length of the column ( $L$ ), mentioned earlier, was defined by the length of the inner steel tube excluding the thickness of the two steel caps. At each end of the outer GFRP tube, four

horizontal screws of the same length were welded to the surface of the inner steel tube to facilitate the positioning of the FRP tube and create a uniform annular space between the two tubes. Wooden moulds were used to cast the corbels into the desired shape (see Figure 8.2). Both ends of the GFRP tube were embedded in the corbels by a depth of 20 mm to ensure good connection between the concrete and the GFRP tube (see Figure 8.1). The presence of the corbel ends brought difficulty in vibrating the concrete during casting. Therefore, self-compacting concrete (SCC) was used in the slender hybrid DSTCs for its high flowability and segregation-resistant ability.

#### **8.2.4 Test Setup and Instrumentation**

The layout of strain gauges and LVDTs is illustrated using Specimen C6-11-50 in Figure 8.3. Strain gauges were installed along seven sections (i.e., Sections A, B, C, D, E, F and G) covering the 1800 mm middle height of the specimen. The mid-height section (i.e., Section A) was expected to be the critical section, so it was most densely installed with strain gauges: the outer surface of both the steel tube and the GFRP tube was respectively installed with eight pairs of uni-directional strain gauges (one axial strain gauge and one hoop strain gauge)  $45^\circ$  apart. In addition, the axial deformation of the 240 mm middle height (spanning Section A) of the column was monitored by four LVDTs (L113 to L116)  $90^\circ$  apart. For the other six sections, only the strains of the FRP tube were monitored with a decreasing number of strain gauges (see Figure 8.3). The lateral deflection at the seven sections was also monitored using seven horizontal LVDTs (L117 to L123) installed at the tension side of the specimen. Another four LVDTs (L124 to L127) were employed to monitor the rotation of both ends of the column. For specimens with a smaller clear length (900 mm, 1800 mm or 2700 mm) than Specimen C6-11-50, the number of sections monitored was 1, 5 or 7, respectively. The same end loading assembly (comprising a steel roller nested in a grooved steel

plate) employed in the eccentric compression tests on short hybrid DSTCs in Chapter 7 was installed at each corbel end to receive compressive load in the desired eccentricity as shown in Figure 8.4. The effective length of columns ( $L_{eff}$ ), defined as the distance between the centers of the two steel rollers, is the sum of the clear length of the column, the thickness of the steel caps and the height of the end loading assemblies. The values of  $L_{eff}$  are given in Table 8.1. The slenderness ratio of the columns ( $\lambda$ ), which varied from 11.77 to 37.93, was calculated based on  $L_{eff}$  using the following equations

$$\lambda = \frac{kL_{eff}}{r_g} \quad (8-1)$$

$$r_g = \sqrt{\frac{I_g}{A_g}} \quad (8-2)$$

where  $k$  is the effective length factor and is equal to unity for pinned-end condition,  $r_g$  is the radius of gyration of the gross cross section,  $I_g$  is the gross moment of inertia of the cross section and  $= \frac{\pi[(D_{in}+t_{frp})^4-(D_{o,s}-t_s)^4]}{64}$ ,  $A_g$  is the cross-sectional area and  $= \frac{\pi[(D_{in}+t_{frp})^2-(D_{o,s}-t_s)^2]}{4}$ ,  $D_{in}$  and  $t_{frp}$  are respectively the inner diameter and thickness of the GFRP tube and  $D_{o,s}$  and  $t_s$  are respectively the outer diameter and thickness of the steel tube.

The compression tests were conducted using a 10,000 kN servo-hydraulic testing machine with displacement control at a constant axial strain rate of 0.0005/min.

## 8.3 TEST RESULTS AND DISCUSSIONS

### 8.3.1 Test Observations

Most of the slender specimens failed by the rupture of the FRP tube induced by the

crushing of concrete in a much less violent manner compared with the eccentrically-loaded short columns tested in Chapter 7. The two most slender specimens (Specimens C9-50-6 and C11-50-6) showed no clear sign of rupture of the FRP tube until the test was terminated for excessive lateral deflection of the specimen due to its large slenderness. For Specimen C6-0-6 which was tested under nominal concentric compression, no noticeable lateral deflection of the specimen was observed at the initial stage of loading. After the axial load reached to about 90% of the peak load, noticeable lateral deflection was observed, as shown in Figure 8.4 (b), due to the eccentricity arising from inevitable geometric and material imperfections. A general view of the slender DSTCs after test is shown in Figure 8.5, in which an obvious deflected shape of specimens due to flexure can be clearly seen.

Figure 8.6 shows more detailed views of all failed specimens. In each sub-figure, six photos of the same specimen taken at three different angles corresponding to the compression face, the profile face and the tension face are shown in sequence from left to right. Each view angle includes two photos, before and after removal of the outer GFRP tube of the failed specimen. In Figure 8.6, intensive tensile cracks (white stripes) along the fiber direction can be seen at the tension side of the GFRP tubes as a consequence of resin damage due to the development of tensile cracks at the corresponding position of the concrete. This statement is substantiated by the coincidence of the positions of cracks in the GFRP tubes and the concrete as can be seen in the pair of photos for the tension side. In addition, the width of concrete cracks at the tension side was observed to increase with increasing eccentricity and slenderness that combined led to an increased bending moment. The maximum value of crack width reached to 1.98 mm and 2.22 mm for Specimens C6-150-6 and C11-50-6, respectively.

A careful observation and comparison of the failed specimens revealed two different failure modes, the flexure-dominated mode and the compression-dominated mode. The flexure-dominated mode was observed in Specimens with a larger slenderness or load eccentricity (i.e., C6-150-6, C9-50-6 and C11-50-6). In these specimens, significant tensile cracks of the GFRP tube and the concrete developed at the tension side of the specimen while there appeared no clear sign of rupture of the GFRP tube at the compression side till the end of testing because the concrete at the extreme compression fiber was not or only slightly crushed in the test. The rest of specimens were governed by the failure on the compression side (i.e., compression-dominated failure mode), characterized by the significant crushing of concrete near specimen mid-height and fracture of GFRP tube. Furthermore, a general view of the inner steel tubes after test is displayed in Figure 8.7. Being different from the short columns tested under eccentric compression in Chapter 7, which were accompanied with local buckling of the inner steel tube near the specimen mid-height in all cases, in the present tests only Specimens C3-50-6 and C6-50-6 experienced a small degree of local buckling of the steel tube near the specimen mid-height, as marked by a red ellipse in Figure 8.8 which shows the close-up view of all steel tubes after test.

### **8.3.2 Axial Strain Distribution over Mid-height Section**

The distribution of axial strains over the mid-height section of specimens is displayed in Figure 8.9. In Figure 8.9, the axial strains were averaged from the readings of axial strain gauges located at different circumferential positions. The hollow symbols represent the axial strain of the GFRP tube and the solid symbols represent the axial strain of the steel tube. In most cases, each curve represents the axial strain distribution under a specified axial load level with the final load level being the peak load of the

specimens. The only exception was Specimen C6-0-6, which was tested under nominal concentric compression and experienced a long process of gradual increase in the axial load. So some of the curves were related to different axial strain levels of the extreme compression fiber. It can be seen that for this specimen, the axial strains over the cross section were almost uniform in the initial stages of loading. However, the axial strains exhibited evident flexural features caused by instability of the specimen under high axial load levels. Overall, the axial strains of steel tubes and GFRP tubes are approximately proportional to the distance from the neutral axis, validating the plane cross-section assumption.

### **8.3.3 Column Lateral Deflection**

The lateral deflections along the column height of all specimens are shown in Figure 8.10. The lateral deflections were obtained from the readings of LVDTs installed at different heights of the columns. In each sub-figure, each curve represents the column lateral deflection profile corresponding to a specific axial load level before the peak axial load is reached. When the axial load enters the descending stage, the lateral deflections are correlated to different axial strain levels at the extreme compression fiber of concrete instead. For Specimen C6-0-6 tested under nominal concentric compression, the lateral deflection kept small until the peak axial load was reached and developed rapidly after that due to instability of the specimen. Compared with the short hybrid DSTCs tested in Chapter 7, the lateral deflection of the slender columns are more symmetrical along the column height.

### **8.3.4 Axial Load-Axial Strain and Axial Load-Lateral Deflection Responses**

Figures 8.11 to 8.13 display the axial load-axial strain at extreme compression fiber curves and the axial load-lateral deflection at specimen mid-height curves to explore

the effects of load eccentricity, slenderness and thickness of FRP tube on the behavior of slender DSTCs, respectively. The axial strain at the extreme compression fiber and the lateral deflection at specimen mid-height were respectively taken from the readings of the longitudinal LVDT nearest to the extreme compression fiber (i.e., L113 in Figure 8.3) and the horizontal LVDT at specimen mid-height (i.e., L117 in Figure 8.3).

#### *8.3.4.1 Effect of load eccentricity*

The effect of load eccentricity is examined in Figure 8.11. As expected, the axial load capacity of the specimen decreases with increasing load eccentricities. In contrast, the axial strain at the extreme compression fiber at ultimate condition (i.e., FRP rupture) generally increases with increasing load eccentricities due to the axial strain enhancement effect discussed in Chapter 7. This trend is violated by Specimen C6-150-6 because of the premature damage of the GFRP tube. The lateral deflection at mid-height section at ultimate condition is also seen to generally increase with increasing load eccentricities. The relatively small lateral deflection of Specimen C6-100-6 is due to unexpected locking of the probe of LVDT at later stages of loading. In addition, the slope of the first segment of axial load-lateral deflection curves decreases with the load eccentricity. The same finding has also been reported by Yao *et al.* (2015) based on their own test results of slender hybrid DSTCs. It is interesting to note that hardly any lateral deflection of Specimen C6-0-6 was detected up to about 90% of the peak load because this specimen was tested under nominal concentric compression, as explained earlier.

#### *8.3.4.2 Effect of slenderness*

The effect of slenderness is examined in Figure 8.12. As expected, the axial load

capacity of the specimens decreases with increasing slenderness. The axial load capacity of Specimen C11-50-6 is only 72% that of Specimens C3-50-6. Of the four specimens compared, only the shortest specimen (C3-50-6) was controlled by material failure while the rest of specimens were all controlled by stability failure as suggested by the shape of the second segment of the curves being ascending or descending. Additionally, the lateral deflection at mid-height at ultimate condition is seen to increase with column slenderness. However, the axial strain at the extreme compression fiber at ultimate condition is seen to decrease with slenderness. This observation appears to contradict the expectation that the axial strain at ultimate condition will be increased in more slender specimens due to the axial strain enhancement effect as the total eccentricity (sum of initial eccentricity and lateral deflection) becomes larger in more slender specimens. This contradiction is believed to be attributed to the early termination of testing of Specimens C9-50-6 and C11-50-6 because of excessive lateral deflection; otherwise, the axial strain at the extreme compression fiber of these two specimens would keep increasing.

#### *8.3.4.3 Effect of thickness of GFRP tube*

The effect of thickness of the GFRP is examined in Figure 8.13. It can be seen that only marginal increases of axial load capacity were achieved by increasing the thickness of the FRP tube. This is mainly because the increase of section strength due to FRP confinement could not be fully translated into an equal increase in column strength because of the significant slenderness effect in the slender columns. On the other hand, increasing the thickness of GFRP tube did not appear to evidently enhance the axial and the lateral deformability of the specimens. However, Specimen C6-50-8 having a stable descending branch indicates that the increase in the confinement stiffness of GFRP tube had a positive influence on the stability of post-peak behavior

especially for hybrid DSTCs made with SCC. Similar smooth descending branches were also observed in Yao *et al.*'s (2015) tests where their slender eccentrically-loaded DSTCs were fabricated with SCC and provided with very strong confinement stiffness (e.g., the number of fiber layers was 12 or 20). The large shrinkage of SCC may result in the separation of concrete from the FRP tube, and thus a delay of the activation of the confinement action. So Specimens C6-50-4 and C6-50-6 under a relatively weak confinement level featured a less stable post-peak descending branch.

### 8.3.5 Key Test Results

The key test results are summarized in Table 8.2. In this table,  $N_{peak}$  is the peak axial load of the specimens, and  $M_u$  is the bending moment at column mid-height at ultimate condition and is the sum of the corresponding first-order bending moment due to the initial eccentricity  $e$  and the corresponding second-order bending moment caused by the lateral deflection  $e'_u$  at column mid-height.  $N_u$  is the corresponding axial load.  $\varepsilon_{h,rupt}$  and  $\varepsilon_{cu}$  are the experimental hoop rupture strain of the FRP tube and the corresponding axial strain at the extreme compression fiber. Note that the ultimate condition of specimens is defined by the rupture of the FRP tube except for Specimens C9-50-6 and C11-50-6, the testing of both of which was terminated before the FRP tube ruptured due to excessive later deflection as mentioned above. For Specimen C9-50-6, the ultimate condition is defined by the condition of the column when testing was terminated. For Specimen C11-50-6, the horizontal LVDT at column mid height was removed before the termination of testing as the lateral deflection there approached the capacity of the LVDT (100 mm). So the ultimate condition of Specimen C11-50-6 is defined by the condition of the column when the horizontal LVDT at column mid height was removed.  $\sigma_{\theta u}$  is the hoop stress of the FRP tube calculated from  $\varepsilon_{cu}$  and  $\varepsilon_{h,rupt}$  considering the nonlinear biaxial tube behavior using

Jones and Nelson's (1975) model.  $\varepsilon'_{h,rupt}$  is the nominal hoop rupture strain and  $= \sigma_{\theta u}/E_{\theta}$ , where  $E_{\theta}$  is the hoop modulus of elasticity of the FRP tube. It is noteworthy that the values of  $\sigma_{\theta u}$  in Table 8.2 are generally significantly smaller than those given in Table 6.2 for concentrically-loaded hybrid DSTCs. A reduction in  $\sigma_{\theta u}$  means a reduction in the lateral confining pressure that can be provided by the same FRP tube. This is because  $\varepsilon_{cu}$  is magnified due to the axial strain enhancement effect as a result of the combined effect of eccentricity and slenderness; a magnified  $\varepsilon_{cu}$  means an increased axial stress of FRP tube at ultimate condition. According to Tsai-Wu failure criterion (Daniel and Ishai 2006), an increased axial compressive stress at ultimate condition will lead to a reduced hoop tensile stress ( $\sigma_{\theta u}$ ). This is another reason why the increase of axial load capacity of specimens by increasing the FRP tube thickness was marginal.

## 8.4 THEORETICAL ANALYSIS

The same analytical approach employed in Chapter 7 is again used in this section to model the behavior of slender DSTCs under eccentric compression. The three stress-strain models, namely, Yu *et al.*'s EccI model, Yu *et al.*'s EccD model and Lin's EccD model, are again incorporated into the column model for comparison purposes. In the analysis procedure, the contribution of the GFRP tube to the axial load was ignored as this simplification has been demonstrated in Chapter 7 to only have a limited effect on the predicted results.

### 8.4.1 Comparison with Test Results

The experimental axial load-axial strain at extreme compression fiber curves and the experimental axial load-lateral deflection at column mid-height curves are compared with the predicted curves in Figures 8.14 and 8.15, respectively. The predicted curves

terminate when the hoop strain at the extreme compression fiber of FRP tube reaches its nominal hoop rupture strain given in Table 8.2 (i.e., the hoop stress of FRP tube equal to the value of  $\sigma_{\theta u}$ ). The solid points on the experimental curves represent the ultimate condition of the corresponding specimens. The predicted values, including the peak axial load, the bending moment at ultimate condition, the corresponding axial strain at the extreme compression fiber and the corresponding lateral deflection at column mid-height, are summarized in Table 8.2.

For Specimens C6-50-6 and C9-50-6, the first segment of the experimental axial load-axial strain at the extreme compression fiber curves noticeably deviates from the predicted curves. This discrepancy might be due to the possible slip between the concrete and the two tubes. This phenomenon was also observed in hybrid FRP-concrete steel double-skin tubular beams reported by Idris and Ozbakkaloglu (2014) and Zhao (2016).

It can be seen from Figures 8.14 and 8.15 and Table 8.2 that the three stress-strain models all provide close predictions for the peak axial load. However, the two indicators related to deformability (i.e., axial strain at the extreme compression fiber at ultimate condition and the corresponding lateral deflection at mid height), especially the former, are significantly underestimated by the three models. Of the three models, Lin *et al.*'s model provides relatively close predictions for the two deformability indicators because it considers the axial strain enhancement effect. A possible reason for the underestimation of deformability is that the significant local buckling of the filament-wound GFRP tubes under a biaxial stress state of a high level of axial compression and a low level of hoop tension was not considered in the analytical approach. The uncertainty in the analysis of behavior of FRP laminates with large

deformation due to delamination and local buckling has been pointed out by Puck and Schürmann (2002).

#### 8.4.2 Axial Load-Bending Moment Interaction Diagrams

Figure 8.16 shows the axial load-bending moment ( $N$ - $M$ ) interaction diagrams for the hybrid DSTC sections. The interaction curves were generated using section analysis incorporating Yu *et al.*'s EccI model, Yu *et al.*'s EccD model and Lin's EccD model, respectively. Figure 8.16 comprises three sub-figures with each examining the effect of one of the three main test variables (eccentricity, slenderness and confinement stiffness). The interaction curves predicted by the three stress-strain models are close to each other. Of the three models, Yu *et al.*'s EccD model provides the most conservative predictions of the entire interaction diagram due to the combined effect of considering axial stress reduction and ignoring axial strain enhancement caused by eccentric loading.

In Figure 8.16, the experimental  $N$ - $M$  paths of the specimens are also shown for comparison. The bending moment was taken to be the sum of the first-order and the second-order moment [i.e.,  $M = N \times (e + e')$ ]. The solid points on the  $N$ - $M$  paths represent the ultimate condition of the corresponding specimens. It is obvious that all specimens except for the shortest one (Specimen C3-50-6) experienced stability failure rather than material failure. Regardless of the type of failure, most of the experimental ultimate condition points are located in the neighborhood of the predicted sectional interaction curves except for Specimen C6-100-6 of which the measured lateral deflection at the mid-height was smaller than the actual value at later stages of loading due to a test error mentioned earlier. Each experimental  $N$ - $M$  path is accompanied with a straight line representing the  $N$ - $M$  path in the absence of slenderness effect (i.e., the

height of the column is reduced to zero).

Figure 8.16 (a) demonstrates that the ascending rate of the experimental  $N-M$  paths depends on the initial eccentricities and the specimens with a smaller initial eccentricity are more susceptible to stability failure because the second-order moment due to lateral deflection occupies a larger proportion in the total moment.

On the other hand, it can be seen from Figure 8.16 (b) that for the four specimens compared, the experimental  $N-M$  paths all follow the accompanying straight line closely at the initial stage of loading because of the identical initial eccentricity of the four specimens and the limited second-order effect in the initial stage of loading. However, the experimental  $N-M$  paths deviate from the straight line by different extents at later loading stages because the difference between the second-order moments specific to the slenderness of the four specimens became significant. The type of failure changed from material failure to stability failure as the column slenderness increased.

Figure 8.16 (c) examines the effect of the confinement stiffness (thickness of FRP tube). It can be seen that an increase in the confinement stiffness leads to an enhanced section strength, as indicated by the enlarged size of the interaction diagrams. The experimental  $N-M$  paths of the three specimens with different thicknesses of GFRP tubes (Specimens C6-50-4, C6-50-6 and C6-50-8) are very close to each other before the FRP tube started to exert a significant confining effect. However, the three loading paths deviate from each other in the confinement-enhanced range and reach distinctly different ultimate conditions.

Finally, the theoretical interaction diagrams for hybrid DSTCs with a range of specific slenderness ratios are shown in Figure 8.17 to provide a more direct and complete demonstration of the slenderness effect. The theoretical interaction curves were produced using the column model with the separate incorporation of the three stress-strain models. Each interaction curve in Figure 8.17 is a collection of points, each representing the maximum axial load that the hybrid DSTC can sustain under a specific load eccentricity and the associated first-order moment. It is evident that the size of the column interaction curves reduces with the slenderness ratio because the slenderness has a weakening effect on the axial load capacity of hybrid DSTCs. The points representing the experimental axial load capacity and the associated first-order moment of Specimens C3-50-6, C6-50-6, C9-50-6 and C11-50-6 are also shown in Figure 8.17 by small solid points for comparison. The only difference between these four specimens was their slenderness. It can be seen that the experimental points lie close to the corresponding interaction curves except for Specimen C3-50-6 for which the axial load capacity is moderately underestimated. The predicted results in Figure 8.17 also confirm that the three stress-strain models are of a similar degree of accuracy in predicting the axial load capacity of slender hybrid DSTCs when incorporated into the same column model.

## **8.5 CONCLUSIONS**

This chapter has presented the results of tests on a total of nine eccentrically-loaded large-scale slender hybrid DSTCs to explore the effects of eccentricity, slenderness and thickness of FRP tube, with an emphasis on the effect of slenderness, on the behavior of slender hybrid DSTCs under eccentric compression. The same analytical approach adopted in Chapter 7 was again employed in this chapter to model the behavior of slender hybrid DSTCs. The following conclusions are drawn based on the

results and discussions presented in this chapter:

- (1) Two different failure modes of slender hybrid DSTCs subjected to eccentric compression were observed, including the flexure-dominated mode and the compression-dominated mode, depending on the eccentricity and the slenderness of columns. Hybrid DSTCs with a larger slenderness and eccentricity are more susceptible to the flexure-dominated failure mode.
- (2) As the slenderness ratio increases, the failure of hybrid DSTCs changes from material failure to stability failure. The latter is featured by a descending branch in the axial load-lateral deflection curve of the column.
- (3) The axial load capacity of hybrid DSTCs decreases with the slenderness and the eccentricity. The lateral deflection of hybrid DSTCs at ultimate condition increases with the slenderness and the eccentricity. The axial strain at the extreme compression fiber at ultimate increases with the eccentricity due to the axial strain enhancement effect. However, it decreased with slenderness in the present tests. This appears to contradict the expectation that the axial strain at ultimate condition will be increased in more slender specimens due to the axial strain enhancement effect as the total eccentricity (sum of initial eccentricity and lateral deflection) becomes larger in more slender specimens. This contradiction is believed to be attributed to the early termination of testing of the two most slender specimens because of excessive lateral deflection; otherwise, the axial strain at the extreme compression fiber of the two specimens would keep increasing.
- (4) Only marginal increases of axial load capacity of hybrid DSTCs were achieved in

the present tests by increasing the confinement stiffness of the FRP tube. This is mainly because the increase of section strength due to FRP confinement could not be fully translated into an equivalent increase in column strength because of the significant slenderness effect in the specimens tested. However, increasing the confinement stiffness of GFRP tubes led to more stable post-peak behavior. So relatively stiff FRP tubes are recommended for use in slender hybrid DSTCs especially when filled with SCC.

- (5) The three stress-strain models all provide reasonable accuracy in predicting the axial load capacity of slender hybrid DSTCs when incorporated into the column model described in Chapter 7. However, Lin's EccD model is more accurate than the other two models in predicting the lateral deflection of eccentrically-loaded slender hybrid DSTCs at ultimate condition due to the consideration of the axial strain enhancement effect.

## 8.6 REFERENCES

- Ata El-kareim S.S. (2011). "Behavior of Long Confined Concrete Column", *Ain Shams Engineering Journal*. Vol. 2(3-4), pp.141-148.
- Daniel, I. M., and Ishai, O. (2006). "Engineering Mechanics of Composite Materials", Oxford University Press, New York.
- Fanggi, B.A.L. and Ozbakkaloglu, T. (2013). "Compressive Behavior of Aramid FRP-HSC-Steel Double-Skin Tubular Columns", *Construction and Building Materials*. Vol. 48, pp.554-565.
- Fitzwilliam, J. and Bisby, L.A. (2010). "Slenderness effects on circular CFRP confined reinforced concrete columns", *Journal of Composites for Construction*, ASCE. Vol. 14(3), pp. 280-288.

- Ghali, K., Rizkalla, S., Kassem, M., Fawzy, T. and Mahmoud, M. (2003). “FRP-Confined Circular Columns under Small Eccentric Loading”, *The 5th Alexandria International Conference on Structural and Geotechnical Engineering*, Alexandria, Egypt; 2003. 10 pp.
- Idris, Y. and Ozbakkaloglu, T. (2014). “Flexural Behaviour of FRP-HSC-Steel Composite Beams”, *Thin-Walled Structures*. Vol. 80, pp. 207-216.
- Hu, F. and Yao, J. (2016). “Experimental Study of FRP-Concrete-Steel Double-Skin Tubular Long Columns Subjected to Axial Compression”, *Industrial Construction*. Vol. 46(9), pp. 130-139. (in Chinese)
- Jiang, T. and Teng, J.G. (2012a). “Theoretical Model for Slender FRP-Confined Circular RC Columns”, *Construction and Building Materials*. Vol. 32(4), pp.66-76.
- Jiang, T. and Teng, J.G. (2012b). “Slenderness Limit for Short FRP-Confined Circular RC Columns”, *Journal of Composites for Construction*, ASCE. Vol. 16(6), pp.650-661.
- Jones, R.M. and Nelson JR, D.A.N. (1975). “A New Material Model for the Nonlinear Biaxial Behavior of ATJ-S Graphite”, *Journal of Composite Materials*. Vol. 9, pp.10-27.
- Lin, G. (2016). “Seismic Performance of FRP –Confined RC Columns: Stress-Strain Models and Numerical Simulation”, Ph.D. thesis, The Hong Kong Polytechnic University, Hong Kong, China.
- Mirmiran, A., Shahawy, M., Samaan, M., El Echary, H., Mastrapa, J. C. and Pico, O. (1998). “Effect of Column Parameters on FRP-Confined Concrete”, *Journal of Composites for Construction*, ASCE. Vol. 2(4), pp. 175-185.
- Mirmiran, A., Shahawy, M. and Beitleman, T. (2001) “Slenderness Limit for Hybrid FRP Concrete Columns”, *Journal of Composites for Construction*, ASCE. Vol.

5(1), pp. 26-34.

- Mohamed H.M., Abdel-baky, H.M. and Masmomudi, R. (2010). “Nonlinear Stability Analysis of Concrete-Filled Fiber-Reinforced Polymer-Tube Columns: Experimental and Theoretical Investigation”, *ACI Structural Journal*. Vol. 107(6), pp.699-709.
- Puck, A. and Schürmann, H. (2002). “Failure Analysis of FRP Laminates by Means of Physically Based Phenomenological Models”, *Composites Science and Technology*. Vol. 62, pp. 1633-1662.
- Qian, J.R. and Liu, M.X. (2006). “Experiment of FRP-Concrete-Steel Double-Skin Tubular Long Columns under Axial Compressive Load”, *Concrete*. Vol. (9), pp.31-34. (in Chinese)
- Qian, J.R. and Liu, M.X. (2008). “Experimental Investigation of FRP-Concrete-Steel Double-Skin Tubular Stubs under Axial Compressive Loading”, *Journal of Building Structures*. Vol. 29(2), pp.104-113. (in Chinese).
- Silva, M. A. G. and Rodrigues, C. C. (2006). “Size and Relative Stiffness Effects on Compressive Failure of Concrete Columns Wrapped with Glass FRP”, *Journal of Materials in Civil Engineering*. Vol. 18(3), pp. 334-342.
- Tao, Z., Teng, J.G., Han, L.H. and Lam, L. (2004). “Experimental Behaviour of FRP-Confined Slender RC Columns under Eccentric Loading”, *Proceedings, Advanced Polymer Composites for Structural Applications in Construction (ACIC 2004)*, University of Surrey, Guildford, UK, pp.203-212.
- Thériault, M., Neale, K. W. and Claude, S. (2004). “Fiber Reinforced Polymer-Confined Circular Concrete Columns: Investigation of Size and Slenderness Effects”, *Journal of Composites for Construction*, ASCE. Vol. 8(4), pp.323-331.
- Wong, Y.L., Yu, T., Teng, J.G. and Dong, S.L. (2008). “Behavior of FRP-Confined Concrete in Annular Section Columns”, *Composites Part B-Engineering*. Vol.

39(3), pp. 451-466.

- Vincent, T. and Ozbakkaloglu, T. (2015). "Influence of Slenderness on Stress-Strain Behavior of Concrete-Filled FRP Tubes: Experimental Study", *Journal of Composites for Construction*. Vol. 19(1), 04014029.
- Yao, J., Jiang, T., Xu, P. and Lu, Z.G. (2015). "Experimental Investigation on Large-Scale Slender FRP-Concrete-Steel Double-Skin Tubular Columns subjected to Eccentric Compression", *Advanced in Structural Engineering*. Vol. 18(10), pp.1737-1746.
- Yu, T., Teng, J.G. and Wong, Y.L. (2010a). "Stress-Strain Behavior of Concrete in Hybrid Double-Skin Tubular Columns", *Journal of Structural Engineering*, ASCE. Vol. 136(4), pp.379-389.
- Yu, T., Wong, Y.L. and Teng, J.G. (2010b). "Behavior of Hybrid FRP-Concrete-Steel Double-Skin Tubular Columns Subjected to Eccentric Compression", *Advanced in Structural Engineering*. Vol. 13(5), pp.961-974.
- Zhang, B., Teng, J.G. and Yu, T. (2017). "Compressive Behavior of Double-Skin Tubular Columns with High-Strength Concrete and a Filament-Wound FRP Tube", *Journal of Composites for Construction*, ASCE. Vol. 21(5): 04017029.
- Zhao, J.L. (2016). "Behavior and Modeling of Large-Scale Hybrid FRP-Concrete Steel Double Skin Tubular Beams with Shear Connectors", Ph.D. thesis, The Hong Kong Polytechnic University, Hong Kong, China.

**Table 8. 1 Geometric and material properties of DSTC specimens**

Steel tube					Concrete			$D_{o,s}/t$	Void ratio $\phi$
$D_{o,s}$ (mm)	$t_s$ (mm)	$E_s$ (GPa)	$f_y$ (MPa)	$f_u$ (MPa)	$E_c$ (GPa)	$\epsilon_{co}$	$f'_{co}$ (MPa)		
219	6.12	278.5	215.4	385.0	33937	0.00290	51.48	35.78	0.73

	Specimen	$L$ (mm)	$L_{eff}$ (mm)	$\lambda$	GFRP tube				
					$D_{in}$ (mm)	$t_{frp}$ (mm)	$E_x$ (GPa)	$\nu_{x\theta}$	$E_\theta$ (GPa)
1	C3-50-6	900	1082	11.77	299.6	2.22	10.94	0.106	39.62
2	C6-0-6	1800	1982	21.54	299.8	2.32			
3	C6-50-4	1800	1982	21.64	298.8	1.73	11.10	0.116	36.48
4	C6-50-6			21.54	299.2	2.30	10.94	0.106	39.62
5	C6-50-8			21.45	298.7	3.73	10.90	0.124	34.82
6	C6-100-6			21.54	299.7	2.30	10.94	0.106	39.62
7	C6-150-6			21.54	299.9	2.28			
8	C9-50-6	2700	2882	31.34	299.6	2.27			
9	C11-50-6	3300	3482	37.93	299.0	2.22			

**Table 8. 2 Key test results of eccentrically-loaded slender DSTCs**

	Specimen	Experiment								Prediction <sup>a</sup>				<i>e</i> (mm)
		$N_{peak}$ (kN)	$M_u$ (kN·m)	$N_u$ (kN)	$e'_u$ (mm)	$\epsilon_{cu}$	$\epsilon_{h,rup}$	$\sigma_{\theta u}$ (kN)	$\epsilon'_{h,rup}$	$N_{peak}$ (kN)	$M_u$ (kN·m)	$e'_u$ (mm)	$\epsilon_{cu}$	
1	C3-50-6	2166	128.11	2076	11.71	0.0472	0.0108	256.29	0.00647	1969/ 1947/ 1981	111.54/ 110.12/ 116.89/	6.65/ 6.57/ 9.01	0.0119/ 0.0119/ 0.0164	50
2	C6-0-6	2957	80.40	2564	33.46	0.0381	0.0119	355.47	0.00897	NA	NA	NA	NA	0
3	C6-50-4	1771	123.08	1633	25.37	0.0261	0.00901	282.37	0.00774	1764/ 1757/ 1760	120.89/ 119.63/ 127.62	19.20/ 18.96/ 24.64	0.0118/ 0.0120/ 0.0167	50
4	C6-50-6	1792	145.79	1493	47.65	0.0405	0.0101	256.47	0.00647	1797/ 1783/ 1788	124.56/ 123.03/ 133.61	19.68/ 19.61/ 26.44	0.0116/ 0.0120/ 0.0169	50
5	C6-50-8	1881	158.00	1737	40.96	0.0410	0.00874	192.46	0.00553	1815/ 1794/ 1802	128.98/ 126.67/ 139.11	21.26/ 21.12/ 28.79	0.0124/ 0.0127/ 0.0177	50

	Specimen	Experiment								Prediction <sup>a</sup>				<i>e</i> (mm)
		<i>N<sub>peak</sub></i> (kN)	<i>M<sub>u</sub></i> (kN·m)	<i>N<sub>u</sub></i> (kN)	<i>e'<sub>u</sub></i> (mm)	$\epsilon_{cu}$	$\epsilon_{h,rup}$	$\sigma_{\theta u}$ (kN)	$\epsilon'_{h,rup}$	<i>N<sub>peak</sub></i> (kN)	<i>M<sub>u</sub></i> (kN·m)	<i>e'<sub>u</sub></i> (mm)	$\epsilon_{cu}$	
6	C6-100-6	1317	122.78	908	35.22	0.0483	0.00996	211.32	0.00533	1253/ 1241/ 1248/	149.64/ 147.52/ 155.06	20.29/ 20.18/ 28.97	0.0103/ 0.0106/ 0.0163/	100
7	C6-150-6	935	160.90	796	52.14	0.0385	0.00860	198.89	0.00502	901/ 893/ 898	154.13/ 151.49/ 156.94	23.27/ 22.07/ 33.75	0.0103/ 0.0102/ 0.0171	150
8	C9-50-6	1652	156.76	1215	79.02	0.0325	0.00850	225.47	0.00569	1660/ 1652/ 1655	134.74/ 133.00/ 144.92	34.08/ 33.83/ 45.76	0.0105/ 0.0108/ 0.0158	50
9	C11-50-6	1557	150.12	1025	96.46	0.0203	0.00625	183.38	0.00463	1550/ 1544/ 1546	136.58/ 135.34/ 145.77	42.69/ 42.67/ 55.99	0.00920/ 0.00960/ 0.0142	50

<sup>a</sup> Yu *et al.*'s Eccl model/Yu *et al.*'s EccD model/Lin's EccD model

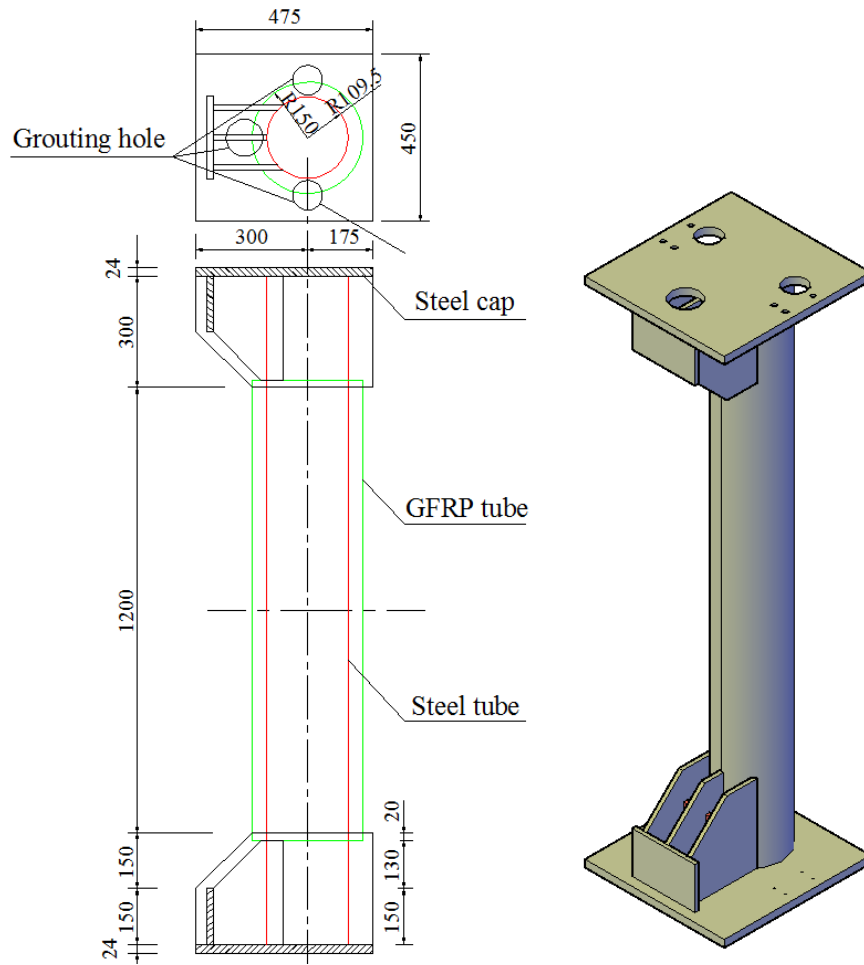


**Figure 8. 1** Schematic diagram of eccentrically-loaded slender DSTCs



**Figure 8. 2** Construction of the corbel ends of eccentrically-loaded slender DSTCs

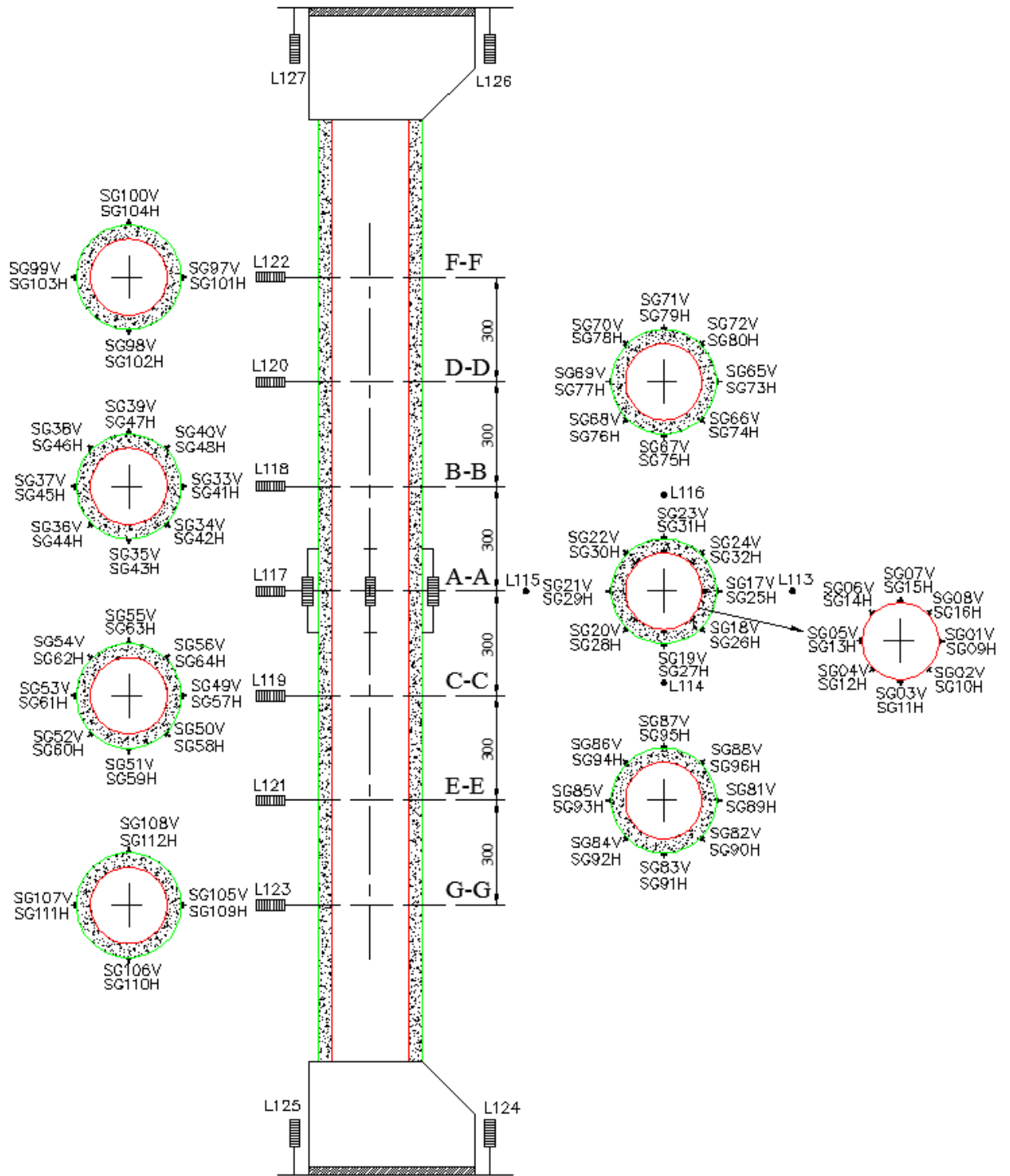


**Figure 8. 3** Layout of strain gauges and LVDTs of Specimen C6-11-50



(a) Specimen C11-50-6



(b) Specimen C6-0-6

**Figure 8. 4** Test setup of eccentrically-loaded slender DSTCs



**Figure 8. 5** General view of all slender hybrid DSTCs after tests



(a) C3-50-6



(b) C6-0-6



(c) C6-50-4



(d) C6-50-6



(e) C6-50-8



(f) C6-100-6



(g) C6-150-6



(h) C9-50-6



(i) C11-50-6

**Figure 8. 6** Failure mode of slender eccentrically loaded hybrid DSTCs



**Figure 8.7** General view of steel tubes after test

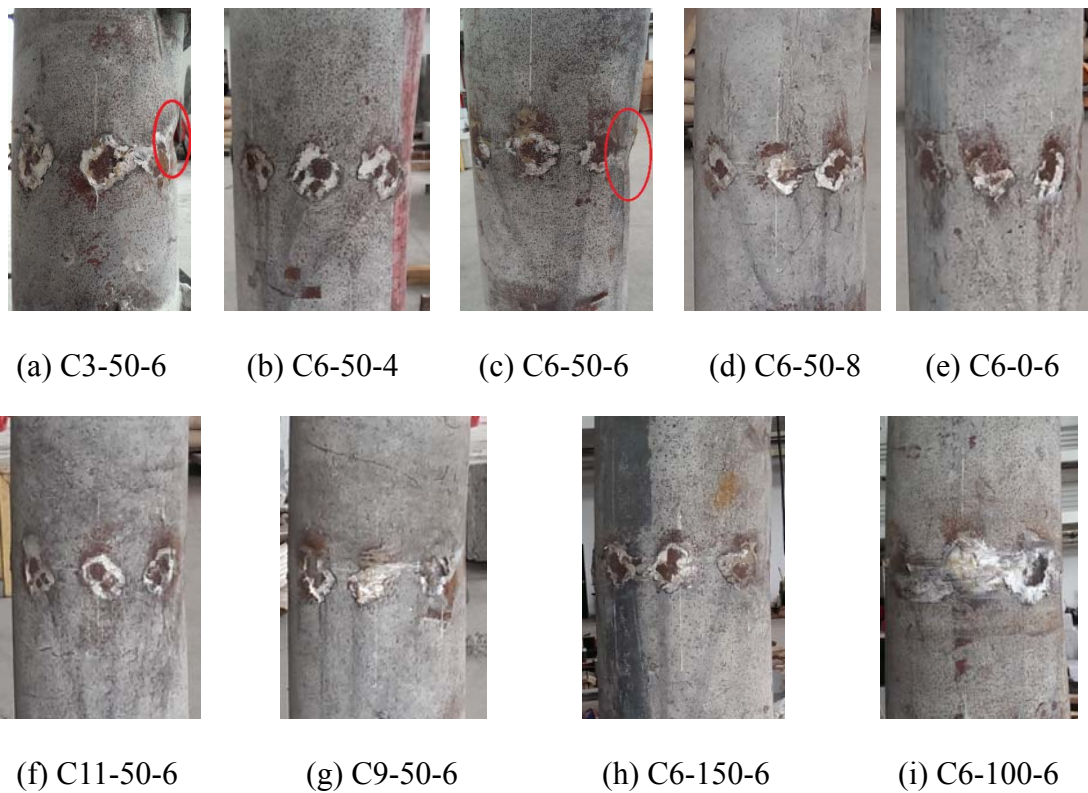
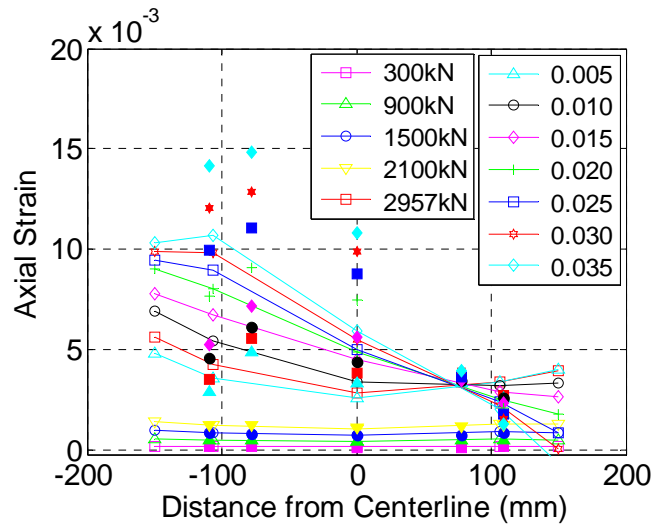
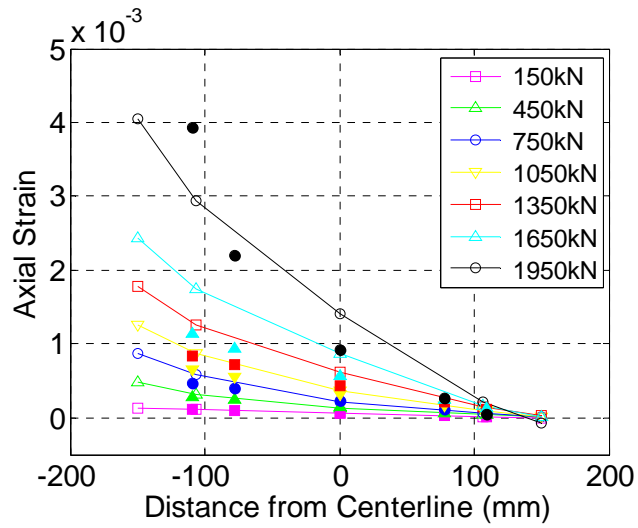


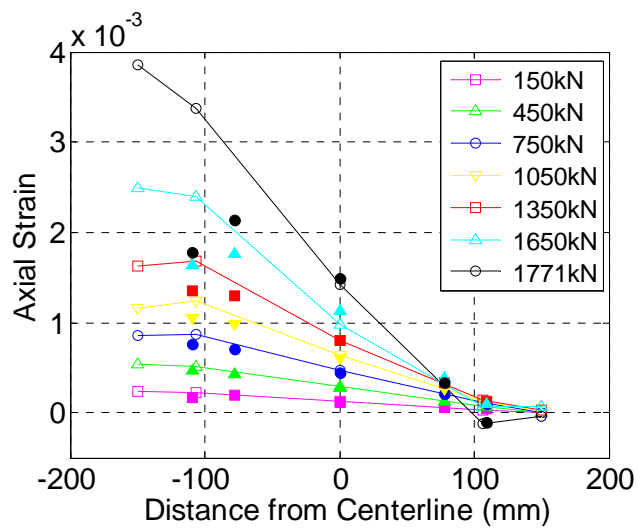
**Figure 8.8** Close-up view of steel tubes after test



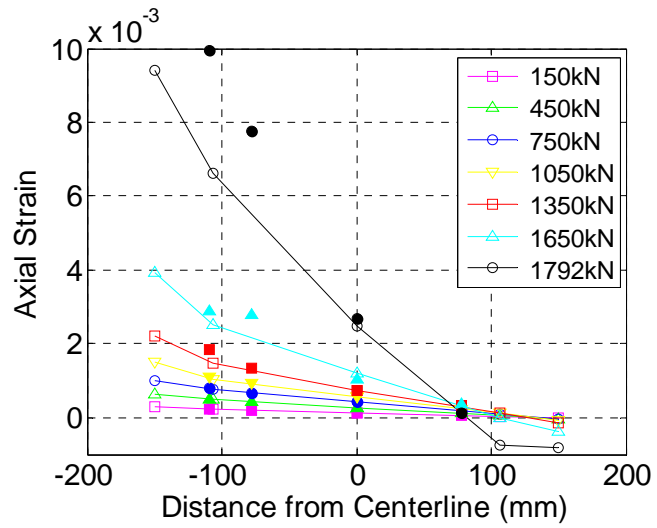
(a) C6-0-6



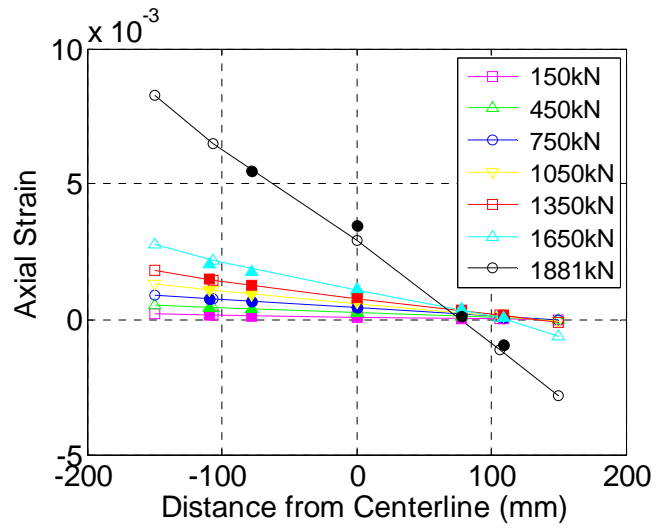
(b) C3-50-6



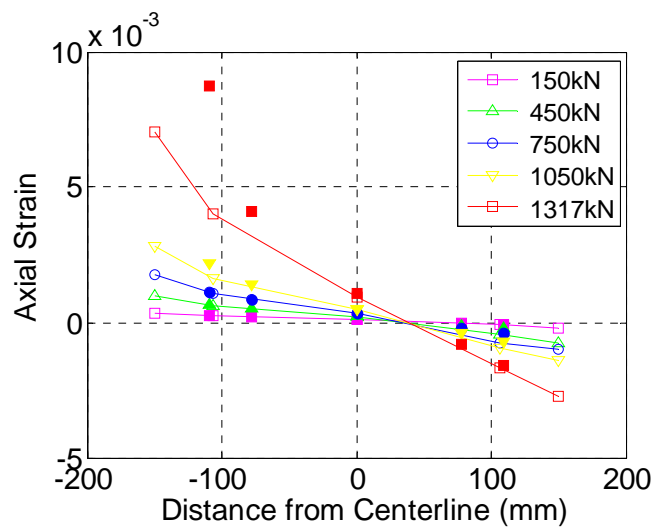
(c) C6-50-4



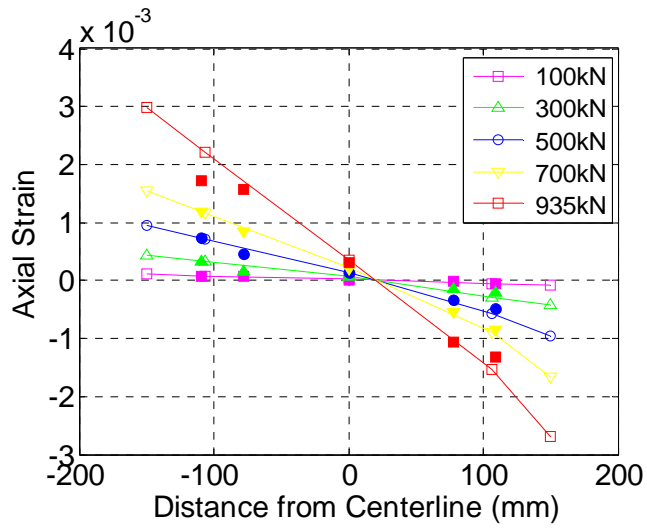
(d) C6-50-6



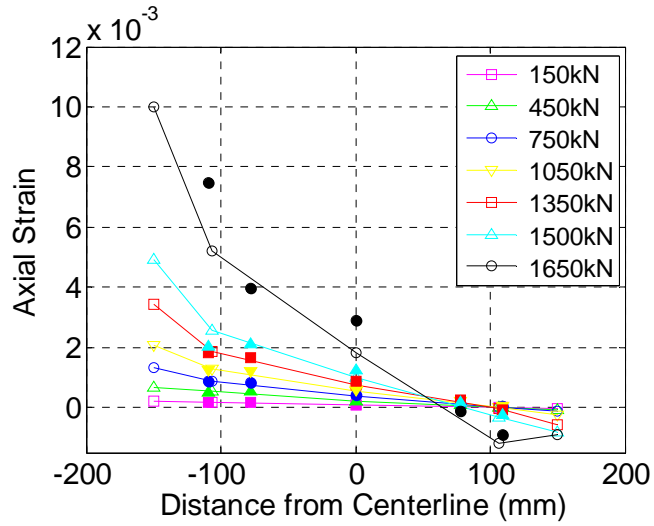
(e) C6-50-8



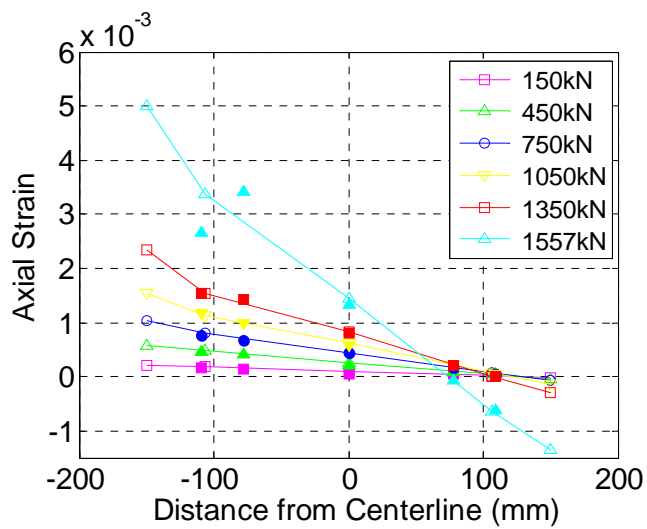
(f) C6-100-6



(g) C6-150-6

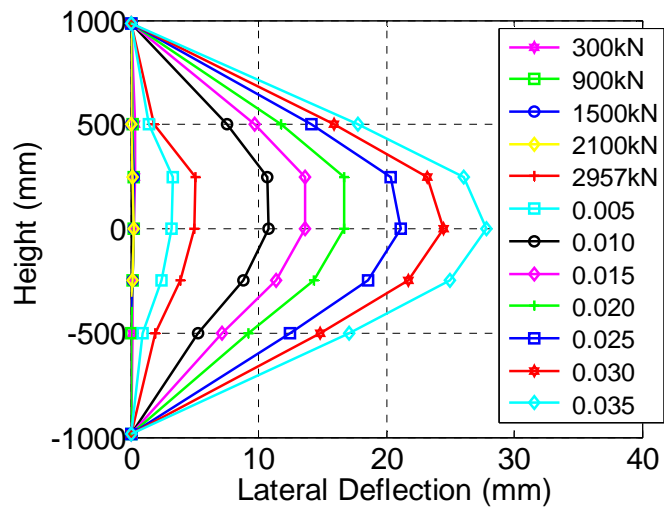


(h) C9-50-6

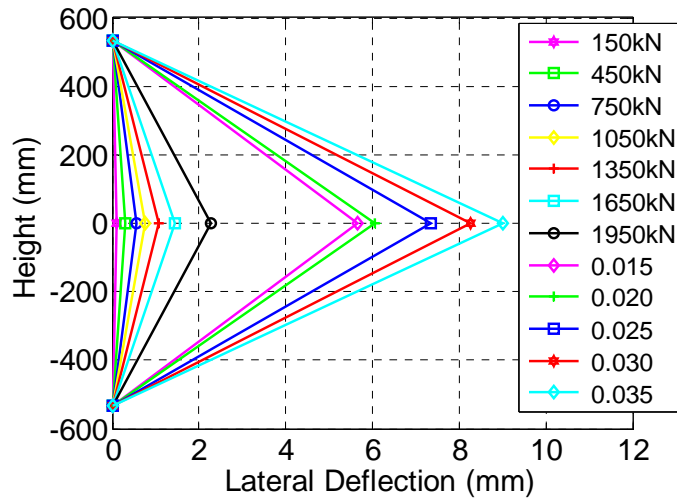


(i) C11-50-6

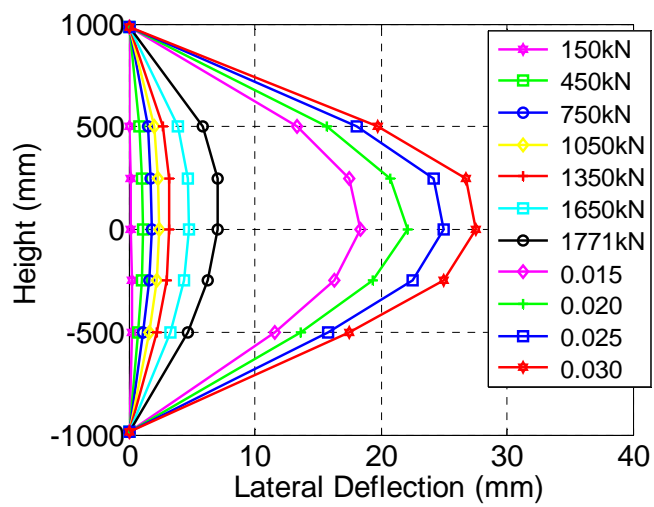
**Figure 8.9** Axial strain distribution over mid-height section



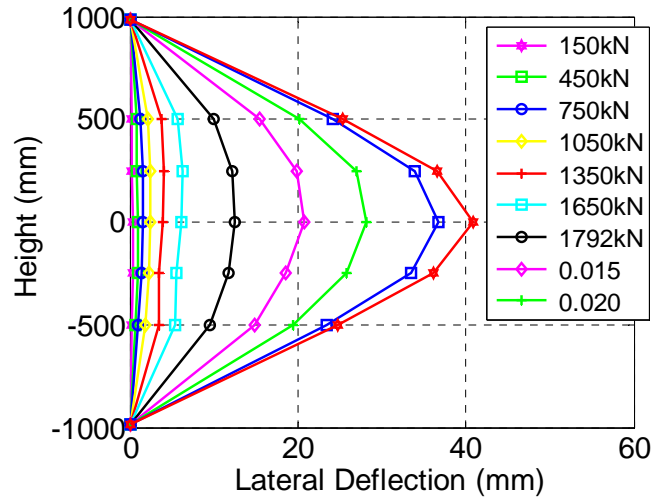
(a) C6-0-6



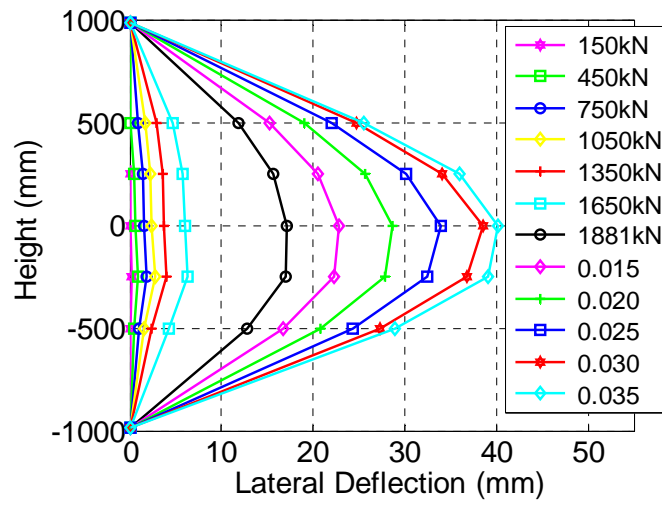
(b) C3-50-6



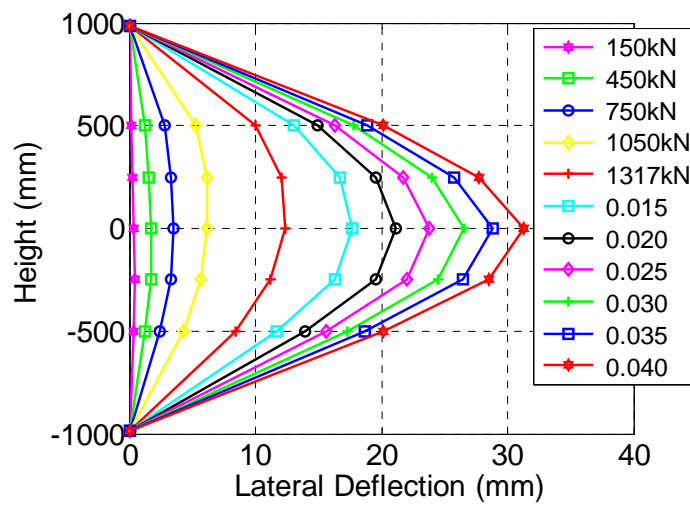
(c) C6-50-4



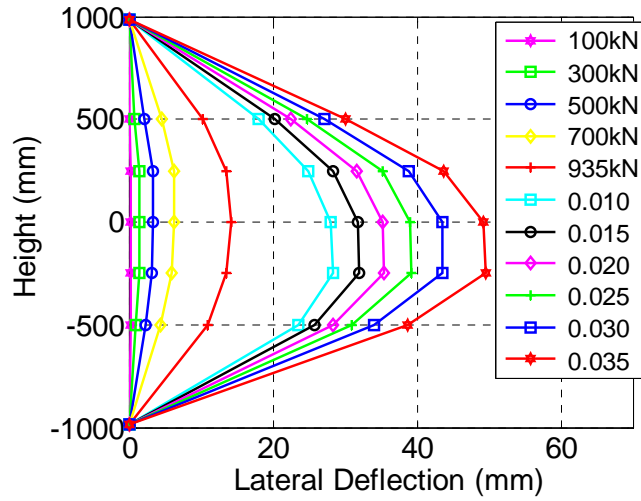
(d) C6-50-6



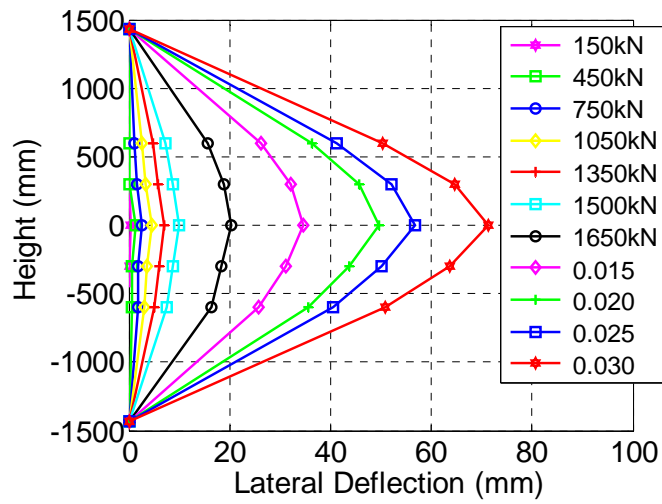
(e) C6-50-8



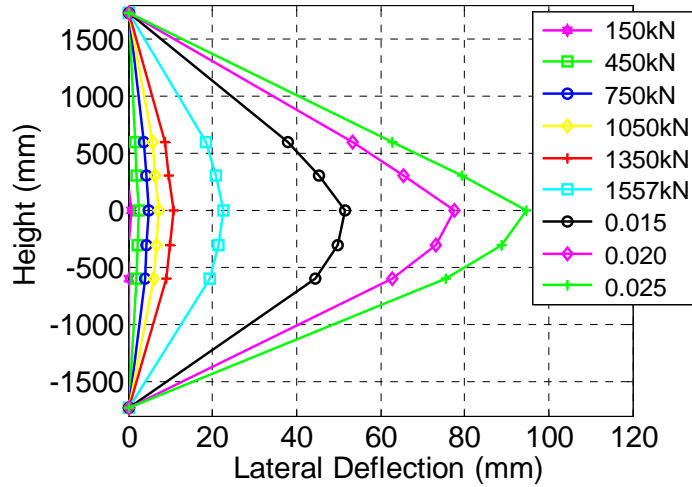
(f) C6-100-6



(g) C6-150-6

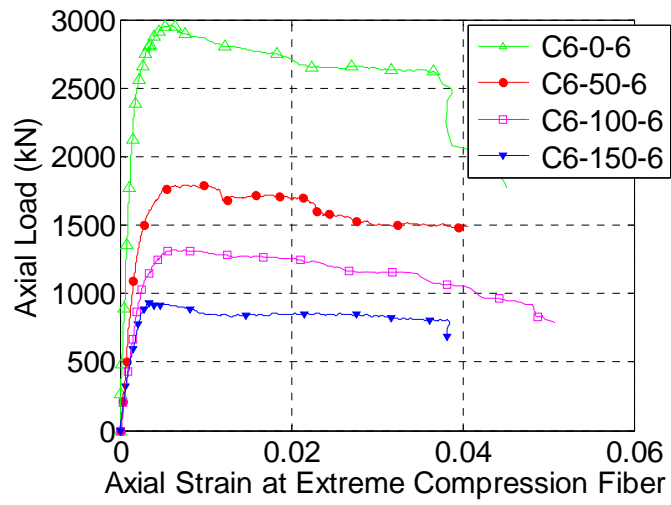


(h) C9-50-6

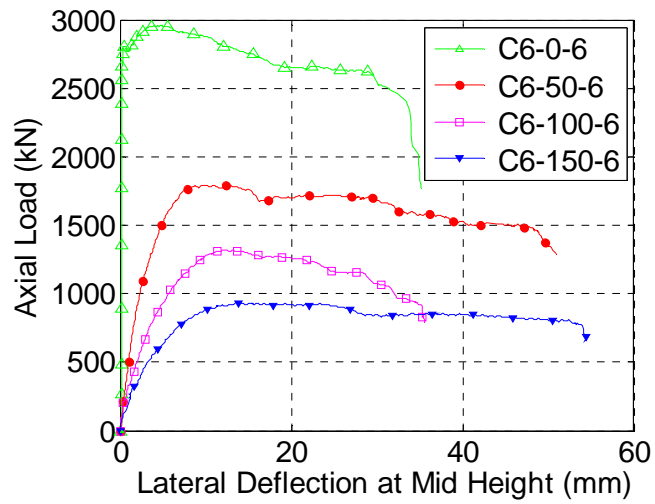


(i) C11-50-6

**Figure 8. 10** Lateral deflections along column height

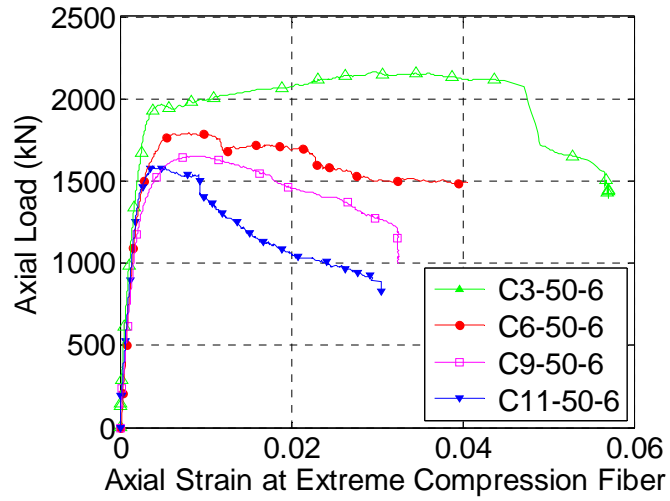


(a)

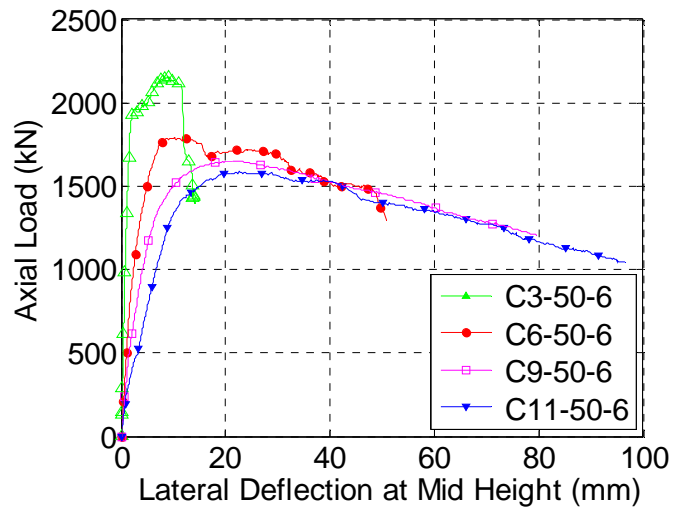


(b)

**Figure 8. 11** Effect of eccentricity

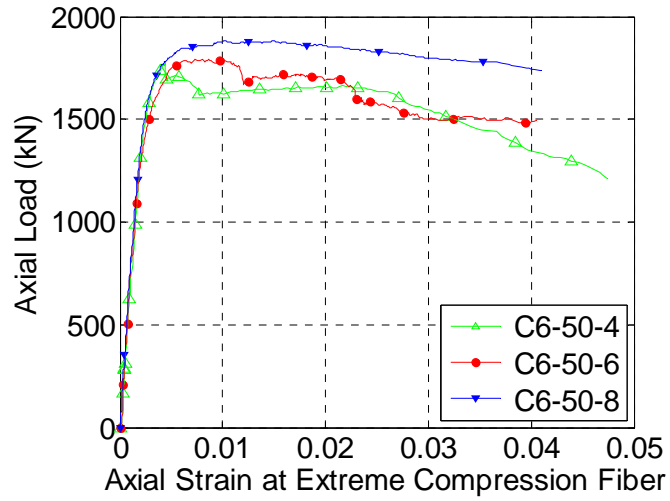


(a)

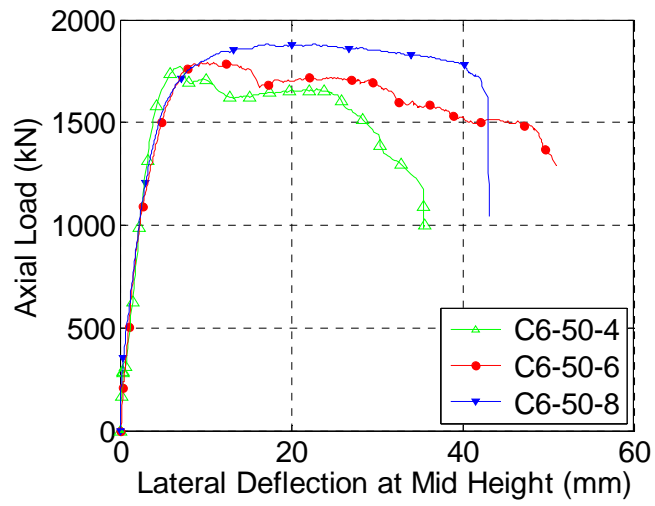


(b)

**Figure 8. 12** Effect of slenderness

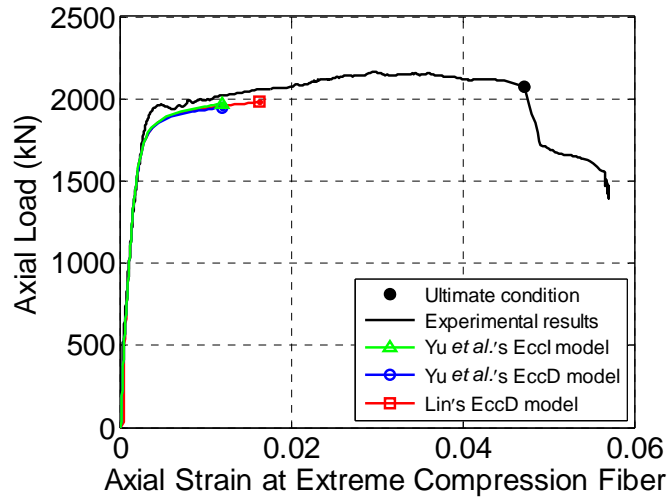


(a)

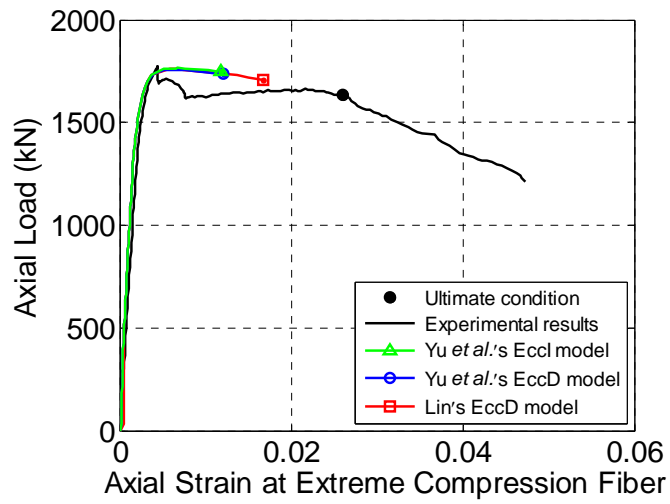


(b)

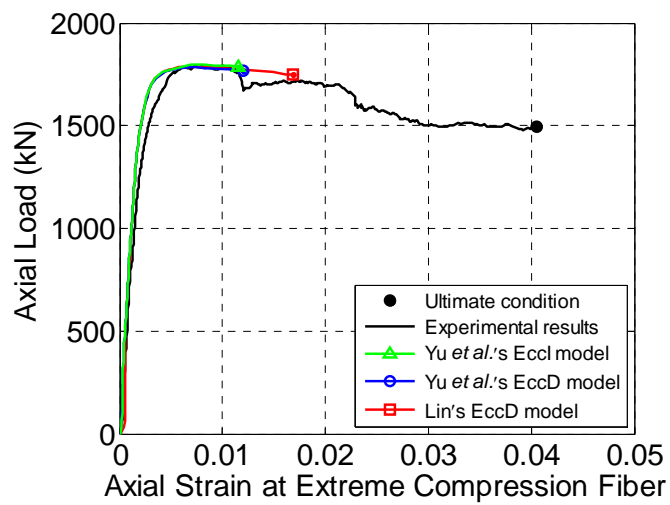
**Figure 8. 13** Effect of thickness of GFRP tube



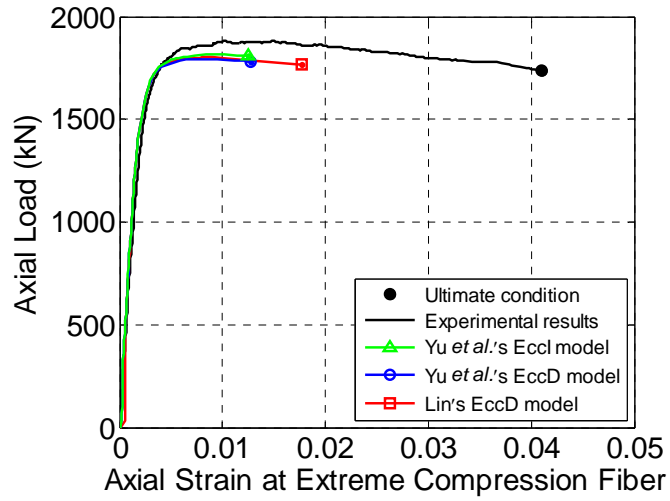
(a) C3-50-6



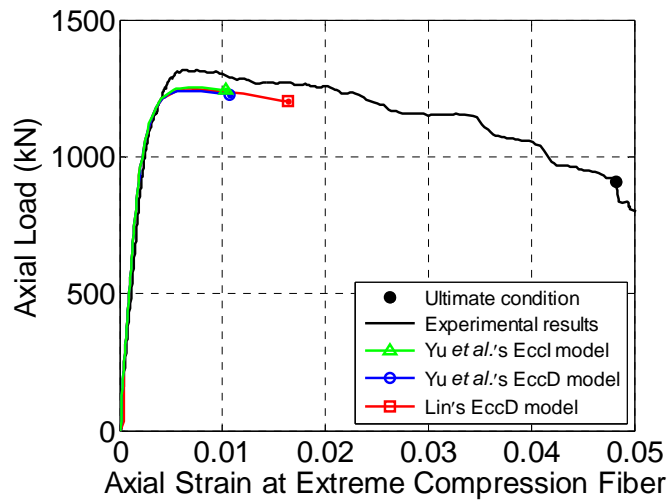
(b) C6-50-4



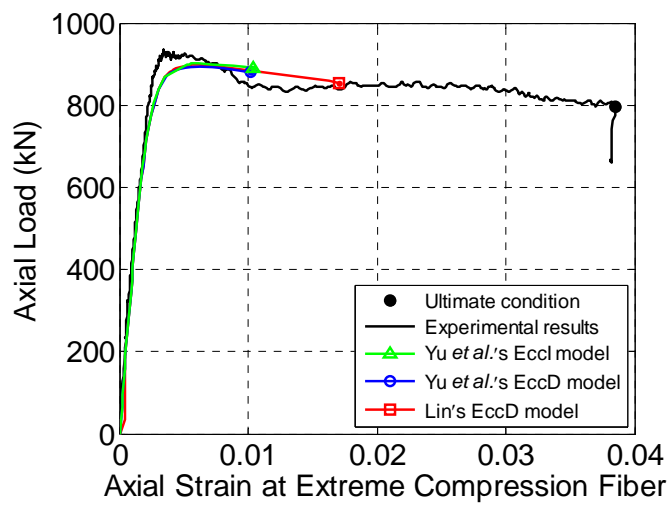
(c) C6-50-6



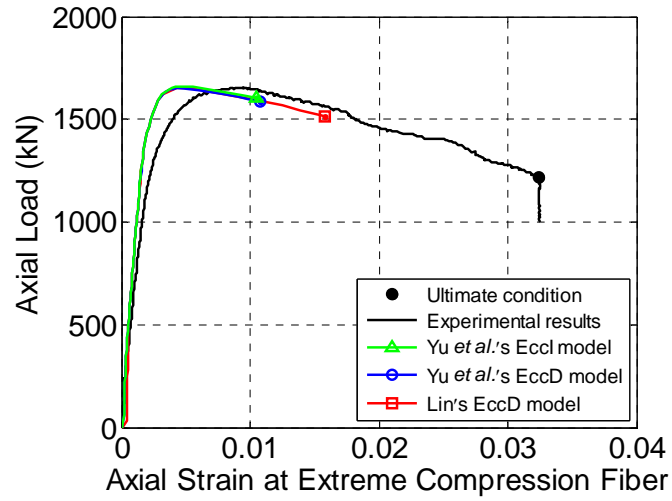
(d) C6-50-8



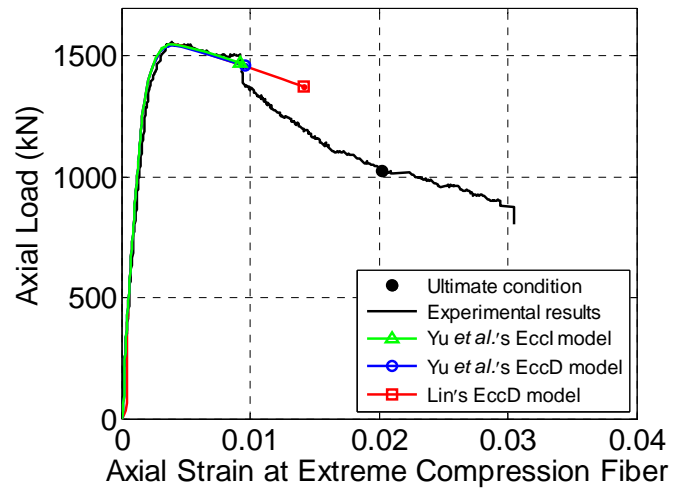
(e) C6-100-6



(f) C6-150-6

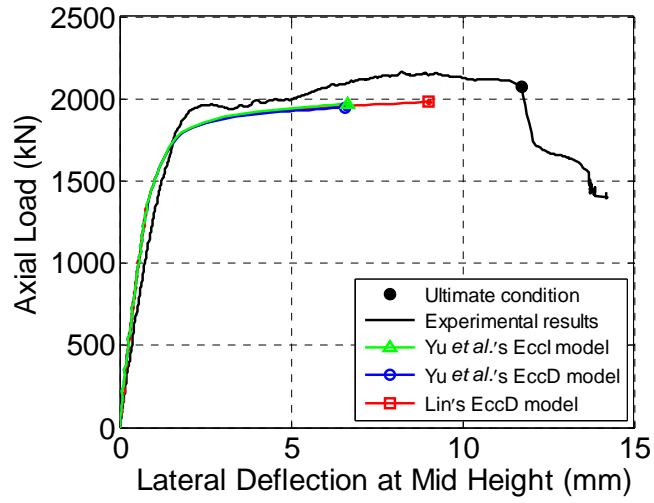


(g) C9-50-6

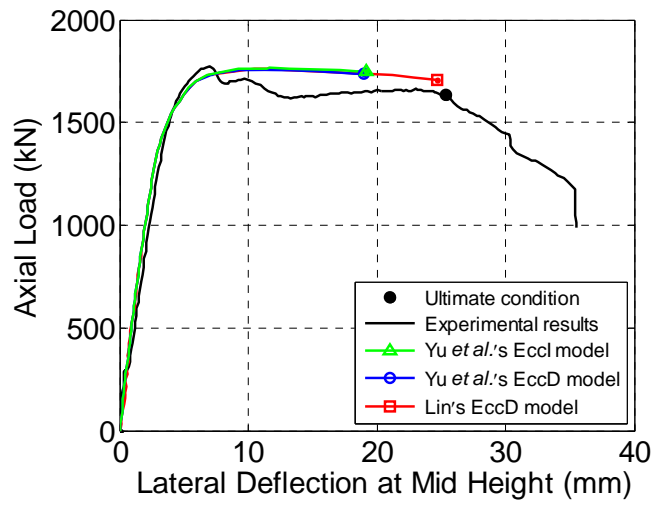


(h) C11-50-6

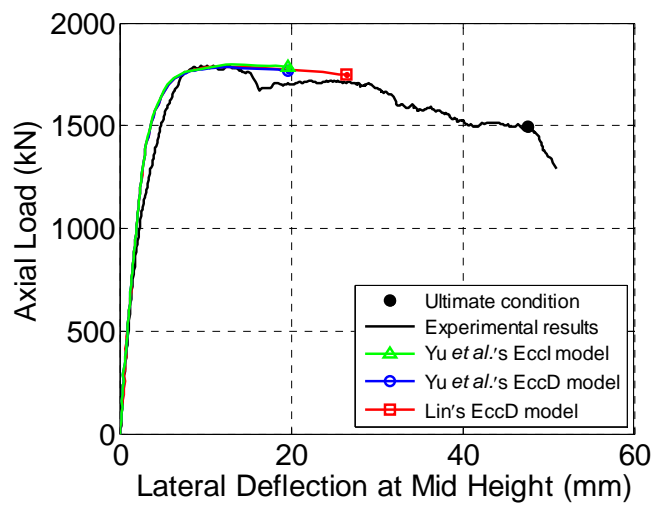
**Figure 8. 14** Comparisons between experimental and predicted axial load-axial strain at extreme compression fiber curves



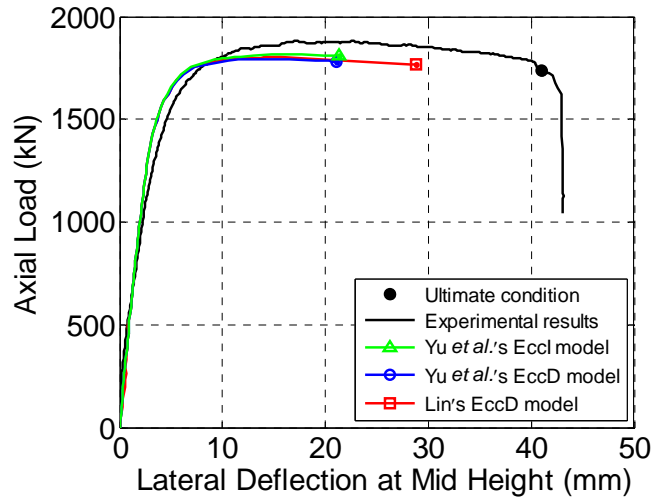
(a) C3-50-6



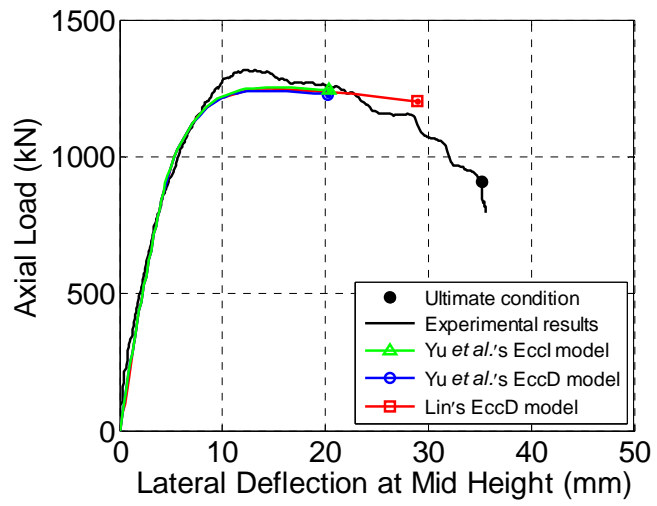
(b) C6-50-4



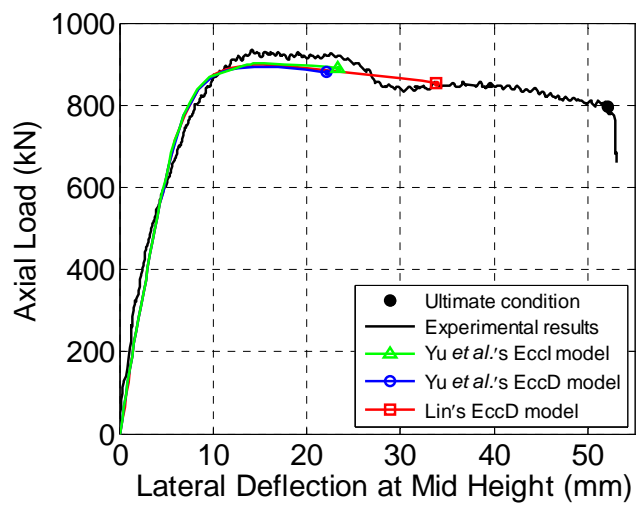
(c) C6-50-6



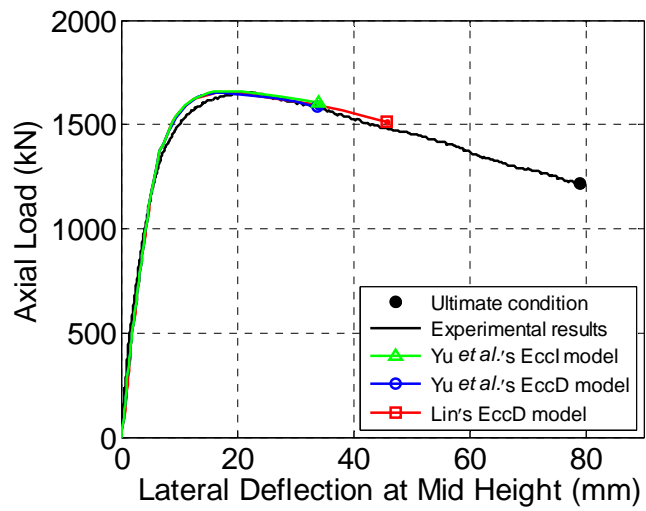
(d) C6-50-8



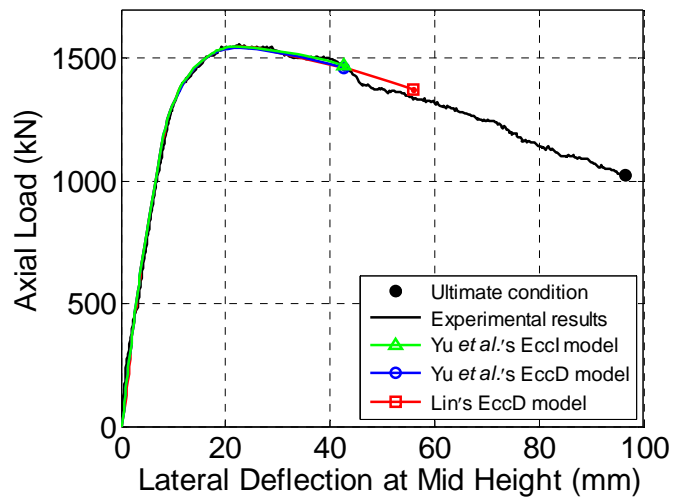
(e) C6-100-6



(f) C6-150-6

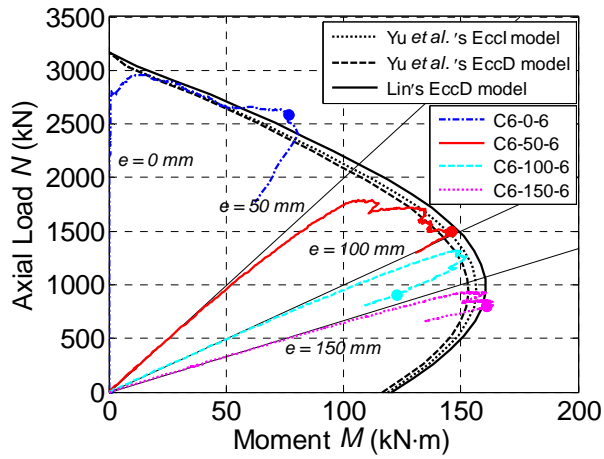


(g) C9-50-6

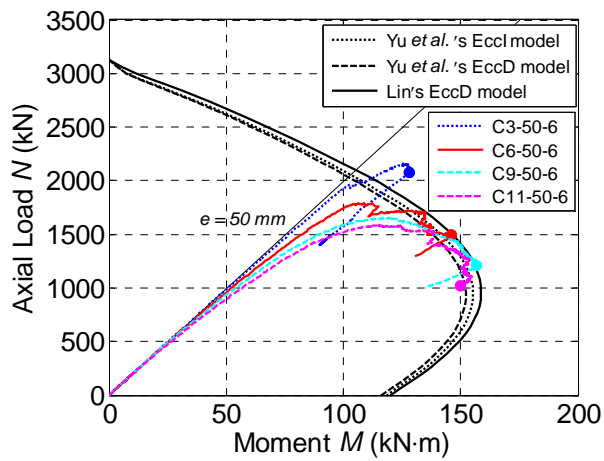


(h) C11-50-6

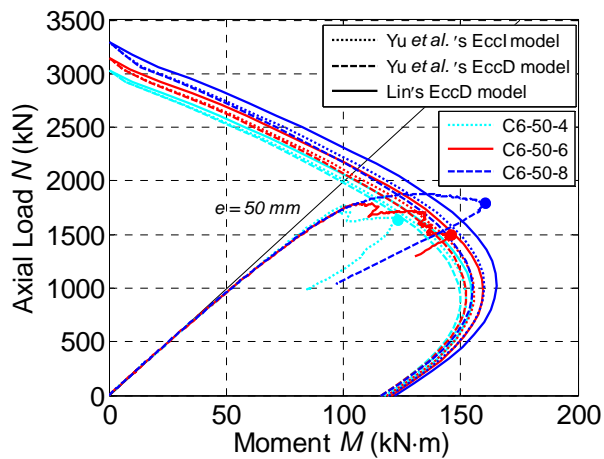
**Figure 8. 15** Comparisons between experimental and predicted axial load-lateral deflection curves



(a) Effect of eccentricity

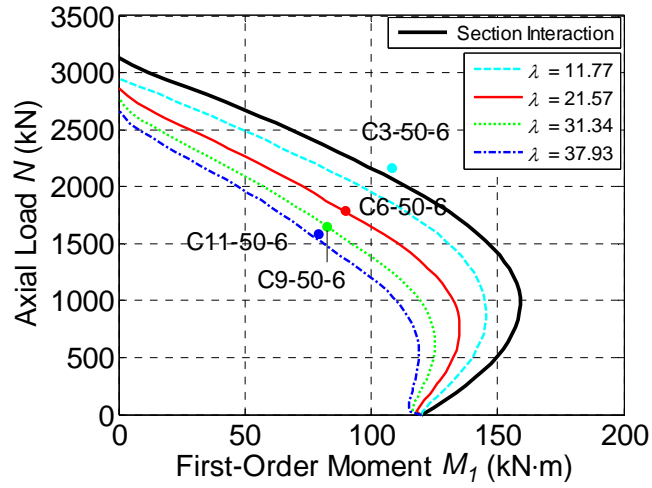


(b) Effect of slenderness

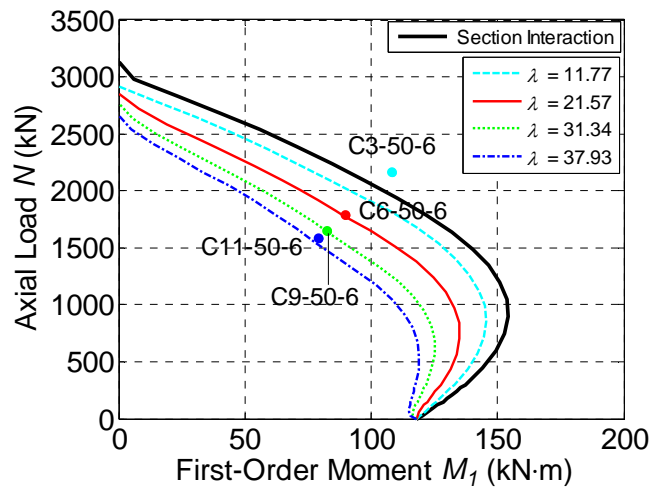


(c) Effect of thickness of GFRP tube

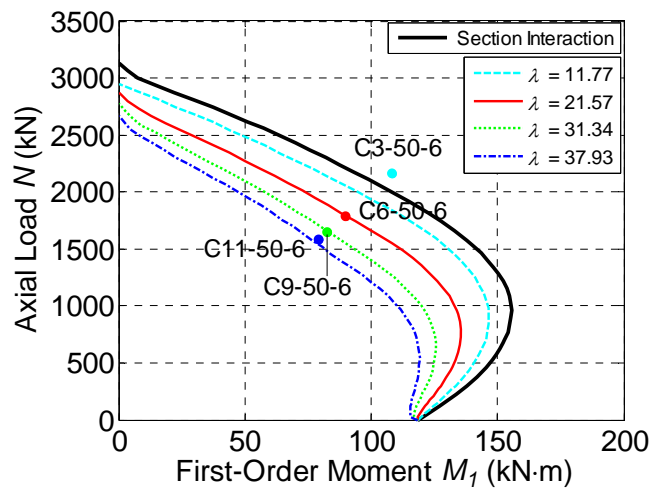
**Figure 8. 16** Experimental axial load-bending moment loading paths and theoretical section interaction diagrams



(a) Lin's EccD Model



(b) Yu *et al.*'s EccD Model



(c) Yu *et al.*'s EccI Model

**Figure 8. 17** Interaction diagrams of hybrid DSTCs

## CHAPTER 9

# SLENDERNESS LIMIT FOR SHORT HYBRID DSTCS

### 9.1 INTRODUCTION

Chapters 7 and 8 have studied the compressive behavior of large-scale short and slender hybrid DSTCs respectively and have shown that the axial load capacity of hybrid DSTCs decreases with column slenderness due to the slenderness effect. It is well-known that in the design of RC columns, the majority of design codes (e.g., ACI-318 2008; GB50010 2010) specify a slenderness limit expression to differentiate short columns from slender columns. This is because the design procedure for short columns is much simpler than that for slender columns as the former does not have to consider the slenderness effect. Similarly, such a slenderness limit expression for hybrid DSTCs is desirable to facilitate the design of short hybrid DSTCs. It should be noted that although hybrid DSTCs have been receiving increasing research attention from all over the world, relevant design provisions for hybrid DSTCs have been very limited so far. Only the Technical Code for Infrastructure Application of Fiber-Reinforced Polymer (FRP) Composites (GB-50608 2010) has specified provisions for the design of hybrid DSTCs under concentric and eccentric loading conditions. These provisions are all for short hybrid DSTCs; no provisions are provided for the design of slender hybrid DSTCs. A slenderness limit expression that defines the boundary between the short hybrid DSTCs and the slender ones is also specified in GB-50608 (2010). However, this slenderness limit expression directly follows the one proposed by Jiang and Teng (2010b) for short FRP-confined solid RC columns. Its applicability for hybrid DSTCs had not been strictly verified due to the lack of a proper theoretical column model for hybrid DSTCs at the time these design provisions were formulated.

Although little work has been carried out on the slenderness limit for hybrid DSTCs, important progresses have been made recently on the slenderness limit for FRP-confined RC columns (Jiang and Teng 2012a, b). Using the theoretical column model they developed (Jiang and Teng 2012a), Jiang and Teng (2012b) conducted a comprehensive parametric study to examine the effects of various parameters on the slenderness limit for FRP-confined circular RC columns. The results of their parametric study revealed that originally short RC columns may need to be classified as slender columns after FRP jacketing due to the increased slenderness effect caused by FRP confinement. This is because FRP confinement leads to a significant increase of the strength of a column section without significantly increasing the flexural rigidity of the section. They also proposed a slenderness limit expression for short FRP-confined circular RC columns. This expression has been adopted by GB-50608 (2010). UK's Concrete Society's TR 55 (2012) has also adopted the part of Jiang and Teng's (2012b) slenderness limit expression that accounts for the increased slenderness effect due to FRP confinement.

Against the background, a comprehensive parametric study using the column model presented in Chapters 7 and 8 will be performed in this chapter to investigate the effects of the main parameters on the slenderness limit for hybrid DSTCs. Based on the numerical results of the parametric study, the relative importance of the parameters examined will be identified and a slenderness limit expression for short hybrid DSTCs will be proposed. The proposed slenderness limit expression takes a form similar to that of Jiang and Teng's (2012b) expression and includes a new item to account for the effect of the void ratio on the slenderness limit for hybrid DSTCs.

## 9.2 DEFINITION OF SLENDERNESS LIMIT

The slenderness limit for short columns refers to such a column slenderness ratio that it causes the axial load capacity of the column to be lower than that of the column section (i.e., zero slenderness column) under the same loading condition by a small prescribed percentage [commonly 5% or 10% (ACI 318, 2008; CEB-FIP, 1993)] due to the slenderness effect. Columns with a slenderness ratio less than the slenderness limit are referred to as short columns as the slenderness effect in such columns is limited. A clear graphical definition of the slenderness limit for short columns can be found in Jiang and Teng (2012b). The slenderness ratio is typically defined as the effective length of a column divided by the radius of gyration of the column section. For hybrid DSTCs, the calculation of the radius of gyration is rather complex due to the annular sectional shape. Considering the fact that the slenderness limit expression is mainly intended for convenient use in design, the slenderness ratio of hybrid DSTCs is defined as the effective length of a hybrid DSTC divided by the outer diameter of the annular concrete section instead in this chapter ( $L_{eff}/D_o$ ).

## 9.2 ANALYTICAL APPROACH

The theoretical column model employed in Chapters 7 and 8 is used again in this chapter to conduct a comprehensive parametric study on the slenderness limit. The analysis procedure finds the slenderness limit for a given hybrid DSTC section (with known geometric and material properties) under a given load eccentricity through the following steps: (1) calculate the axial load capacity of the given section under the given eccentricity by setting the column slenderness to be zero in the column model; (2) assign the column with an assumed length and obtain the axial load capacity of the column using the column model; (3) adjust the column length and repeat step (2) until

the axial load capacity of the column is equal to the prescribed proportion of the sectional axial load capacity obtained in step (1) (e.g., 95% of the sectional axial load capacity if a 5% axial load reduction criterion is adopted in defining the slenderness limit); (4) the slenderness limit for the case under consideration is calculated based on the column length found in step (3).

In the above analysis procedure, the hybrid DSTCs were analyzed under pinned-end conditions so that the effective length of the column is equal to its physical length ( $L_{eff} = L$ ). The determination of the effective length of restrained hybrid DSTCs is beyond the scope of this thesis and needs further research. Besides, the columns were analyzed under braced (non-sway) conditions in which lateral displacement at the two column ends is prevented. Columns under unbraced (sway) conditions are more susceptible to the slenderness effect, creating the need of developing a separate slenderness limit expression, also beyond the scope of this thesis. Lin's EccD stress-strain model (Lin 2016) was chosen for incorporation into the column model as Lin's EccD model has been shown to be more accurate than Yu *et al.*'s EccI model (Yu *et al.* 2010a) and Yu *et al.*'s EccD model (Yu *et al.* 2010b) in Chapters 7 and 8.

## **9.3 PARAMETRIC STUDY**

### **9.3.1 Parameters Considered**

A parametric study using the theoretical column model was conducted to examine the effects of various parameters on the slenderness limit for short hybrid DSTCs. The reference hybrid DSTC section in the parametric study was assigned with an outer diameter of the annular concrete section of 600 mm. The material properties of concrete and steel tubes were fixed because it has been proved by Pfrang and Siess

(1961) and MacGregor *et al.* (1970) that they only have minor effects on the structural behavior of slender RC columns. The concrete filled between the inner steel tube and the outer FRP tube was assigned with a characteristic compressive strength of 20.1 MPa, which represented Grade C30 concrete according to the Chinese design code for RC structures (GB50010 2010). The steel tube had a characteristic yield strength  $f_y = 335$  MPa and an elastic modulus  $E_s = 200$  GPa.

The other parameters having an effect on the slenderness limit for short hybrid DSTCs, including the strain ratio ( $\rho_\epsilon$ ), the strength enhancement ratio ( $f'_{cc}/f'_{co}$ ), the normalized eccentricity ( $e_2/D_o$ ), the eccentricity ratio ( $e_1/e_2$ ), the void ratio ( $\phi$ ) and the diameter-to-thickness ratio of steel tube ( $D_{o,s}/t_s$ ), were also considered in the parametric study. The values of the parameters studied are listed in Table 9.1. The justification for the ranges of values adopted in the parametric study is given in the following paragraphs.

For fully exploiting the advantage of hybrid DSTCs being light weight, the void ratio should not be too small. On the other hand, an oversized void is neither desirable as it undermines the strength of the column due to the small cross-sectional area of concrete and brings difficulty in concrete casting. Thus, the practical range of void ratio values are defined by GB 50608 (2010) to be between 0.6 and 0.8. An additional void ratio of 0.5 was included in the present parametric study because a preliminary analysis by the column model indicates that the slenderness effect is more pronounced in hybrid DSTCs with a smaller void ratio. The diameter-to-thickness ratio is defined as the ratio of the outer diameter to the thickness of the steel tube. The diameter-to-thickness ratio is restricted to 70 in GB 50608 (2010) to prevent the rapid loss of axial load resistance due to local buckling of the inner steel tube and a value of 40 is recommended in GB 50608 (2010). So the void ratio was varied between 40 and 70 at an interval of 10.

The outer FRP tube in a hybrid DSTC is primarily intended for providing hoop confinement to concrete rather than directly contributing to the axial load resistance. So the axial stiffness of the FRP tube in a hybrid DSTC is normally considerably smaller than its hoop stiffness. As a result, the axial stiffness of the FRP tube was not considered in the present parametric study. To account for the confining effect of the FRP tube, the strength enhancement ratio ( $f'_{cc}/f'_{co}$ ) and the strain ratio ( $\rho_\varepsilon$ ) were adopted because these two ratios combined are able to reflect the effects of the basic parameters including the thickness, hoop modulus of elasticity and hoop rupture strain of FRP tubes. More importantly, the use of ( $f'_{cc}/f'_{co}$ ) and  $\rho_\varepsilon$  instead of the basic parameters facilitates the construction of a neat form for the slenderness limit expression, as has been shown in Jiang and Teng (2012b) in their development of a slenderness limit expression for short FRP-confined circular RC columns. The values of ( $f'_{cc}/f'_{co}$ ) were set to vary from 1.25 to 2 at an interval of 0.25 as this range of values was believed to well represent most cases in practical applications. Indeed, GB 50608 (2010) limits ( $f'_{cc}/f'_{co}$ ) to 1.75. The values of  $\rho_\varepsilon$  were set to be 1.5, 3.75 and 7.5, intended to represent the characteristic hoop rupture strains (0.003, 0.0075 and 0.015) of high modulus CFRP, CFRP and GFRP, respectively, in confinement applications. The same values of  $\rho_\varepsilon$  have also been adopted in Jiang and Teng (2012b).

The eccentricities at the two column ends under eccentric loading are respectively represented by  $e_1$  and  $e_2$ . The latter is always assigned with a non-negative value and has an absolute value no smaller than the former. A positive  $e_1/e_2$  means the column is bent in single curvature while a negative  $e_1/e_2$  means column is bent in double curvature. The normalized eccentricity ( $e_2/D_o$ ) is defined as the ratio of eccentricity ( $e_2$ ) to the outer diameter of the annular concrete ( $D_o$ ). Considering the

unintended load eccentricity as a result of geometric and material imperfections and accidental load eccentricity, an additional or a minimum eccentricity is commonly specified in design codes and imposed on column design. For example, GB-50010 (2010) specifies an additional eccentricity of  $D/30 \geq 20 \text{ mm}$  and BS-8110 (1997) specifies a minimum eccentricity of  $0.05D \leq 20 \text{ mm}$ , where  $D$  is the diameter of a solid RC column and it should be replaced by the outer diameter of annular concrete ( $D_o$ ) for a hybrid DSTC. Thus, in the present parametric study, the minimum eccentricity value was set to be  $0.05D_o$ . On the other hand, the normalized eccentricity ( $e_2/D_o$ ) is generally less than 0.84 according to a comprehensive survey by MacGregor *et al.* (1970). So the upper limit for  $e_2/D_o$  was set to be 0.8 in the parametric study. The end eccentricity ratio ( $e_1/e_2$ ) can vary between -1 and 1 in theory. In practice,  $e_1/e_2 = -1$  only represents an idealized antisymmetric loading condition; in fact the behavior of columns with a slightest disturbance tends to be considerably different. Thus, the value of -1 was replaced by -0.99. Furthermore, the interval for end eccentricity ratios between 0.5 and 1 was taken to be 0.1 and was increased to 0.5 for eccentricity ratios smaller than 0.5. This is because columns with larger eccentricity ratios are more susceptible to the slenderness effect with  $e_1/e_2 = 1$  being the most critical case.

### 9.3.2 Results of Parametric Study

The combinations of all parameters considered generated 8640 cases based on a 5% axial load capacity reduction criterion. Figures 9.1 to 9.6 display the numerical results of the parametric study. Each figure shows the slenderness limit ( $L_{crit}/D_o$ ) varying with one of the six parameters and the values of the other five parameters used to generate the numerical results are also provided in the same figure.  $L_{crit}$  is the maximum physical length of a pinned-end hybrid DSTC that can be defined as a short

hybrid DSTC.

Figure 9.1 shows the variation of slenderness limit ( $L_{crit}/D_o$ ) against the end eccentricity ratio ( $e_1/e_2$ ) with each subfigure associated with one of the four values examined for the strength enhancement ratio ( $f'_{cc}/f'_{co}$ ). Each subfigure shows a family of five curves corresponding to five values of the normalized eccentricity ratio ( $e_2/D_o$ ) (i.e., 0.05, 0.1, 0.2, 0.4 and 0.8). The other three parameters, on which the numerical results shown in Figure 9.1 were based, were fixed ( $\rho_\varepsilon = 3.75$ ,  $\phi = 0.6$  and  $D_{o,s}/t_s = 40$ ). A change in the values of these three parameters does not affect the overall trend of the numerical results and are thus not shown herein due to space limitation. It can be seen from Figure 9.1 that for a given normalized eccentricity ratio the slenderness limit for hybrid DSTCs decreases almost linearly with an increase of the end eccentricity ratio. This is because columns bent in symmetric curvature ( $e_1/e_2 = 1$ ) are most susceptible to the slenderness effect while columns bent in antisymmetric curvature ( $e_1/e_2 = -1$ ) are least. On the other hand, an increase of normalized eccentricity generally causes an increased slenderness limit, especially for cases with a negative end eccentricity ratio. The beneficial effect of the normalized eccentricity gradually diminishes as the end eccentricity ratio increases, and almost vanishes when the end eccentricity ratio approaches unity.

Figure 9.2 shows the relationship between the slenderness limit and the normalized eccentricity ratio. It can be seen that the slenderness limit increases with the end eccentricity ratio and the increasing rate markedly decreases with increasing end eccentricity ratio. For the extreme case of  $e_1/e_2 = 1$ , the curves almost remain flat, in consistence with the numerical results shown in Figure 9.1. The differences between the curves become smaller as the normalized eccentricity ratio decreases. This trend is

reasonable because these curves converge at a very small value of  $e_2/D_o = 0.001$  as the end eccentricity ratio would have hardly any effect under such condition. Note that  $e_2/D_o = 0.001$  was only used in Figure 9.2 for illustrative purposes and was not used elsewhere in the parametric study.

Figure 9.3 shows the effect of strength enhancement ratio on the slenderness limit. The five curves shown in each subfigure correspond to five specific values of the normalized eccentricity (i.e., 0.05, 0.1, 0.2, 0.4 and 0.8). It can be seen from the Figure 9.3 that a higher strength enhancement ratio leads to a lower slenderness limit, meaning an increased slenderness effect is introduced by FRP confinement. This is because FRP confinement can substantially increase the axial load capacity of a hybrid DSTC section, but the flexural rigidity of such a section in the range of confinement-enhanced resistance is much lower than its initial flexural rigidity.

Figure 9.4 shows the effect of the strain ratio. The six subfigures of Figure 9.4 are arranged in a matrix of three rows by two columns for ease of comparison. Each row corresponds to a specific normalized eccentricity ratio (0.05, 0.2 and 0.8) and the two columns correspond to the minimum and the maximum values of strength enhancement ratio ( $f'_{cc}/f'_{co} = 1.25$  and 2), respectively. Firstly, it is evident that the slenderness limit decreases with an increase of the strain ratio. This is easy to understand because under a given strength enhancement ratio a larger strain ratio leads to a higher ultimate axial strain of the confined concrete and thus a flatter second portion of its stress-strain curve, causing a reduced flexural rigidity of the column section which gives rise to a more significant slenderness effect. Secondly, the decreasing rate of the slenderness limit with respect to the strain ratio becomes slightly smaller (i.e., the corresponding curve becomes less steep) as the normalized

eccentricity ratio increases. The less significant role of the strain ratio under such condition is because columns with a larger eccentricity are less susceptible to the slenderness effect due to the larger proportion of the first-order moment. Thirdly, the effect of the strain ratio becomes more significant as the strength enhancement ratio increases. This is also easy to understand because the difference in the ultimate axial strain of the confined concrete caused by the difference in the strain ratio becomes larger when the strength enhancement ratio is higher (higher confinement level). Overall, the effect of the strain ratio on the slenderness limit is not as significant as those of the above three parameters examined.

Figure 9.5 shows the effect of the void ratio. The numerical results in Figure 9.5 were all produced for the maximum strength enhancement ratio ( $f'_{cc}/f'_{co} = 2$ ) as the effect of the void ratio was most significant at the highest confinement level. It can be seen that under a small eccentricity (i.e.,  $e_2/D_o = 0.05$ ) the slenderness limit slightly decreases with the void ratio while it increases with the void ratio under larger eccentricities (i.e.,  $e_2/D_o = 0.1, 0.2, 0.4, 0.8$ ). This discrepancy in trend is explained as follows. The effect of the void ratio on the slenderness limit is twofold: (1) a larger void ratio causes a higher ultimate axial strain [see Eq. (6.9)], which induces a more pronounced slenderness effect; and (2) a larger void ratio correlates to a smaller area of the annular concrete and a larger area of the steel tube, causing the flexural rigidity of the column section more dominated by the steel tube due to its increased lever arm as well as its area, helping the column to resist the slenderness effect. These two effects counteract with each other. The case of  $e_2/D_o = 0.05$  represents a loading condition similar to concentric loading where the flexural behavior is not significant, so the former effect slightly outweighs the latter. Nevertheless, the flexural behavior becomes more significant as the eccentricity increases, so the latter effect starts to play a more

dominant role than the former. Overall, the effect of the void ratio on the slenderness limit is much less significant than those of the first three parameters examined and is also less significant than that of the strain ratio by a lesser degree.

Finally, Figure 9.6 shows the effect of the diameter-to-thickness ratio of steel tube. It can be seen that the slenderness limit is hardly affected by this ratio for all cases shown in Figure 9.6, suggesting that the effect of this ratio is very limited.

According to the numerical results and discussions presented above, the six parameters can be classified into three categories in terms of the relative importance of their effects on the slenderness limit: (1) Parameters of a significant effect. This category includes the normalized eccentricity ratio, the end eccentricity ratio and the strength enhancement ratio; (2) Parameters of a moderate effect. This category includes the strain ratio and the void ratio; and (3) Parameters of a minor effect. This category includes the diameter-to-thickness ratio of steel tube. It is obvious that the first category of parameters should be taken into account in the development of the slenderness limit expression while the last category may be ignored. Whether the second category of parameters should be included or disregarded in the slenderness limit expression is discussed in the following sub-section.

## **9.4 PROPOSED SLENDERNESS LIMIT EXPRESSION**

### **9.4.1 Slenderness Limit Expression Proposed by Jiang and Teng (2012b)**

The present study was mainly motivated by the need to formulate the design provisions for hybrid DSTCs for “Technical Code for Infrastructure Application of FRP Composites” (GB-50608 2010). Therefore, it is desirable to develop the slenderness

limit expression for hybrid DSTCs within the framework of that code. In that code, a slenderness limit expression for CFFTs is already specified

$$\frac{L_{crit}}{D_o} = \frac{15 \frac{e_2 - e_1}{D_o} + 5}{\frac{f'_{cc}}{f'_{co}}(1 + 30\varepsilon_{h,rup})} \quad (9.1)$$

In Eq. (9.1),  $D_o$  denotes the inner diameter of the FRP tube (i.e., outer diameter of the concrete core in a CFFT). This expression is a variant of the slenderness limit expression proposed by Jiang and Teng (2012b) for short FRP-confined circular RC columns with substituting the radius of gyration ( $r_g$ ) by  $D_o/4$  ( $r_g = D_o/4$  holds for circular sections) and setting  $\varepsilon_{co} = 0.002$ . Jiang and Teng (2012b)'s expression is given below

$$\frac{L_{crit}}{r_g} = \frac{60 \frac{e_2}{D_o} \left(1 - \frac{e_1}{e_2}\right) + 20}{\frac{f'_{cc}}{f'_{co}} \left(1 + 0.06 \frac{\varepsilon_{h,rup}}{\varepsilon_{co}}\right)} \quad (9.2)$$

This expression has a clear physical meaning. The numerator defines the slenderness limit for RC columns without FRP confinement while the denominator accounts for the effect of FRP confinement. The separate treatment of the effect of FRP confinement allows for convenient upgrading of existing slenderness limit expressions for RC columns to cater for the design of FRP-confined RC columns by incorporating the denominator of the proposed expression. For example, UK's Concrete Society's TR 55 (2012) has directly adopted the denominator of Eq. (9.2) in its slenderness limit expression for FRP-confined RC columns with the numerator of the expression being the slenderness limit expression for RC columns specified in BS EN 1992-1-1 (2004).

It should be noted that in GB-50608 (2010), Eq. (9.1) also applies for hybrid DSTCs although its applicability for hybrid DSTCs had not been strictly verified due to the lack of a proper theoretical column model for hybrid DSTCs at the time the relevant design provisions were formulated. The parametric study presented in this chapter offers an opportunity to examine the applicability of Eq. (9.1) to hybrid DSTCs. Such an examination is shown in Figure 9.7 by comparing the numerical results generated by the parametric study and those predicted by Eq. (9.1). The numerical results were generated based on the 5% axial load reduction criterion. It can be seen from Figure 9.7 that Eq. (9.1) yields unconservative results for cases having low values of slenderness limit. An analysis of the numerical results revealed that Eq. (9.1) is unconservative for a total of 906 cases and the unconservativeness is partially caused by ignoring the effect of void ratio on the slenderness limit. For consistency purposes, it is advisable that the modified slenderness limit expression for hybrid DSTCs features a mathematical form similar to that of Eq. (9.1). Based on such a consideration, a new slenderness limit expression is proposed with the inclusion of a linear item to reflect the effect of the void ratio

$$\frac{L_{crit}}{D_o} \leq \frac{\phi+1}{2} \cdot \frac{15 \frac{e_2 - e_1}{D_o} + 5}{\frac{f'_{cc}}{f'_{co}}(1+30\varepsilon_{h,rup})} \quad (9.3)$$

Figure 9.8 compares the numerical results of the parametric study and the predictions of Eq. (9.3). This time, the number of unconservative cases is reduced to 165. However, if the criterion for slenderness limit is loosened to permit a 10% reduction in the axial load, Eq. (9.3) provides a lower-bound prediction for all cases examined, as shown in Figure 9.9. It should be noted that the 10% axial load reduction criterion has been adopted in the existing literature (e.g., CEB-FIP 1993).

## 9.5 CONCLUSIONS

This chapter has presented a comprehensive parametric study to identify the effects of six main parameters on the slenderness limit for short hybrid DSTCs. Based on the numerical results of the parametric study, a new slenderness limit expression for short hybrid DSTCs was proposed. According to the numerical results and discussions presented in this chapter, the following conclusions can be drawn:

- (1) The six parameters examined in the parametric study can be classified into three categories in terms of the relative importance of their effects on the slenderness limit for short hybrid DSTCs: (1) Parameters of a significant effect. This category includes the normalized eccentricity ratio, the end eccentricity ratio and the strength enhancement ratio; (2) Parameters of a moderate effect. This category includes the strain ratio and the void ratio; and (3) Parameters of a minor effect. This category includes the diameter-to-thickness ratio of steel tube.
- (2) The slenderness limit expression for hybrid DSTCs in GB-50608 (2010) yields some unconservative results for low slenderness limit values; the unconservativeness is partially caused by ignoring the effect of void ratio on the slenderness limit. Therefore, a new slenderness limit expression is proposed by adding a simple linear item to the GB-50608 expression to account for the effect of the void ratio. The proposed expression is more conservative than the GB-50608 expression and provides a lower-bound prediction for all cases examined if a 10% loss of axial load capacity is acceptable.

## 9.6 REFERENCES

- ACI-318 (2008). “Building Code Requirements for Structural Concrete and Commentary”, American Concrete Institute, Farmington Hills, MI.
- BS 8110 (1997). “Structural Use of Concrete-Part 1: Code of Practice for Design and Construction”, British Standards Institution, London, UK.
- BS EN 1992-1-1 (2004). “Eurocode 2: Design of Concrete Structures-Part 1-1: General Rules and Rules for Building”, European Committee for Standardization.
- CEB-FIP (1993). “Model Code 1990”, CEB-Bulletin No. 213/214, Comité Euro-International du Béton.
- GB-50010 (2010). “Code for Design of Concrete Structures”, China Architecture and Building Press, Beijing, China.
- GB-50608 (2010). “Technical Code for Infrastructure Application of FRP Composites”, China Planning Press, Beijing, China.
- Jiang, T. and Teng, J.G. (2012a). “Theoretical Model for Slender FRP-Confined Circular RC Columns”, *Construction and Building Materials*. Vol. 32(4), pp.66-76.
- Jiang, T. and Teng, J.G. (2012b). “Slenderness Limit for Short FRP-Confined Circular RC Columns”, *Journal of Composites for Construction*, ASCE. Vol. 16(6), pp.650-661.
- Lin, G. (2016). “Seismic Performance of FRP-Confined RC Columns: Stress-Strain Models and Numerical Simulation”, Ph.D. thesis, The Hong Kong Polytechnic University, Hong Kong, China.
- MacGregor, J. G., Breen, J. E., and Pfrang, E. O. (1970). “Design of Slender Concrete Columns”, *Journal Proceedings*. Vol. 67(1), pp.6–28.
- Pfrang, E. O., and Siess, C. P. (1961). “Analytical Study of The Behavior of Long

Restrained Reinforced Concrete Columns Subjected to Eccentric Loads”,  
Structural Research Series, No. 214, University of Illinois, Urbana, USA.

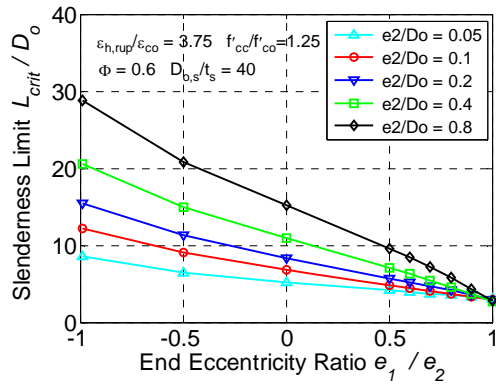
TR 55 (2012). “Design Guidance for Strengthening Concrete Structures Using Fibre Composite Materials”, Concrete Society Technical Report 55. The Concrete Society, Crowthorne, UK.

Yu, T., Teng, J.G. and Wong, Y.L. (2010a). “Stress-Strain Behavior of Concrete in Hybrid Double-Skin Tubular Columns”, *Journal of Structural Engineering*, ASCE. Vol. 136(4), pp.379-389.

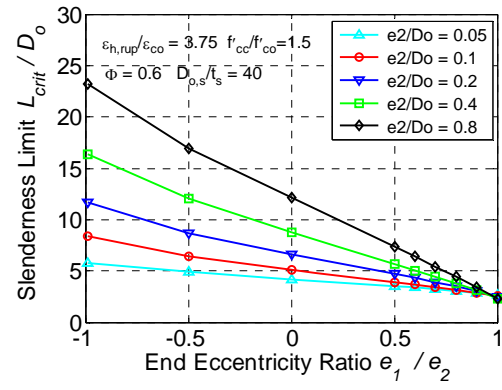
Yu, T., Wong, Y.L. and Teng, J.G. (2010b). “Behaviour of Hybrid FRP-Concrete-Steel Double-Skin Tubular Columns Subjected to Eccentric Compression”, *Advances in Structural Engineering*. Vol. 13(5), pp.961-974.

**Table 9. 1 Values of parameters considered in the parametric study**

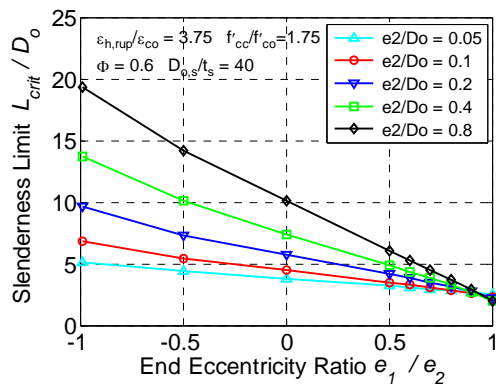
<b>Parameter</b>	<b>Values</b>
$\phi$	0.5, 0.6, 0.7, 0.8
$D_{o,s}/t_s$	40, 50, 60, 70
$\rho_\varepsilon$	1.5, 3.75, 7.5
$f'_{cc}/f'_{co}$	1.25, 1.5, 1.75, 2
$e_2/D_o$	0.05, 0.1, 0.2, 0.4, 0.8
$e_1/e_2$	1, 0.9, 0.8, 0.7, 0.6, 0.5, 0, -0.5, -0.99



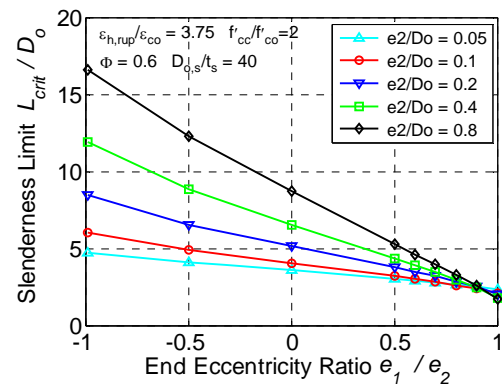
(a)  $f'_{cc} / f'_{co} = 1.25$



(b)  $f'_{cc} / f'_{co} = 1.5$

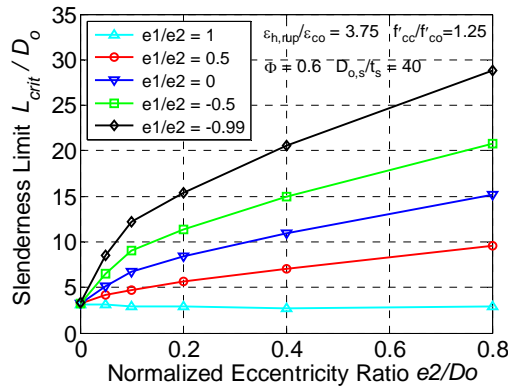


(c)  $f'_{cc} / f'_{co} = 1.75$

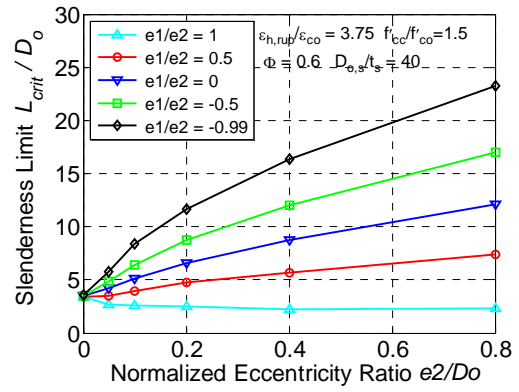


(d)  $f'_{cc} / f'_{co} = 2$

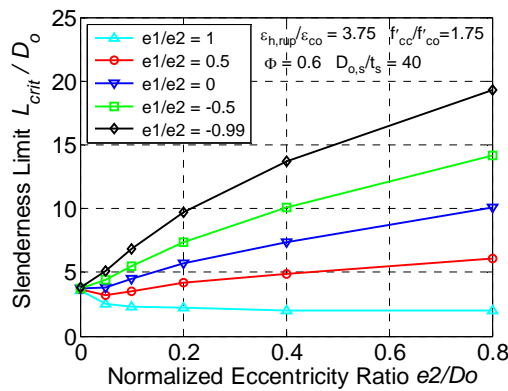
**Figure 9.1** Effect of end eccentricity ratio



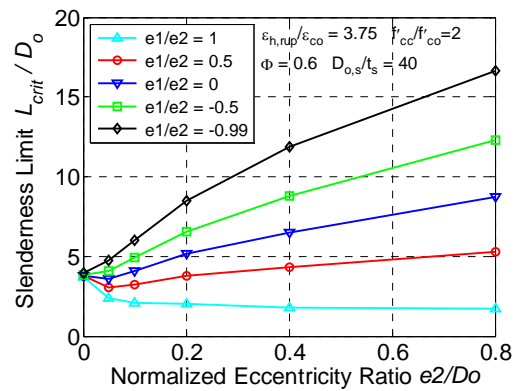
(a)  $f'_{cc}/f'_{co} = 1.25$



(b)  $f'_{cc}/f'_{co} = 1.5$

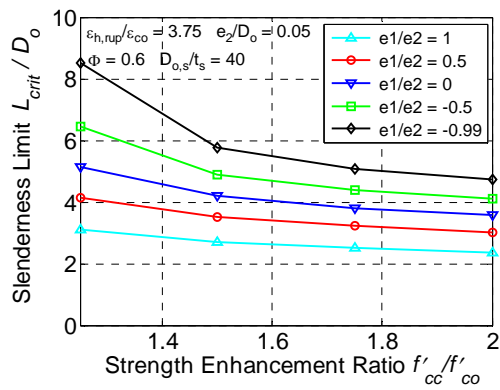


(c)  $f'_{cc}/f'_{co} = 1.75$

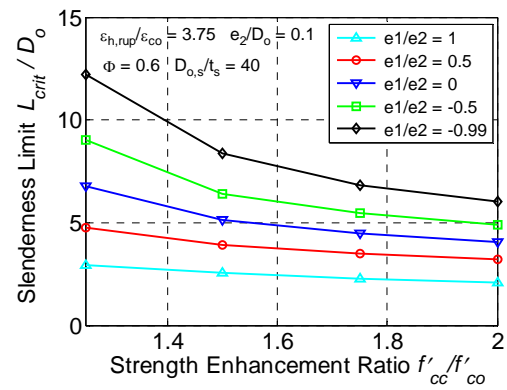


(d)  $f'_{cc}/f'_{co} = 2$

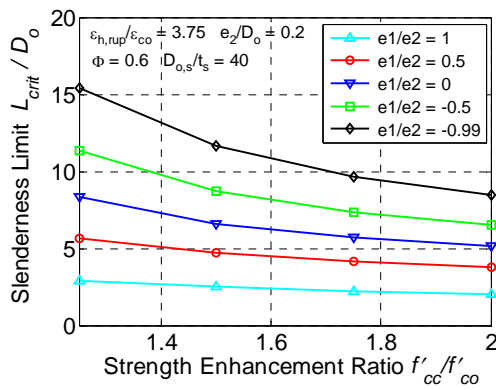
**Figure 9.2** Effect of normalized eccentricity ratio



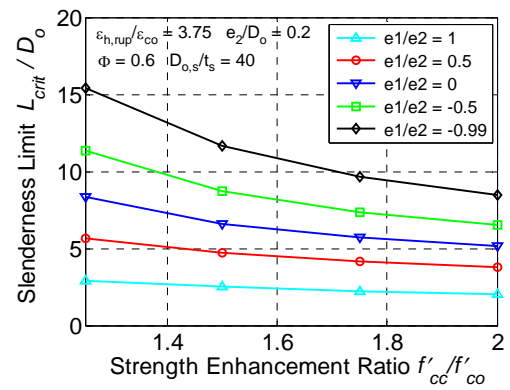
(a)  $e_2/D = 0.05$



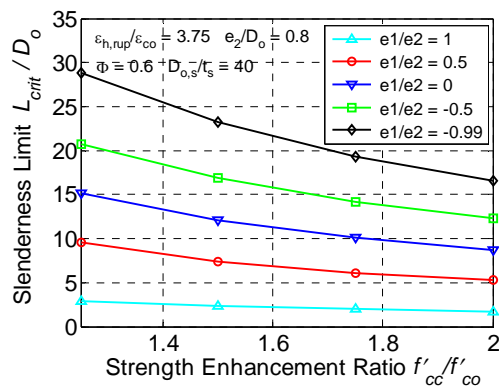
(b)  $e_2/D = 0.1$



(c)  $e_2/D = 0.2$

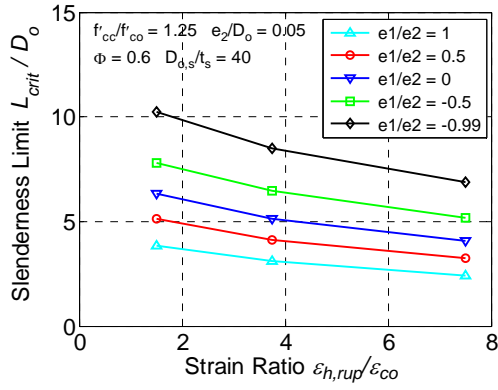


(d)  $e_2/D = 0.4$

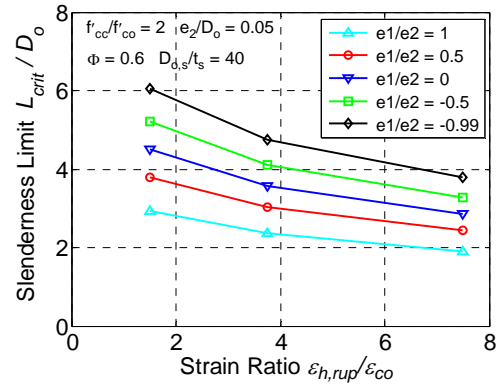


(e)  $e_2/D = 0.8$

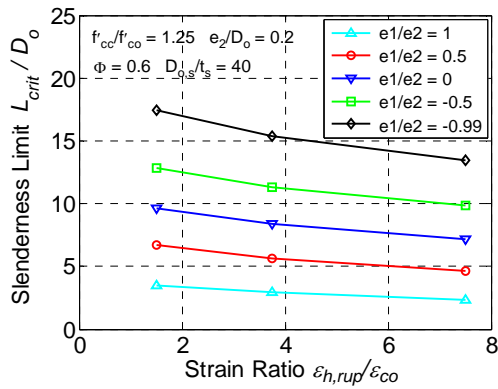
**Figure 9. 3** Effect of strength enhancement ratio



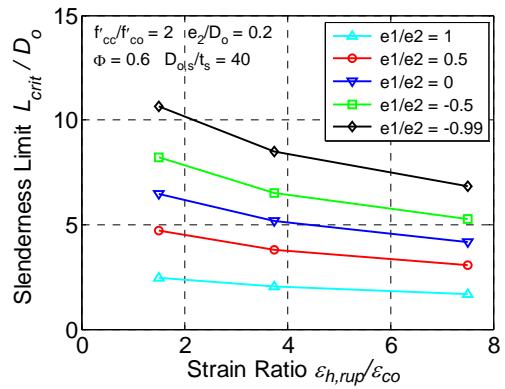
(a)  $e_2/D = 0.05, f'_{cc}/f'_{co} = 1.25$



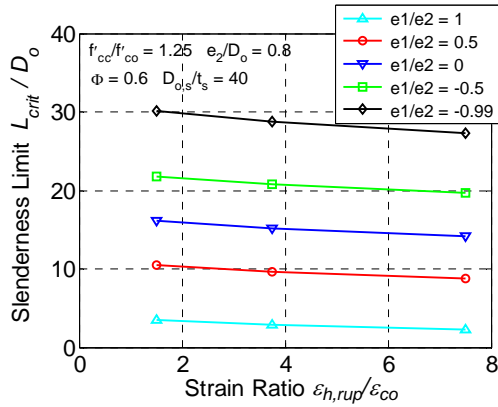
(b)  $e_2/D = 0.05, f'_{cc}/f'_{co} = 2$



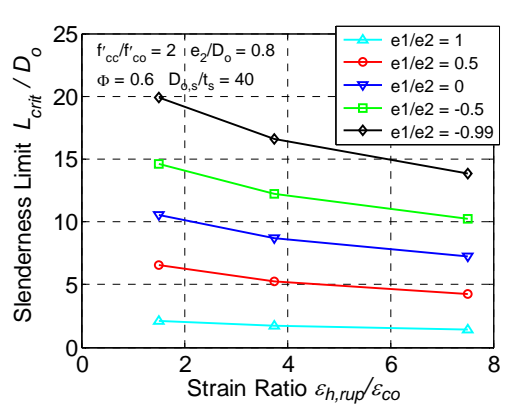
(c)  $e_2/D = 0.2, f'_{cc}/f'_{co} = 1.25$



(d)  $e_2/D = 0.2, f'_{cc}/f'_{co} = 2$

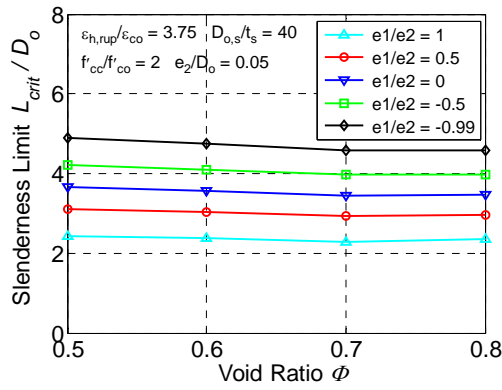


(e)  $e_2/D = 0.8, f'_{cc}/f'_{co} = 1.25$

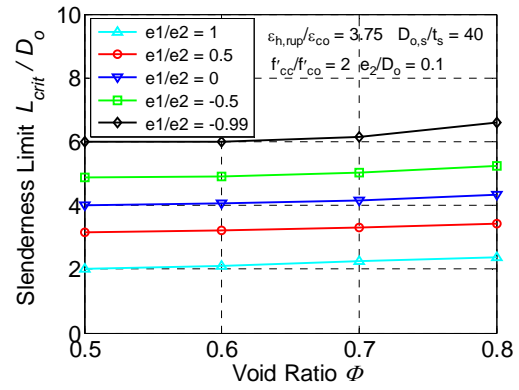


(f)  $e_2/D = 0.8, f'_{cc}/f'_{co} = 2$

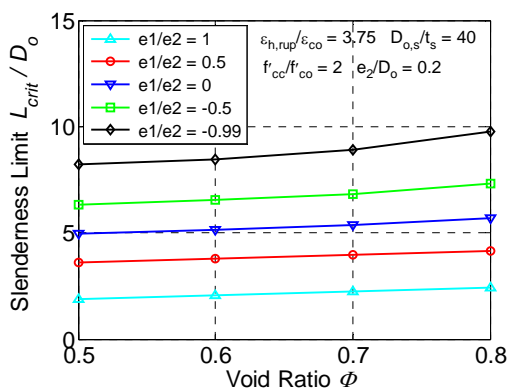
**Figure 9. 4** Effect of strain ratio



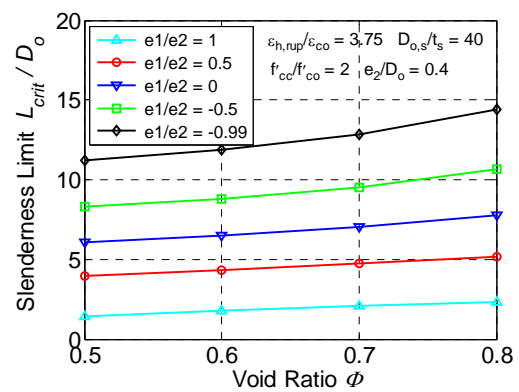
(a)  $e_2/D = 0.05$



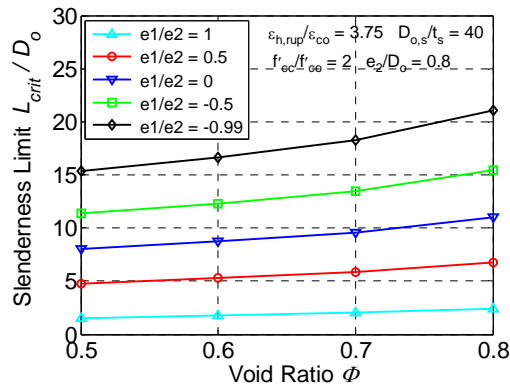
(b)  $e_2/D = 0.1$



(c)  $e_2/D = 0.2$

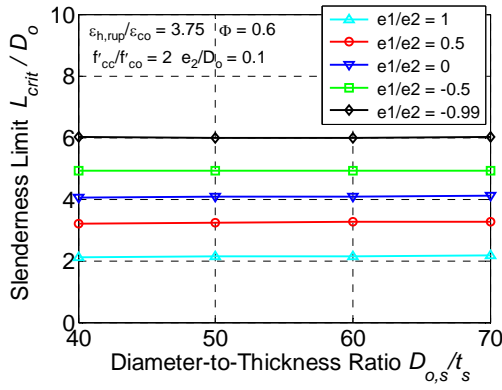


(d)  $e_2/D = 0.4$

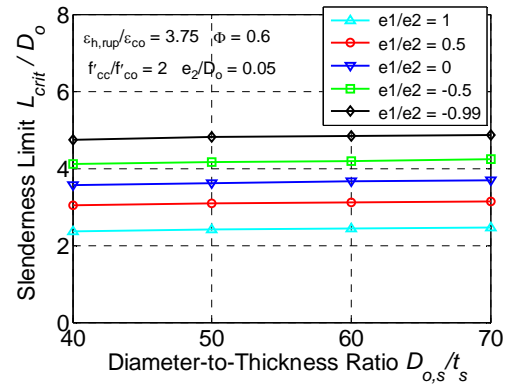


(e)  $e_2/D = 0.8$

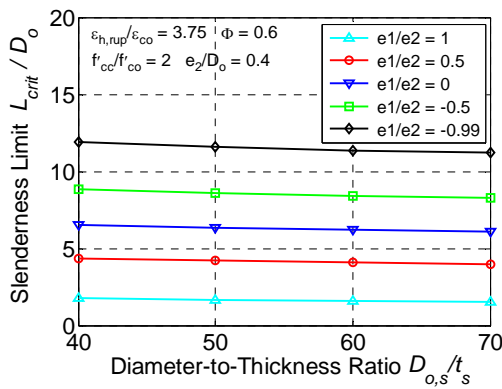
**Figure 9.5** Effect of void ratio



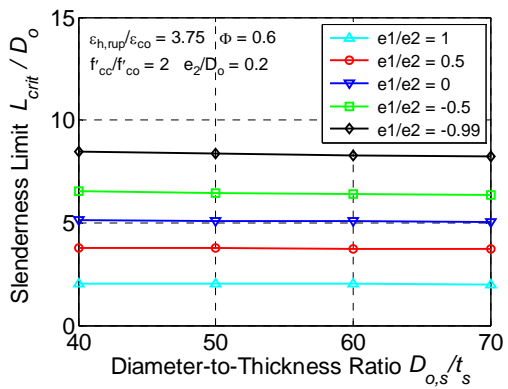
(a)  $e_2/D = 0.05$



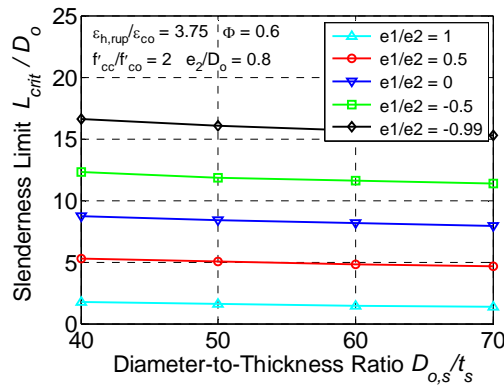
(b)  $e_2/D = 0.1$



(c)  $e_2/D = 0.2$



(d)  $e_2/D = 0.4$



(e)  $e_2/D = 0.8$

**Figure 9.6** Effect of steel tube diameter-to-thickness ratio

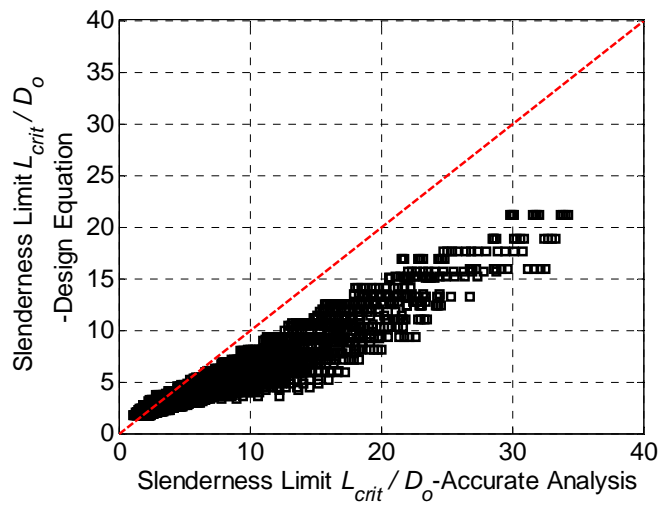


**Figure 9.7** Performance of Eq. (9.1) based on 5% axial load reduction criterion

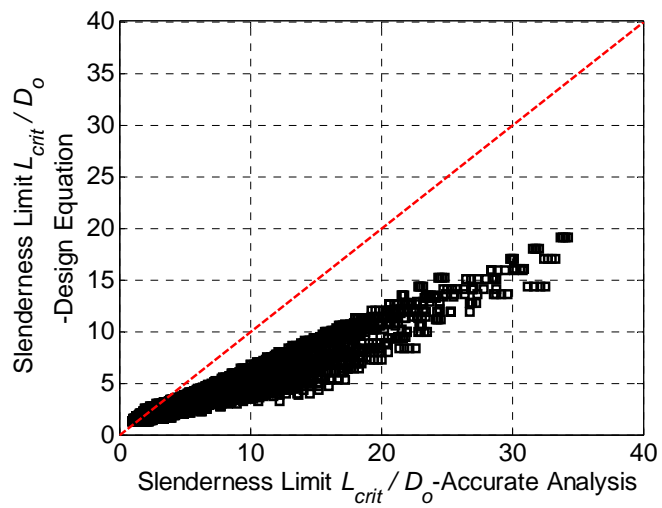


**Figure 9.8** Performance of Eq. (9.3) based on 5% axial load reduction criterion

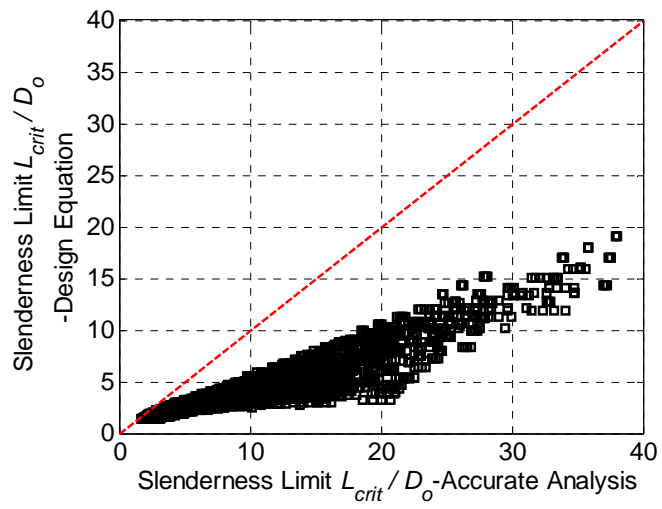


**Figure 9. 9** Performance of Eq. (9.3) based on 10% axial load reduction criterion



# CHAPTER 10

## CONCLUSIONS

### 10.1 INTRODUCTION

This thesis has presented an in-depth investigation into the behavior of large-scale SCC-filled hybrid DSTCs, both short and slender, subjected to concentric and eccentric compression. The previous studies on hybrid DSTCs have generally been limited to small-scale specimens and paid limited attention to the use of SCC although it stands a promising candidate as the infill material for the relatively narrow annular space of hybrid DSTCs due to its excellent flowability. Several issues related to the use of filament-wound FRP tubes and SCC in CFFTs have also been examined in this thesis as a prerequisite.

A compression test method and a hydraulic pressure test method to respectively characterize the longitudinal and the circumferential properties of filament-wound FRP tubes for confining concrete were first proposed. A theoretical model for CFFTs subjected to axial compression was next developed, in which the biaxial stress state and the material nonlinearity of the FRP tube are properly accounted for. In parallel, results of concentric compression tests conducted on 23 CFFTs filled with NC or SCC of four different sizes were presented. Then, the experimental program on large-scale hybrid DSTCs were presented. The experimental program comprised concentric compression testing of 11 short large-scale hybrid DSTCs and eccentric compression testing of six short and nine slender large-scale hybrid DSTCs, under various combinations of test parameters, which included mainly the load eccentricity, column slenderness, thickness of FRP tube and void ratio. The majority of the specimens were filled with SCC. To capture the effects of slenderness and eccentricity on the

compressive behavior of hybrid DSTCs, a theoretical column model, which traces the lateral deflection of columns using the numerical integration method and incorporates an eccentricity-dependent stress-strain model for concrete in hybrid DSTCs, was formulated. Finally, a slenderness limit expression, which differentiates short hybrid DSTCs from the slender ones, was proposed, based on the results of a comprehensive parametric study performed using the theoretical column model.

This chapter summarizes the conclusions drawn from the experimental and theoretical work of this thesis and highlights the further research needs towards the end of this chapter.

## **10.2 TEST METHODS FOR DETERMINING MATERIAL PROPERTIES OF FILAMENT-WOUND FRP TUBES**

Motivated by the need to provide accurate material properties of filament-wound GFRP tubes for use in the subsequent studies, Chapter 3 was concerned with the exploration of suitable test methods to fulfill this goal. Several test methods, including strip tension tests, strip compression tests, split disk tests, compression tests on FRP tubes and hydraulic pressure tests, were conducted. The first three types of tests were conducted under the guidance of existing test standards. It was shown that the strip tension and strip compression tests in which the strips were cut along the longitudinal direction of the tube cannot supply accurate measure of properties of filament-wound FRP tubes with a large fiber winding angle due to the lack of enough anchorage of the cut fibers. It was also shown that the split disk tests cannot accurately measure the hoop modulus of elasticity of filament-wound GFRP tubes either as a result of existence of bending in gauge section or friction between the split disks and the ring specimen. For the last two types of tests, since existing codified test methods of the

same type are not directly applicable to tube specimens with a relatively large dimensional variation, a compression test method on FRP tubes and a hydraulic pressure test method, both involving the use of specifically designed test fixtures, were proposed. The proposed test methods are more accurate than conventional test methods based on strip specimens and ring specimens. Meanwhile, they are easier to operate and allow for a relatively large dimensional variation in the tube specimens, compared with existing codified test methods of the same type. Therefore, the proposed test methods were used to characterize the material properties of the filament-wound FRP tubes for use in the subsequent theoretical analyses in this thesis.

### **10.3 EFFECTS OF SCC AND NONLINEAR BIAxIAL TUBE BEHAVIOR ON THE BEHAVIOR OF CFFTS**

The effects of SCC and nonlinear biaxial behavior of filament-wound FRP tube on the compressive behavior of CFFTs were examined in Chapter 4 and 5 as a prerequisite for studying the compressive behavior of hybrid DSTCs. Chapter 4 presented the results of axial compression tests on three series of CFFT specimens, filled with normal concrete (NC), SCC and self-compacting expansive concrete (SCEC), respectively. The diameter of the specimens ranged from 150 mm to 400 mm. The test results revealed that the stress-strain curves of the three types of confined concrete feature a similar bilinear shape and are similarly affected by the level of confinement provided by the FRP tube. However, CFFTs made with SCC have a stronger dilation tendency than those made with NC and SCEC, leading to a larger lateral-to-axial strain ratio and unstable axial stress-axial strain response of the former if the stiffness of the confining FRP tube does not exceed a certain threshold value. This difference in behavior is believed to be attributed to the large shrinkage of SCC. The unstable performance of SCC-filled FRP tubes under a weak confinement level can be

improved by adding an appropriate amount of shrinkage-reducing admixture or increasing the confinement level.

Chapter 5 presented the formulation of a theoretical model for CFFTs considering the nonlinear biaxial behavior of the filament-wound FRP tube. The proposed model combines Jiang and Teng's (2007) stress-strain model for FRP-confined concrete and a nonlinear biaxial model for the FRP tube. For the latter, both Hahn and Tsai's (1973) model and Jones and Nelson's (1975) model were examined. For comparison purposes, less sophisticated modeling approaches which ignore the axial stiffness or the material nonlinearity of the FRP tube were also performed. The predictions by different modeling approaches were compared with the results of tests on CFFTs presented in Chapter 4. The comparisons indicated that: (1) if the FRP tube is assumed to be linear elastic and possess only stiffness in the hoop direction (1D analysis), the theoretical model may significantly underestimate the axial load resisted by the CFFT; (2) if the FRP tube is assumed to be linear elastic and in a biaxial stress state (2D analysis), the theoretical model may overestimate the axial load resisted by the CFFT; (3) if the nonlinear biaxial behavior of the FRP tube is properly accounted for, the theoretical model can provide accurate predictions of the axial compressive behavior of CFFTs; and (4) the use of Jones and Nelson's (1975) model in the proposed theoretical model for CFFTs leads to more accurate predictions than the use of Hahn and Tsai's (1973) model; therefore, the use of Jones and Nelson's (1975) model is recommended.

#### **10.4 COMPRESSIVE BEHAVIOR OF LARGE-SCALE HYBRID DSTCS**

The behavior of large-scale hybrid DSTCs, both short and slender, subjected to concentric and eccentric compression, was studied in Chapters 6 to 8. The majority of

the specimens were filled with SCC. On the experimental side, a total of 17 large-scale short hybrid DSTCs and nine large-scale slender hybrid DSTCs were tested. The majority of the specimens were filled with SCC. On the theoretical side, a column model was developed to capture the effects of slenderness and eccentricity on the compressive behavior of hybrid DSTCs.

#### **10.4.1 Behavior of Short Hybrid DSTCs under Concentric Compression**

The behavior of large-scale short hybrid DSTCs under concentric compression was studied in Chapter 6. The main test parameters included the types of concrete (i.e., NC and SCC) and FRP tubes (post-applied GFRP wraps and filament-wound GFRP tubes), the void ratio and the thickness of FRP tubes. The test results indicated that:

(1) Similar to small-scale hybrid DSTCs, large-scale hybrid DSTCs possess excellent ductility under axial compression and their axial load capacity and ductility increase with the thickness of FRP tubes.

(2) The enhancement of axial load capacity of a hybrid DSTC due to the interaction between the constituent materials (i.e., confinement action) is limited for cases with a large void ratio and a relatively weak confinement level. This suggests that hybrid DSTCs with a large void ratio should be provided with relatively stiff FRP tubes to ensure the beneficial effect of the confinement action.

(3) A drop in axial load undertaken by the concrete in hybrid DSTCs may occur once the unconfined concrete strength is reached when the confinement is provided by filament-wound FRP tubes instead of post-applied FRP wraps. It is believed that the axial load drop is attributed to a gap between the annular concrete and the wall of the

outer FRP tube due to concrete shrinkage, which delays the activation of the confinement action of the filament-wound FRP tube. The axial load drop is more substantial for SCC and may translate into a drop in the total axial load of the hybrid DSTC.

The test results were also compared with Yu *et al.*'s EccI stress-strain model for concrete in hybrid DSTCs originally developed on the basis of test results of concentrically-loaded small-scale hybrid DSTCs. It was shown that Yu *et al.*'s EccI stress-strain model can provide reasonably accurate predictions for the stress-strain behavior of concrete in large-scale hybrid DSTCs for cases without axial stress drop of concrete. However, Yu *et al.*'s EccI model is unable to predict the axial stress drop of concrete due to its simple nature.

#### **10.4.2 Behavior of Short Hybrid DSTCs under Eccentric Compression**

The behavior of large-scale short hybrid DSTCs under eccentric compression was studied in Chapter 7. The main test parameters included the load eccentricity and the thickness of FRP tubes. The test results indicated that:

(1) The failure mode of eccentrically-loaded short hybrid DSTCs is the rupture of the outer FRP tube at the compression side at or near specimen mid-height. Buckling of the inner steel tube may occur due to the combined effect of axial shortening and bending.

(2) The axial load capacity of eccentrically-loaded short hybrid DSTCs decreases with load eccentricity and increases with thickness of FRP tubes. Short hybrid DSTCs may experience a sudden drop in axial load once the unconfined concrete strength is

reached, a phenomenon similar to that observed in the concentric compression tests on hybrid DSTCs presented in Chapter 6, but to a much less significant extent.

(3) When a hybrid DSTC is loaded under eccentric compression, an axial strain gradient exists over its section with the distribution of axial strains generally conforming to the plane section assumption. The axial strain gradient causes the concrete at the more compressed region to have a tendency to dilate to the less compressed region. As a result, the same concrete in a hybrid DSTC features a larger axial strain at ultimate condition under eccentric compression than under concentric compression. This phenomenon is termed “axial strain enhancement effect” and indicates that the eccentricity has a certain effect on the stress-strain behavior of confined concrete in hybrid DSTCs.

To capture the effect of eccentricity on the stress-strain behavior of confined concrete in hybrid DSTCs, three existing stress-strain models (Yu *et al.*'s EccI model, Yu *et al.*'s EccD model and Lin's EccD model) were employed and compared with the test results. The three stress-strain models were respectively incorporated into a theoretical column model which can deal with the slenderness effect. The use of a column model instead of simple section analysis for short hybrid DSTCs was intended to achieve higher accuracy of analysis since a certain slenderness effect existed in the tested columns despite their short length. It was shown that when incorporated into the theoretical column model, Yu *et al.*'s EccI model, Yu *et al.*'s EccD model and Lin's EccD model all provide fairly accurate predictions for the axial load capacity of eccentrically-loaded hybrid DSTCs. However, Lin's EccD model performs much better in predicting the axial strain and the lateral deflection of eccentrically-loaded hybrid DSTCs because it takes the axial strain enhancement effect into consideration.

### 10.4.3 Behavior of Slender Hybrid DSTCs

The compressive behavior of large-scale slender hybrid DSTCs was studied in Chapter 8. Most specimens were tested under eccentric compression while one specimen was tested under concentric compression as a reference. The main test parameters included the column slenderness, the load eccentricity and the thickness of FRP tubes. The test results indicated that:

(1) Two different failure modes of slender hybrid DSTCs subjected to eccentric compression were observed, including the flexure-dominated mode and the compression-dominated mode, depending on the eccentricity and the column slenderness. Hybrid DSTCs with a larger slenderness and eccentricity are more susceptible to the flexure-dominated failure mode.

(2) As the slenderness ratio increases, the failure of hybrid DSTCs changes from material failure to stability failure. The latter is featured by a descending branch in the axial load-lateral deflection curve of the column.

(3) Slender hybrid DSTCs exhibit excellent ductility under both concentric and eccentric compression. The axial load capacity of slender hybrid DSTCs decreases with column slenderness and load eccentricity. The lateral deflection of slender hybrid DSTCs at ultimate condition increases with column slenderness and load eccentricity.

(4) Increasing the thickness of FRP tube has a reduced effect in enhancing the axial load capacity of hybrid DSTCs as the column slenderness increases. This is mainly because the increase of section strength due to FRP confinement could not be fully

translated into an equivalent increase in column strength because of the increased slenderness effect. However, increasing the thickness of FRP tube can lead to more stable post-peak behavior of slender hybrid DSTCs. So relatively stiff FRP tubes are recommended for use in slender hybrid DSTCs especially when filled with SCC.

To capture the slenderness effect, the theoretical column model formulated in Chapter 7 was employed to simulate the behavior of slender hybrid DSTCs. Again, Yu *et al.*'s EccI model, Yu *et al.*'s EccD model and Lin's EccD model were respectively incorporated into the column model. It was shown that the three analytical approaches all provide reasonable accuracy in predicting the axial load capacity of slender hybrid DSTCs. However, the approach incorporating Lin's EccD model is more accurate than the other two in predicting the lateral deflection of eccentrically-loaded slender hybrid DSTCs at ultimate condition due to the consideration of the axial strain enhancement effect.

## **10.5 SLENDERNESS LIMIT FOR SHORT HYBRID DSTCS**

Finally, Chapter 9 proposed a slenderness limit expression which differentiates short hybrid DSTCs from the slender ones to complete an existing design procedure for short hybrid DSTCs. To this end, a comprehensive parametric study was performed using the theoretical column model formulated in Chapter 7 to clarify the effects of a variety of parameters on the slenderness limit for short hybrid DSTCs. The examined parameters include the end eccentricity ratio, the normalized eccentricity ratio, the strength enhancement ratio, the strain ratio, the void ratio and the diameter-to-thickness ratio of steel tube. Parameters of a major, moderate or minor effect on the slenderness limit for short hybrid DSTCs are identified based on the results of the parametric study, laying a solid theoretical foundation for the development of the

slenderness limit expression. The proposed slenderness limit expression takes a form similar to that of the slenderness limit expression specified in GB-50608 (2010) and includes a new item to account for the effect of the void ratio. The proposed expression is more conservative than the GB-50608 expression and is intended to provide a lower-bound prediction.

## **10.6 FUTURE RESEARCH**

The present research program has led to an in-depth understanding of the structural behavior of large-scale hybrid DSTCs. However, much further research is still needed to address several issues remained not completely clear and to promote the applications of hybrid DSTCs in practice. The main issues needing further research are detailed below:

(1) To mitigate the adverse effect of shrinkage of SCC on the behavior of hybrid DSTCs, the use of self-compacting expansive concrete (SCEC) as the infill material stands a promising solution. Much more tests on large-scale hybrid DSTCs filled with SCEC are needed to verify their structural performance and to prescribe the dosage of the expansive agent.

(2) A three-dimensional FE model should be developed to simulate the behavior of eccentrically-loaded hybrid DSTCs and verified against a much more comprehensive test database. Based on the results of the FE analysis, the exact effect of load eccentricity on the stress-strain behavior of confined concrete in hybrid DSTCs can be identified and thus a more accurate EccD stress-strain model can be developed.

(3) A set of reliable design equations need to be established for hybrid DSTCs,

especially slender hybrid DSTCs to facilitate wider applications of hybrid DSTCs. The design equations should be prepared in a format familiar to the design community.

## 10.7 REFERENCES

- Hahn, H.T. and Tsai, S.W. (1973). “Nonlinear Elastic Behavior of Unidirectional Composite Laminae”, *Journal of Composite Materials*. Vol.7, pp.102-118.
- Jones, R.M. and Nelson JR, D.A.N. (1975). “A New Material Model for the Nonlinear Biaxial Behavior of ATJ-S Graphite”, *Journal of Composite Materials*. Vol.9, pp.10-27.
- Jiang, T. and Teng, J.G. (2007). “Analysis-Oriented Stress-Strain Models for FRP-Confined Concrete”, *Engineering Structures*. Vol. 29(11), pp.2968-2986.
- Teng, J.G., Yu, T., Wong, Y.L. and Dong, S.L. (2007). “Hybrid FRP-Concrete-Steel Tubular Columns: Concept and Behavior”, *Construction and Building Materials*. Vol. 21(4), pp. 846-854.